UNIVERSITAT DE BARCELONA

Usefulness of in vivo reflectance confocal microscopy and automated videomosaics in the treatment and management of skin cancers

Ús de la microscòpia confocal de reflectància in vivo i dels videomosaics automatitzats en el tractament i seguiment dels càncers cutanis

Oriol Yélamos i Pena

Usefulness of in vivo reflectance confocal microscopy and automated videomosaics in the treatment and management of skin cancers

Ús de la microscòpia confocal de reflectància in vivo i dels videomosaics automatitzats en el tractament i seguiment dels càncers cutanis

Memòria presentada per

Oriol Yélamos i Pena

Per optar al títol de Doctor per la Universitat de Barcelona

Milind Rajadhyaksha, PhD

Director

Dermatology Service

Memorial Sloan Kettering Cancer Center

New York City

Susana Puig i Sardà, MD, PhD

Tutora

Servei de Dermatologia

Hospital Clínic de Barcelona

Universitat de Barcelona

Tesi inscrita en el programa de Doctorat en Medicina i Recerca Translacional

Grup d'investigació: Melanoma: Imatge, genètica i immunologia

Facultat de Medicina – Campus Casanova, Universitat de Barcelona

Barcelona, Juny de 2019

“Carpe diem”

A la meva família, d’aquí i d’allà, qui sempre ha cregut en mi m’ha fet somiar

To my family, from here and there, who always believed in me and made me dream

AGRAÏMENTS / ACKNOWLEDGEMENTS

Hi ha tanta i tanta gent a la que vull agraïr en aquesta tesi que quasi no sé ni per on començar. Vull començar agraïnt al meu director, Milind Rajadhyaksha, per la seva inspiració, guia i ajuda en els diferents estadis de la tesi doctoral. I want to really thank you Milind for inventing the reflectance confocal microscope (of course) as well as always having the door open to discuss new ideas and projects, either at the office but also at your house or at a bar. Milind, you have been one of the most insipirational people I have ever met and I hope we keep our friendship forever.

I also want to thank all my colleagues from Milind's lab (and now friends) with whom I have worked with and enjoyed my two years in New York: Miguel, Kivanc, Gary, Aditi, Eileen, Heidy... and especially the research fellows who have been crucial to survive and enjoy two amazing years in NYC; thanks Konstantinos Lyopiris, Cristián Navarrete, Shamir Geller, Azael Freites and also Mr Arevalo! L'únic castellà políglota i capaç de cantar l'Estaca en mig de Manhattan! I also want to thank the Mohs team (Jason Chen, Kishwer Nehal, Anthony Rossi, Erica Lee) for letting me image patients while they had to perform surgery on them. Thanks for the patience!

Of course I want to thank Drs Allan Halpern and Ash Marghoob for their mentorship and guidance in melanoma management, dermoscopy, confocal microscopy and for believing in me during this exciting period of time I had the honor to share with all of you. There are many more I want to thank from MSKCC; Mike Marchetti, Manu Jain, the rest of attendings, all the nurses, technicians and in general all the crew from that amazing dermatology department.

Vull també agraïr a la meva tutora, Susana Puig, per haver-me permès entrar al grup de recerca del servei de dermatologia del Clínic, i creure en mi un cop vaig tornar dels EUA per poder seguir fent recerca i aprendre dels grans experts que sou tot el grup de del Clínic. Entre ells, vull destacar la gran feina feta pels Drs Josep Malvehy i Cristina Carrera, que m'han estat de gran ajuda i referent durant tots aquests anys. Que sapigueu que tot i que ara no estic directament amb vosaltres, no us desempallegareu tan fàcil de mi perquè seguirem col·laborant ja que tenir el Clínic a casa nostra és un gran orgull i referent. Per tot el que m'heu ensenyat i pel que encara aprendré de vosaltres, les meves més profundes gràcies. Gràcies també a TOT el servei de dermatologia del Clínic, incloents els adjunts, residents, fellows i especialment infermeria i tècnics d'imatge, sense els quals no hagués pogut ni tant sols utilitzar el SAP.

El cert és que aquesta tesi no seria possible si no fos per tota la gent que m'ha animat des del principi a perseguir els meus somnis i a mirar de no rendir-me davant cap adversitat. Lògicament, els primers de la llista són els meus pares, Tomàs i Pepita, sense els quals RES del que he fet seria possible (lògicament la concepció hi té un paper important). Sense cap mena de dubte ells han estat els impulsors de la meva carrera professional, han confiat en mi, essent sempre molt crítics amb totes les decisions que

prenia per tal que quan prengués un camí, fos el que fos, cregués que era el més adequat, profitós i apassionant. D'ells vull destacar el seu afecte i amor, però també haver-me aguantat durant tants anys d'estudi, però sobretot la seva passió pel coneixement, i per fer-me veure que la vida és massa curta com per penedir-se del que un no ha fet. "Si no te quejas, no te quejes" i "carpe diem" oi? Us estimo amb bogeria.

Però ells no són els únics familiars als que els dec aquest doctorat. Els meus avis, tots 4, estarien molt més que orgullosos del meu doctorat, i sé que sobretot un d'ells, el primer Yélamos, el meu iaio, n'estaria més que orgullós. D'ell surt aquesta faceta inquieta i insaciable de coneixement que duc dins. I d'ell va passar al meu pare, l'únic Doctor Yélamos (en Biologia, òbviament) que hi ha (havia) a la família. I és que mai m'ha agradat que em diguin doctor, ja que l'únic doctor que hi ha és el que té el doctorat. Afortunadament, això ja canvia i ja podré dir que sóc veritablement Doctor. Va per vosaltres, papa, mama, iaio, iaia, padrí, i especialment PADRINA! Els de Seròs, qui no en fa una en fa dos!

Podria passar-me hores i hores agraïnt a la meva família, tiets, tietes, cosines, avis segons... Gent que m'han fet suport i m'han ajudat a ser qui sóc avui en dia. En aquest sentit no vull passar per alt els meus amics de la infantesa, els 4 amics veritables, amb els que realment parlo (tot i que menys del que voldria) però que adoro i amb els quals hem compartit bons i mals moments, creixent i avançant al llarg del temps. Gràcies Albert Sanjuàs per alegrar-nos la vida amb la teva música i el teu humor àcid. Gràcies Xavi Omella (mami) per ser qui ets, quelcom conformista, però bé, és el que tenen els genis, que aneu sobrats. Il faut parler en français plus souvent Mr Omeille! I finalment gràcies gràcies gràcies al Santi Marfà, company inseparable de batalles, i sense el qual la tesi no seria possible (més que res perquè li he copiat el format de la seva tesi i no he parat de torturar-lo a base de preguntes tècniques sobre la burocràcia de la tesi). Merci crack!

Voldria també destacar el paper crucial en aquesta tesi dels meus mentors durant la residència a l'Hospital de Sant Pau, al cap de servei Lluís Puig pel seu feedback sempre crític, a la Lali Baselga per estimular-me a escriure el meu primer article en anglès i veure que es pot fer recerca a Catalunya. Gràcies a tota la resta d'adjunts (Dalmau amb qui vam escriure un article explosiu sobre nitroglicerina, Barnadas per la seva sistemàtica rotació, Esters pel vostre coneixement i caliu, Didac Barco per ensenyar-me una manera de tractar als pacients de 10! Tots tots tots! Voldria agrair també als meus co-Rs de derma (Caridad, Alba, Jorge, Anna, Vero, Elena, Paulina Joan, Miquel), i a taaants co-Rs de la resta de l'hospital (Mar, Marta, Irati, X Lassaro, i mil més) per haver estat el gran suport que heu estat durant i després de la residència. I voldria agrair en especial a la Dra Pilar Garcia Muret, possiblement la persona que més m'ha estimulat a nivell professional des de l'inici. Pili, tu sempre em vas dir que confiés en mi, que demanés beques, que voltés pel món, que publiqués, que fes el que la gent no fa... I així vaig marxar a Chicago, i allà tot va canviar.

Gràcies al conjunt de caramboles més gran del món, vaig conèixer al Joan Guitart i l'Estela Martínez qui em van ensenyar que Chicago és LA MILLOR ciutat dels Estats Units, que no només hi ha Trump a EUA i que s'hi fan coses genials en aquell país, com captar el millor talent per fer que el coneixement creixi i creixi. Gràcies a vosaltres vaig tenir l'oportunitat de treballar a Northwestern i compartir la recepta del Thanksgiving turkey (això gràcies a la Gerta!), això per no oblidar-nos d'haver conegut la penya del Barça de Chicago amb tots els seus integrants (gràcies a vosaltres també Chi people!).Thanks Dr Pedram Gerami for your mentorship during my stay in Chicago, for pushing the limits of knowledge and for making me publish 1 article per month! Your capacity to understand science in unbelievable! I les caramboles van seguir perquè gràcies a Chicago vaig poder anar al Memorial de Nova York on realment la tesi es va gestar gràcies a la col·laboració entre la Cristina Carrera, Susana Puig i en Milind Rajadhyaksha (thanks again!).

I les caramboles van seguir perquè va ser a Chicago on vaig conèixer la persona que realment ho ha canviat tot, la meva estimada Rachel. Thanks Rachel for always being here, also when we were apart. Thanks for being crazy enough to leave everything behind to pursue a dream of happiness here in Barcelona. Without your support (and patience) nothing would have happened. Please, never give up, dream big and follow your dreams. I love you so much! T'estimo!!

Finally I want to thank the thesis jury for having had the patience to read the thesis, evaluate it and I hope you enjoy it, as much as I have enjoyed working on it.

The show must go on!

PRESENTACIÓ I RESUM

El càncer de pell representa un important problema de salut pública ja que la seva incidència no ha parat d'augmentar en les darreres dècades. El tractament estàndard del càncer de pell segueix essent la cirurgia, que sovint pot ser complexa i potencialment morbida ja que la majoria dels càncers de pell aparèixen en sones zones visibles com la cara. Per tant, qualsevol mètode que permeti millorar-ne el tractament i minimitzar-ne les cicatrius és crucial. En aquest sentit, les tecnologies d'imatge no invasives poden ser de gran ajuda per determinar els marges tumorals abans del seu tractament, controlar la resposta al tractament i detectar la presència de persistència o recurrència de forma precoç.

La microscòpia confocal de reflectància és una d'aquestes tecnologies d'imatge no invasiva que posseeix una resolució cel·lular i ha demostrat tenir una alta precisió diagnòstica per als diferents tipus de càncers de pell, ja siguin carcinomes queratinocítics, melanomes o la malaltia de Paget. Actualment dos microscopis confocals de reflectancia estan disponibles al mercat: 1) un microscopi de sonda àmplia que requereix adherir un anell de metall/plàstic a la pell per tal obtenir mosaics d'imatges de fins a 8 x 8 mm; 2) un microscopi de mà que permet obtenir imatges de forma lliure amb un camp de visió que oscil·la entre 0,75 i 1 mm. El microscopi de mà té l'avantatge que permet avaluar àrees superiors a 8 x 8 mm navegant pel damunt de la pell segons les necessitats de l'operador, però no té la capacitat de generar mosaic en el seu programari natiu, de manera que l'orientació és complicada. No obstant, és lògic pensar que el microscopi de mà és l'eina ideal per predefinir els marges dels càncers de pell i controlar-ne la resposta al tractament gràcies a la seva versatilitat, especialment quan la mida del tumor és superior a 8 mm.

La present tesi doctoral és el resultat de la col·laboració entre els departaments de dermatologia de l'Hospital Clínic de Barcelona i el Memorial Sloan Kettering Cancer Center (MSKCC) de Nova York, i també va ser parcialment finançada per la Fundación Piel Sana a través de la "Beca Excelencia 2016". Des de 2015 fins a 2017 he treballat a Nova York per estudiar l'impacte de la microscòpia confocal i com l'addició dels videomosaics pot millorar el seguiment dels càncers de pell. L'objectiu d'aquesta tesi doctoral ha estat desenvolupar un algoritme informàtic per obtenir mosaics 2D estàtics obtinguts a partir de vídeos dinàmics obtinguts amb el microscopi confocal de mà, i aplicar aquesta tècnica per abordar alguns dels reptes que els metges es troben en fer front a càncers de pell, com ara definir els marges dels càncers de pell abans de la cirurgia (especialment important en alguns d'ells com el lentigen maligne que tenen marges mal definits), identificar el tumor residual directament a la ferida quirúrgica, així com identificar petits focus de tumor recurrents o persistents en entitats com la malaltia de Paget extramamària. Les meves responsabilitats principals en la tesi actual han estat l'obtenció dels vídeos i imatge de microscòpia confocal, la seva conversió en videomosaics utilitzant el nou algoritme informàtic, l'anàlisi tant dels vídeos com dels

videomosaics, i l'anàlisi de totes les dades clíniques presentades en les 5 publicacions incloses en aquesta tesi.

La **primera publicació** d'aquesta tesi descriu l'algoritme informàtic que permet generar videomosaics a partir de videos de micròscopia confocal. En aquest manuscrit es descriu l'algoritme i es proporcionen exemples clínics per mostrar-ne l'aplicabilitat a la pràctica clínica i el seu potencial ús en altres sistemes microscòpics. La **segona publicació** aplica els videomosaics per delimitar els marges preoperatoris en una sèrie consecutiva de 23 lentigens malignes, mostrant que el confocal de mà amb videomosaics pot predir correctament el defecte quirúrgic després de la cirurgia. A la **tercera publicació**, es va utilitzar el confocal de mà per identificar la persistència o la recurrència de malaltia de Paget extramamària després de diferents tractaments. En aquesta publicació es van utilitzar videomosaics només en alguns pacients però es va demostrar que la precisió diagnòstica millorava amb l'addició dels videomosaics comparat amb el confocal de mà convencional. A la **quarta i cinquena publicacions**, es van fer servir els videomosaics per identificar tumor residual directament dins de la ferida quirúrgica després de tractar carcinomes de queratinòcits (després d'ablació làser en la quarta publicació i després de cirurgia de Mohs en la cinquena publicació), mostrant que és possible identificar petits focus de tumor residual utilitzant videomosaics directament dins de la ferida quirúrgica.

En resum, aquesta tesi demostra que els videomosaics amplien la utilitat del microscopi confocal de reflectància de mà pel que fa al tractament i seguiment del càncer de pell, permetent superar els principals obstacles d'aquesta tecnologia, mitjançant l'ampliació del camp de visió i l'obtenció d'informació arquitectònica crucial per a l'avaluació d'imatges microscòpiques.

PRESENTATION AND SUMMARY

Skin cancer is major health problem due to its increased incidence in the last decades. Standard treatment of skin cancer is still surgery, which can be challenging to perform since most skin cancers are located in visible areas such as the face. Hence, methods to improve skin cancer treatment and minimize scarring are crucial. In this sense, non-invasive imaging technologies can be of great help in determining the margins of skin cancers prior to their treatment, as well as they offer a great opportunity to monitor its treatment and detect early relapses.

Reflectance confocal microscopy (RCM) is one of this non-invasive imaging technologies which has cellular resolution and has shown to have high diagnostic accuracy for different types of skin cancers such as keratinocyte carcinomas, melanomas or Paget disease. Currently two RCM microscopes are commercially available: 1) a wide-probe microscope which requires attaching a metal/plastic ring on the skin to obtain image mosaics up to 8 x 8 mm; 2) a handheld RCM (HRCM) microscope which allows free imaging along the skin with a field of view which ranges from 0.75 to 1 mm. HRCM has the advantage that permits imaging areas larger than 8 x 8 mm by navigating over the skin but lacks mosaicking capabilities in its native software, making orientation complicated. However, it is intuitive to think that HRCM is the ideal tool to predefine the margins of skin cancers and to monitor its responses to treatment due to its versatility, especially when the size of tumor is larger than 8 mm.

The current PhD thesis is the result of the collaboration between the departments of dermatology of the Hospital Clínic de Barcelona – Universitat de Barcelona, and Memorial Sloan Kettering Cancer Center (MSKCC) in New York, and was also partially funded by the Fundación Piel Sana through the “Beca Excelencia 2016”. From 2015 until 2017 I have worked in New York in order to study the impact of HRCM and how the addition of videomosaicking could improve the management of skin cancers. The goal of this PhD thesis was to develop a computer algorithm to obtain static 2D mosaics obtained from dynamic videos obtained with HRCM, and to apply this technique to address some of the challenges that physicians encounter when managing skin cancers, such as defining the skin cancer margins prior to surgery (particularly important in some skin cancers such as lentigo maligna [LM] which have ill-defined margins), identifying residual tumor directly in the surgical wound, and identifying small foci of tumor in recurrent or persistent skin cancers which present in a patchy fashion such as extramammary Paget’s disease. My roles in the current thesis have been obtaining the HRCM videos, converting them into videomosaics using the novel computer algorithm, analyzing both the videos and videomosaics, and analyzing all the clinical data presented in the 5 publications included in this thesis.

The **first publication** of this thesis describes the videomosaicking algorithm developed by the joint efforts of the team at MSKCC and the team of Northeastern University in Boston. In this manuscript the algorithm is described as well as clinical examples are provided in order to showcase how this algorithm can be used not only in RCM but in other microscopic imaging systems. The **second publication** applies the videomosaicking algorithm to delineate the preoperative margins in a consecutive series of 23 LM/LM melanoma, showing that the HRCM with videomosaicking can correctly predict the surgical defect after staged excision with minimal variations. In the **third publication**, HRCM was used to identify persistence or recurrence of EMPD after different treatments. Here, the videomosaicking algorithm was used in some of the patients and showed that the diagnostic accuracy improved when videomosaics were added to the conventional HRCM examination. In the **fourth and fifth publications** HRCM and videomosaics were used to image directly in the surgical wound after treating keratinocyte carcinomas (after laser ablation in the 4th publication, and after Mohs surgery in the 5th publication), showing it is possible to identify residual tumor using HRCM and videomosaics directly inside the surgical wound.

In summary, this thesis shows how videomosaics expand the usefulness of HRCM in skin cancer management and overcome its main challenges by expanding the field of view and obtaining architectural information which is crucial when evaluating microscopic images.

ABBREVIATIONS

BCC: Basal Cell Carcinoma

CT: Computerized Tomography

KC: Keratinocyte Carcinoma

DEJ: Dermal epidermal junction

EDC: Electrodessication and Curettage

EMPD: Extramammary Paget Disease

FOV: Field Of View

HRCM: Handheld Reflectance Confocal Microscopy

HRCM-RV: Handheld Reflectance Confocal Microscopy With Radial Videomosaicking

LC-OCT: Line-Field Confocal Optical Coherence Tomography

LM: Lentigo Maligna

LMM: Lentigo Maligna Melanoma

MMS: Mohs Micrographic Surgery

MRI: Magnetic Resonance Imaging

MSKCC: Memorial Sloan Kettering Cancer Center

NMSC: Non-Melanoma Skin Cancers

OCT: Optical Coherence Tomography

RANSAC: RANdom SAmple Consensus

RCM: Reflectance Confocal Microscopy

SCC: Squamous Cell Carcinoma

SIFT: Scale Invariant Feature Transformation

SSM: Superficial Spreading Melanoma

SURF: Speeded Up Robust Features

UV: Ultraviolet

VM: videomosaics

CONTENTS

INTRODUCTION

1. Skin cancer

a) Epidemiology and significance

Skin cancers are the most common cancers in humans, being keratinocyte carcinomas (KC) and especially basal cell carcinoma (BCC) the most common of all skin cancers.[1] In the USA the age-adjusted prevalence and incidence for BCC is 226 and 343/100,000 people per year, respectively, which means around 4 million new cases of BCC per year.[1] In Europe the numbers are less striking but still very important, with an incidence about 50-80/100,000 people per year. Regarding the second most common KC, squamous cell carcinoma (SCC), its incidence varies from 32-270/100,000 people.[2] Importantly, the overall incidence of all skin cancers is growing every year due to several factors such as increased sun-exposure, immunosuppressant medications and increased life expectancy.[1]

Since the majority of skin cancers are located in cosmetically-sensitive locations such as the face, Mohs surgery, a form of surgery which controls the margins and minimizes disfiguration, is extensively used. This technique, besides being highly curative, is expensive and not always available in all practices. In addition, patients with previous skin cancers are more prone to develop additional cancers [3]. Melanoma is less common than KC but represents the main cause of mortality among all skin cancers. In fact, melanoma is the second cause of mortality among young individuals [4], resulting in very severe socioeconomic consequences. Other less frequent skin cancers such as Paget disease can have numerous recurrences, resulting in multiple biopsies and surgeries to identify persistence/recurrence[5,6]. Hence, skin cancer is currently a significant public health problem.[7]

Conversely, it is well known that early detection of skin cancers results in high cure rates and in addition is cost-effective.[8,9] Hence, methods to diagnose and optimize the treatment of skin cancers are necessary to improve the effectivity of our health systems. In this sense, in order to improve the diagnosis of skin cancer, several non-invasive tools have been developed such as dermoscopy or reflectance confocal microscopy (RCM). These techniques, discussed in this thesis, have shown to diagnose skin cancer with high diagnostic accuracy,[10-12] as well as they have a great potential to manage and guide treatment of skin cancers. This thesis will discuss a novel approach using RCM together with automated videomosaics to manage skin cancers such as KCs, melanomas on sun-exposed skin such as lentigo maligna, and extramammary Paget's disease (EMPD).

b) Types of skin cancers

Skin cancers include different subtypes of neoplasms according to its originating cell in the skin (Figure 1). When skin cancers originate from the keratinocytes in the epidermis they are named keratinocyte carcinomas (formerly known as non-melanoma skin cancers[13]). In addition, if cancer originates from the melanocytes, the cells which provide pigment to the skin, one may encounter a melanoma. Other rarer types of skin cancers can originate from the remaining cellular components of the skin, such as Merkel cell carcinomas (originated from Merkel cells), dermatofibrosarcoma protuberans (originated from fibroblasts in the dermis), or angiosarcomas (originated from the vascular cells within the dermis). More rarely, skin cancers can originate from cells present on the ducts or the sweat apocrine glands. Extramammary Paget disease (EMPD) is one of these cancers, which is considered an intraepithelial adenocarcinoma originating in areas rich of apocrine glands such as milky line which extends from the axilla to the groin.[14,15]

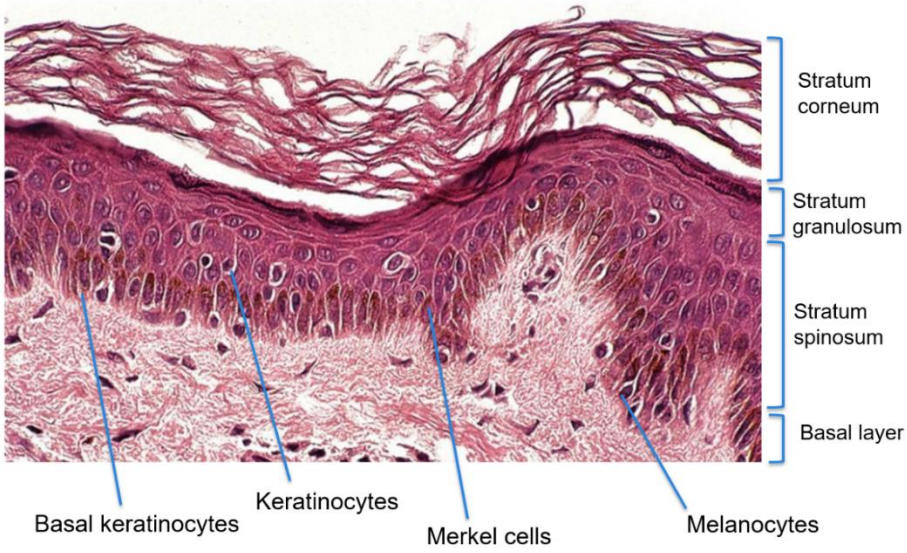

***Figure 1**: Structure and components of the epidermis (source: Oriol Yélamos)*

i. Keratinocyte carcinomas

Keratinocyte carcinomas include two types of skin cancers: basal cell carcinomas (BCCs) and squamous cell carcinomas (SCCs). **BCCs** are caused mainly due to cumulative ultraviolet radiation and occur in sun-exposed areas such as the head and neck area, limbs or upper trunk. Although BCC rarely produces metastasis, it grows slowly leading to local invasion that can be disfiguring either due to tumor destruction itself, or due to aggressive surgical treatments. Clinically BCC classically presents with red eroded patches that do not heal and eventually bleed, or with white pearly papules (Figure 2).

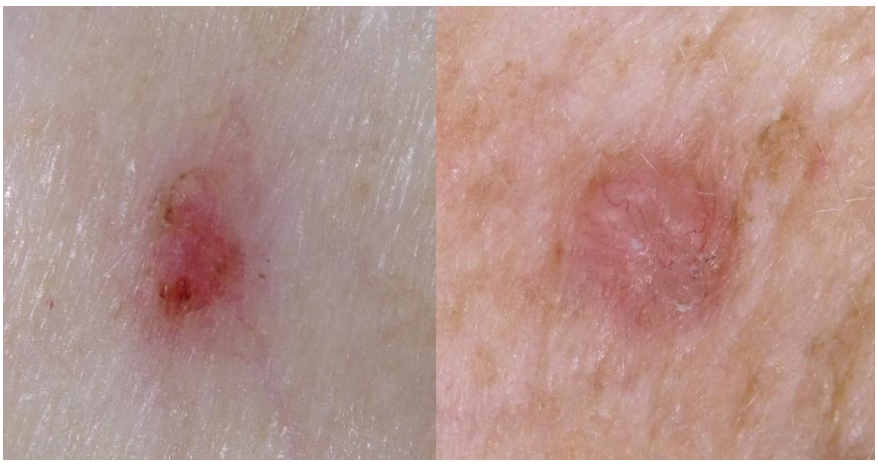

***Figure 2**: Two classic clinical presentations of basal cell carcinoma. On the left a superficial basal cell carcinoma presenting a non-healing red erosion. On the right a nodular basal cell carcinoma presenting as a pink and pearly whitish papule (source: Memorial Sloan Kettering Cancer Center).*

Although no universal classification exists, histologically up to 26 subtypes of BCC have been described.[16] From a practical standpoint BCCs can be divided in indolent-growth BCCs and aggressive-growth BCCs.[17] Aggressive-growth BCCs include mainly infiltrative, morpheaform, basosquamous and micronodular BCCs. These subtypes tend to invade initially the dermis and if left untreated can cause local destruction by extending to the fat, muscle, bone or cartilage. Aggressive BCC require surgery with safety margins to completely remove the tumor. Conversely, indolent-growth BCCs include superficial and early nodular subtypes and are restricted to the upper dermis of the skin. Indolent BCC can be treated with surgery but also non-surgically using topical treatments or physical treatments (discussed in section 2b).[17-19] However, the main limitation of non-surgical treatments is the absence of confirmation that the tumor has been completely removed. In fact, when evaluating electrodessication and curettage (EDC), the first line treatment in the USA for superficial BCC, up to 45% of cases show residual BCC after conventional EDC.[20] Hence, although non-surgical treatments can be cheaper, faster and more available that surgery, they are limited due to the lack of histological confirmation that the tumor is completely eliminated.

Besides the histological subtype, other factors may determine whether a BCC is considered to have low risk or high risk for recurrence (summarized in Table 1). In such high-risk cases, surgical techniques that assess the margins intraoperatively such as Mohs surgery (described in section 2a) are recommended in order to remove completely the tumor tissue while keeping as much healthy skin as possible to minimize scarring.

	Low risk	High risk
Histological subtype	Nodular, superficial	Infiltrative, morpheaform, basosquamous, micronodular
Perineural invasion	No	Yes
Location/size	Area L < 20 mm Area M < 10 mm Area H < 6 mm	Area L ≥ 20 mm Area M ≥ 10 mm Area H ≥ 6 mm
Borders	Well defined	Ill defined
Primary vs recurrent	Primary	Recurrent
Immunosuppression	No	Yes
Site of prior radiotherapy	No	Yes

Table 1: *Risk factors for basal cell carcinoma recurrence according to the National Comprehensive Cancer Network guidelines [21] (Abbreviations: Area L = trunk and extremities. Area M = cheeks, forehead, scalp, neck. Area H = central face, eyelids, eyebrows, periorbital, nose, lips, chin, mandible, preauricular, postauricular, temple, ear, genitalia, hands, feet.*

SCC is another variant of KC and originates from epidermal keratinocytes. SCC are also mainly caused by chronic sun exposure but can also occur overlying chronic skin diseases such as lichen planus, porokeratosis and virtually any chronic inflammation of the skin.[22] SCC can also produce local invasion and, contrarily to BCC, SCC metastasizes in around 2 to 5% of cases.[23] SCC typically presents as a red non-healing plaque in the Bowen disease form, or as a scaly indurated papule or nodule in more hypertrophic forms (Figure 3). SCC treatment also depends on the level of invasion. When SCC is restricted to the epidermis (SCC in situ or Bowen disease), it can be removed surgically but can also can be treated non-surgically, similarly to low-risk BCCs. When SCC invades the dermis, surgery, either conventional or margin-controlled, is needed.

Figure 3: *Clinical pictures of squamous cell carcinoma (SCC). On the left, a Bowen disease (SCC in situ) presenting as non-healing red scaly patch. On the right, an invasive squamous cell carcinoma presenting as a red papulonodule with central crusting (sources: Memorial Sloan Kettering Cancer Center and Hospital Clínic de Barcelona).*

ii. Melanoma

Cutaneous melanoma originates from the melanocytes which are located mainly in the basal layer of the epidermis. When melanoma is located only on the epidermis is considered melanoma in situ and has a very good prognosis if treated. When the melanoma cells invade the dermis, the potential of metastases increases with the depth of invasion as well as the melanoma subtype characteristics. Melanoma can present with different subtypes, which have different clinical, histologic, genetic, and prognostic features. Classically, melanomas have been divided into superficial spreading, nodular, acral lentiginous and lentigo maligna melanoma. Among them, **superficial spreading melanoma** (SSM) accounts for 65% of all melanomas and is the classic form of melanoma presenting with a flat lesion typically showing multiple shades of brown, blue and black (Figure 4). SSM is related to intermittent sun exposure and is more common on the legs of women and on the back of men.[22]

Figure 4: *Clinical image of a superficial spreading melanoma showing asymmetry, irregular borders and multiple colors (source: www.wikipedia.com)*

Nodular melanoma accounts for 20% or melanomas and is characterized by the presence of a raised lesion (nodule) which translates a very fast vertical growth phase that invades the dermis and potentially expands throughout the rest of the body. **Acral lentiginous melanoma** accounts for 4% of melanomas, occurs on the palms and soles and is not related to sun exposure but rather to other factors such as genetic or environmental factors such as mechanical stress.[24] **Lentigo maligna** (LM) and its invasive variant called LM melanoma (LMM) represent around 8-10% of melanomas and occur mostly in the head and neck due to chronic sun exposure rather than sunburns.[25] LM/LMM is a relatively indolent variant with a slow growth but has frequent recurrences since clinically it presents with light brown patches with ill-defined borders admixed within a background of photodamaged skin (Figure 5) and typically presents with follicular involvement which acts as a reservoir for malignant cells.[26]

Figure 5: *Clinical image of a lentigo maligna presenting as a red and brown patch admixed within a background of lentigines (sun spots) which obscure the delineation of the tumor margins (Source: Memorial Sloan Kettering Cancer Center).*

In general, surgery with safety radial margins around the visible tumor is the mainstay of treatment of melanoma and if performed at early stages provides high curative rates. The surgical margins are determined by the Breslow index (depth of invasion measured in millimeters), and range from 5 mm of radial margins in melanomas in situ to 2 cm in melanomas with a Breslow thickness of ≥2 mm.[27] However, in the LM/LMM subtype such margins may not be adequate (LM frequently presents with subsurface tumor spread invisible to the naked eye) or may not be feasible to obtain (LM/LMM arises frequently on the face limiting wide margins). In other words, the LM/LMM tumor cells tend to be obscured within the surrounding sun-damaged skin, and appear relatively small in extent (~ millimeters) on the surface, but sub-clinically and below the surface the lesions often spread over much longer distances (~ centimeters) in thin branching dendritic patterns, similar to the roots of a tree. This frequently leads to narrower excisions and results in frequent recurrences. Margin-controlled surgical techniques such as Mohs surgery or staged excision have been successfully used to treat LM/LMM showing that even for in situ lesions margins wider than 5 mm are necessary.[28,29] In addition, when surgery cannot be performed or is not feasible/desirable, non-surgical approaches such as imiquimod or radiotherapy can also be used after making sure no dermal invasion exists.[30,31] However, this is not always easy since invasion in LM/LMM can present in a patchy fashion, often requiring multiple scouting biopsies to assess whether invasion exists or not.

iii. Extramammary Paget disease

Extramammary Paget disease (EMPD) is a rare form of adenocarcinoma which originates from cells present in the apocrine glands and ducts along the milky line. The most commonly affected areas include the vulva, scrotum, perianal region, and pubis.[5,15] EMPD has an incidence of 0.11 per 100,000 person-year being more frequent among females (80% of cases of EMPD), with a presentation age around 60 years.[15] EMPD is a variant of Paget disease, which is more common and typically occurs in women with primary breast adenocarcinoma as red plaques around the areola. Conversely, EMPD rarely is associated with an internal neoplasia, being the most common ones genitourinary and gastrointestinal cancers. [5,15]

EMPD is challenging in terms of diagnosis as well as treatment. EMPD presents initially with pruritus which later can progress to red scaly plaques, often covering large areas, which most of the times are misdiagnosed as infections (tinea cruris, candidiasis), irritation, psoriasis, or eczema (Figure 6).[5,15] In addition, biopsies of the area sometimes do not reveal tumor cells. This is due to the fact that Paget cells (Figure 7), the tumor cells present in EMPD, are often distributed in a patchy fashion, requiring multiple biopsies or large excisional biopsies to render the correct diagnosis.

***Figure 6**: Comparison of the clinical appearance of a case of scrotal extamammary Paget disease (left) and a case of tinea cruris (right). Both can present with an erythematous slightly scaly plaque which tends to grow slowly and can be itchy (sources: www.myempd.com and https://specialty.mims.com/).*

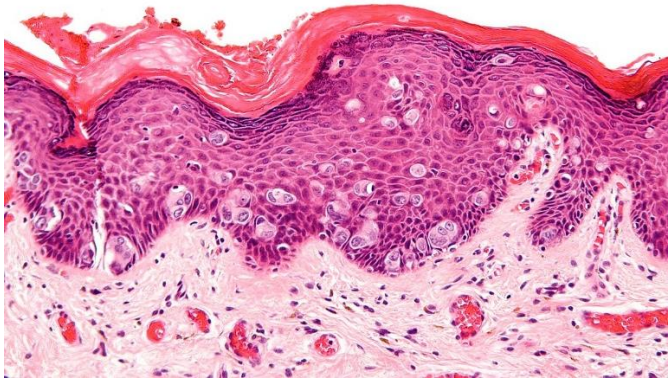

***Figure 7**: Histological image of a case of extramammary Paget disease showing scattered large cells with pale cytoplasm present in the epidermis. These cells are typically CK7 positive and negative for S100 and HMB45 (Source: www.wikipedia.com)*

Different treatment modalities are used to treat EMPD and include surgery (conventional, Mohs, staged excision), radiotherapy, 5-fluorouracil, imiquimod, and chemotherapy.[32-34] Although margin-controlled surgery offers the highest complete response rate, recurrences (appearance of tumor after a period of time of clearance) and disease persistence (presence of small foci of tumor not detected just after treatment) are very common with all treatment modalities for EMPD. Recurrences or persistence of EMPD can present with pruritus and/or red patches similar to the initial presentation of the disease. However, sometimes irritative dermatitis with an identical presentation can also occur after treatments such as radiation therapy or imiquimod. Hence, biopsies are often performed but may fail to reveal active EMPD since the distribution of the Paget cells in recurrent/persistent EMPD also occurs in a patchy manner. Therefore, often to identify such recurrences/persistence, multiple scouting biopsies are necessary to be obtained, which is not always possible or desirable in such cosmetically-sensitive area such as the genitalia.

2. Treatment methods of skin cancers

Although skin cancers can be very diverse, since the skin is the most accessible organ, surgery remains the mainstay for the majority of skin cancers. However, non-surgical alternatives have been developed for superficial skin cancers such as superficial skin cancers thus avoiding the need for invasive procedures.

a) Surgery

Surgery is still to date, the most used modality to treat the majority of skin cancers. According to most cancer guidelines,[35-37] conventional surgery with a safety margins (3 mm to 2 cm depending on the type of cancer and level of invasion) is the method of choice to treat skin cancer. However, since many skin cancers occur in cosmetically-sensitive areas such as the face, wide safety margins are not always possible or desirable to obtain due to potentially disfiguring consequences. Hence, in such cases margin controlled surgical approaches such as Mohs micrographic surgery or its variant staged excision may be used since they achieve high curation rates by just removing the malignant tissue.[28,38,39]

Mohs micrographic surgery (MMS) was initially described by Dr Frederic Mohs in the 1930s and was based on the controlled removal of cancer by fixing the tissue in vivo using a paste with zinc chloride. Later, fixed tissue was removed and analyzed on the microscope to identify any residual tumor.[40,41] This technique was painful and time-consuming (fixation could take up to one day). Later this technique evolved and nowadays fresh tissue is excised under local anesthesia, ink-marked, frozen and stained for immediate histopathological analysis.[42] Current protocols initiate the procedure by removing the visible tumor (debulking). Later, the lateral margins are excised and oriented horizontally, similarly to cake slices, allowing 100% analysis of the tumor margins (Figure 8). If a piece is affected, further stages of removal in the affected area are performed until histological clearance is achieved. Hence, MMS allows the excision and repair of a defect in a single day in the majority of cases. MMS specimens can also be sent to the pathology laboratory in order to perform conventional non-frozen sections, which may be needed in some cases of melanocytic lesions or in cancers where special immunohistochemical stains or molecular studies may be necessary such as in EMPD or dermatofibrosarcoma protuberans.[43-45] This form of MMS is slower and requires multiple days to finish the surgery, leading to the name of “slow Mohs technique”.

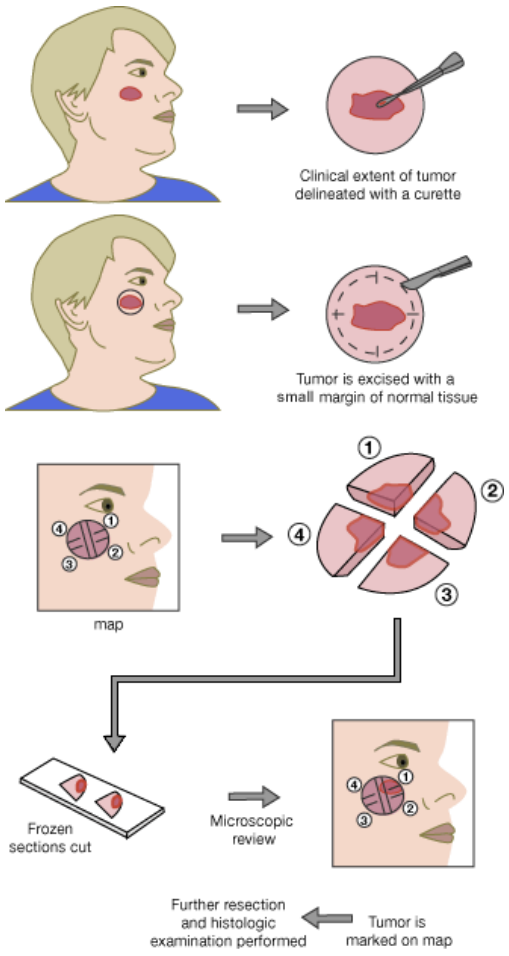

Figure 8: *Schematic of Mohs surgery. Note that excised specimens are analyzed horizontally to assess the entire tumor margins (source http://www.renewaldermatology.com)*

Staged excision is a variation of slow Mohs surgery in which the tumor tissue is excised similarly to Mohs surgery, but is later processed for rushed pathological analysis to allow immunohistochemical analysis. What makes staged excision unique is that the tissue is not processed to obtain horizontal sections, but to obtain multiple vertical sections that allow assessing the tumor progression from the center to the periphery (Figure 9).[28,39] This is particularly useful in subtypes of skin cancers such as LM/LMM which decrease their tumor cell density towards the periphery of the tumor.

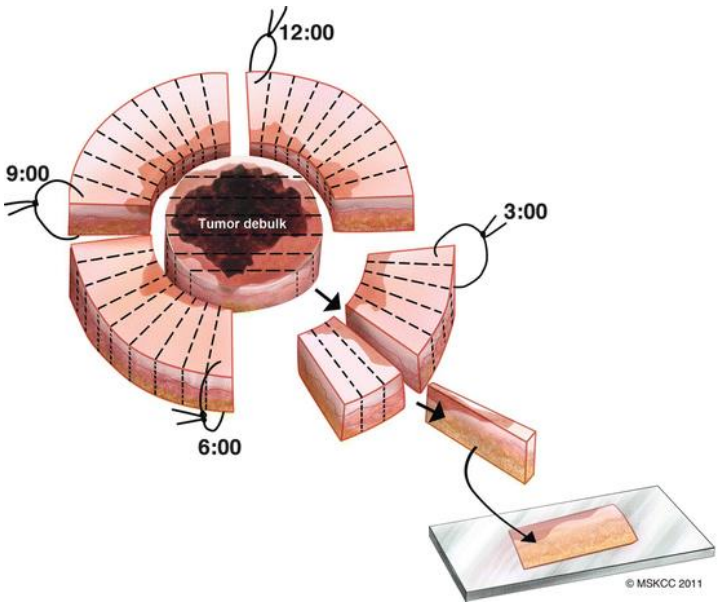

***Figure 9**: Schematic of staged excision: initially the visible tumor is debulked similarly to Mohs surgery. Later, the margins are excised also in a cake-like fashion but later cut to obtain vertical sections (source: Memorial Sloan Kettering Cancer Center)*

Margin-controlled surgery techniques provide cure rates around 90-95% for the most common skin cancers such as BCC or SCC and even for LM.[17,28,39] However, they are time-consuming, labor intensive, and expensive.[46] In addition, a proportion of BCCs occur in elderly population, with limited life expectancy, prone to surgical side-effects.[47] In addition, since margin-controlled surgery requires trained surgeons, dedicated equipment and technicians to perform the histopathological analysis, is not always available in all centers. Hence, alternative therapies may we preferred in low risk skin cancers, as well as methods to predefine the margins prior to surgery may be useful in centers where margin-controlled surgery is not available.

b) Non-surgical approaches

As discussed earlier, small (<2 cm), superficial BCC especially if located on the trunk or extremities are considered low-risk and are amenable to non-surgical treatment. Similarly, other types of skin cancers such as SCC in situ or LM can also be treated non-surgically, although general surgery is preferred due to the potential risk of metastases. Non-surgical treatment can be divided into topical (e.g. imiquimod, 5-fluorouracil, ingenol mebutate) and physical treatments (e.g. EDC, cryotherapy, radiotherapy, photodynamic therapy, ablative lasers).[17-19,37] Unlike surgical techniques, these treatments do not allow histological control to guarantee total elimination of the tumor. Abundant literature is available about the success rates using the newer treatments modalities such as imiquimod or photodynamic therapy for BCC or SCC in situ. These treatments stimulate the innate immunity of the patient to selectively destroy the tumor cells, achieving high cure rates which range from 70 to 100%.[48] Imiquimod has also been used to treat LM and EMPD achieving complete response rates of 50-93%[49] and 72%[50], respectively.

However, in the particular case of ablative techniques such as ablative lasers (CO2 laser, erbium:YAG laser) or EDC, the absence of histological control is especially important since tumor elimination occurs due to evaporation in the case of lasers or by mechanical destruction in the case of EDC, and not through a direct stimulus of innate immunity, such as with topical treatments. Therefore, in the case of ablative treatments, if the technique is performed too conservatively residual tumor may be left, while if the technique is performed too aggressively excessive scarring may occur. This fact is evident with EDC, a very old technique in which tumor elimination is performed by performing 1, 2 or 3 passes with a curette followed by electrocoagulation guided by the tactile sensation of the operator.[51] While the success rates of the EDC can be more than 90%, the technique depends primarily on the operator's experience. Also, up to 37% of the BCC cases treated with EDC present residual tumor after performing 3 EDC passes.[51] Regarding laser ablation for the treatment of BCC, there are no clinical data on its effectiveness in the medium or long term, but the cases described in the literature seem promising since ablative lasers allow fast, controlled and precise tissue destruction due to predefined ablation parameters. [52-54] However, they share the same limitation of non-surgical treatment modalities for BCCs: the lack of histological confirmation of margins clearance. In this sense, RCM has been used to assess the presence of residual tumor after ablative treatments in isolated case series,[54,55] showing promising results but having the main limitation of providing a limited field of view which may not enable a full evaluation of the entire wound after treatment.

3. Non-invasive methods to evaluate skin cancers

a) Dermoscopy/dermatoscopy

Dermoscopy, also called dermatoscopy, is a non-invasive imaging tool that has shown to improve the diagnostic accuracy of skin cancer compared to naked eye examination. [56,57] Dermoscopy uses a handheld magnifying lens called dermatoscope, which is coupled to an illumination source which can emit cross-polarized light, non-polarized light or both. Most common dermatoscopes have a magnification of 10x, although some devices, especially the ones attached to a digital video-camera, can obtain magnifications up to 100x.

Dermoscopy allows the visualization of surface and subsurface skin structures not visible with the naked eye. Many of these structures correspond to histopathological features and thus give information about the cellular nature of the lesion [58,59]. The polarized light or the non-polarized light plus an interface liquid (oil, alcohol, water or gel) eliminate surface reflection to allow inspection of structures and blood vessels in the epidermis, dermo-epidermal junction and the superficial dermis [60]. These two modalities are comparable in their ability to assess overall dermoscopic patterns; however, certain structures are better viewed by one or other, therefore complementing each other. Many modern dermatoscopes have the capability to toggle from one modality to the other by just pressing a button (Figure 10), thus leading to a "blinking" effect which allow identifying areas visible with one or the other modality.

***Figure 10**: Example of a hybrid dermatoscope, which can use cross-polarized light and non-polarized light by toggling a lateral button (Source: Dermlite www.dermlite.com).*

Typically dermoscopy has been used to diagnose skin cancers; however, recently a better understanding of the dermoscopic and histopathologic correlates has allowed the use of dermoscopy to predict given histological features with therapeutic and prognostic implications.[12]

b) Wood's light

First described by Robert Williams Wood in 1903,[61] Wood's light has been used in dermatology to diagnose multiple diseases such as pigmentary disorders, cutaneous infections, porphyrias or skin cancers.[62] A Wood's lamp (Figure 11) emits ultraviolet light which is later absorbed and reflected differently according to the chromophores present on the skin. The reflected light is then filtered through a filter composed of barium

silicate glass with 9% metal oxide. This filter is opaque to all light except for the light between 320-400 nm (with a peak around 360 nm). Hence, Wood's light induces different types of fluorescence according to the presence or absence of select chromophores. A typical example is the presence of coral red fluorescence when evaluating the bacterial infection erythrasma, since the *Corynebacterium* that originate erythrasma produces coproporphyrine III which when stimulated with ultraviolet (UV) light shines red.[63]

***Figure 11**: Examples of a commercially available Wood's lamp (Source: www.tecnosa.es)*

When evaluating pigmented skin cancers such as melanoma, the most important chromophore is melanin. Melanin absorbs the majority of light received by the skin which is light between 350 to 1,200 nm. Since most of the spectrum of Wood's light is within this range, UV light is also intensely absorbed by melanin. In addition, longer wavelengths from the visible spectrum (400-700 nm) penetrate deeper than UV light, which has a shorter penetration. This results in a filtering of longer wavelengths and an increase in the contrast between superficial epidermal pigmented lesions from surrounding normal skin. [62] This fact can be used to distinguish areas with different amounts of melanin, especially when pigment is located in the epidermis. Hence, areas with increased epidermal melanin will appear darker on Wood's light examination than areas with normal amounts of epidermal melanin. This phenomenon has been used from the 1980s to delineate the margins of pigmented skin cancers such as melanoma.[64,65]

The main advantage of Wood's light is that it is a fast, cheap and easy method to evaluate the margins of pigmented skin cancers. However, Wood's light is sometimes not a precise method to delineate these margins. Wood's light can underestimate the margins in cases of amelanotic or hypomelanotic melanomas (relatively common in LM/LMM present in patients with phototypes I and II). In this sense, June Robinson studied the impact of digital dermoscopy when assessing the presurgical margins of 26 consecutive LM initially guided by Wood's light.[66] She found that in all cases the Wood's light border was larger than the clinical border, but that in most cases (19/26) the

dermoscopic borders were larger than the Wood's light ones. In addition, when assessing these borders with the surgical defects, she identified an increase in the final surgical defect (11.6 cm^2) vs the area based on dermoscopy (8.1 cm^2) (p=0.01), suggesting that Wood's light margins are generally smaller than the surgical margins.

Conversely, Wood's light can also overestimate the tumor margins especially in cases of intense photodamage, since lentigines or simply activated melanocytes present in sun-damaged skin can also appear dark under Wood's light examination. This scenario can be worrisome if surgery should be performed using only Wood's lamp guidance, since the surgical margins will be clear but unnecessarily large. Walsh et al.[62] studied the accuracy of Wood's light when excising melanoma in situ. They performed Wood's light evaluation in 60 patients which underwent staged excision for melanoma in situ and found that in 7 cases, Wood's light highlighted beyond the clinically-visible margin. In all 7 cases, if surgery would have been guided with Wood's light the defect would have been larger than the final surgical defect using staged excision. Therefore, since results are conflicting and false positives and false negatives occur with Wood's light in margin delineation, it has been advocated that Wood's light and also dermoscopy should be the first step to determine the potential margins of a LM/LMM which later need to be confirmed using other methods such as scouting biopsies or RCM prior to surgery.

For other subtypes of non-pigmented skin cancers, Wood's light examination can also have a relevant role. Recently several studies have shown the utility of this technique after the application of methyl-aminolevulinate or aminolevulinic acid. These molecules, which are photosentizers, are absorbed by cells with a high replication cells such as cancer cells. After a period of absorption, generally around 3 hours under occlusion, cancer cells intake the photosensitizers and when stimulated with UV light emit fluorescence that is visible through the Wood's lamp. In other words, due to the increased intake of photosensitizer within the cancer cells, it is possible to visualize the cancer margins. This method, known as **photodynamic diagnosis or fluorescence diagnosis**, has been used to delineate the margins of non-pigmented BCCs, SCCs and EMPD.[67-69]

c) Reflectance confocal microscopy

i. Fundamentals of reflectance confocal microscopy

Reflectance confocal microscopy (RCM) is a non-invasive imaging tool that can obtain *in vivo*, real-time images and videos with a lateral resolution of 1 µm and 4 µm optical sectioning, which results in the visualization of cellular structures up to approximately 250 µm in depth.[70] This allows an *en face* examination of the epidermis and the upper dermis with near-histological resolution.

RCM uses an 830 nm near-infrared diode laser which emits monochromatic and coherent light. This laser source, which is harmless to the skin, emits light at a point of interest on the skin which afterwards is backscattered. This light is later filtered through a pinhole which only collects light from the point of interest, thus allowing the alignment of the point of interest and the pinhole in the same focal plane (con-focal) (Figure 12). [70,71] By changing the location of the microscope and the depth one can obtain grayscale images at very high resolution. Since RCM images are grayscale, depending on the cellular refractive index, structures are brighter if their refractive index is high (e.g. melanin, keratin), whereas they are seen dark if their refractive index is low (e.g. water present inside the nuclei) [72].

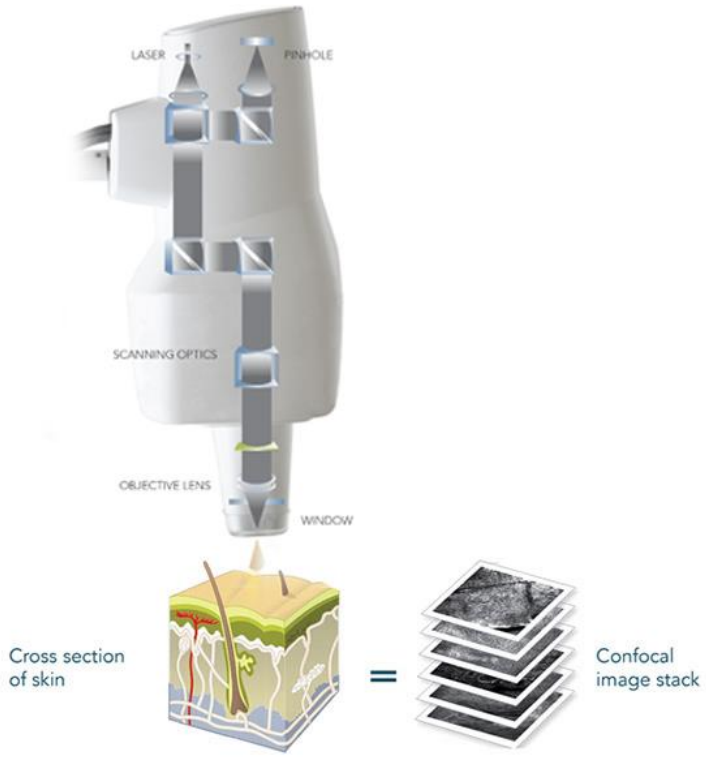

***Figure 12**: Elements present in the in vivo wide-probe reflectance confocal microscope (Source: Caliber ID www.caliberid.com).*

ii. Types of reflectance confocal microscopes

Currently, two reflectance confocal microscopes to be used in vivo are commercially available: a wide-probe microscope (Figure 13 A; Vivascope 1500, Caliber ID, Rochester, NY) and a handheld microscope (Figure 13 B; Vivascope 3000, Caliber ID, Rochester, NY).

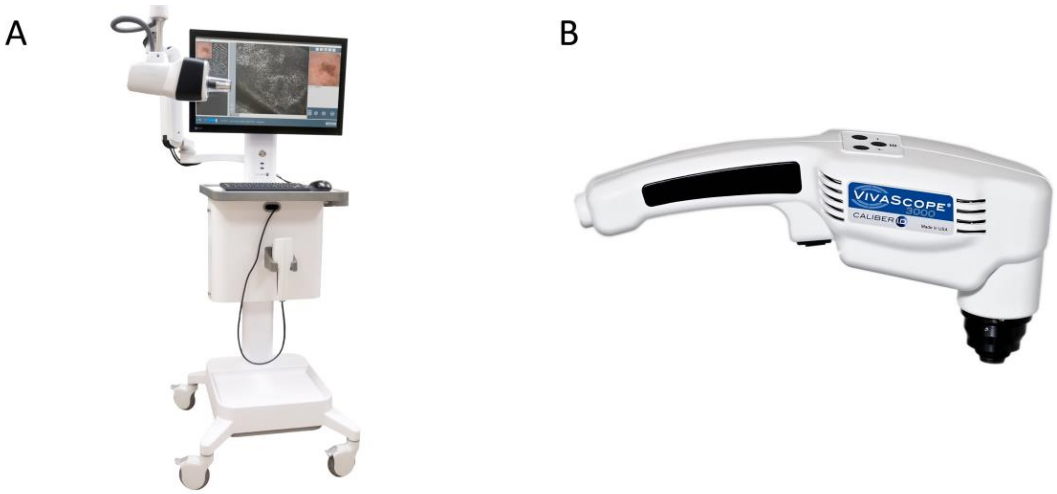

***Figure 13**: Types of commercially available in vivo reflectance confocal microscopes. The left image (A) shows the wide-probe microscope, whereas the right image (B) shows the handheld microscope (Source: Caliber ID www.caliberid.com).*

The **wide-field confocal microscope** requires attaching a metal or plastic (depending on the microscope version) ring of 2 cm onto the skin using an adhesive plastic window in order to allow the movement of the microscope (Figure 14). The microscope slides over the skin in a stepwise manner, obtaining individual 500 x 500 µm images which later are stitched by the software to produce a mosaic of images up to 8 x 8 mm (Figure 15). By obtaining multiple mosaics of horizontal images at different depths, as well as individual vertical images, called stacks, one can obtain a 3D approximation of a given lesion. This allows the user to start reviewing the architecture of a lesion at low magnification, and later zooming in a region of interest to assess the cellular characteristics of a lesion. This approach is in parallel to the one used by pathologists who start evaluating a slide at low magnification (40x) to then transition to a more detailed magnification (100-200x).

***Figure 14**: Pictures showing the 2 cm metal ring that is attached to the skin with an adhesive plastic window and later magnetically attached to the probe. Later, the microscope slides over the skin to obtain images in a standardized predefined manner (Source: Caliber ID www.caliberid.com).*

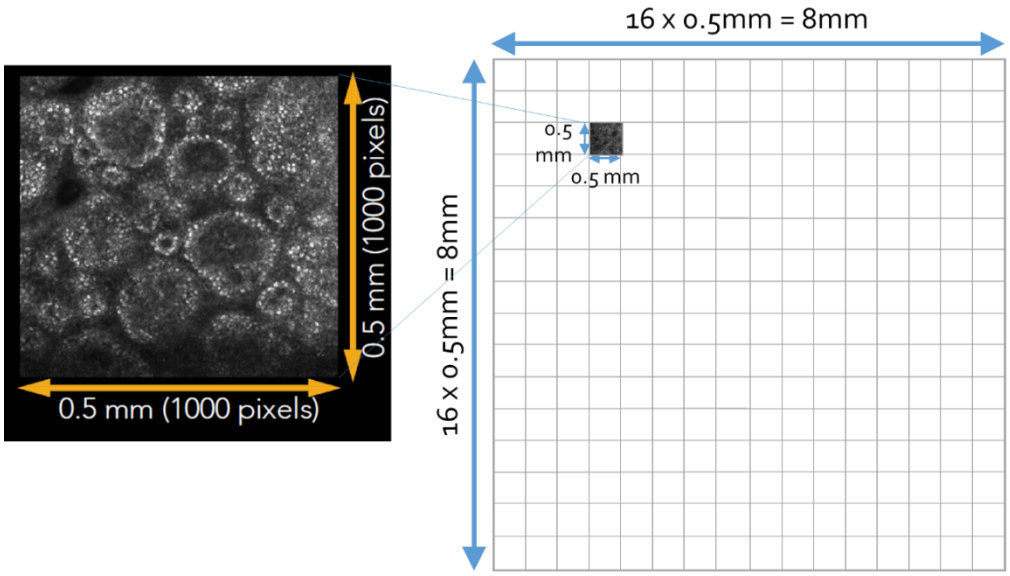

***Figure 15**: Schematic representation of the mosaics obtained with the wide-probe reflectance confocal microscope (source: Oriol Yélamos).*

The **handheld confocal microscope** (HRCM) allows free-hand movement along the skin and can acquire videos and single images of 0.75 x 0.75 mm or 1 x 1 mm depending on the microscope generation (1x1 mm in the 3rd generation, and 0.75x0.75 mm in the 4th generation; Figure 16). It is possible to obtain stacks of vertical images, but horizontal mosaicking does not exist in the native software. Since the probe size is small (5 mm in the 3rd generation and 1.5 cm in the 4th generation), this microscope is mostly used to assess lesions located in uneven areas such as bony areas, flexures, the face, the genitalia and mucosae where the 2 cm metal ring is more difficult to be attached.

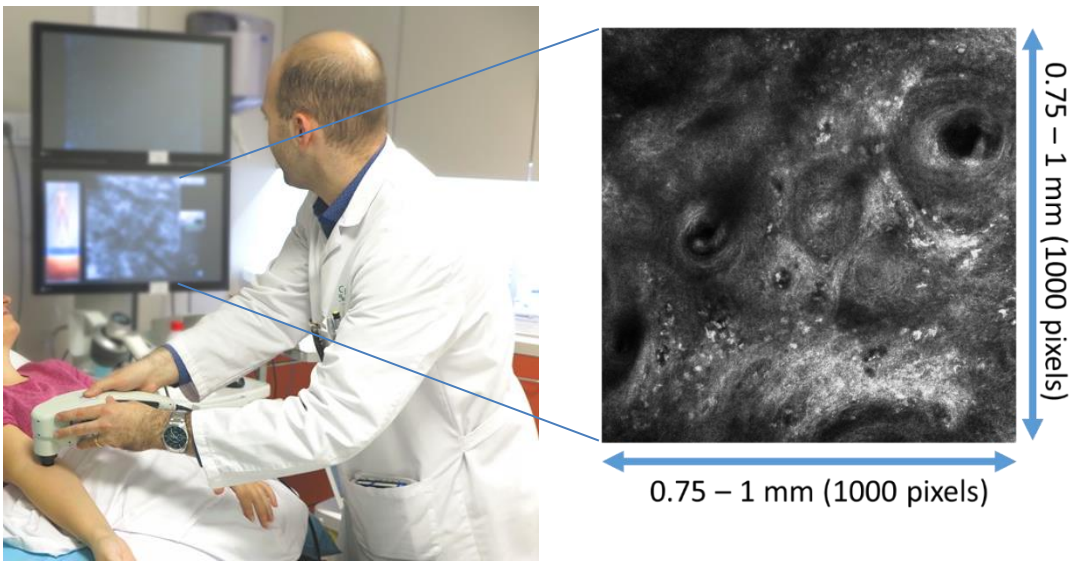

***Figure 16**: Picture of the use of the handheld reflectance confocal microscope and its field of view (0.75 to 1mm depending on the generation of the device). The microscope is moved along the skin without a predefined path and without the need of attaching a metal ring onto the skin (source: Oriol Yélamos).*

iii. Reflectance confocal microscopy findings of skin cancers

Basal cell carcinoma

The RCM features of BCC can vary depending on the histological characteristics of the tumor. Grossly, superficial BCC is characterized by the presence of epidermal streaming, cord-like structures attached to the epidermis with peripheral palisading, peritumoral clefting, and eventually a reactive stroma with plump cells, white dots and horizontal blood vessels (Figure 17A). Nodular BCC can present with the same features but, instead of cord-like structures, presents with tumor nests that also show peripheral palisading and clefting (Figure 17B). When deep tumor nests are present, dark silhouettes (areas that resemble tumor nests but do not show clear details) can be seen. When BCC is pigmented, one can also identify dendritic cells within the tumor nests.

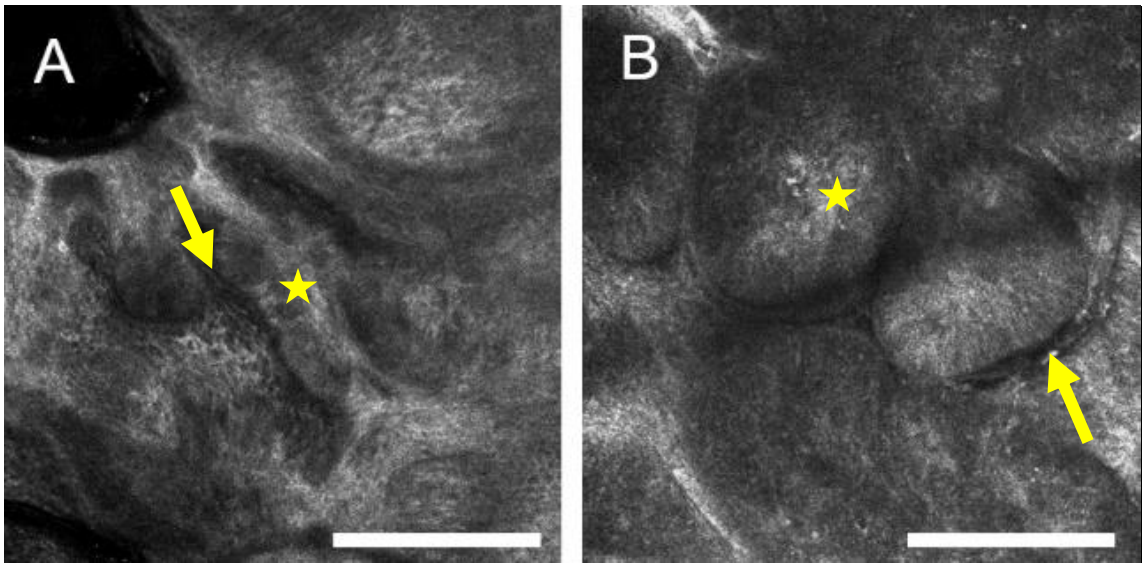

Figure 17: Examples of basal cell carcinomas on reflectance confocal microscopy. (A, left) Superficial basal cell carcinoma showing cordlike structures with peripheral palisading (star), surrounded by clefting and horizontal vessels (arrow). (B, right) Nodular basal cell carcinoma showing round tumor nests with peripheral palisading and peritumoral clefting (Depth 125 µm, scale bar 200 µm). (Source Hospital Clínic)

Squamous cell carcinoma

SCCs can show different patterns under RCM, depending whether they are in situ or invasive. However, a common finding is the presence of an irregular honeycomb pattern that sometimes is totally disarrayed. It is also common to find erosions and crust, parakeratosis, and sometimes dyskeratotic cells which are seen as round, nucleated cells present in the epidermis. In cases of invasive SCC, the dermal epidermal junction (DEJ) is disarrayed. Round looped blood vessels crossing the dermal papillae are also common and are called glomerular vessels or button-hole vessels (Figure 18).[73]

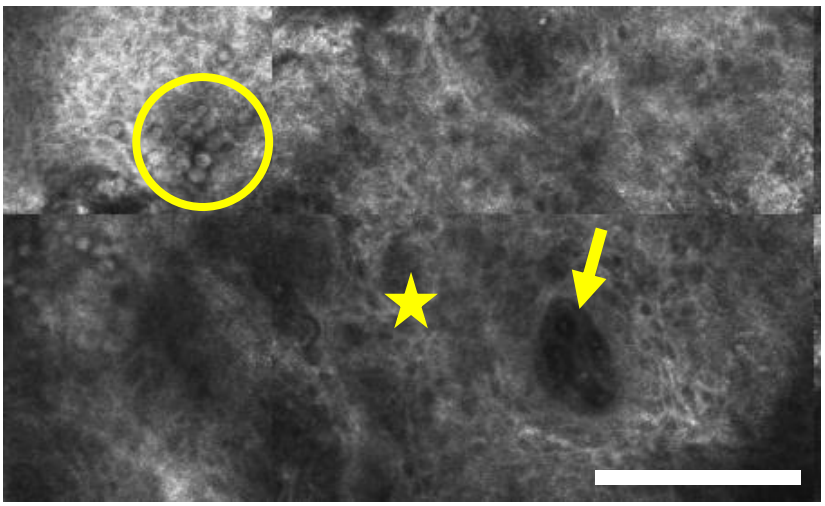

Figure 18: Example of a squamous cell carcinoma visualized on reflectance confocal microscopy. Note dyskeratotic cells (circle), an atypical honeycomb pattern (star), and glomerular vessels (arrow). (Depth 100 µm, scale bar 250 µm). (Source: Memorial Sloan Kettering Cancer Center)

Melanoma

The RCM features that characterize melanoma also differ depending on the melanoma subtype (figures 19 and 20). In general, RCM allows the identification of atypical melanocytes which are seen either as large dendritic nucleated cells, or as large round nucleated cells. These cells can be found in the epidermis as pagetoid cells, but can also be found on the DEJ as single cells, sheets of atypical cells, within junctional thickenings of the epidermis or in nests. Atypical cells can also eventually disrupt the normal edged-papillae pattern. Several RCM algorithms have been described to help in the diagnosis of melanoma and are summarized in Table 2.

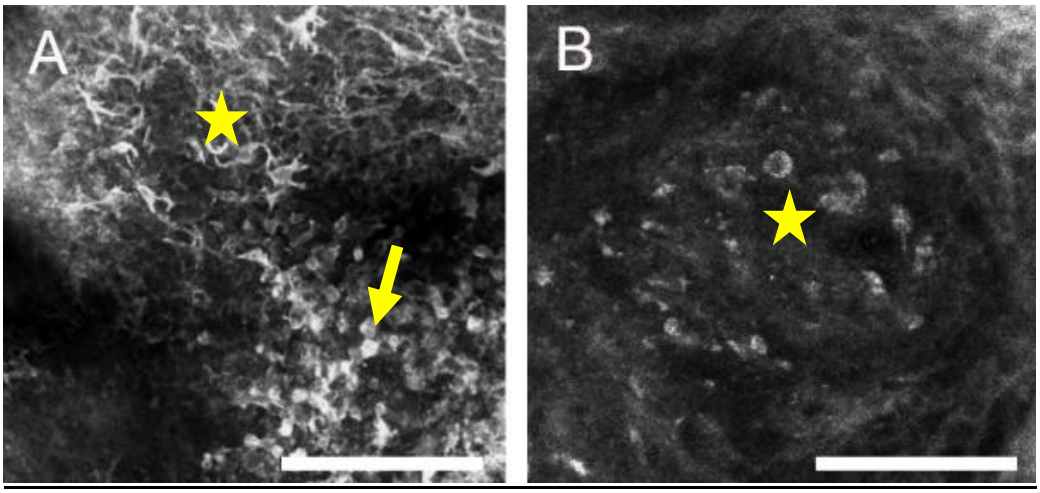

Figure 19: *Two example of superficial spreading melanomas on reflectance confocal microscopy. On the left (A) one can note multiple atypical dendritic pagetoid cells (asterisk) admixed with nucleated round cells (arrow) (Depth 50 µm, scale bar 250 µm). On the right (B) one can identify a deeper nest composed of atypical nucleated cells (star) (Depth 200 µm, scale bar 200 µm). (Source Hospital Clínic de Barcelona)*

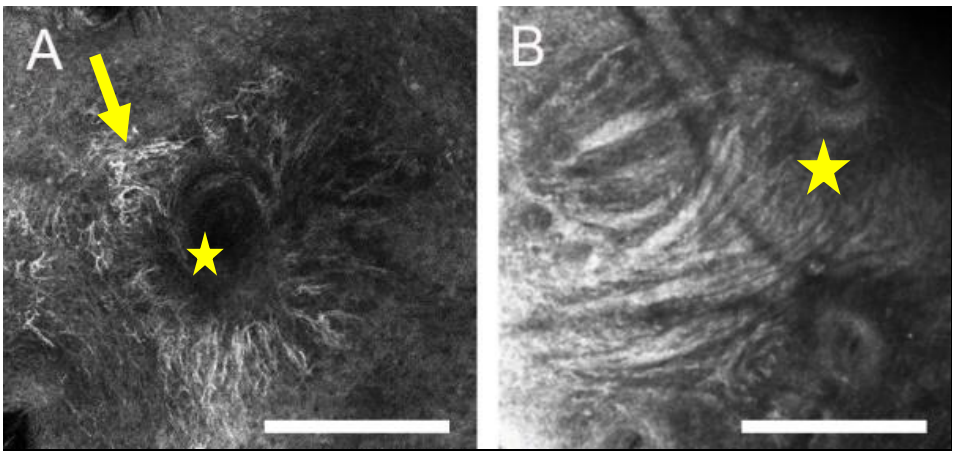

Figure 20: *Examples of lentigo maligna melanomas on reflectance confocal microscopy. On the left (A) one can see atypical dendritic cells (arrow) invading a hair follicle (star) (Depth 100 µm, scale bar 200 µm). On the right (B) one can identify numerous irregular junctional thickenings arranged in a mitochondria-like pattern (star) (Depth 120 µm, scale bar 200 µm). (Source Hospital Clínic de Barcelona)*

Algorithm	Confocal Features	Scoring	Interpretation
Modena algorithm[74]	**Major**: Non-edged papillae Cellular atypia at dermo-epidermal junction **Minor**: Cerebriform nests Roundish pagetoid cells Widespread pagetoid infiltration Nucleated cells in the upper dermis	 2 2 1 1 1 1	Score ≥3 indicates a melanoma
Barcelona algorithm[75]	**First step: lesion is melanocytic if** Dermal papillae present AND at least one of: • Cobblestone pattern • Pagetoid cells • Refractile nests **Second step (for melanocytic lesions):** <u>Risk features</u> Pagetoid roundish cells in the superficial epidermis Atypical nucleated cells in papillary dermis <u>Protective features</u> Typical basal cells Edged papillae	 +1 +1 -1 -1	Score ≥0 indicates a melanoma
Lentigo maligna algortihm[76]	**Major criteria:** Non-edged papillae Round large pagetoid cells **Minor criteria:** Nucleated cells in dermal papillae Nucleated cells in dermal papillae Atypical cells at the DEJ (+1) Follicular localization of atypical cells Broadened honeycomb pattern	 2 2 1 1 1 1 -1	Score ≥2 indicates a lentigo maligna

Table 2: *Reflectance confocal microscopy diagnostic algorithms for melanoma.*

Extramammary Paget disease

Paget cells are seen on RCM as large, round, hyporefractile cells (also known as dark holes), generally twice as big as normal keratinocytes. Sometimes these cells show a central gray nucleus which resembles a target. These cells can be seen isolated in the epidermis or forming nests typically at the DEJ. Other RCM findings may support the diagnosis but are not specific such as increased dermal vessels and inflammatory cells seen as dendritic cells or white dots.

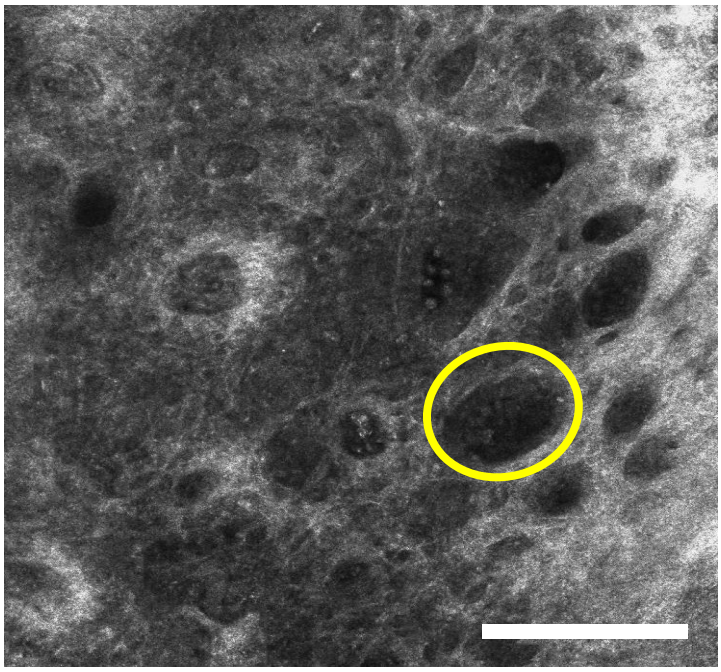

***Figure 21**: Example of extramammary Paget disease on reflectance confocal microscopy. Note multiple target-like cells present in nests forming "dark holes" (circle, depth 175 µm, scale bar 200 µm). (Source: Memorial Sloan Kettering Cancer Center).*

iv. Uses and challenges of in vivo reflectance confocal microscopy

Several studies have demonstrated that RCM has high diagnostic accuracy for skin cancer (sensitivity and specificity 91-100% and 68-98%, respectively[77]). This is especially significant when used as a complementary tool in sequential digital dermoscopy surveillance on patients with high number of nevi since it decreases the number needed to excise or benign to malignant ratio around to 1:1.8 - 1:2.4. [78-81] Therefore, RCM allows a high detection of skin cancer (high sensitivity) without excising more benign lesions (high specificity). This is mainly due to the fact that RCM has cellular resolution and can identify very small amounts of melanin which are not visible to the naked eye or even with dermoscopy.[72]

For more than 20 years, research has been focused towards the use of RCM in aiding the diagnosis of skin cancer. However, recent studies have shown that RCM can also be an excellent tool to guide and monitor treatments. Some studies have used RCM to monitor the therapeutic results of various non-surgical treatments used in cutaneous oncology such as imiquimod[30], ingenol mebutate,[82] or photodynamic therapy.[83,84] In addition, other studies have evaluated the feasibility to delineate with RCM the pre-surgical margins of LM/LMM[85] or EMPD[86], or even using RCM to identify residual BCC directly inside surgical wounds.[87]

Most of these studies used the wide-probe RCM since it allows a comprehensive evaluation of a given area up to 8 x 8 mm, therefore allowing the identification of small foci of tumor cells which is crucial when mapping or monitoring a tumor. However, the wide-probe RCM can be very challenging to use in uneven surfaces such as the head and neck or the genitalia, since the metal ring and the plastic adhesive window may not stick correctly. In addition, if RCM is needed to evaluate areas larger than 8 x 8 mm, using the wide-probe RCM can be very labor intensive and slow since it may require to change the location of the metal ring in order to completely map a given lesion.

Hence, it seems intuitive that pre-surgical mapping or evaluation of uneven areas should be performed using the HRCM since it is more versatile and allows a fast evaluation over large areas of tissue. However, commercially-available HRCM has some important challenges: 1) spatial orientation can be difficult to obtain; 2) it lacks architectural information due to a small FOV and absence of mosaicking capabilities in the native software. Research has been done to solve these issues. To improve orientation, it has been suggested that scoring the outer limits of lesion with a scalpel can be useful to explore the margins of lesions that will be removed.[88,89] While this is useful in small lesions which have been anesthetized, it may not be feasible or desirable in all cases since sometimes the lesion may not be removed if deemed benign, and also when mapping lesions before surgery imaging and surgery may be performed in different days. Hence, an alternative, non-invasive method has been suggested by using adhesive paper[90] or plastic[91] rings applied on the skin. Typically the rings may be placed outside the lesion to be explored with HRCM thus helping delineate the exploration margins and allow the HRCM users to know whether they are inside or outside a given lesion. This is possible because the fibers of the ring are visible under confocal microscopy (Figure 22).

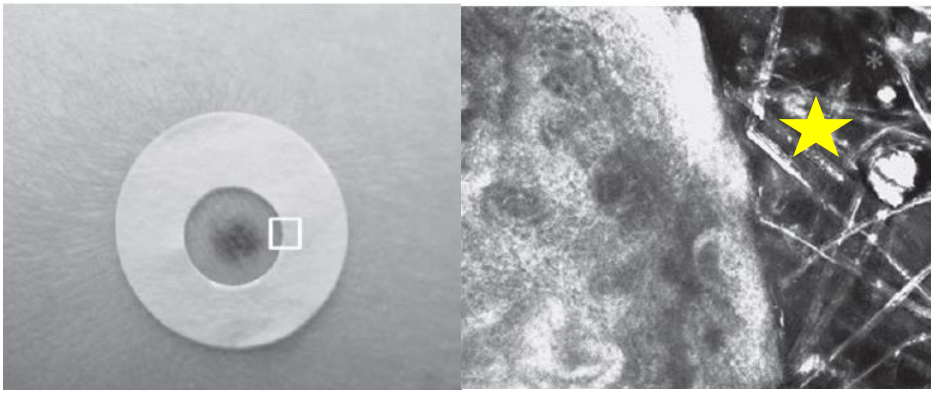

Figure 22: *Adhesive rings can help orient the HRCM user since the fibers are visible on RCM (yellow star) (Adapted with permission from Marino et al. Skin Res Technol. 2016 Nov;22(4):519-520.)*

To improve the limited FOV provided by the HRCM and obtain larger image with architectural information, some attempts have been made to create mosaics obtained from HRCM videos, in a process called **videomosaicking**. The previous experience with videomosaicking and HRCM was performed using commercially-available software (Microsoft ICE®) which rendered small strips of images which would help enlarge the FOV but were still limited to a few millimeters (Figure 23).[92] In addition, this software required a very smooth acquisition since abrupt changes may cause deformations in the image which would not reflect the real architecture of the area imaged. In this sense, a novel automated videomosaicking algorithm has been developed and is described in this thesis to address the issues encountered while using in vivo HRCM. Further details on videomosaicking and image stitching are described in the next section of the thesis.

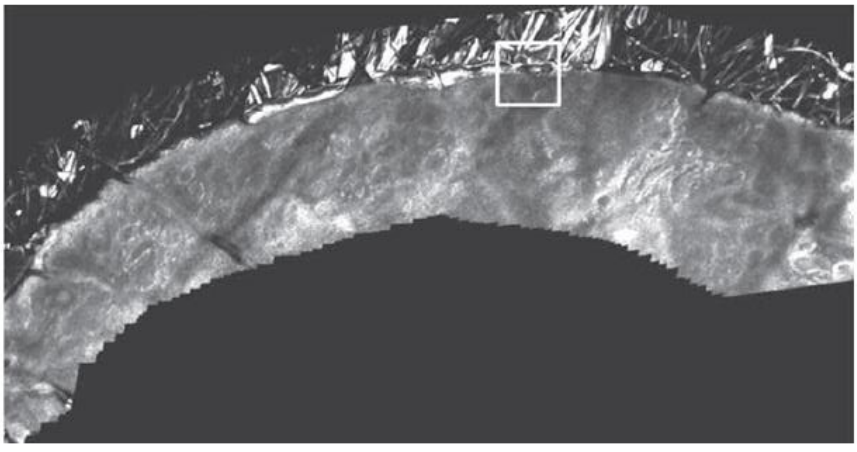

Figure 23*: Example of a videomosaic obtained with Microsoft ICE surrounding a paper ring. (Adapted with permission from Marino et al. Skin Res Technol. 2016 Nov;22(4):519-520.)*

d) Other imaging methods to evaluate skin cancers

Optical coherence tomography (OCT) is a non-invasive imaging technology which uses near-infrared laser light and combines it with low-coherence light with interferometry to obtain cross-sections of the skin (Figure 24).[93] Multiple OCT devices are currently available in the market, and they allow scanning the skin to a depth of 0.4 to 2 mm with an optical resolution of 3 to 15 µm.[94] Compared to RCM, OCT allows deeper imaging but at a worse image resolution. In addition, some devices such as dynamic OCT allow the visualization of the vessels by identifying mobile elements (blood) in consecutive cross-sections. Hence, OCT has mainly been used to evaluate the architecture of skin tumors, and therefore help in delineating the skin cancer margins, triage lesions prior to treatment, and monitor treatment response. A study by De Carvalho et al. showed that OCT could correctly guide surgical removal of BCC in 8 out of 10 cases, and in the remaining ones the authors claimed OCT helped reduce the number of Mohs stages.[94] In another study performed by the group of Pascale Guitera, they evaluated 168 consecutive skin lesions for which BCC was suspected and demonstrated that OCT could correctly triage lesions that should undergo surgery (>400 µm deep) or could be treated with non-surgical techniques such as imiquimod or photodynamic therapy (≤400 µm deep).[95] However, the main problems with currently available OCT devices are its high cost, and especially its lower resolution compared to RCM, making small subtle foci of tumor extremely challenging to identify. Hence, according to a recent Cochrane meta-analysis, current OCT devices have a poor degree of recommendation to be used in skin cancer diagnosis and only seem to be moderately useful when evaluating challenging BCCs compared to the naked eye plus dermoscopy evaluation.[96] However, novel devices with better resolution or combining different imaging modalities could make OCT a great device to assess skin cancers due to its larger field of view both in the vertical and horizontal plane.

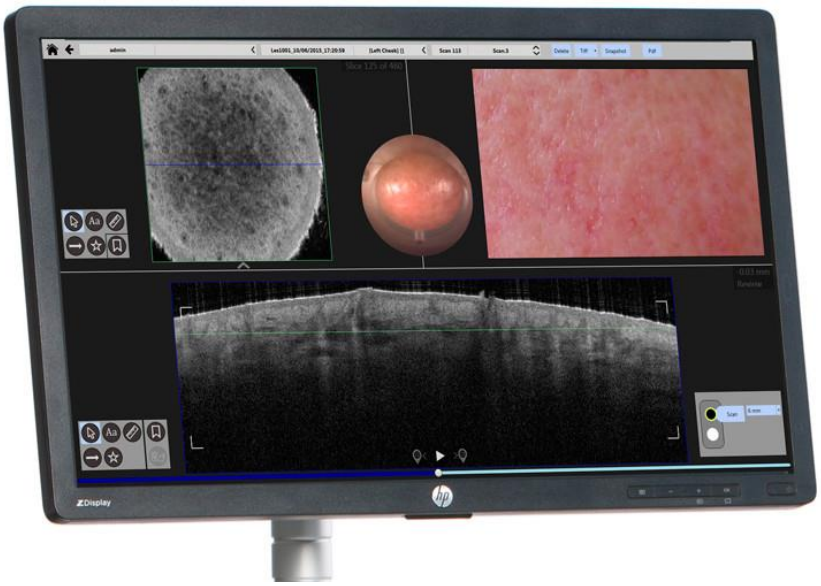

Figure 24: *Image of an optical coherence tomography device showing a vertical section (lower image) as well as an en face image (top left) created using multiple vertical sections (Source: www.vivosight.com)*

Ultrasonography, an imaging technique that uses sound instead of light, has also been used to assess skin cancers. Current high-frequency 20 MHz ultrasound probes provide a resolution of 0.1 mm and a penetration of 6 to 7 mm.[97] Hence, they have the same issues as OCT in terms of margin delineation: poor image resolution. Nevertheless, ultrasonography can be useful to assess tumor extension to deeper tissues such as the bone or fat, and some preliminary studies have used it to guide shave-excisions or predict the histological subtype of BCC.[98-100] With the advent of novel probes and the addition of Doppler and elastography, ultrasonography can potentially be used in skin cancer management due to its lower cost, deeper imaging and versatility.

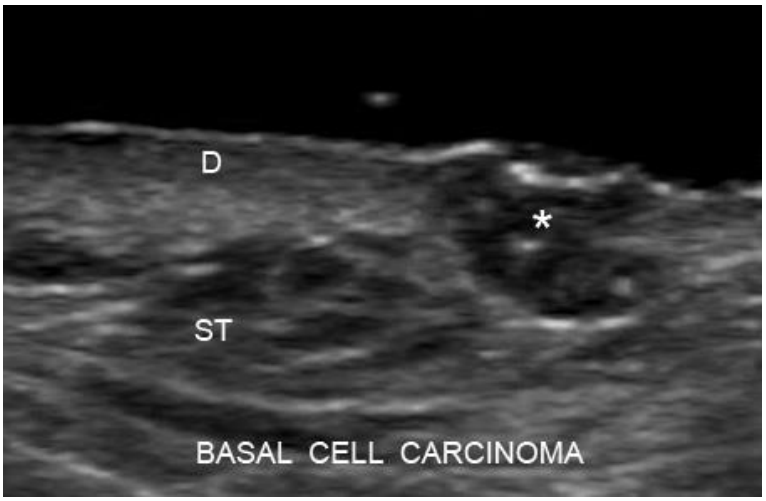

Figure 25: Example of basal cell carcinoma (asterisk) seen using high-frequency ultrasound. Note that the margins expand laterally to the dermis (D) and deep into the subcutaneous tissue (ST) (source: www.ximenawortsman.com)

Raman spectroscopy is another optical technique that has been mostly used to distinguish benign from malignant lesions. Raman spectroscopy measures the chemical vibrational modes of molecules in a given tissue by assessing color shifts in scattered photons. Later, these data are converted into a probability of malignancy, which can be used to diagnose a lesion but can also be used to distinguish if a given tissue is part of the tumor or is part of the surrounding healthy tissue. Feng et al.[101]used Raman spectroscopy to delineate the pre-surgical margins of 30 BCCs and showed that there were significant differences in the biomarkers found in BCCs compared to normal skin, especially regarding the nucleus, keratin, collagen, triolein and ceramide. However, the usefulness of this technique in tumor margin delineation is still in its early stages.

Finally, other imaging methods such as **magnetic resonance imaging** (MRI) or **computed tomography** (CT) have also been used to detect invasion of local structures (bone, soft tissues), or distant tumor extension.[102] However, since these scenarios are mostly related to staging techniques rather than primary tumor management, these technologies will not be discussed in depth in the current thesis.

4. Image stitching and videomosaicking

a) Fundamentals of image stitching and videomosaicking

Image stitching or image mosaicking is the process of combining multiple adjacent images to create a single, high-resolution, seamless, larger image (mosaic). Image stitching is normally performed by dedicated computer software but some cameras and other imaging equipment have stitching algorithms incorporated in their native software. Image stitching has been used for many years in computer vision for example to generate satellite images and maps[103], but current daily examples of image mosaics include the panoramic pictures obtained with consumer smartphones (Figure 26).

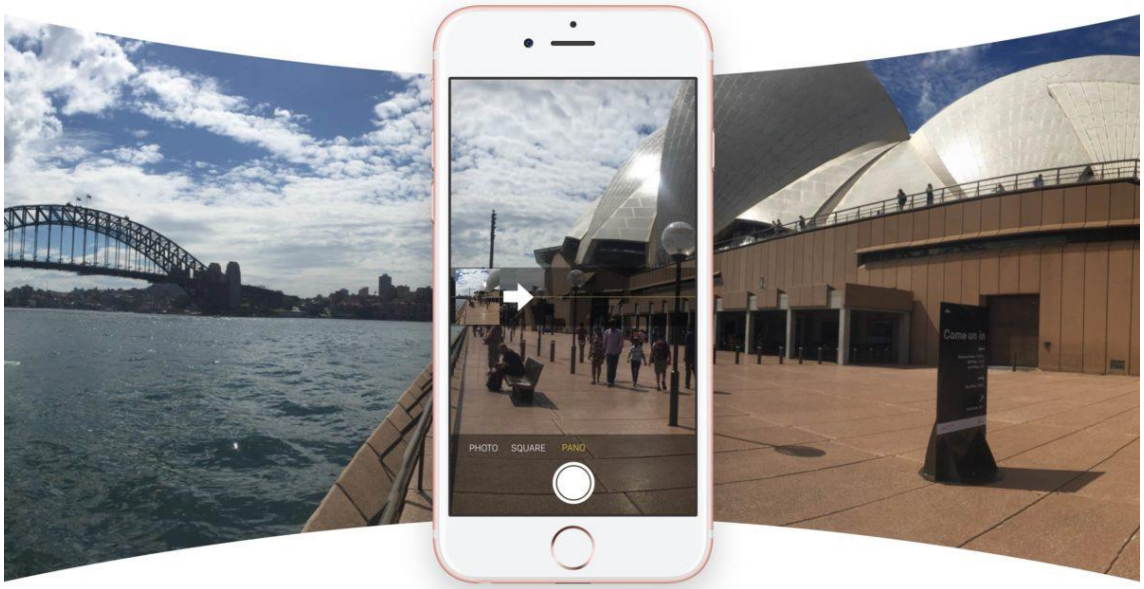

***Figure 26**: Example of a panoramic picture (mosaic) obtained with a consumer smartphone (Available at https://blog.mozaicme.com/en/iphone-panorama-pictures/)*

In order to create a mosaic it is very important to acquire multiple images that have some degree of overlap. In other words, that a given image and the adjacent one (image pair) need to have some elements in common (Figure 27). These elements in common need to be identified and matched in order to later obtain a mosaic. Mosaics can also be obtained from videos, by combining consecutive frames which first need to be extracted, in a process called **videomosaicking**.[104] Videomosaicking is widely used in videocamera stabilizers, but has also been used in medicine to convert videos obtained for example from endoscopes into 2D images which can later be reviewed more carefully.[103,105]

***Figure 27**: Example of a mosaic obtained from 3 different pictures generated using Adobe Lightroom 6.0. Note that in order to obtain the mosaic it is necessary to obtain a degree of overlap between the previous and following image. For example, the part of the tree is present in the first two images, whereas the golden tower is partially present in the second and third image. The result of stitching the 3 images results in a panoramic mosaic (Temple of Ananda, Bagan, Myanmar; Oriol Yélamos©)*

Nevertheless, regardless if the images are obtained from static images or from a video, image stitching requires a number of steps that include keypoint extraction, keypoint matching, image calibration and blending.[103] These steps will be discussed herein.

Keypoint extraction:

The first step of image stitching includes identifying which features in a given image are unique in order to identify these same areas in the adjacent image. These features areas are called **keypoints**. Good keypoints should allow accurate localization, be invariant against shift, rotation, scale, brightness change, and be high repeatable.[106] Hence, typically good keypoints include angles, corners or blobs (Figure 28).

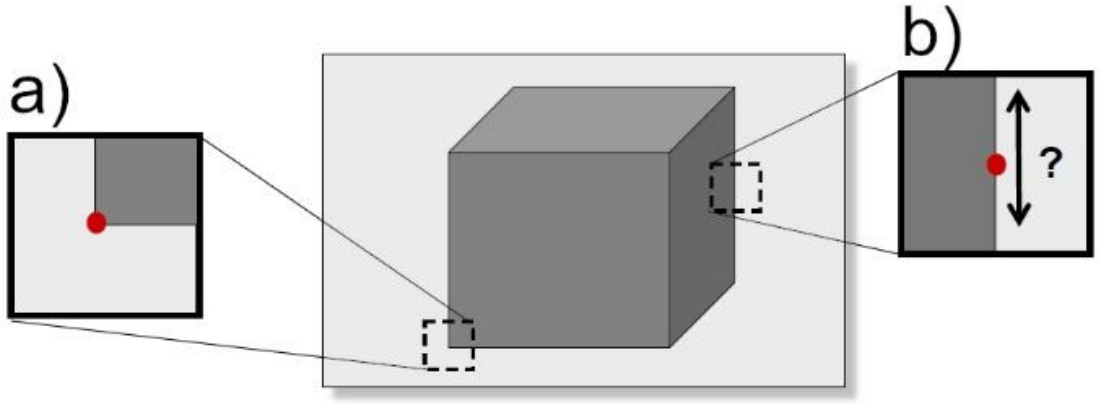

***Figure 28**: Good keypoints are located at corners or edges since they represent unique areas within an image (inset a). Conversely, areas which are straight lines can be found in other areas other image and are bad areas to be selected as keypoints (inset b) (adapted from Girod 2013[106]).*

However, in certain situations such as medicine, identifying features such as angles is not easy. Alternative methods to feature-based keypoint detection methods include direct-based methods, which are mathematical algorithms that automatically identify pixels that are unique among their neighbors.[107] Two of the most used algorithms include the Scale Invariant Feature Transformation (SIFT) descriptor or its variant Speeded Up Robust Features (SURF).[108] These are patented algorithms that look at each pixel and the surrounding ones to identify the histogram of the local gradient orientations surrounding a given pixel. In other words, they look at the orientation of each pixel surrounding a given pixel (Figure 29). The advantage of this method is that later this process can be repeated in the adjacent image thus identifying the same pattern of histograms. Hence, SIFT is intended to extract and match the keypoints, in a process called **image registration**.

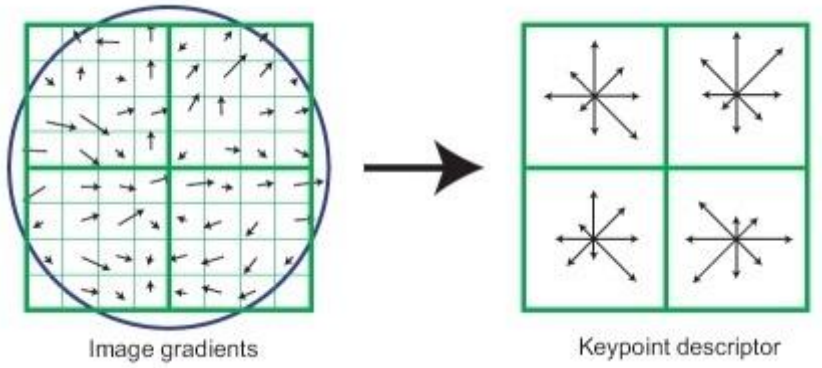

Figure 29: *Schematic representation of SIFT descriptors. Within a given image, SIFT analyzes the histograms of gradient orientations surrounding a given pixel. This information can then be compared in the adjacent image and allow the matching of keypoints (source: https://researchweb.iiit.ac.in/~wasif.mpg08/SIFT/).*

Keypoint matching:

Once the keypoints are identified, they need to be matched in both adjacent images. This can be done using different algorithms, but one of the most commonly used is the RANdom SAmple Consensus (RANSAC) algorithm. This is an iterative algorithm which starts analyzing the matches in a random fashion, and keeps repeating the analysis until finds which keypoints match more frequently (inliers) and which ones do not match (outliers).[103] This method produces a probability of match, which is more robust if more repetitions (iterations) are performed. The number of matches and times the algorithm is repeated can be determined beforehand, in order to increase the robustness of the algorithm.

However, the keypoint matching process may need corrections since problems occur during matching regarding the orientation, size and proportion of the images. For example, when two pictures are obtained from a similar focal point but with a different angle (Figure 30), the perspective can change (Figure 31). If not corrected, this may result in deformations and misalignments between the two images. Hence, stitching algorithms need to correct these issues, in a process called **image calibration**.

Figure 30*: When two adjacent pictures are taken from a similar focal point at a different angle, the perspective can change.*

***Figure 31**: Example of keypoint matching. The yellow lines link the same keypoints in image 1 and image 2. Note that the lines are not completely parallel, suggesting that the perspective in the two images is different, thus requiring image calibration (Temple of Ananda, Bagan, Myanmar; Oriol Yélamos©).*

Calibration:

Image calibration can be performed after, or in parallel with keypoint matching. As stated before, when two images are taken next to each other there may be differences among them regarding the orientation, or the perspective of the images. However, other challenges may occur regarding scene motion (e.g. the same element moves between the two images, such as branches moving because of the wind), lens distortion and vignetting (presence of darker edges at the corners of an image), or differences in exposure (different lens aperture or shutter speed result in different color and image characteristics).

Most of these challenges can be prevented during image acquisition (e.g. obtaining the images using the same exact shutter speed and lens aperture, not using bull-eye lenses to prevent vignetting) but when elements move or deform, the images need to be corrected in a process called **image alignment**.

Image alignment requires identifying the same keypoints in the different pictures, evaluate which is the geometrical relationship between them, and transform the images so they share the same viewpoint.[109] In other words, alignment is the transformation from a coordinates system to another one that matches the viewpoint we want to obtain. Based on the perspective and warping of the images, different types of 2D transformations can occur and include translation, rigid (Euclidean), similarity, projective, and affine transformations (Figure 32). These transformations can also be combined and are based on the fact that they preserve certain characteristics (Table 3).

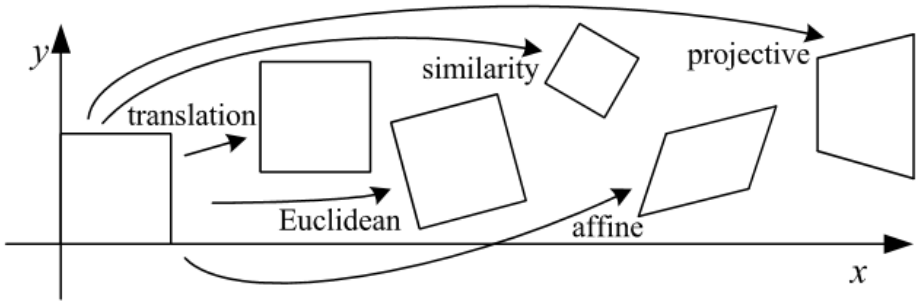

Figure 32: *Examples of 2D transformations that can be performed during image alignment (Adapted from Szeliski 2006[103]).*

Transformation	Preserves	Icon
Translation	Orientation	
Rigid (Euclidean)	Lengths	
Similarity	Angles	
Affine	Parallelism	
Projective	Straight lines	

Table 3: *Types of transformations and which elements are preserved (Adapted from Szeliski 2006[103]).*

Among these transformations, the ones that typically occur when imaging in vivo tissue are affine transformations. When the image acquisition requires contacting the tissue (for example live microscopes used to image the skin or the gastrointestinal tract), if the imaging device moves over the tissue, this can be deformed due to its elasticity, resulting in affine transformations.

Another problem that can happen is that sometimes there may be cuts or "jumps" between the images due to movement or extreme deformation. This is particularly important in videomosaicking, when abrupt movements during the video recording may result in sharp cuts or very blurry images that make image alignment impossible since no common elements are found between the two "adjacent" images. In such cases, the stitching process may be stopped where the jump occurred, or conversely may result in incorrect stitching producing deformed images. Therefore, identifying the image cuts is also important in order to determine whether to stop the mosaic generation or not.

In order to align the images and also to identify scene cuts, multiple methods have been used but again RANSAC can be used to randomly select for example three keypoints and estimate the transformation matrix. This is then repeated multiple times using different keypoints to obtain the best transformation and ultimately aligning the two images, which are ready to be stitched. When no matches are identified, a stop in the image stitching should occur.

Blending:

Once the images are aligned, it is necessary to choose which pixels should be included and how to create a final composite image. The ideal scenario is when all the images are obtained with the same perspective, parameters and exposition. If this is the case, averaging the pixels will work perfectly. However, most of the times there are differences regarding focusing, exposition and changing elements which can result in blurring, differences in color and ghosting if we simply average the pixels (Figure 33).[110]

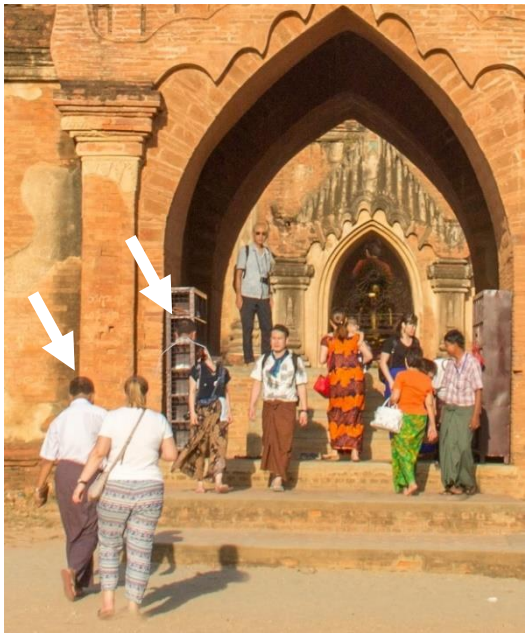

***Figure 33**: Example of ghosting after stitching different images. Since the man on the left was moving during acquisition of the different pictures (arrows), averaging of the two images resulted in the presence of a "ghost" in the composite image (temple of Sulamani Phaya, Bagan, Myanmar; Oriol Yélamos ©).*

An alternative option is to select which pixels are relevant from each image, and then stitch the two images at a given cutting point. In other words, we can select which area of the image has less differences with the following image (minimum cut), segment the images and stitch them following this imaginary line, like if we were making a jigsaw. This approach is called **graph-cut stitching** (Figure 34).[111]

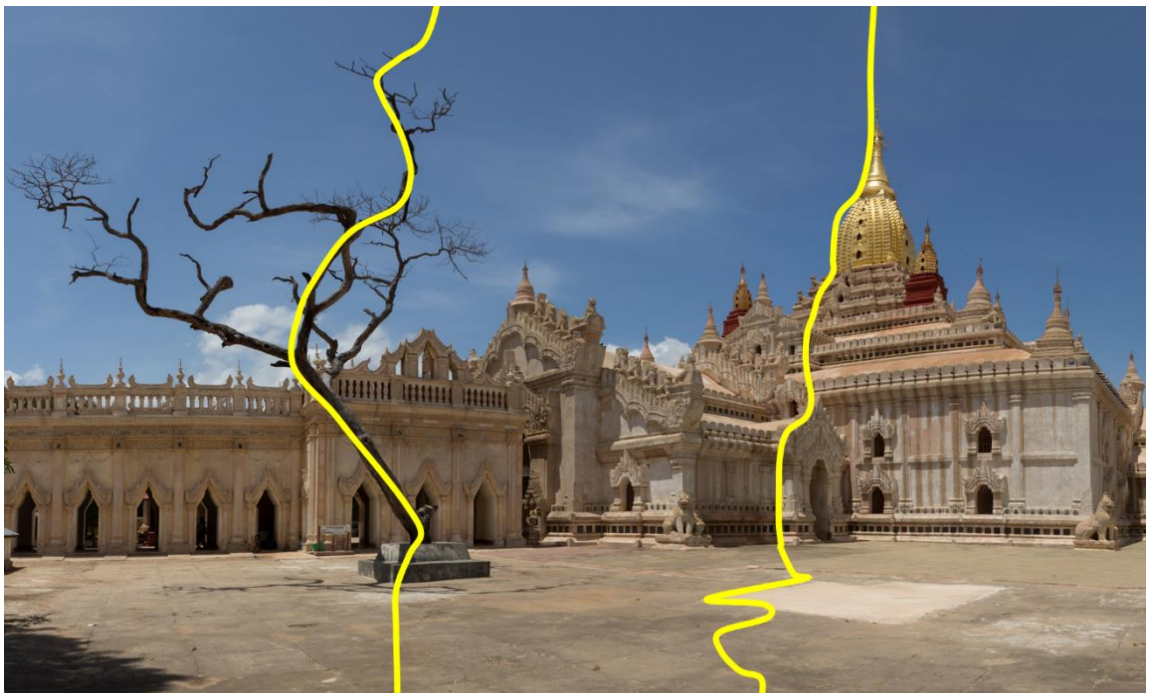

***Figure 34**: Schematic representation of a graph-cut based stitched image. The images are segmented based on areas with minimal differences and later stitched in a jigsaw-like manner (Temple of Ananda, Bagan, Myanmar; Oriol Yélamos©).*

b) Applications of image stitching in medicine

In medicine, image stitching is common, not only in the 2D plane but also in the 3D plane (3D reconstruction of organs based on multiple planar images obtained from CT scans or MRI images). A particular situation in medicine is when multiple images need to be acquired to cover a relatively large area. This can happen for example when obtaining large X ray images,[107] or when using devices that have very high resolution but a small FOV, such as in vivo microscopes or endoscopes. In the latter situation, expanding the FOV by obtaining large mosaics is crucial to assess the architecture of a given tissue, while retaining the ability to zoom into the tissue to assess cellular details, in a parallel approach to conventional pathology analysis. Since most of these devices acquire videos, consecutive frames are stitched to form videomosaics. In this sense, multiple studies have evaluated the feasibility to develop videomosaics while imaging the breast,[112] colon,[113] or cervical tissue[114] using endoscopes (Figure 35).

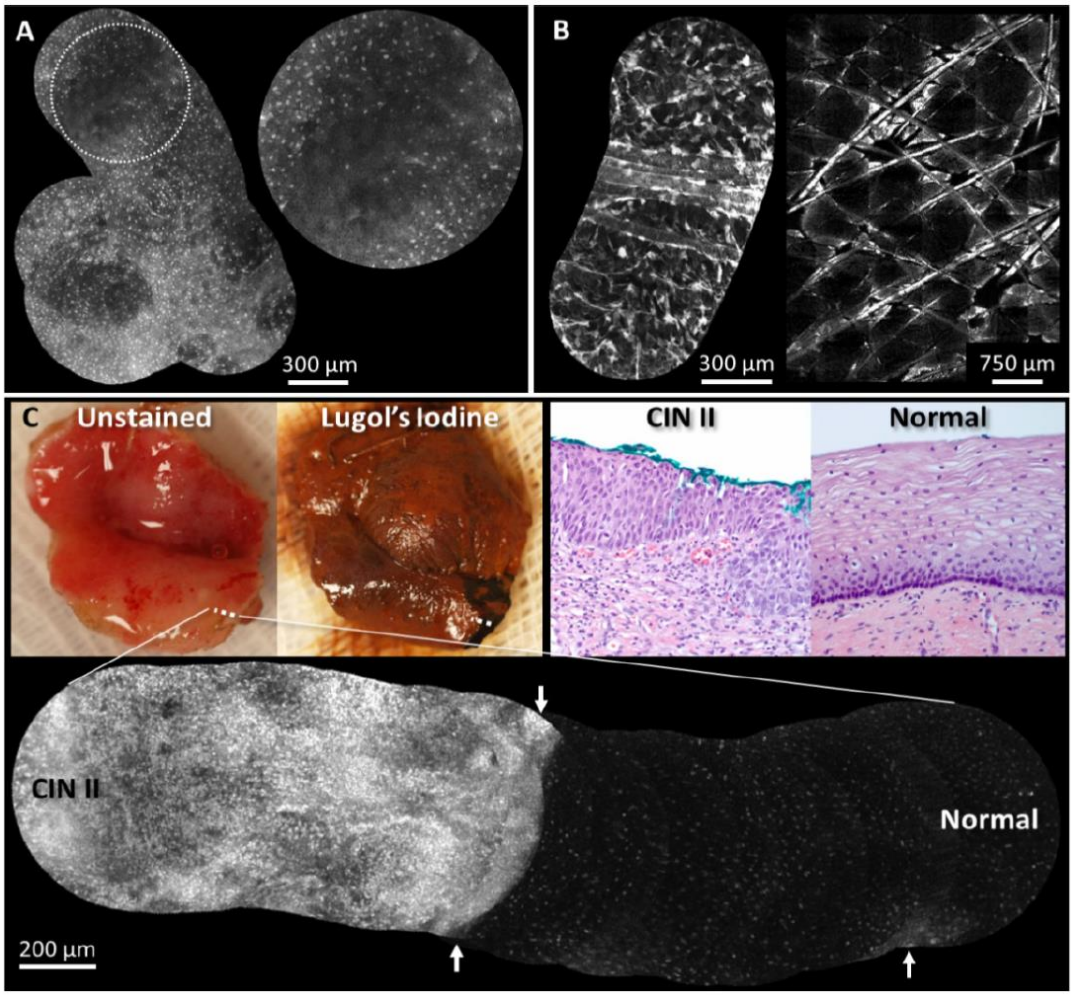

***Figure 35**: Real-time video mosaics using videos obtained with a microendoscope. The images show (A) normal in vivo oral tissue, (B) normal in vivo epidermis, and (C) pre-cancerous ex vivo cervical tissue. [Adapted with permission from Bedard et al. Biomed Opt Express. 2012 Oct 1;3(10):2428-35[114]]*

When focusing in dermatology and in particular in RCM, some preliminary studies showed that it is possible to generate videomosaics obtained with the handheld probe by imaging within the Mohs surgery wounds.[88,92] However, these videomosaics were obtained using commercial software (Microsoft ICE®) which resulted in issues regarding deformation artifacts (would not identify jumps in the video), and slow performance when having to stitch numerous frames coming from a long video. Hence, these mosaics would not correctly reflect the tissue size (would not be useful to correctly determine structures and measurements) and would not be useful in clinical practice due to its slow performance.

HYPOTHESES AND OBJECTIVES

1 Hypotheses

- It is possible to generate automated videomosaics obtained from videos acquired using HRCM which correctly reflect the architectural details of the skin imaged.
- Videomosaics can expand the FOV of HRCM and help obtain an architectural view of the skin.
- Videomosaics together with scoring systems can improve the spatial orientation while using HRCM.
- Automated videomosaics are feasible to be obtained from videos acquired using HRCM directly in surgical wounds.
- HRCM and videomosaics complement dermoscopic and Wood lamp evaluation of hypopigmented skin tumors and allow precise delineation of preoperative tumor margins in lentigo maligna and lentigo maligna melanoma.
- HRCM and videomosaics can help identify tumors that are distributed in a patchy fashion (BCC, EMPD), just after treatment or during follow-up.

2 Objectives

- To develop an algorithm to generate automatic videomosaics in HRCM.
- To use scoring methods that improve the orientation of HRCM evaluation.
- To estimate preoperative margins in LM/LMM melanoma cases using HRCM and videomosaics, and correlate these margins with actual staged-excision margins.
- To use HRCM and videomosaics to identify the margins of KCs before and after Mohs surgery.
- To use HRCM and videomosaics to identify residual KC after laser ablation.
- To monitor the response after laser ablation of basal cell carcinomas using HRCM and videomosaicking.
- To evaluate the diagnostic accuracy for identifying persistent/recurrent extramammary Paget disease using HRCM and videomosaics.

MATERIAL AND METHODS. RESULTS

Publication 1: Automated video-mosaicking approach for confocal microscopic imaging in vivo: an approach to address challenges in imaging living tissue and extend field of view

Kivanc Kose, Mengran Gou, Oriol Yélamos, Miguel Cordova, Anthony M. Rossi, Kishwer S. Nehal, Eileen S. Flores, Octavia Camp, Jennifer G. Dy, Dana H. Brooks & Milind Rajadhyaksha

Scientific Reports 2017 Sep 7;7(1):10759. doi: 10.1038/s41598-017-11072-9.

SUMMARY

Background: Reflectance confocal microscopy (RCM) is a microscopic imaging technique, which enables the users to rapidly examine tissue in vivo. Providing resolution at cellular-level morphology, RCM imaging combined with mosaicking has shown to be highly sensitive and specific for non-invasively guiding skin cancer diagnosis. However, current RCM mosaicking techniques with existing microscopes have been limited to two-dimensional sequences of individual still images, acquired in a highly controlled manner, and along a specific predefined raster path, covering a limited area. The recent advent of smaller handheld microscopes is enabling acquisition of videos, acquired in a relatively uncontrolled manner and along an ad-hoc arbitrarily free-form, non-rastered path. Mosaicking of video-images (video-mosaicking) is necessary to display large areas of tissue.

Aim: To describe an automated computer vision-based mosaicking method for in vivo videos of reflectance confocal microscopy.

Material and methods: The algorithm handles unique challenges encountered during video capture such as motion blur artifacts due to rapid motion of the microscope over the imaged area, warping in frames due to changes in contact angle and varying resolution with depth. We address all these challenges by (i) directly modeling deformations, (ii) automatically detecting abrupt motion artifacts (discontinuities) in the image sequence, and (iii) robustly stitching the registered frames with an approach that combines overlapped images flexibly, in a data-driven fashion, without blurring or loss of resolution.

Results: We present the algorithm and test examples of video-mosaics obtained with our algorithm of melanoma and non-melanoma skin cancers, to demonstrate potential clinical utility.

Conclusions: Our video-mosaicking methods addresses the challenges of automated videomosaicking in handheld RCM and could be included in the RCM native software.

SCIENTIFIC REPORTS

OPEN

Received: 7 March 2017
Accepted: 11 August 2017
Published online: 07 September 2017

Automated video-mosaicking approach for confocal microscopic imaging *in vivo*: an approach to address challenges in imaging living tissue and extend field of view

Kivanc Kose[1], Mengran Gou[2], Oriol Yélamos[1,3], Miguel Cordova[1], Anthony M. Rossi[1], Kishwer S. Nehal[1], Eileen S. Flores[1], Octavia Camps[2], Jennifer G. Dy[2], Dana H. Brooks[2] & Milind Rajadhyaksha[1]

We describe a computer vision-based mosaicking method for *in vivo* videos of reflectance confocal microscopy (RCM). RCM is a microscopic imaging technique, which enables the users to rapidly examine tissue *in vivo*. Providing resolution at cellular-level morphology, RCM imaging combined with mosaicking has shown to be highly sensitive and specific for non-invasively guiding skin cancer diagnosis. However, current RCM mosaicking techniques with existing microscopes have been limited to two-dimensional sequences of individual still images, acquired in a highly controlled manner, and along a specific predefined raster path, covering a limited area. The recent advent of smaller handheld microscopes is enabling acquisition of videos, acquired in a relatively uncontrolled manner and along an ad-hoc arbitrarily free-form, non-rastered path. Mosaicking of video-images (video-mosaicking) is necessary to display large areas of tissue. Our video-mosaicking methods addresses this need. The method can handle unique challenges encountered during video capture such as motion blur artifacts due to rapid motion of the microscope over the imaged area, warping in frames due to changes in contact angle and varying resolution with depth. We present test examples of video-mosaics of melanoma and non-melanoma skin cancers, to demonstrate potential clinical utility.

Imaging over large areas of tissue is often necessary in clinical and research settings. However, high-resolution microscopy is limited to a small field of view in a single image acquisition. To extend the field of view, mosaicking techniques – acquiring a sequence of adjacent images and stitching or blending them together at the boundaries – have been developed[1,2–8]. Approaches for mosaicking of a two-dimensional matrix of individual still images have been developed for bench-top work on tissue specimens *in vitro*, and *ex vivo*[4,9–16]. In bench-top settings, still images are typically acquired in a highly controlled manner along a specific predefined raster path. However, mosaicking for the newer, increasingly powerful and widespread implementation of video-imaging on living tissue *in vivo* is significantly more challenging. In this situation, video-images are acquired in a relatively uncontrolled manner and along an ad-hoc arbitrarily free-form, non-rastered path on living humans and animals. Approaches for mosaicking of a sequence of images from a video are called "video-mosaicking[17]".

Three problems commonly occur when video-mosaicking *in vivo* are (i) deformations - i.e. warping or distortion in images - due to physical changes (angle, pressure) at the microscope lens-to-tissue contact, (ii) abrupt motion artifacts - i.e. "jumps" or discontinuities between consecutive frames that are caused by sudden changes in depth or topography of tissue motion and/or manual and variable operator control of the microscope during imaging, and iii) optical sectioning and resolution may vary between consecutive images due to scattering and

[1]Dermatology Service, Memorial Sloan Kettering Cancer Center, New York, NY, USA. [2]Electrical and Computer Engineering, Northeastern University, Boston, MA, USA. [3]Dermatology Department, Hospital Clínic, Universitat de Barcelona, Barcelona, Spain. Kivanc Kose and Mengran Gou contributed equally to this work. Correspondence and requests for materials should be addressed to K.K. (email: kosek@mskcc.org)

aberrations induced by changes in depth and morphology. In the presence of these difficulties, spatially overlapping images need to be "combined" to produce a video-mosaic.

Although these challenges, and our solutions presented in this paper are generic for any setting in which large field of view video-mosaics are needed from deep, high-resolution microscopic imaging in living tissue, we are, in this paper, specifically focused on the use of video-mosaicking for reflectance confocal microscopy (RCM) imaging in human skin *in vivo*. RCM imaging non-invasively acquires nuclear- and cellular-level detail with thin optical sectioning ($1-3\,\mu m$) and high resolution ($0.5-1\,\mu m$)[18,19].

Several clinical studies have consistently reported RCM imaging to be capable of diagnosing melanocytic and non-melanocytic cancers with high sensitivity and specificity[19–22]. Recently, the Centers for Medicare and Medicaid Service in the USA granted current procedural terminology (CPT) codes, which means that RCM imaging is now a billable and reimbursable procedure[23]. The imaging is advancing toward routine implementation for guiding diagnosis as it has shown to increase diagnostic accuracy while maintaining a good specificity (and reducing the rate of biopsies of benign lesions per detected malignancy)[24–28]. Meanwhile, with the advent of a new generation of handheld confocal microscopes, acquisition of videos instead of only still images is becoming increasingly useful[29–31] to consistently and rapidly display tumor morphology and surrounding normal tissue over much larger areas of skin (from $2\,mm \times 2\,mm$ up to $10\,mm \times 10\,mm$).

In such settings, the special challenges are that the microscope is manually controlled and focused at varying depths (50 to 200 μm) in living tissue, resulting in varying resolution, exaggerated motion and distortion between images in any video. Moreover, the regions to be imaged differ greatly from subject to subject, skin site to skin site, and lesion to lesion, so operator flexibility in acquisition is necessary. Although "playback" of videos can be useful, the ability to spatially "map" the imaged region and display the entire field of view at once, by constructing a mosaic, allows much more "natural" analysis by trained clinicians or (semi-)automated algorithms[29]. Reading and interpreting a mosaic more closely mimics the standard procedure for examining pathology slides, which usually starts by looking at 10 mm × 10 mm areas of a tissue section with 2× magnification. Thus, there is a need in the clinic for video-mosaicking of RCM images, toward wider acceptance and adoption for routine use.

In this paper, we present a new algorithm for video-mosaicking of subsurface confocal microscopic images, which addresses all of the expected challenges. Earlier video-mosaicking techniques, for both confocal and non-confocal endoscopy, either address only a subset of these problems, or attempt to avoid some of them by limiting the freedom of motion during acquisition[1–3]. Video-mosaicking was demonstrated for imaging of oral and cervical tissue[1]. However, the imaging depth was close to the surface of tissue, so tilt and loss of resolution were not significant. Similarly, another algorithm was reported on human skin and mouse brain tissue[2], but, again, no attempt was made to handle the warp or deformation that can happen when imaging at greater depth[2]. In another study on human and mouse colon tissue[3], the algorithm models both rigid and non-rigid deformations in a linear fashion. However, the algorithm does not consider abrupt motion artifacts between frames and, furthermore, can enhance blurring at image boundaries through the use of blending to produce the final mosaic.

We address all these challenges by (i) directly modeling deformations, (ii) automatically detecting abrupt motion artifacts (discontinuities) in the image sequence, and (iii) robustly stitching the registered frames with an approach that combines overlapped images flexibly, in a data-driven fashion, without blurring or loss of resolution. Our algorithm is based in part on adaptation of methods from computational photography[32]. In particular, we describe the use of keypoint matching to design affine transformations to allow warping among consecutive video frames (images) during registration. The properties of the resulting affine transformations are also used to detect abrupt motion artifacts between frames. Finally, we developed an approach, based on a graph-cuts based model[33], to stitch overlapping frames together along arbitrary (non-rectilinear) boundaries, driven by the image data itself, without the loss of resolution that, otherwise, would occur from blurring or other blending techniques, and without imposing arbitrary pre-defined stitching boundaries. Herein, we describe our method in detail, and then present illustrative video-mosaicking results on human skin lesions *in vivo*. The advantages and limitations of our algorithm are discussed, as well as the possible future directions for both research and clinical applications.

Results

Video-mosaicking is of particular interest for rapid assessment of skin lesions that can be arbitrarily large and/or located at curved, irregular anatomical sites. We illustrate the capabilities of our approach by presenting results for three distinct clinical cases, each of which presents a particular set of imaging requirements. The flexibility and robustness of our approach is demonstrated for producing useful video-mosaics in all three settings.The first case is a lentigo maligna melanoma (LMM), where the need for accurate planning of surgical margins at non-flat corrugated and irregular anatomical sites is met by video-mosaicking over arbitrarily large predefined areas of tissue. In the second case, we show how video-mosaicing can help in adaptively detecting small and focal sites of suspicion within widely spread areas for diagnosing and monitoring of extramammary Paget disease. In the third case, we illustrate how video-mosaicking can help in rapid intraoperative detection of residual basal cell carcinoma in surgical wounds. All the videos acquired for this study were obtained after Institutional Review Board approval.

Case 1: Lentigo Maligna Melanoma (LMM). In Fig. 1, we illustrate the use of our approach for pre-surgical planning of LMM excisions. LMMs frequently occur on the face, head. and neck. The lesions usually appear to be small on the surface (millimeters in extent), but the subclinical, subsurface spread is often substantially larger (centimeters), and is also often obscured within surrounding degraded photo-aged skin. Moreover, the subsurface spread of melanoma cells is typically highly dendritic, like the roots of a tree, and therefore the thin tendrils that define the outermost margins are difficult to determine using current approaches, namely visual (clinical, dermoscopic) inspection and Wood's lamp (ultraviolet-excited fluorescence) examination.

Following an initial diagnostic biopsy (at the location of the red asterisk at the center of panels (A), (B), and (C)), the clinical margin (yellow dotted circle) of the lesion is determined with dermoscopy and Wood's lamp

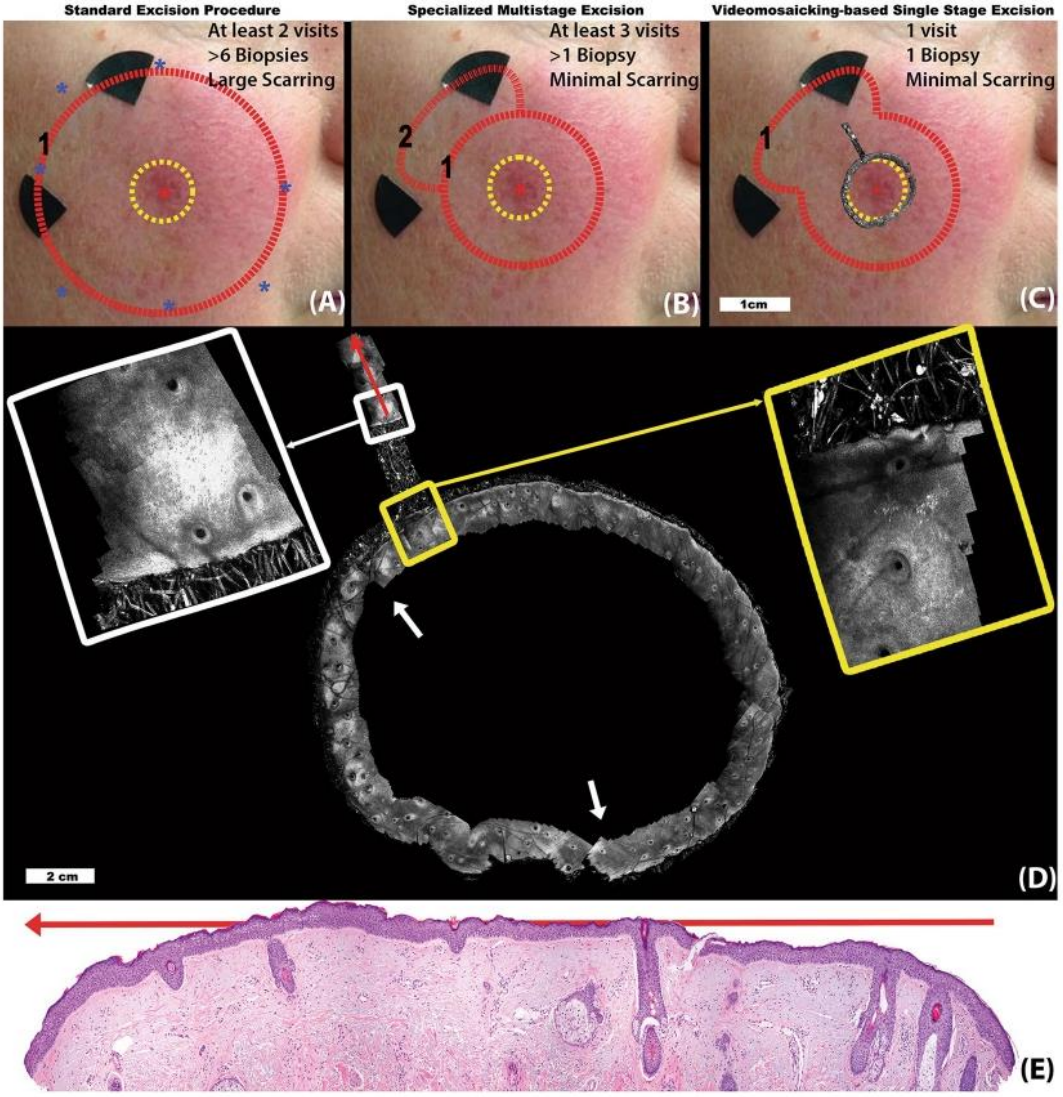

Figure 1. Lentigo Maligna Melanoma (LMM): Figure illustrates three potential methods to treat an LMM lesion in the clinical setting and how RCM video-mosaicking can improve LMM management. In all three approaches, following an initial diagnostic biopsy (red asterisk), the clinical margin (yellow dotted circle in (**A**–**C**)) is determined through macro imaging (dermoscopy and Wood's lamp examination). (**A**) In the standard surgical procedure, completely excising cancer in least number of surgery is the primary concern and tissue conservation secondary. After diagnosis, in a single visit, the lesion is excised with a 1 cm wide surgical margin around the clinical margin. (**B**) At specialized cancer care clinics, in order to spare healthy tissue, multi-staged excision may be performed. In the case illustrated here, first an excision with a conservative margin (5 mm, red circle 1) was conducted. Histological examination of the excised tissue, indicated residual tumor at 11 o'clock spreading in a radial direction. Thus, after a few days, a second excision was planned and executed in that region only (red circle 2). In (**C**) we show how RCM video-mosaicking can streamline and improve the procedure. The video-mosaic of the clinical margin was created from *in vivo* RCM videos (shown overlaid on the clinical image) by the algorithm described here. Expert examination of the video-mosaic revealed tumor extension at the 11 o'clock location and extending radially (yellow inset), therefore, we extended the video-mosaic in that direction (the radial mosaic in the direction of the red arrow, white inset), all in one visit. Histopathological examination along the same line as the extended mosaic (red arrows in panels (**D**) and (**E**)) confirmed the findings in the RCM video-mosaic, showing the extent and margin of tumor cell spread towards the periphery of the lesion.

examination. In the standard surgical procedure, removal of the disease is the primary concern and tissue conservation the secondary one. Therefore, as shown in Fig. 1A, a wide "safety" margin (red dotted circle), up to 1 cm, beyond the clinical margin is estimated. The estimated margin is interrogated by blindly sampling the margin via "mapping" biopsies (blue asterisks)[34]. Several days later, if all biopsy reports result in negative findings at the margin, the lesion is excised along the surgical margins. In case any of the biopsies turn out to be positive, the surgical margin is extended further along that direction. After the surgery, if residual tumor is found at the edges of the excised tissue, then further surgery is performed on a third visit.

In specialized cancer care centers, in order to conserve more of the healthy tissue, alternative multi-stage excision guided by histology is sometimes performed (Fig. 1B). After the initial diagnostic biopsy, the central part of the lesion corresponding to the clinical margin (yellow dotted circle) plus an initial narrower "safety" margin (usually 5 mm) is excised (red dotted circle). After histopathological analysis of the excised tissue, if it turns out that the excision margin in any quadrant contains residual tumor, the patient undergoes further excision in those positive quadrant(s) (red dotted curve) and the excised tissue is processed again by pathology. This process iterates until tumor-free margins are achieved and can take several days to several weeks, depending on the size and irregularity of the tumor.

In contrast, our video-mosaicking method offers a streamlined diagnostic and therapeutic procedure, as illustrated in Fig. 1C. Subsurface structures are visualized non-invasively along the clinical margin (yellow dashed circle), as shown in the circular video-mosaic superimposed in gray-scale at the clinical margin. Assessment of the video-mosaic revealed tumor in one quadrant (yellow inset) and consequently a localized radial scan was performed next (illustrated in detail in Fig. 1D). Expanded views of the yellow and white insets show two frames along this radial scan. Analysis of the radial mosaic correctly determined the extent of the tumor growth (without the need for mapping biopsies) in the associated quadrant. of the tissue to guide further surgery. Immediately after imaging, the lesion was excised with an appropriate "safety" margin (red dotted lines). Note that the capability of RCM for subsurface imaging with cellular resolution allows non-invasive detection of the extent of disease, which otherwise is not possible without invasive biopsy.

Histopathology from this particular case confirmed the margin determined in the video-mosaic. Note that he white arrows in panel D show two locations at which our tailored video-mosaicking algorithm automatically compensates for "jumps" (discontinuities) in the video, allowing correct mosaicking of the three distinct arcs. The individual sub-mosaics are put together manually in an image editor. This is a simple procedure as the first and last frame of consecutive sub-mosaics are spatially located next to (or very close to each other), and their relative location to each other can typically be estimated using the RCM video.

The resulting video-mosaicking method allows sufficiently precise determination of the appropriate surgical margin[35]. The excision is tissue-conserving, similar to that of the staged excision approach used in specialized clinics, but all accomplished in a single visit without the need for repeated visits and repeated biopsies.

Case 2: Extramammary Paget disease (EMPD). In Fig. 2, we illustrate the use of video-mosaicking to improve the sampling accuracy and guide diagnosis of extramammary Paget disease (EMPD). EMPD is a rare skin cancer that appears on the genitalia, often covering large areas, and that is frequently mistaken for an inflammatory or infectious condition. In addition, due to a patchy and focal distribution of tumor cells, sampling the lesion for diagnosis and management requires numerous biopsies, most of which typically turn out to be benign.

In order to cover such large areas with curved surface topography, clinicians move the confocal microscope over the region of interest in a free-hand fashion. The approach is to acquire RCM videos in the suspicious area, starting from the center of the lesion and navigating towards the outer borders in a spiral path, aiming to cover the entire area in a rapid fashion without missing any regions. This approach allows identification of areas with higher tumor cell density, which can then be selectively biopsied to confirm diagnosis[36].

Being able to image in a user-determined irregular trajectory is important in EMPD as tumor cells are sparsely distributed in a patchy fashion. To illustrate, in Fig. 2, we indicate a region (yellow asterisk on panels A and B) that is well within the clinical lesion but determined in the video-mosaic to be free of tumor cells. Furthermore, we also illustrate a positive area (white dotted circle in A and B), where video-mosaic suggests signs of EMPD in a clinically suspected area. The findings from video-mosaicking are also confirmed by histological examination (Fig. 2C) of the biopsied sample from the region.

Case 3: Basal Cell Carcinomas. Fig. 3 illustrates the use of video-mosaicking for the intraoperative assessment of residual basal cell carcinoma (BCC) margins during surgery. BCC is often treated with a tissue conserving procedure called Mohs micrographic surgery, in which the surgeon is guided by the preparation and reading of frozen pathology of thin excisions, taken in successive stages. This is a relatively slow procedure since each stage takes 20–45 minutes to be processed for frozen sections and two or more stages are often required for clearance.

Video-mosaicking performed directly in the Mohs surgical wound allows rapid detection of residual tumor[30]. This enhances the ease of correlating microscopic cellular detail with macroscopic location in the wound, which would be much more difficult with standard RCM imaging or by simply observing the original videos. Since the video-mosaic has the same resolution as in the original images, the surgeon can zoom in on suspicious areas and examine them in detail, with higher magnification, without loss of any information (e.g., inset in Fig. 3).

Discussion

In this paper, we present a new way of imaging large areas of tissue at microscopic resolution, even when the anatomical sites of interest are hard to access and/or present uneven, corrugated and irregular topology. To image such large and challenging regions of interest, clinicians must often rely on video-microscopy. Typically, a video sequence is captured over the area of interest by moving a handheld microscope manually over the tissue. The need to maintain cellular resolution means that each frame of these videos has a small field of view, and thus the video presents a rapid succession of small correlated areas of tissue but viewing them as a video does not reveal their spatial relationship. As an example of possible consequences, in the case of RCM imaging of skin, a recent study[37] showed that diagnostic capabilities decrease slightly when the handheld version of the microscope is used. The authors attributed this decrease to the lack of mosaicking capability of the handheld microscope, and inability to quickly examine large field of view (large area of tissue). Video-mosaicking thus solves this problem by registering, concatenating, and stitching together microscopic images to produce a large field of view.

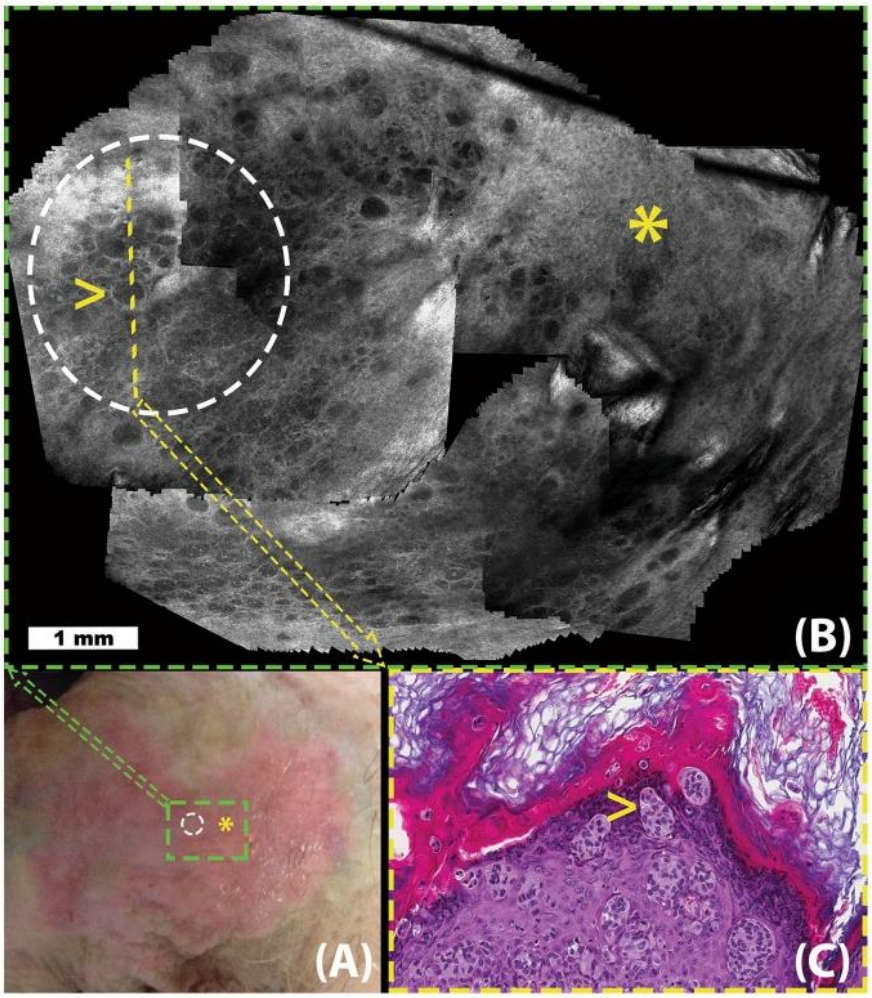

Figure 2. Extramammary Paget Disease (EMPD): Figure illustrates the use of video-mosaicking for non-invasive examination of tumor spread in a suspected case of EMPD. Panel A (lower left) shows a clinical image exhibiting the suspicious lesion, whose red color and appearance is suggestive of EMPD. In panel B (top), a video-mosaic is obtained by imaging with a handheld confocal microscope in a spiral fashion intended to largely and efficiently cover the green box in panel A. The region inside the white circle on panels A and B was determined to be suspicious in the video-mosaic, and thus a histological section (yellow line in panel B) was excised (shown in panel C). Histological examination of the slice confirmed the findings from the video-mosaic, as illustrated by the high density of tumor cells visible at the yellow arrow in both panels B and C. Unfortunately, during such imaging along a spiral path, the operator could not keep the imaging depth constant and the resulting artifact, as seen in upper left side of the mosaic, occurred at the overlap area. Although the algorithm stitching artifacts through grapcuts based method, such artifacts cannot be completely avoided due to the nature of RCM imaging and challenges in image capture.

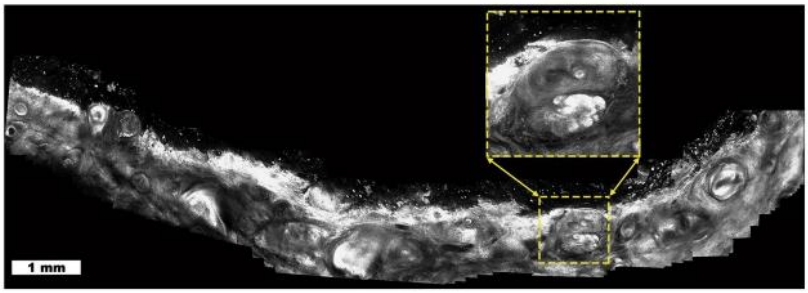

Figure 3. Basal cell carcinoma (BCC): Video-mosaic showing residual tumor (inset, bright lobular nests) in a quadrant of a Mohs surgical wound. Video-mosaicking enables the localization of the residual tumor by providing architectural information that is not readily available when viewing the original videos.

However *in vivo* microscopic video-mosaicking is challenging for both image capture and mosaic composition. The quality of the final mosaic is sensitive to the motion of the microscope over the imaged area. The operator must to avoid rapid motion, while maintaining smooth translation across the skin and constant depth of the focal plane, with micron-level accuracy. Rapid motion can result in blurring and warping deformations in the final mosaic, while rapid change in depth can result in jumps in the imaging plane between frames. Although such artifacts can not be totally avoided during clinical imaging, one of the novelties of our approach, the scene cut detection step, can detect and handle both types of rapid motion and thus minimize these artifacts in the mosaic.

Another novelty that distinguishes other video-mosaicking methods in the literature is our graph-cuts based seamless stitching approach. This method has previously been used in computational photography; however, as far as we know, this is the first study that utilizes it in the microscopy setting. The challenge it solves is that traditional blending methods will lead to blur, and thus loss of the cellular resolution that is critical to diagnosis, while image-to-image variability and edge artifacts in the images make an a priori fixed cut-and-stitch approach suboptimal. Using graph-cuts based stitching, we allow the data itself to drive the merging of adjacent overlapping images, thus preserving the resolution of the original images without altering pixel values, while providing maximally smooth transitions, across stitching seams.

However, one current challenge of video-mosaicking is processing delay. Our current implementation stitches a 500 frame video (where each frame is 1000 pixels on a side, for a total of of 500 megapixels) into a video-mosaic in less than 30 minutes, using a MATLAB based implementation with a few C MEX libraries. The timing varies depending on the specifics of the scene geometry, which affects the number of reliable keypoint matches that are used in the registration step. This is adequate for some clinical settings and indeed is being actively validated by our clinicians, as in the examples shown in the Results section. However this delay is clearly an impediment to wider adoption; being able to present video-mosaics on-the-fly to the clinician would provide valuable live visual feedback, which would not only make it more clinically useful but would also help decrease motion artifacts and ensure appropriate coverage of the region of interest. Currently, the registration step is the bottleneck to increasing the speed of video-mosaic composition. We note that our MATLAB code is not optimized for such processing, and thus we are confident that significant increase in speed is feasible without significant loss of performance. Highly efficient codes have already been developed in C and C++ that provide real time feature extraction and tracking capabilities, such as in the OpenCV computer vision library[38,39]. In addition, all the registration steps, including the SIFT keypoint extraction, matching, and RANSAC-based keypoint elimination steps, are parallelizable and could also be implemented on GPUs for further acceleration. Therefore, we believe that substantial increase in computational speed will be achieved, enabling stitching that essentially keeps up with the image acquisition.

Another approach to lessen motion artifacts is the potential availability of smaller and faster microscopes with frame rates higher than the current 7 frames per second. Besides, with increase in processing speed, smaller microscopes would allow enhanced operator control of free-hand movement and, along with higher frame rates, further facilitate real-time stitching, thus improving both the quality of the mosaics as well as the ability to rapidly and reliably cover an entire arbitrarily shaped region of interest. Availability of real-time video-mosaicking has the potential to enable the clinicians to be more time/cost efficient and precise in their diagnostic assessments and surgical practice.

Finally, as shown by the clinical examples in the results section, video-mosaicking has the potential to open new alleys in imaging based diagnosis and surgery, that in the past the clinicians were not able to do due to technical limitations. Moreover, the initial clinical success in imaging skin, is being translated to other setting and applications. One example is video-microscopy in the oral cavity. Head and neck surgery group in our institute is currently testing handheld microscope with a new telescopic probe for intra-oral imaging during head-neck surgery. Testing has thus far been performed on then patients, with video-mosaic being assessed for correlation to pathology for delineation of margins. Again real-time mosaicing has the potential to provide live feedback to the surgeon and make surgical planning and procedure more efficient.

Need for video-mosaicking has already raised in other fields such as video-microscopy of oral cavity, where confocal microscopy has also begun to show its usability. Head and neck group in our institute is currently testing a new telescopic attachment on the handheld microscope, which was designed by our group, to acquire video-microscopy videos. Their investigate the potential use of video-microscopy in image guided surgery of the oral cancer patients. The videos that they acquire during in the OR are converted into video-mosaics for diagnostic correlation studies. Again, real-time video-mosaicking has the provide critical feedback to the surgeon throughout the surgery and make surgical planing and procedure more efficient.

Methods

Ethics Statement. Prior to enrollment to the study and RCM imaging, all patients signed an informed consent to an institutional review board (IRB) approved protocol at Memorial Sloan Kettering Cancer Center. The study and the experiments were conducted in accordance with the MSKCC IRB regulations and the Declaration of Helsinki principles.

Algorithm Overview. The algorithm is composed of a series of steps (Fig. 4) designed to handle each of the three challenges listed in the introduction. We started with a classical image mosaicking pipeline from the multiview 3D reconstruction literature[32] and added methods to *identify discontinuities* (called "scene cuts") between frames, requiring separation into individual "subvideos" and to *stitch* with maximal preservation of image fidelity, both specifically tailored for application to video-microscopy.

Overall, the algorithm takes an RCM video as an input, registers the consecutive small FOV frames, detects any rapid motions indicating the need for scene cuts, and finally stitches all frames into a large FOV mosaic, automatically within subvideos and automatically or semi-automatically across scene cuts (Fig. 4). The registration

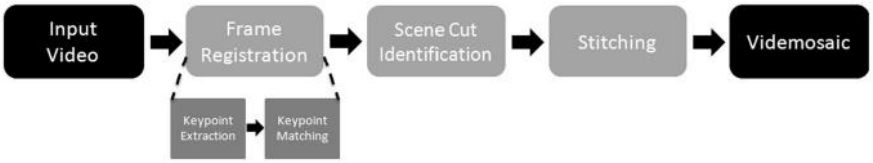

Figure 4. Flowchart of video-mosaicking process. The individual steps are further described in the methods section, with further details in the supplementary material.

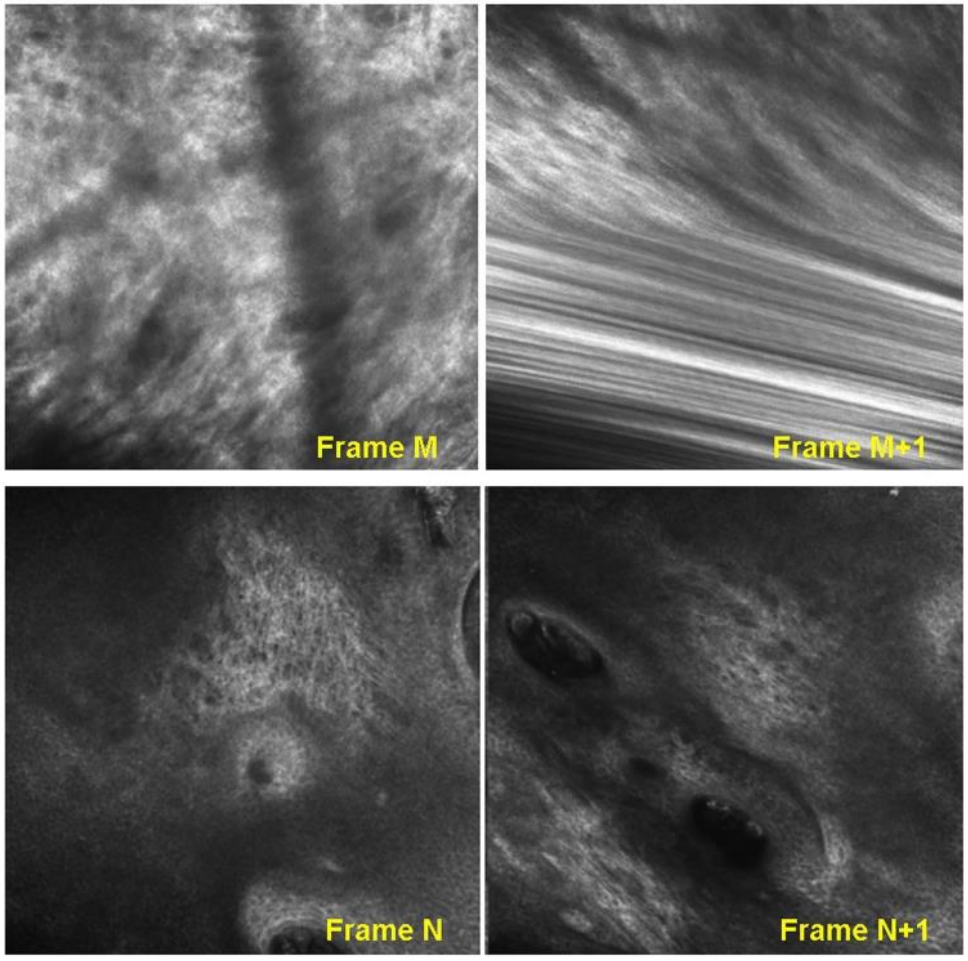

Figure 5. Common problems in imaging that will lead to discontinuities or "scene-cuts" in the RCM video-mosaics; (i) Blur due to rapid motion (**Row-1**), (ii) Lack of overlap between frames (**Row-2**).

procedure itself is composed of two subroutines, keypoint extraction[32,40] and keypoint matching[32]. During *keypoint extraction*, uniquely identifiable pixel locations in each frame are determined. Then, through *keypoint matching*, keypoints are matched between consecutive frames and their inter-frame displacement is tracked. These displacement parameters are then used to estimate registration parameters to map the pixels of each successive frame to the reference frame of the mosaic. These registration parameters also provide quantitative estimates of inter-frame motion. Therefore, the algorithm uses them to identify rapid and/or tilted motion in the videos where inter-frame registration is either not feasible or unreliable; at those frames the algorithm automatically imposes scene cuts (Fig. 5). Each resulting contiguous segment is stitched into an individual video-mosaic. Since consecutive frames overlap significantly, rather than using common algorithms based on blending, which blur details and coarsen resolution, we adopted a graph-cuts based stitching algorithm[41] which retains the original values for each pixel in the mosaic, critical to preserve cellular detail. In the following sections, we briefly describe each of these steps; details are in the supplementary material.

Frame Registration. Since the user moves the microscope freely over the region of interest without any positioning feedback, motion information must be extracted by analyzing the image frames themselves. We use

a two step approach (Fig. 4) to estimate the microscope motion information: (i) keypoint extraction, and (ii) keypoint matching.

Keypoint extraction. We use an optical flow estimator that tracks the inter-frame motion of uniquely identifiable spatial locations, referred as "keypoints". In macroscopic images of the natural world images, keypoints are usually found at high-contrast locations such as corners and local extrema. Here they are not as clearly identifiable, which necessitates some further processing as described below. Keypoints are detected by their relation with their neighbors, and matched between consecutive frames using their descriptors.

Due to changes in microscope-to-skin contact parameters (angle, pressure, velocity) during video capture, the scale, orientation, and intensity value of keypoints may change slightly between consecutive frames. To improve robustness, we use "Scale-Invariant Feature Transform" (*SIFT*)[40] keypoints and descriptors, among several available descriptors in the literature[32]. SIFT is invariant to commonly encountered variation in images such as uniform scaling and changes in orientation, and also robust against affine distortion and changes in intensity. The first step in the SIFT algorithm is keypoint identification. Keypoints are typically high contrast pixels within their neighbors. SIFT uses a difference-of-Gaussian (DoG) representation (Sup. Fig. S1) At the end of this keypoint extraction stage, we typically acquire ~3000 keypoints per frame. Each keypoint is composed of two components, a spatial location (coming from the extrema detection step) and a 128-length descriptor vector (histogram representing the distribution of the gradients coming from the SIFT algorithm) (Sup. Fig. S2).

Keypoint Matching. In order to estimate a geometric transformation between frames, corresponding keypoints must be reliably matched despite varying intensity and scale. The keypoint descriptor used by SIFT is robust to such changes because it relies on the distribution of the gradients (histogram) in the local neighborhood of the keypoint; moreover we normalize orientation using the direction of the maximum gradient[40] in the keypoint's neighborhood to provide invariance against rotational motion.

We used the two step keypoint matching procedure described in ref. 32 to estimate displacement between consecutive frames. Two requirements are considered during the matching procedure: (i) descriptors of the keypoints should be similar, and (ii) relative displacement of the matched keypoints should be similar. The second condition follows from the fact that all keypoints should move in a tandem fashion, consistent with translation, rotation, and change of (projection) angle of the microscope, but not a general non-rigid morphing. Specifically, the global displacement of the keypoints should be well approximated using a single registration transformation.

Since the keypoint estimator itself is noisy with many outliers, we systematically eliminate unreliable matches that do not comply with this restricted type of motion. All keypoints in a subsequent frame are provisionally matched with the two "most similar" keypoints in the previous frame as determined by the ℓ_2 (Euclidean) distances between their SIFT descriptors, which we use as our keypoint similarity metric. A keypoint is then considered non-uniquely matched, and therefore the match is designated as unreliable, if the two most similar keypoints in the previous frame are nearly equally similar to the given keypoint, as measured by their similarity metric ratio being below a threshold (heuristically set in our experiments to 1.2). For example, a keypoint located in a region with similar or repeating textures is typically not unique. We prune our set of keypoint matches by discarding matches deemed unreliable by this procedure.

Next, the pruned matches are used to model the transformation that best registers consecutive frames. In principle, only 3 keypoint matches are needed to determine the three registration parameters, and those parameters should be consistent across the choice of any three keypoints. However, in practice there will still be outlier correspondences, even after the previous refinement step, since even after refinement we typically have more than 1000 pairs of keypoint matches between frames. Thus, we find a consistent single transformation using the well-known "RANdom SAmple Consensus (RANSAC)" algorithm[42]. RANSAC iteratively estimates models from randomly chosen subsets of the set of observations and then chooses the model that generalizes best to the whole set. In each iteration, an affine transformation between consecutive frames is estimated using a randomly chosen subset of three matches and an error measure is calculated by generalizing this transformation to the rest of the matches. We then chose the affine transformation that minimizes the generalization error over the random subsets. In our experiments we observed that 3000 trials gave a good balance between computational complexity and generalizability. The list of matches is then pruned again by discarding keypoints whose displacement cannot be estimated with at least 50 pixel (ℓ_1 distance based threshold that is determined experimentally) accuracy by the chosen transformation matrix.

We then run a final optimization over all matches that remain in this refined set and find the best transformation that describes their motion. The cost that we minimize is the sum of the ℓ_2 distances between the estimated location of the keypoint matches in the latter frame and their real locations. Since we are matching consecutive frames that were collected through smooth motion of the microscope, the scale and warping introduced through the final registration transformation should be relatively small. However, when the set of matches remaining after RANSAC pruning happen to be spatially concentrated in a relatively small spatial portion of the frames, the transformation matrix is susceptible to over-fitting to that region, leading to distortions in the rest of the frame. In order to avoid such distortions, we added an additional penalty term to the cost that penalizes scale change and shear in the final registration, and thus avoids distortions due to over-fitting. The effect of this new penalty parameter is minimal as long as the matches are relatively homogeneously spread across the frames.

Scene Cut Identification. To avoid distortion of the mosaic due to artifacts such as warping/distortion in frames or abrupt motion between them (Fig. 5), we cut the image sequence when an artifact is detected and start a new sequence from the subsequent frame. We automatically determine where to locate the cuts based on the calculated registration transformations. In particular, the diagonal coefficients of the transformation matrix control the amount of warping and distortion. Since a pure translation would result in those coefficients all being equal to

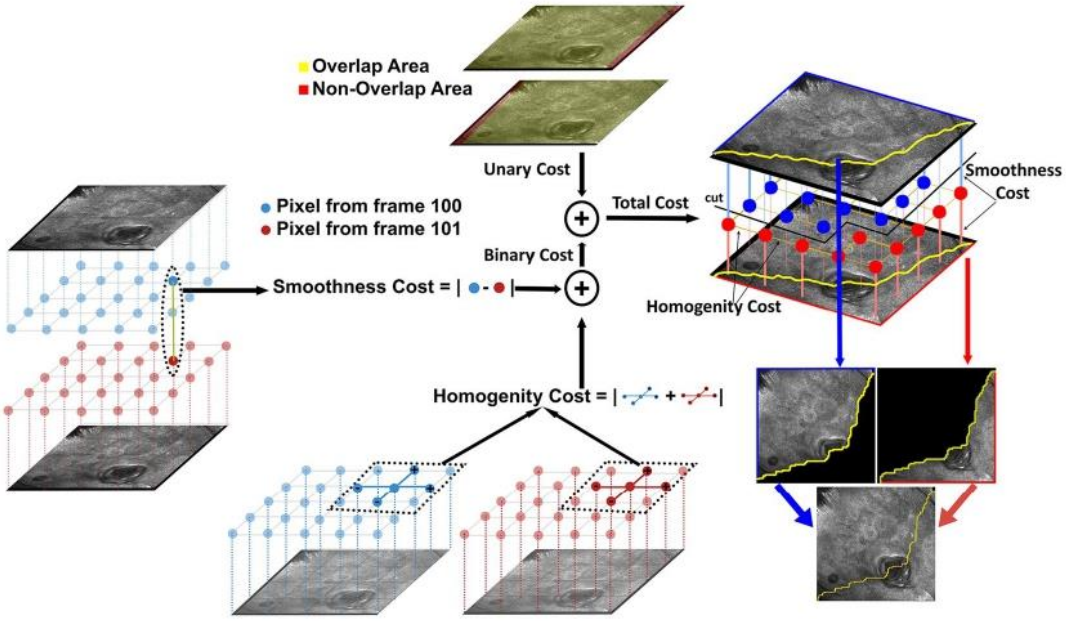

Figure 6. Example illustration of graph-cuts based stitching. In the overlapping areas of the registered images, the algorithm finds a stitching boundary by minimizing a local pixel variation based cost metric, which is composed of two parts a unary and binary cost. The unary costs (upper middle) depends on the intensity difference between overlapping images. The binary costs (lower middle and left) is calculated using intensity variations between neighboring pixel values within the images. The graph-cut algorithm finds a continuous stitching path (upper right) that goes through pixels in overlap area, whose accumulated cost is minimum among all possible such paths. The two images are then stitched together using this boundary (lower right).

1, we place cuts when the trace of the matrix,ideally equal to 3, is above an experimentally determined threshold (in the work presented here the threshold used was 3.5). Once the cut locations are determined, each resulting subsequence is mosaicked separately. These subsequences can then be assembled manually or semi-automatically, and a mosaic covering the whole imaging area can be obtained. An example of this is shown in Fig. 1 (scene cut locations are shown by white arrows).

Graph-Cut Based Stitching. After registration, given the large overlap between consecutive frames, we need to "merge" frames to construct the mosaic. As noted above, typical blending methods such as averaging or multi-resolution pyramid blending will lead to blurring, while the common alternative of choosing the maximum (or minimum) pixel value across the overlapped frames is not appropriate here since there is no reason to prefer dark versus bright intensities. In addition, the highly textured nature of RCM images will cause a loss of coherent structure and important cellular detail if extremal methods are used. Thus, we needed a method that keeps the actual pixel values while maintaining image fidelity. Simply choosing acquisition frame boundaries will lead to artifacts as well, due to imaging aberrations at frame edges as well as illumination changes between frames. Thus we devised an approach that meets this criteria by objectively choosing a single continuous boundary through the overlap area, driven by the pixel values themselves.

For simplicity of exposition, we concentrate here on the case where only two frames overlap; the extension to multi-frame overlap is straightforward. Since we want to retain the original pixel intensities, we have two candidate pixels to choose between, one from the previous and one from the subsequent frame. Our stitching algorithm determines a contiguous boundary through the overlap region, with the mosaic on one side coming from the previous frame and on the other from the subsequent frame (Fig. 6). From a graph cut perspective the optimal boundary traverses the overlap region along the trajectory on which variation in the pixel values is minimum. To accomplish this, we assign a cost of having the stitching border go through each pixel, defined as the sum of (i) the absolute intensity difference between the candidate pixels from the two frames, and (ii) the absolute intensity differences between neighboring pixel locations in the same frame. We model the problem of estimating the optimal stitching border as a graph-cuts based labeling problem[33], an approach which has been applied to many computer vision applications including photomontage[41], texture synthesis[43] and segmentation[44], resulting in a data-driven optimized boundary. (For in-depth technical description of our implementation, please refer to supplementary materials).

References

1. Bedard, N., Quang, T., Schmeler, K., Richards-Kortum, R. & Tkaczyk, T. S. Real-time video mosaicing with a high-resolution microendoscope. *Biomedical Optics Express* **3**, 2428–2435 (2012).
2. Loewke, K. *et al. In vivo* micro-image mosaicing. *Biomedical Engineering, IEEE Transactions on* **58**, 159–171 (2011).
3. Vercauteren, T., Perchant, A., Malandain, G., Pennec, X. & Ayache, N. Robust mosaicing with correction of motion distortions and tissue deformations for *in vivo* fibered microscopy. *Medical Image Analysis* **10**, 673–692 (2015).

4. Piccinini, F., Bevilacqua, A. & Lucarelli, E. Automated image mosaics by non-automated light microscopes: the micromos software tool. *Journal of Microscopy* **252**, 226–250 (2013).
5. Sun, C., Beare, R., Hilsenstein, V. & Jackway, P. Mosaicing of microscope images with global geometric and radiometric corrections. *Journal of Microscopy* **224**, 158–165 (2006).
6. Hsu, W.-Y., Poon, W.-F. P. & Sun, Y.-N. Automatic seamless mosaicing of microscopic images: enhancing appearance with colour degradation compensation and wavelet-based blending. *Journal of Microscopy* **231**, 408–418 (2008).
7. Schroeder, J., Bakalar, M., Pohida, T. & Balaban, R. Rapid overlapping-volume acquisition and reconstruction (rovar): automated 3D tiling for high-resolution, large field-of-view optical microscopy. *Journal of Microscopy* **243**, 103–110 (2011).
8. Legesse, F. *et al.* Seamless stitching of tile scan microscope images. *Journal of Microscopy* **258**, 223–232 (2015).
9. Chow, S. K. *et al.* Automated microscopy system for mosaic acquisition and processing. *Journal of Microscopy* **222**, 76–84 (2006).
10. Saldua, M. A., Olsovsky, C. A., Callaway, E. S., Chapkin, R. S. & Maitland, K. C. Imaging inflammation in mouse colon using a rapid stage-scanning confocal fluorescence microscope. *Journal of Biomedical Optics* **17**, 016006–1–016006–7 (2012).
11. Yang, T. *et al.* Rapid imaging of large tissues using high-resolution stage-scanning microscopy. *Biomed. Opt. Express* **6**, 1867–1875 (2015).
12. Gao, L. Extend the field of view of selective plan illumination microscopy by tiling the excitation light sheet. *Opt. Express* **23**, 6102–6111 (2015).
13. Tao, Y. K. *et al.* Assessment of breast pathologies using nonlinear microscopy. *Proceedings of the National Academy of Sciences* **111**, 15304–15309 (2014).
14. Giacomelli, M. G., Sheikine, Y., Vardeh, H., Connolly, J. L. & Fujimoto, J. G. Rapid imaging of surgical breast excisions using direct temporal sampling two photon fluorescent lifetime imaging. *Biomed. Opt. Express* **6**, 4317–4325 (2015).
15. Gareau, D. S. *et al.* Confocal mosaicing microscopy in mohs skin excisions: feasibility of rapid surgical pathology. *Journal of Biomedical Optics* **13**, 054001–054001–12 (2008).
16. Abeytunge, S., Li, Y., Larson, B., Toledo-Crow, R. & Rajadhyaksha, M. Rapid confocal imaging of large areas of excised tissue with strip mosaicing. *Journal of Biomedical Optics* **16**, 050504 (2011).
17. Szeliski, R. Video mosaics for virtual environments. *IEEE Comput. Graph. Appl.* **16**, 22–30 (1996).
18. Salvador Gonzalez, A. C. n. & Gill, M. *Reflectance Confocal Microscopy of Cutaneous Tumors: An Atlas with Clinical, Dermoscopic and Histological Correlations* (CRC Press, 2008), 1st edition edn.
19. Rajadhyaksha, M., Marghoob, A., Rossi, A., Halpern, A. C. & Nehal, K. S. Reflectance confocal microscopy of skin *in vivo*: From bench to bedside. *Lasers in Surgery and Medicine* n/a–n/a (2016).
20. Stevenson, A. D., Mickan, S., Mallett, S. & Ayya, M. Systematic review of diagnostic accuracy of reflectance confocal microscopy for melanoma diagnosis in patients with clinically equivocal skin lesions. *Dermatology Practical & Conceptual* **3**, 19–27 (2013).
21. Xiong, Y. *et al.* A meta-analysis of reflectance confocal microscopy for the diagnosis of malignant skin tumours. *Journal of the European Academy of Dermatology and Venereology* **30**, 1295–1302 (2016).
22. Kadouch, J. D. *et al.* Treatment of basal cell carcinoma using a one-stop-shop with reflectance confocal microscopy: Study design and protocol of a randomized controlled multicenter trial. *JMIR Res Protocols* **4**, e109 (2015).
23. *Current Procedural* Terminology (CPT*) Professional* (American Medical Association, 2016).
24. Pellacani, G., Pepe, P., Casari, A. & Longo, C. Reflectance confocal microscopy as a second-level examination in skin oncology improves diagnostic accuracy and saves unnecessary excisions: a longitudinal prospective study. *British Journal of Dermatology* **171**, 1044–1051 (2014).
25. Alarcon, I. *et al.* Impact of *in vivo* reflectance confocal microscopy on the number needed to treat melanoma in doubtful lesions. *British Journal of Dermatology* **170**, 802–808 (2014).
26. Ferrari, B. *et al.* Dermoscopic difficult lesions: an objective evaluation of reflectance confocal microscopy impact for accurate diagnosis. *Journal of the European Academy of Dermatology and Venereology* **29**, 1135–1140 (2015).
27. Stanganelli, I. *et al.* Integration of reflectance confocal microscopy in sequential dermoscopy follow-up improves melanoma detection accuracy. *British Journal of Dermatology* **172**, 365–371 (2015).
28. Lovatto, L. *et al. In vivo* reflectance confocal microscopy of equivocal melanocytic lesions detected by digital dermoscopy follow-up. *Journal of the European Academy of Dermatology and Venereology* **29**, 1918–1925 (2015).
29. Kose, K. *et al.* Video-mosaicing of reflectance confocal images for examination of extended areas of skin *in vivo*. *British Journal of Dermatology* **171**, 1239–1241 (2014).
30. Flores, E. S. *et al.* Intraoperative imaging during mohs surgery with reflectance confocal microscopy: initial clinical experience. *Journal of Biomedical Optics* **20**, 061103 (2015).
31. Fraga-Braghiroli, N. *et al.* Use of handheld reflectance confocal microscopy for *in vivo* diagnosis of solitary facial papules: a case series. *Journal of the European Academy of Dermatology and Venereology* **28**, 933–942 (2014).
32. Hartley, R. I. & Zisserman, A. *Multiple View Geometry in Computer Vision* (Cambridge University Press, ISBN: 0521540518, 2004), second edn.
33. Boykov, Y., Veksler, O. & Zabih, R. Fast approximate energy minimization via graph cuts. *Pattern Analysis and Machine Intelligence, IEEE Transactions on* **23**, 1222–1239 (2001).
34. Dengel, L., Turza, K., Noland, M.-M. B., Patterson, J. W. & Slingluff, C. L. Skin mapping with punch biopsies for defining margins in melanoma: When you don't know how far to go. *Annals of Surgical Oncology* **15**, 3028–3035 (2008).
35. Yélamos, O. et al. Correlation of Handheld Reflectance Confocal Microscopy With Radial Video-Mosaicing for Margin Mapping of Lentigo Maligna and Lentigo Maligna Melanoma: A Prospective Study. JAMA Dermatology, accepted for publication, 28 Jun 2017.
36. Yélamos, O. *et al.* Handheld reflectance confocal microscopy for the detection of recurrent extramammary paget disease. *JAMA Dermatology* **153**(7), 689–693 (2017).
37. Castro, R. *et al.* Accuracy of *in vivo* confocal microscopy for diagnosis of basal cell carcinoma: a comparative study between handheld and wide-probe confocal imaging. *Journal of the European Academy of Dermatology and Venereology* **29**, 1164–1169 (2015).
38. Bradski, G. Dr. Dobb's Journal of Software Tools (2000).
39. mexopencv. https://github.com/kyamagu/mexopencv. Last Accessed: 2016-11-27.
40. Lowe, D. Object recognition from local scale-invariant features. In *Computer Vision, 1999. The Proceedings of the Seventh IEEE International Conference on*, vol. 2, 1150–1157 (1999).
41. Agarwala, A. *et al.* Interactive digital photomontage. *ACM Trans. Graph.* **23**, 294–302 (2004).
42. Fischler, M. A. & Bolles, R. C. Random sample consensus: A paradigm for model fitting with applications to image analysis and automated cartography. *Commun. ACM* **24**, 381–395 (1981).
43. Kwatra, V., Schödl, A., Essa, I., Turk, G. & Bobick, A. Graphcut textures: Image and video synthesis using graph cuts. *ACM Trans. Graph.* **22**, 277–286 (2003).
44. Felzenszwalb, P. F. & Huttenlocher, D. P. Efficient graph-based image segmentation. *Int. J. Comput. Vision* **59**, 167–181 (2004).

Acknowledgements

This work was supported by several agencies: in part by National Cancer Institute under Grant R01CA156773 and Grant R01CA199673, in part by the NIBIB's Image Guided Interventions Program under Grant R01EB012466,

in part by the National Science Foundation under Grant IIS-1318145, in part by NCI Core Center grant P30CA008748, in part by NIBIB Grant R01EB020029, in part by Skin Cancer Foundation and in part by Beca Excelencia Fundación Piel Sana.

Author Contributions

K.K. has contributed to all of the presented research, conducted testing and the preparation of the manuscript. He is the corresponding author of the paper. M.G. contributed to algorithmic development, implementation and testing. O.Y., M.C., A.R., E.F., K.N. designed the clinical tests, and conducted imaging on patients. O.Y. and E.F. tested the video-mosaicking algorithm, analyzed the results, O.Y. prepared the clinical part of the results section. O.C., J.D., D.B., M.R. contributed to the development of technical parts of the algorithm. All authors reviewed the manuscript.

Additional Information

Supplementary information accompanies this paper at doi:10.1038/s41598-017-11072-9

Competing Interests: Dr. Rajadhyaksha holds equity in Caliber ID, the manufacturer of the handheld confocal microscope used in this study. None of the other authors have a competing financial interests.

Publisher's note: Springer Nature remains neutral with regard to jurisdictional claims in published maps and institutional affiliations.

Supplementary material

Automated video-mosaicking approach for confocal microscopic imaging in vivo: an approach to address challenges in imaging living tissue and extend field-of-view

Kivanc Kose[1,+,*], Mengran Gou[2,+], Oriol Yélamos[1,3], Miguel Cordova[1], Anthony Rossi[1], Kishwer Nehal[1], Eileen Flores[1], Octavia Camps[2], Jennifer Dy[2], Dana H. Brooks[2], and Milind Rajadhyaksha[1]

[1]Memorial Sloan Kettering Cancer Center, Dermatology Service, New York, NY, USA
[2]Electrical and Computer Engineering, Northeastern University, Boston, MA, USA
[3]Dermatology Department, Hospital Clínic, Universitat de Barcelona, Barcelona, Spain
[*]kosek@mskcc.org
[+]these authors contributed equally to this work

Supplementary Material

In this section, we give further technical details of the methods that we developed or tailored for our developing our videomosaicking framework. For the sake of completeness, we briefly mention the standard methods that we used in the framework and refer readers to the cited literature for details. The focus of this supplementary material is on the modifications and additions that we made at individual steps of the framework. We will also provide the values of the parameters that were used during the implementation.

Extraction of SIFT Keypoints

In order to extract and describe keypoints, we used an off-the-shelf version of the SIFT algorithm[1] that was implemented in opencv[2] and ported into Matlab as mex libraries[3]. The SIFT algorithm has been extensively tested on natural images, from which values of its default parameters have been set. We made a few modifications in its default values to increase the efficiency of the algorithm for our specific reflectance confocal microscopy (RCM) data. SIFT is basically composed of 2 steps; detection of keypoints and calculation of the keypoint descriptors. In the SIFT algorithm, keypoints are defined by their high contrast relative to their neighbors. Useful keypoints may occur at different spatial scales (fine to coarse) of the image. SIFT explores this space using a Difference-of-Gaussian (DoG) representation in a two-step algorithm. First the image is downsampled repeatedly at different octave-based scales (e.g. downsampled by 2 in each direction). Then at each octave the image is filtered by Gaussian filters with different variances, and these images are then subtracted from each other. This procedure allows a search for keypoints at multiple octaves and at multiple scales within the octave, as illustrated in Figure S1. In order to obtain enough keypoints that lead to reliable matches between RCM frames, we experimented with different numbers of octave and scale parameters in the DoG representation (Figure S1). We observed that using a DoG representation with five octaves (corresponds to five times downsampling) and five scales (different variances of the Gaussian filter) at each octave gave a good balance between computational complexity and the number of extracted keypoints (which was typically ~ 3000 as noted in Methods). The initial variance of the Gaussian filters was $\sigma = 1.6$ pixels, and it increases as $k\sqrt{(2)}\sigma$ for $k \in [1,\ldots,5]$

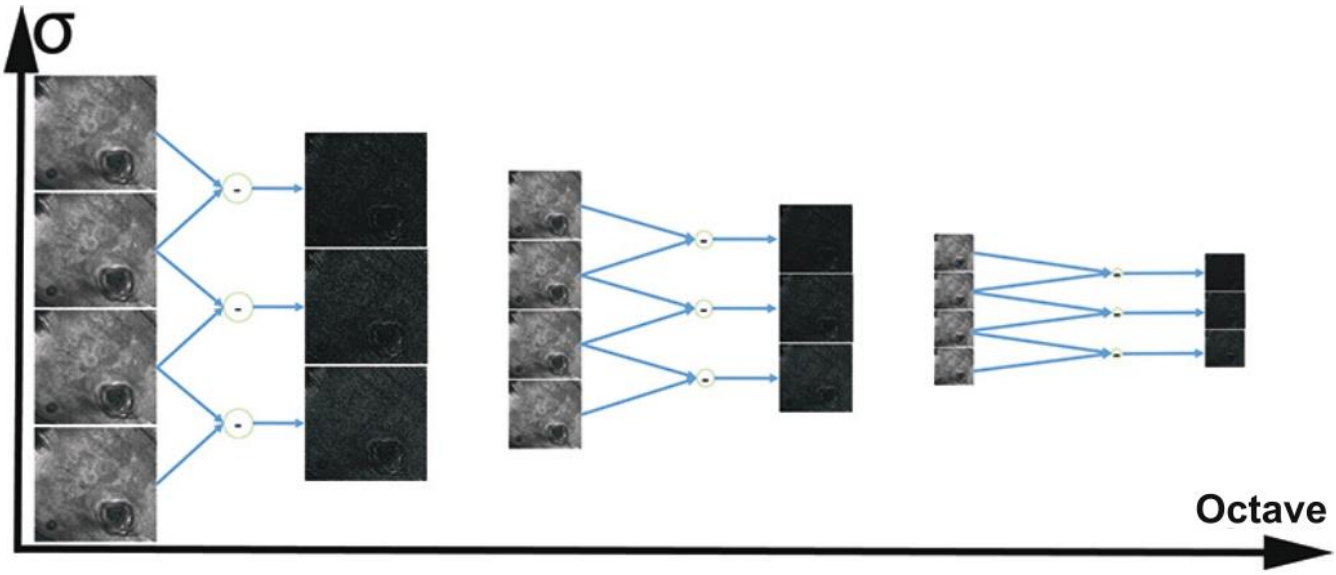

Figure S1. An example DoG representation: At each octave, the frame is convolved with Gaussian filters with increasing variances (called scales) and the convolved images are subtracted from each other to create the DoG representation at that particular octave. For illustrative purposes we show three DOG levels at three octaves, different from what we actually used in practice.

The second stage of SIFT is to calculate descriptors for each keypoint. We used standard SIFT descriptor[1]. These SIFT descriptors are feature vectors which concatenate histograms of the gradients at different angles in a spatial region around the keypoint. See Fig. S2 for a detailed illustration of this process.

Registration

Registration parameters between two consecutive frames can be calculated by analyzing the displacement of the keypoints in these images (optical flow). First, we matched the keypoints between two consecutive frames. The initial tentative matching is done by calculating a similarity metric between keypoint descriptors using an ℓ_2 (euclidean) distance. Each keypoint in each

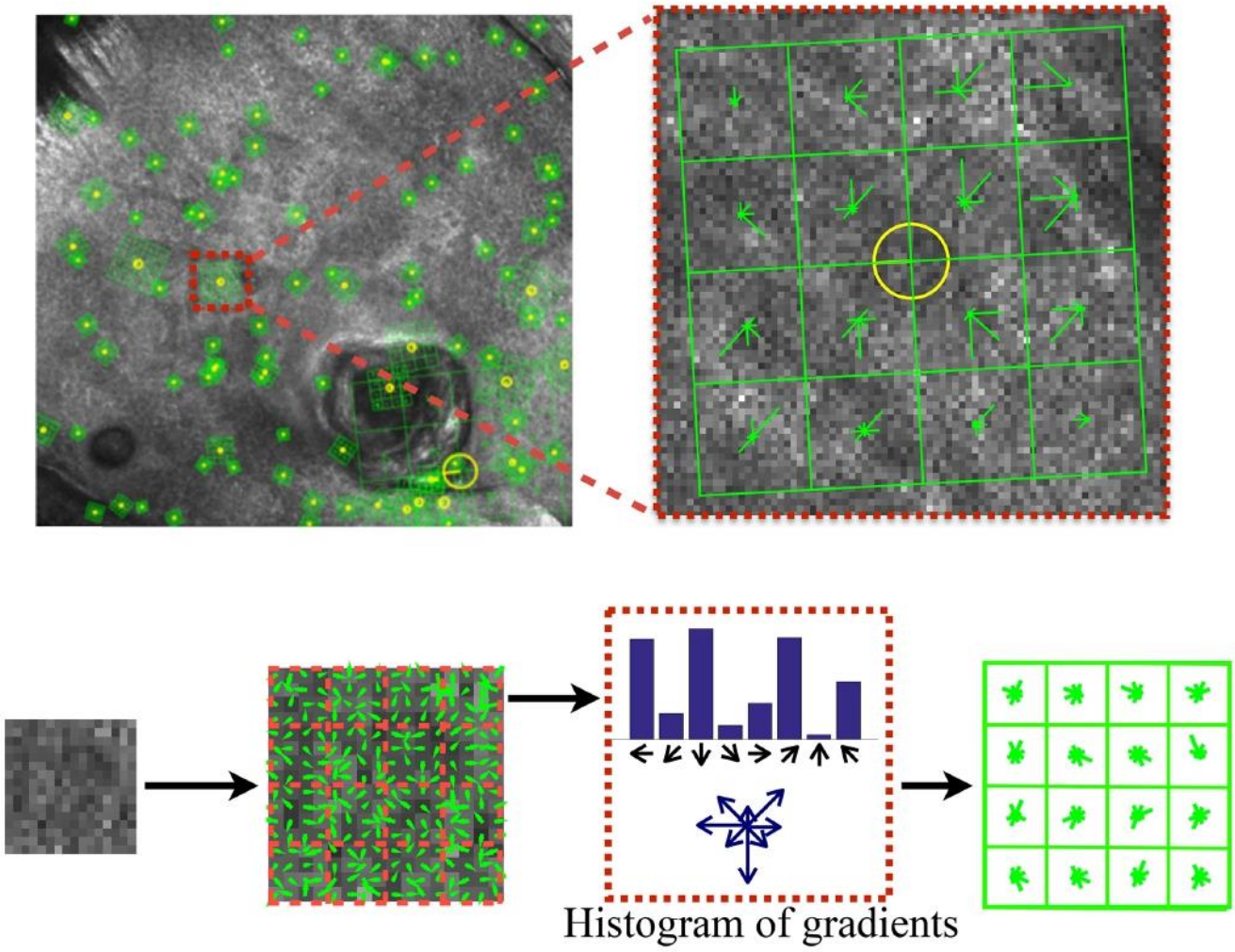

Figure S2. Histograms of gradients around each keypoint are used as descriptors. For each of the 16 subregions (each subregion is 4×4 pixels) around the keypoint, an 8 bin histogram of gradients is formed. These 16 histograms are concatenated to form a length-128 SIFT descriptor. For visual purposes, we only show a few of the keypoints

frame was matched with the 2 most similar keypoints in the following frame. Keypoints for which the ratio of its distance to its second closest match to its distance to the closest match was larger than 1.5 were counted as strong matches. The rest of the pairs (and the respective keypoints) were eliminated from the list of potential matches for subsequent processing.

Unfortunately, matching the keypoint based only on similarity between their descriptors is unreliable, as microscopic images often contain repeated textural patterns with similar appearance. For any microscope motion, all keypoints should move in a tandem fashion. Therefore, the relative displacement between the matched keypoints pairs must be similar, and thus should be well approximated by a single transformation matrix:

$$K_{t+1} = H_t K_t \tag{1}$$

where H_t is a 3-by-3 transformation matrix and K_t, K_{t+1} are triplets of homogeneous coordinates of matched keypoints between consecutive frames t and $t+1$. In general, for more than 3 matches, solutions to (1) will be inconsistent as we have many more constraints than free parameters. To robustly find a representative transformation, we used a procedure called RANSAC[4] to find an H_t that describes the motion between all matched keypoints with small error. In a single iteration, RANSAC solves (1) for one randomly-chosen triplet of matches, resulting in an estimate $\hat{H}_t^j$, where j is the iteration number. The resulting $\hat{H}_t^j$ is then used to calculate expected locations of all remaining keypoints from the earlier frame in the next frame. An estimation error E^j associated with transformation matrix $\hat{H}_t^j$ is then calculated by summing the ℓ_2 distance between the estimated keypoint locations $(H_t^j K_t)$ and their actual location (K_{t+1}) in the following frame.

By solving (1) multiple times on randomly selected triplets, RANSAC calculates a vector of error values E^j, whose ℓ_2 is taken as measure of the robustness of H_t^j. The $\hat{H}_t^j$ matrix that results in the smallest error over all iterations is chosen as the transformation matrix $\hat{H}_t$. Testing many subsets is computationally costly, while testing on a smaller number of subsets leads to poor generalizability and thus poor registration. We observed experimentally that for the RCM images 3000 trials gave a good balance between computational complexity and generalizability.

Even with this choice of H_t, there are typically keypoint matches that are significantly inconsistent with the resulting transformation. Thus we made a second pass through the keypoint matches to discard those matches whose projected location in the second frame was not consistent with their actual location. Our experiments on RCM images suggested that discarding matches for which this location error was larger than 50 pixels gave a good trade-off between consistency and having too few matches. We will refer in the sequel to the remaining set of matches as inlier matches.

After RANSAC, the final step in registration is the refinement of $\hat{H}_t$ to best fit all inlier matches. In addition, in our application, we are only interested in registering consecutive frames that were collected during smooth motion of the microscope. In such cases the change in scale and warping (distortion) between the registered frames should be relatively small. Moreover, when the inlier matches are mostly concentrated on a portion of the frames, we want to prevent having a transformation matrix that is overfit to that portion of the image, which can lead to distortion in the rest of the frame. These goals can be characterized by an optimization problem which aims to find the registration transformation H_t that minimizes the total mismatch over all inlier matches while leading to the small frame-to-frame warping and scale change.

The total mismatch between the inlier matches can be calculated using the ℓ_2 error metric described before. The distortion induced by the registration can be quantified by analyzing the coefficients of the affine transformation matrix H. More specifically, the upper left 2-by-2 portion of the matrix controls the rotation and shearing in the registration and the entries in the first two rows of the last column (H(1,3) and H(2,3)) control the translation. Finally, the last row (H(3,1),H(3,2),H(3,3)) controls the projective geometry, which represents how the matches deviate from a 2D geometry. In order to avoid transformation matrices that lead to too much distortion, we introduced an additional cost parameter that penalizes the scale change and shear in the final transformation matrix. This parameter serves as a regularization term to force the final affine transformation matrix to favor translation and rotation motion between frames and limit shearing that may warp and distort the frame. Given the inlier matches $\bar{K}_t$ and $\bar{K}_{t+1}$ that we found through RANSAC, we solve the following optimization problem

$$min_H ||\bar{K}_{t+1} - H_t \bar{K}_t|| * (1 + pen), \tag{2}$$

$$pen = |1 - H_t(1,1)| + |1 - H_t(2,2)| + |H_t(1,2) + H_t(2,1)| + |H_t(3,1) + H_t(3,2)| * 10^2. \tag{3}$$

The first two terms in the penalty limit scale changes, the third term limits shearing and warping, and the last term limits the projective warping (deviation from 2D). Here we optimize Eq. 3 over all inlier matches. As an aside, we noted that, as expected, the effect of the additional penalty parameter was minimal when the inlier matches were homogeneously spread across the frames.

Scene Cut Identification

As described in Methods, our framework was designed to automatically detect sudden and unwanted motion of the microscope and then cut the longer sequence into internally consistent subsequences as needed. We developed a method that uses the coefficients of the transformation matrix H_t to determine where to cut. Since, as described in detail above in the Frame Registration section of the manuscript, the diagonal coefficients of H_t encode how much warping and distortion is introduced in the final registration, we quantify warping and distortion as

$$DeformationFactor = (1 - \frac{H(1,1)}{H(3,3)}) + (1 - \frac{H(2,2)}{H(3,3)}), \tag{4}$$

which is similar to the regularization term in Eq. (3). This factor quantitatively determines the degree to which the final transformation matrix imposes translation, rotation, and shearing. We place cuts between frames when this deformation factor is larger than 1. In addition, we calculate the ratio between the area covered by the earlier frame before and after the registration transformation. If this ratio is larger (smaller) than an experimentally determined threshold of 2.5 (1/2.5), then we also place a scene cut between those two frames.

Graph-cut based Stitching

As noted in the Methods section, in order to preserve resolution and cellular detail, we designed a method that retains the actual measured pixel values while ensuring image fidelity. Specifically, we adopted a graph-cuts based stitching algorithm that determines where to place a flexible, data-driven boundary that in effect composes the stitched image from two parts, each coming from pairs of neighboring original frames.

In the exposition here, we refer to the current state of the mosaic, composed from the previous and current images in the video sequence, as M and an "incoming" frame that we wish to stitch as F. After registration we obtain a transformed version of F, which we denote F', which overlaps with some pixels of M. Thus in each location of the overlap area, we have two candidates pixels to choose from, one from M and the other from F'. The stitching step seeks a *single continuous stitching boundary* going through the overlap area, one side of which comes from M and the other side from F', as shown in Fig. 6 in the manuscript. We model the problem of finding the optimal stitching border as a graph-cuts based labeling problem, where the label $L(p)$ of each pixel p in the new video-mosaic is either M or F'. This pixel labeling problem can be approached as a graph partitioning by representing the pixels of the two images as the nodes of the graph. In this graph topology, labeling two neighboring pixels with different labels means the stitching boundary cuts the edge between these two pixels. The total cost of choosing a certain stitching boundary is associated with sum of the cost of the individual edges that the boundary cuts through (Fig. 6).

In our implementation the total cost of cutting an edge is composed of 2 terms as

$$C(L) = C_u(p, L(p)) + C_b(p, L(p)), \tag{5}$$

where the terms are the "unary cost" (C_u) and the "binary" cost (C_b)). Since we want to insure that the stitching boundary goes through the overlap area, we defined the unary cost as

$$C_u(p, L(p) = \begin{cases} 0 & p \in \{M \cap F'\} \\ \Omega & else \end{cases} \tag{6}$$

where $\{M \cap F'\}$ is the set of pixels in the overlap area of M and F' and Ω is a very large cost value, which always dominates the binary cost.

In the overlap region, the unary cost is set to be zero as noted above for all pixels because each pixel has the same equal probability of being in the final mosaic. Therefore, only the binary cost determines where the stitching border goes within the overlap area. The binary cost term for the cutting the connection between two pixels is calculated in two terms as:

$$C_b(p, L(p)) = C_s + C_h \tag{7}$$

where C_s, is the "similarity" cost, and C_h is the homogeneity cost. The similarity cost

$$C_s(p) = G_h(|M - F'|) \times K_h(p) + G_v(|M - F'|) \times K_v(p) \tag{8}$$

with

$$K_h(p) = \begin{cases} 0 & \text{if } L(p) = L(q),\ q \text{ is 2 horizontal neighborhoods of } p \\ 1 & \text{else.} \end{cases} \tag{9}$$

and

$$K_v(p) = \begin{cases} 0 & \text{if } L(p) = L(q),\ q \text{ is 2 vertical neighborhoods of } p \\ 1 & \text{else.} \end{cases} \tag{10}$$

is the absolute difference between the two candidate pixel intensity values from M and F'. It forces the stitching boundary to go through pixels with are similar in both M and F'. The homogeneity cost

$$C_h(p) = |\nabla_x M + \nabla_x F'| \times K_h(p) + |\nabla_y M + \nabla_y F'| \times K_v(p) \tag{11}$$

is the absolute intensity differences between candidate pixels and their spatial neighbors ("homogeneity" cost, C_h) (Fig. 6-Left column). It forces the stitching boundary to go through areas with small intensity variation.

Once the cost (function of labels) is calculated for each pixel, we minimize the overall cost with respect to the labels using Boykov's graph-cut method[5]. In the highly unlikely case that this solution is not unique, the algorithm randomly picks one of the candidate stitching borders. In this way, the pixels of the final mosaic are uniquely chosen from pixels of either of the frames as shown in Fig. 6.

References

1. Lowe, D. Object recognition from local scale-invariant features. In *Computer Vision, 1999. The Proceedings of the Seventh IEEE International Conference on*, vol. 2, 1150–1157 (1999).

2. Bradski, G. *Dr. Dobb's Journal of Software Tools* (2000).

3. mexopencv. https://github.com/kyamagu/mexopencv. Accessed: 2016-11-27.

4. Fischler, M. A. & Bolles, R. C. Random sample consensus: A paradigm for model fitting with applications to image analysis and automated cartography. *Commun. ACM* **24**, 381–395 (1981). URL http://doi.acm.org/10.1145/358669.358692.

5. Boykov, Y., Veksler, O. & Zabih, R. Fast approximate energy minimization via graph cuts. *Pattern Analysis and Machine Intelligence, IEEE Transactions on* **23**, 1222–1239 (2001).

Publication 2: Correlation of Handheld Reflectance Confocal Microscopy With Radial Video Mosaicing for Margin Mapping of Lentigo Maligna and Lentigo Maligna Melanoma

Oriol Yélamos, Miguel Cordova, Nina Blank, Kivanc Kose, Stephen W. Dusza, Erica Lee, Milind Rajadhyaksha, Kishwer S. Nehal, Anthony M. Rossi

JAMA Dermatology 2017 Dec 1;153(12):1278-1284. doi: 10.1001/jamadermatol.2017.3114.

SUMMARY

Background: The management of lentigo maligna (LM) and LM melanoma (LMM) is challenging because of extensive subclinical spread and its occurrence on cosmetically sensitive areas. Reflectance confocal microscopy (RCM) improves diagnostic accuracy for LM and LMM and can be used to delineate their margins.

Aim: To evaluate whether handheld RCM with radial video mosaicing (HRCM-RV) offers accurate presurgical assessment of LM and LMM margins.

Material and methods: This prospective study included consecutive patients with biopsy-proven LM and LMM located on the head and neck area who sought consultation for surgical management from March 1, 2016, through March 31, 2017, at the Dermatology Service of the Memorial Sloan Kettering Cancer Center. Thirty-two patients underwent imaging using HRCM-RV, and 22 patients with 23 LM or LMM lesions underwent staged surgery and contributed to the analysis. Clinical lesion size and area, LM and LMM area based on HRCM-RV findings, surgical defect area estimated by HRCM-RV, and observed surgical defect area. In addition, the margins measured in millimeters estimated for tumor clearance in each quadrant based on HRCM-RV findings were calculated and compared with the surgical margins.

Results: Among the 22 patients (12 men and 10 women; mean [SD] age, 69.0 [8.6] years [range, 46-83 years]) with 23 lesions included in the final analysis, the mean (SD) surgical defect area estimated with HRCM-RV was 6.34 (4.02) cm2 and the mean (SD) area of surgical excision with clear margins was 7.74 (5.28) cm2. Overall, controlling for patient age and previous surgery, surgical margins were a mean of 0.76mm (95%CI, 0.67-0.84 mm; $P < .001$) larger than the HRCM-RV estimate.

Conclusions: Mapping of LM and LMM with HRCM-RV estimated defects that were similar to but slightly smaller than those found in staged excision. Thus, mapping of LM using HRCM-RV can help spare healthy tissue by reducing the number of biopsies needed in clinically uncertain areas and may be used to plan treatment of LM and LMM and counsel patients appropriately.

JAMA Dermatology | Original Investigation

Correlation of Handheld Reflectance Confocal Microscopy With Radial Video Mosaicing for Margin Mapping of Lentigo Maligna and Lentigo Maligna Melanoma

Oriol Yélamos, MD; Miguel Cordova, MD; Nina Blank, BA; Kivanc Kose, PhD; Stephen W. Dusza, DrPH; Erica Lee, MD; Milind Rajadhyaksha, PhD; Kishwer S. Nehal, MD; Anthony M. Rossi, MD

IMPORTANCE The management of lentigo maligna (LM) and LM melanoma (LMM) is challenging because of extensive subclinical spread and its occurrence on cosmetically sensitive areas. Reflectance confocal microscopy (RCM) improves diagnostic accuracy for LM and LMM and can be used to delineate their margins.

OBJECTIVES To evaluate whether handheld RCM with radial video mosaicing (HRCM-RV) offers accurate presurgical assessment of LM and LMM margins.

DESIGN, SETTING, AND PARTICIPANTS This prospective study included consecutive patients with biopsy-proven LM and LMM located on the head and neck area who sought consultation for surgical management from March 1, 2016, through March 31, 2017, at the Dermatology Service of the Memorial Sloan Kettering Cancer Center. Thirty-two patients underwent imaging using HRCM-RV, and 22 patients with 23 LM or LMM lesions underwent staged surgery and contributed to the analysis.

MAIN OUTCOMES AND MEASURES Clinical lesion size and area, LM and LMM area based on HRCM-RV findings, surgical defect area estimated by HRCM-RV, and observed surgical defect area. In addition, the margins measured in millimeters estimated for tumor clearance in each quadrant based on HRCM-RV findings were calculated and compared with the surgical margins.

RESULTS Among the 22 patients (12 men and 10 women; mean [SD] age, 69.0 [8.6] years [range, 46-83 years]) with 23 lesions included in the final analysis, the mean (SD) surgical defect area estimated with HRCM-RV was 6.34 (4.02) cm^2 and the mean (SD) area of surgical excision with clear margins was 7.74 (5.28) cm^2. Overall, controlling for patient age and previous surgery, surgical margins were a mean of 0.76 mm (95% CI, 0.67-0.84 mm; $P < .001$) larger than the HRCM-RV estimate.

CONCLUSIONS AND RELEVANCE Mapping of LM and LMM with HRCM-RV estimated defects that were similar to but slightly smaller than those found in staged excision. Thus, mapping of LM using HRCM-RV can help spare healthy tissue by reducing the number of biopsies needed in clinically uncertain areas and may be used to plan treatment of LM and LMM and counsel patients appropriately.

Video

Supplemental content

Author Affiliations: Dermatology Service, Department of Medicine, Memorial Sloan Kettering Cancer Center, New York, New York (Yélamos, Cordova, Blank, Kose, Dusza, Lee, Rajadhyaksha, Nehal, Rossi); Dermatology Department, Hospital Clínic, Universitat de Barcelona, Barcelona, Spain (Yélamos).

Corresponding Author: Anthony M. Rossi, MD, Dermatology Service, Department of Medicine, Memorial Sloan Kettering Cancer Center, 16 E 60th St, 4th Floor, New York, NY 10022 (rossia@mskcc.org).

JAMA Dermatol. doi:10.1001/jamadermatol.2017.3114
Published online October 11, 2017.

Delineating the borders of lentigo maligna (LM) and LM melanoma (LMM) is challenging because they occur in heavily sun-damaged areas and may be hypomelanotic or amelanotic, with subclinical spread not visible to the naked eye.[1] This situation can lead to underestimation of surgical margins, resulting in positive surgical margins and subsequent recurrences.[2,3] In addition, because LM and LMM occur on cosmetically sensitive areas, such as the face, and can have extensive subclinical spread, complete margin assessment and control with techniques such as Mohs micrographic surgery, staged excision, or the spaghetti technique are important. Surgical margins needed to clear LM and LMM on the head and neck area are also greater than those needed for traditional trunk and extremity melanomas.[4-6]

Dermoscopy and Wood lamp examination have improved the delineation of LM and LMM margins.[7] However, false-positive and false-negative findings occur,[8] and scouting biopsies are often performed.[9,10] Scouting biopsies provide static information that can be difficult to contextualize because certain features, such as melanocytic hyperplasia, occur in benign, sun-exposed skin and at the trailing edge of LM and LMM. Reflectance confocal microscopy (RCM) is a noninvasive imaging system that allows in vivo cellular evaluation of the epidermis and upper dermis.[11,12] Reflectance confocal microscopy has a sensitivity of 85% and specificity of 76% to diagnose LM and LMM[13] and has been used to delineate their margins.[14,15] Most of this work has been based on traditional widefield-probe RCM, which requires attaching a metal ring on the skin and allows imaging of areas to 8 × 8 mm. However, LM and LMM can be larger than 8 mm and can occur at uneven surfaces where the metal ring may detach. Thus, mapping the LM and LMM margins with widefield-probe RCM can be a labor-intensive and time-consuming process (approximately 1 hour per lesion).[14] Conversely, handheld RCM (HRCM) can acquire images and videos along ad hoc, arbitrarily freeform, nonrastered paths and over large areas that the user determines in real time, allowing a live approach to mapping margins over large areas. Although HRCM allows less restrictive imaging acquisition, the data regarding its use in diagnosing and mapping LM and LMM are limited[15,16] owing mainly to the lack of orientation during image acquisition and lack of mosaicing capabilities in the HRCM software. However, with the advent of HRCM video mosaicing, dynamic videos can now be transformed into static video mosaics to help obtain architectural information.[17-19]

Herein, we describe a novel imaging technique for obtaining radial HRCM videos and video mosaics from the LM or LMM center to the periphery, guided by the use of adhesive paper rings. The aim of this study was to evaluate whether radial imaging offers accurate presurgical assessment for LM and LMM margins and anticipates surgical defects.

Key Points

Question Is handheld reflectance confocal microscopy with radial video mosaicing accurate for noninvasive delineatation of subclinical lentigo maligna and lentigo maligna melanoma borders and estimation of its margins?

Findings In this study, 23 lentigo maligna and lentigo maligna melanoma lesions from 22 patients were evaluated. Overall, controlling for patient age and previous surgery, surgical margins were a mean of 0.76 mm larger than the estimate obtained with reflectance confocal microscopy.

Meaning Handheld reflectance confocal microscopy with radial video mosaicing findings correlated well with histologic findings and may be useful in planning treatment and counseling patients.

Methods

Clinical Information

From March 1, 2016, through March 31, 2017, we conducted a prospective study including consecutive patients with LM and/or LMM who consulted for surgical advice in the Dermatology Service of Memorial Sloan Kettering Cancer Center, New York, New York. We included patients who had biopsy-proven LM or LMM located in the head and neck area and who underwent imaging using HRCM radial video mosaicing (HRCM-RV) before staged excision with complete circumferential margin control. We excluded patients with LM and LMM not located in the head and neck area, patients who decided not to undergo staged excision, and patients who pursued treatment elsewhere. This study was approved by the institutional review board of Memorial Sloan Kettering Cancer Center. All patients provided written informed consent to imaging with confocal microscopy and to have surgery performed.

We collected patient demographic information, prior LM and LMM treatments, lesion location, Breslow thickness, and numeric surgical stages. We calculated the clinical lesion size and area, the LM or LMM area based on HRCM-RV findings, the surgical defect area estimated using HRCM-RV, and the observed surgical defect area. To calculate the areas, we obtained digital images of the lesions and surgical defects using a digital camera (PowerShot G10; Canon, Inc) or a dermoscopy system (Veos DS3; Canfield Scientific). Using Mirror software (version 7.5; Canfield Scientific), we retrieved the images and calculated the areas after image calibration with a ruler placed in the image field, anthropometric measurements, or annotations in the medical record, such as defect size. To ensure measurement accuracy, 2 calibration methods were used for each image.

Clinical Margin Delineation and Confocal Imaging

Clinical margins were determined using dermoscopy and Wood lamp examination. To facilitate RCM navigation and margin calculation, we surrounded this margin with adhesive paper rings (product number 1529; 3M)[20] (**Figure 1**). In irregularly shaped lesions, multiple paper rings were placed and eventually overlapped to allocate the entire lesion inside the paper rings and image its entire border. Several paper ring diameters are available; however, all paper rings have a rim width of 2.5 mm, which was used to calculate the estimated surgical margins. We imaged the lesions with an HRCM device (VivaScope 3000; Caliber Imaging and Diagnostics), which has a lateral resolution of approximately 1 µm, optical sectioning of

Figure 1. Lentigo Maligna (LM) Margin Determination Using Dermoscopy, Wood Lamp Examination, and Handheld Reflectance Confocal Microscopy (HRCM)

A, Dermoscopy evaluation reveals a pigmented lesion with ill-defined margins, asymmetric pigmented follicular openings (arrow), and a circle within a circle (arrowheads). B, Paper ring placed outside the clinical margin determined with dermoscopy and Wood lamp examination to facilitate confocal navigation. C, The HRCM evaluation was performed by initially imaging the center to determine the cellular morphologic features (asterisk), and later by imaging clockwise the peripheral margin inside (black arrows) and outside (blue arrows) the ring. Radial videos were obtained (yellow arrows) in the areas where a higher degree of atypia was identified outside the paper ring to determine the LM or LM melanoma subclinical extension.

approximately 3 µm, and a field of view of 1 × 1 mm. Two of us (O.Y. and M.C.) with 1 year and more than 5 years of experience, respectively, performed image acquisition together for the first 10 cases, and later acquired images together or alone depending on availability in the clinic.

Initially, we imaged the lesion center to identify the predominant morphologic features of the melanoma cell (large round, dendritic, or pleomorphic).[13] Next, we navigated clockwise along the ring's inner margin to confirm the dermoscopic or Wood lamp margins. Then, we imaged along the outer ring margin to identify LM or LMM subclinical spread. When a positive area was identified outside the ring, we captured a video at the plane where the highest degree of atypia was identified and navigated radially from the lesion center toward the LM-positive area outside the ring until no LM features were observed (Figure 1C). Radial videos were obtained in all the quadrants that were positive outside the paper ring.

To consider an area as positive on HRCM, the features present in the LM algorithm (**Table**),[13,15] validated to diagnose LM using widefield-probe RCM and HRCM, were used.[13,16] When further evaluating the periphery, margins were considered to be positive for LM if any of the positive criteria of the LM algorithm were present and if a single large round or large dendritic cell was identified on RCM.[15] Based on previous studies and the results obtained when imaging complex LM and LMM cases,[17] we also considered the margin to be positive if smaller atypical dendritic cells were observed continuing from the LM trailing edge (Table).

Determination of Subclinical Tumor Margins Using HRCM-RV

To calculate subclinical margins with HRCM-RV, the acquired videos were converted into video mosaics using an algorithm written in MATLAB (MathWorks).[18] In brief, frames were extracted and then stitched together to create mosaics of the imaged area. Video mosaics were used to calculate the subsurface extension by measuring the distance between the inner part of the paper ring (clinical margin) and the furthest HRCM-positive finding identified (confocal margin) (**Figure 2** and **Video**). To determine these measurements, the following 2 reference variables were used: (1) the ring rim width of 2.5 mm and (2) each HRCM field of view of 1 × 1 mm, which equals 1000 × 1000 pixels. We overlaid these measurements on the clinical pictures and calculated the HRCM-estimated area. Margin determination was performed by one of us (O.Y.) with experience in RCM and dermatopathology by reviewing the radial video mosaics obtained in each quadrant.

Staged Excision and Determination of Surgical Margins Using HRCM-RV

According to our practice protocol and standard of care,[4,21,22] 3 of us (K.S.N., E.L., and A.M.R.) performed staged excisions blinded to HRCM calculations with an initial 5-mm margin beyond the clinical margin, which the surgeons determined using dermoscopy and Wood lamp examination. After radial histopathologic sectioning, further excision stages guided by histopathologic findings were performed until reaching at least 3 mm of histologic clearance.[4,21,22] Thus, before surgery and based on these variables, we determined the estimated surgical defects from the HRCM-RV findings. A hypothetical LM or LMM extending just to but not beyond the outer edge of the paper ring would yield 2.5 mm of histologic clearance rather than 3 mm. However, we considered the 0.5 mm to be negligible because such variations occur depending on the surgical technique.[23] If a quadrant was positive outside the ring on HRCM, we added 3 mm to the margin calculated using HRCM-RV (eFigure in the Supplement).

Statistical Analysis

Descriptive statistics, such as means, SDs, medians, ranges, and relative frequencies, were used to describe the patient, lesion, imaging, and surgical characteristics. Normality of

Table. RCM Features Considered as Positive for LM at the Edges

Source	RCM Features Positive for LM
Guitera et al,[13] 2017	
Major criteria	Nonedged dermal papillae
	Round, large pagetoid cells
Minor criteria	
	Nucleated cells in dermal papillae
	Atypical cells at DEJ
	Follicular localization of atypical cells
	Broadened honeycomb pattern (negative feature)
Champin et al,[15] 2014	Single large round cell or a large dendritic cell
Present study	Atypical dendritic cell (any size) continuing from the LM trailing edge

Abbreviations: DEJ, dermal-epidermal junction; LM, lentigo maligna; RCM, reflectance confocal microscopy.

interval-scaled variables was assessed using graphic methods. The imaging data were assessed using the following 2 approaches: a lesion-based approach, with each lesion contributing 1 pair of surgical and HRCM measures (total lesion area in square centimeters), and a radial quadrant-based approach, with each lesion contributing 4 pairs of surgical and HRCM measures of length (in millimeters) based on the distances calculated emanating from the clinical margin to the surgical and HRCM margins at perpendicular 90° points around the lesion. For the lesion-based approach, a comparison was performed between the defect area estimated by HRCM imaging and the final surgical margin. We used paired *t* tests to assess differences in the estimated lesion area measured by HRCM and surgical excision. To assess differences in radial length between surgical margins and HRCM imaging, we used random-effects models. All analyses were performed using Stata SE software (version 14.1; StataCorp).

Results

Thirty-two patients consented to participate in the study and underwent imaging using HRCM-RV. Seven patients decided not to undergo surgery, and 3 decided to have treatment elsewhere. Nineteen LM and 4 LMM (median Breslow thickness, 0.37 mm; range, 0.30-1.05 mm) from 22 patients (12 men and 10 women) with a mean (SD) age of 69.0 (8.6) years (range, 46-83 years) contributed to the analysis. None of the LM or the LMM cases were upstaged after staged excision. Patient characteristics and imaging measurements are summarized in the eTable in the Supplement. The mean (SD) visualized clinical maximum diameter of the lesions was 1.86 (1.77) cm (range, 0.5-4.9 cm), and the mean (SD) area determined by clinical examination was 1.85 (1.77) cm^2 (range, 0.3-6.5 cm^2). The mean (SD) LM area based on HRCM was 3.9 (3.3) cm^2 (range, 1.1-16.0 cm^2). In all cases, HRCM confirmed the diagnosis of LM within the margin determined using dermoscopy or Wood lamp examination. In 40 of 92 quadrants (43.5%), HRCM identified LM beyond the clinical margin, extending a mean (SD) of 3.60 (2.60) mm (range, 0.50-11.00 mm). The mean (SD) surgical defect area estimated with HRCM was smaller than the surgical margin area (6.34 [4.02] vs 7.74 [5.28] cm^2; $P = .01$) (**Figure 3**).

A total of 92 pairs of radial measurements (4 per lesion, 1 per quadrant) were made from the clinical margin to the HRCM-estimated surgical margin. When evaluating the millimeters needed to be excised to achieve clearance, no differences were found in 58 of the 92 quadrants (63.0%) between the values estimated with HRCM and the observed surgical values. In 25 quadrants (27.2%), the defect was larger than the HRCM estimate by a mean of 2.24 mm (range, 1.00-6.00 mm), and in 9 quadrants (9.8%), HRCM overestimated the margin by a mean of 1.27 mm (range, 0.50-3.00 mm). Overall, after controlling for patient age, previous surgery, and clustering of observation within a given patient, surgical margins were a mean of 0.76 mm larger (95% CI, 0.67-0.84 mm; $P < .001$) than the HRCM estimate (**Figure 4**).

Discussion

Although dermoscopy and Wood lamp examination have been used to guide LM excisions, in our study in approximately 40% of the quadrants, HRCM identified LM and/or LMM extending beyond the dermoscopic and Wood lamp margins. These results highlight that HRCM improves LM and LMM margin evaluation[12,14,15] and confirm the need for increased surgical margins to achieve clear margins.[4,24-26] We used an imaging approach that parallels the design of staged excision with radial histopathologic sectioning by imaging with HRCM radially from the center to the periphery. Our results suggest that HRCM-RV correlates with surgical defects after staged excision of LM and LMM, although the mean HRCM-RV estimates were smaller than the actual defect. This finding may be attributable to difficulty assessing LM edges in a background of sun-damaged skin, more precise margin delineation with RCM, or errors in margin estimation.

In this study, to consider an area at the lesion edges as positive for LM on HRCM, we used the features present in the original LM diagnostic algorithm,[13] the presence of isolated large atypical cells at the edges,[15] and the presence of smaller atypical dendritic cells continuing from the LM trailing edge (Table). Because atypical melanocytes can occur in healthy sun-exposed skin, distinguishing LM from sun-reactive melanocytic hyperplasia can be challenging on confocal and histopathologic evaluations.[27] Thus, by considering smaller atypical cells as being positive for LM, one could argue that numerous false-positive findings may occur because they could correspond to activated melanocytes that frequently occur in sun-exposed skin. However, our findings suggest that in most quadrants, HRCM estimates were equivalent to the final surgical margins or slightly smaller (mean of 0.76 mm), and we overcalled photodamage as LM only in 9 of 92 quadrants. The cases with bigger differences came from previously treated LM and LMM, suggesting that our approach performs better in nonrecurrent LM and LMM (eTable in the Supplement). Therefore, we believe that atypical melanocytes, regardless of their size if evolving from a fully fledged LM or LMM, should be con-

Figure 2. Margin Determination in Case 3 Using Handheld Reflectance Confocal Microscopy With Radial Video Mosaicing (HRCM-RV)

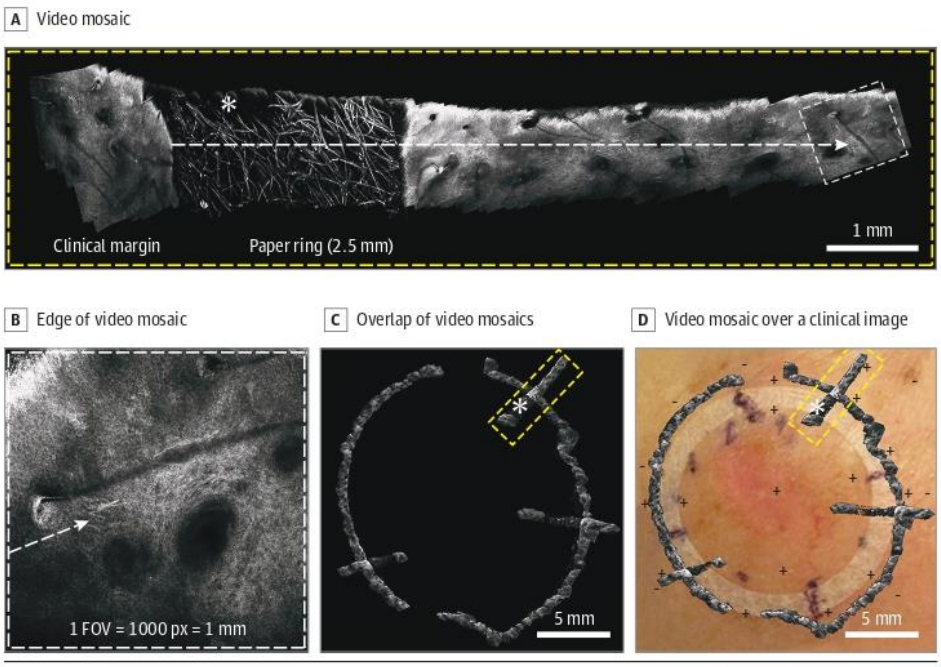

A, Video mosaic obtained from a video acquired at the 1-o'clock position from the center to the periphery (**Video**). Lentigo maligna (LM) extension was based on the paper ring rim width of 2.5 mm (asterisk), and the field of view (FOV) of the HRCM (dashed-edge box) is 1 mm, which equals 1000 pixels. B, The dashed-edge box from part A depicts a single FOV at the edge showing single dendritic cells continuing from the trailing edge of an LM at the 1-o'clock position. C, Digital overlap of 3 radial video mosaics obtained in 3 different lesion quadrants. D, A video mosaic map is digitally overlaid on a clinical image to estimate the surgical margin based on 3-mm histologic clearance. The yellow dashed-edge rectangles and asterisks correspond to the image in part A (C and D).

Figure 3. Examples of Lentigo Maligna Melanoma (LMM) and LM Imaged With Handheld Reflectance Confocal Microscopy With Radial Video Mosaicing (HRCM-RV) and Corresponding Surgical Defects After Staged Excision

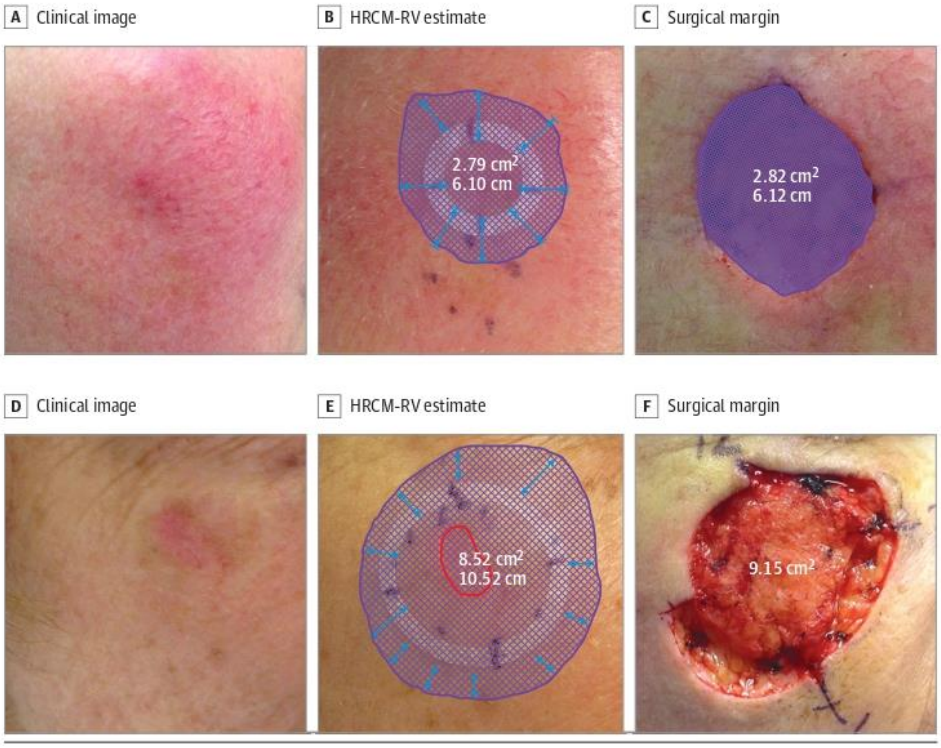

Images A through C depict findings from case 2. A, Clinical image reveals an amelanotic, ill-defined LMM (Breslow thickness, 0.39 mm) with a clinical size of 0.26 cm^2. B, Estimated surgical margin after HRCM-RV finding of a 2.79-cm^2 defect. C, Final surgical defect was 2.82 cm^2 after 2 stages of excision. Images D through F depict findings from case 3. D, Clinical image reveals a hypomelanotic, ill-defined LM with a clinical size of 0.54 cm^2. E, Estimated surgical margin after HRCM-RV finding of an 8.52-cm^2 defect. F, Final surgical defect was 9.15 cm^2 after 3 stages of excision.

sidered as positive because they may reflect the trailing edge of an LM or LMM (Figure 2B).

Another explanation why our HRCM-estimated defects were smaller than the surgical defects may be that HRCM provides better margin delineation. Although our staged excision was conservative in terms of tissue sparing, several factors can influence the amount of tissue excised, including the thickness of the marking pen, the use of a magnifying glass to draw the marking, or where the incision is performed (inside or outside the skin marking).[23] These limitations are not present

Figure 4. Plot of the Paired Observations of the Surgical Margins and Estimated Handheld Reflectance Confocal Microscopy With Radial Video Mosaicing (HRCM-RV) Margins

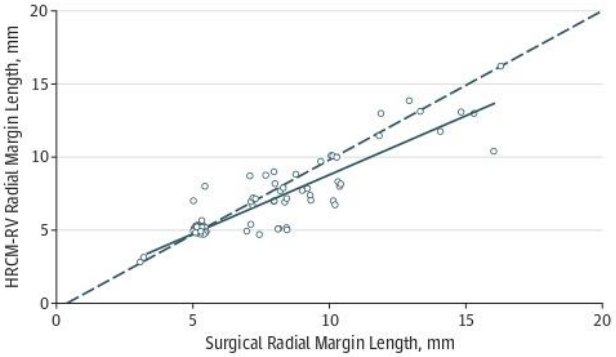

Four measures were obtained from each sample, 1 from each lesion quadrant measured from the center of the lesion to the perceived margin. The dashed line represents the linear function (y = x), where surgical measures and HRCM-RV estimates are equal. The solid line represents the least squares fitted regression line for the association between the 2 measurement types. Hollow circles below the dotted line indicate observations for which the surgical margin was greater than the HRCM-RV margin; hollow circles on the dotted line, similar estimates; and hollow circles above the dotted line, observations for which HRCM-RV margins were larger than surgical margins. Observations were slightly offset to visualize overlapping data points. Overall, from our random-effects regression model and controlling for patient age and previous surgery, surgical margins were a mean of 0.76 mm (95% CI, 0.67-0.84 mm; $P < .001$) larger than the HRCM-RV estimates.

when digitally diagramming the margins on an image. However, in quadrants where we did not identify LM outside the paper ring, we may have underestimated the margins by considering a quadrant negative if 2.5 mm of clearance were obtained. However, the clinical relevance of such small differences is unknown, and other margin-controlled surgical procedures may use less than 3 mm of histologic clearance for negative margins.[5] Therefore, if HRCM-RV was used to guide surgery, it could be the starting point of margin-controlled surgical procedures because it estimated a smaller and not a larger defect. This point is important because the presence of false-positive findings could lead to negative but wider-than-necessary margins.

Limitations

This study has several challenges and limitations. We observed 9 false-positive quadrants, which corresponded to areas of photodamage with small dendritic cells on HRCM. The overestimation was a mean of 1.27 mm (range, 0.50-3.00 mm), which represents approximately an additional 6% to 37% margin relative to the real margin size. Previous studies have shown that variations owing to the surgical technique can range from 8% to 45% when margins from 2 to 10 mm are drawn on the skin.[23] In our study, overestimation occurred in fewer than 10% of quadrants and by a range that occurs in standard surgical procedures. To overcome variation in margin estimation owing to wound retraction after electrocoagulation, specimen shrinkage after formalin fixation,[28] or inaccuracy in the digital margin calculation, we performed 2 methods of image calibration, margin estimation, and video mosaic quadrant size estimation that, to our knowledge, have not been described in previous studies assessing LM and LMM margins.[7,8,14,15] However, additional studies involving multiple readers with varying levels of experience are needed to validate these results because our study included only 2 of us (M.C. and O.Y.) who acquired data and 1 (O.Y.) who analyzed the results.

Our approach combines 2 major innovations—adhesive rings and video mosaics—to guide navigation and calculate the surgical margins. A common challenge when using HRCM is identifying the exact area on the skin being imaged. Recently, adhesive rings have been used to define the area of interest when imaging with HRCM.[19,20,29] Adhesive rings are inexpensive, can be adapted to the shape of the lesion by slightly bending them or placing multiple rings outside the lesion margins, and can easily facilitate orientation because the fibers can be identified on HRCM, thus allowing a single operator to perform the image acquisition as opposed to the 2 operators needed with other LM mapping techniques that use HRCM.[15] We used commercially available paper rings with a rim width of 2.5 mm to calculate the surgical margins by combining them with video mosaicing; however, the diameter and rim width can be customized by cutting adhesive plastic,[29] thus permitting tailored HRCM navigation and margin estimation.

Another challenge when using HRCM is the absence of architectural information owing to lack of mosaicing capabilities in its native software. The ability to observe and examine architectural information in large fields of view is necessary, similar to that in pathologic analysis. For the newer HRCM with video acquisition, an algorithm has been developed to transform videos into video mosaics.[17,18,30] In the present study, we used RV to help delineate the LM and LMM margins. However, video mosaicing is not integrated in the HRCM software, and the postprocessing video takes approximately 10 minutes per 1 minute of each video. Nevertheless, each radial video is approximately 20 seconds long; thus, the whole HRCM-RV process is approximately 30 minutes long. Therefore, our next phase of research will focus on increasing the speed of postprocessing and integrating video mosaicing into the native HRCM software to obtain real-time video mosaics. This increase would allow faster margin estimation at the patient bedside and in the operating room. In the meantime, a simplified and less precise method to perform our radial imaging approach could be counting in real time the number of positive fields of view outside the paper ring while imaging radially from the center to the periphery.

Conclusions

Our results suggest that HRCM-RV margin mapping correlates well with histologic findings and can estimate the subclinical extension and presurgical margins. Management of LM and LMM can benefit from noninvasive radial imaging, because evaluating an LM or LMM from the center toward the periphery illustrates its trailing edge as it dissipates into melanocytic hyperplasia[4]—a feature that can be difficult to contextualize when seen in an isolated sample, such as a scouting biopsy. Thus, we believe that our approach can result in

sparing of healthy tissue by reducing the number of biopsies in clinically uncertain areas. Furthermore, anticipation of the LM or LMM size and the estimated surgical defect may enable the clinician to decide the most adequate treatment, plan the surgical reconstruction in advance, and counsel the patient appropriately.

ARTICLE INFORMATION

Accepted for Publication: June 28, 2017.

Published Online: October 11, 2017. doi:10.1001/jamadermatol.2017.3114

Author Contributions: Drs Yélamos and Rossi had full access to all the data in the study and take responsibility for the integrity of the data and the accuracy of the data analysis.
Study concept and design: Yélamos, Rajadhyaksha, Nehal, Rossi.
Acquisition, analysis, or interpretation of data: Yélamos, Cordova, Blank, Kose, Dusza, Lee, Nehal, Rossi.
Drafting of the manuscript: Yélamos, Dusza, Rajadhyaksha, Rossi.
Critical revision of the manuscript for important intellectual content: Cordova, Blank, Kose, Dusza, Lee, Rajadhyaksha, Nehal, Rossi.
Statistical analysis: Dusza.
Obtained funding: Yélamos, Rajadhyaksha.
Administrative, technical, or material support: Yélamos, Cordova, Blank, Kose, Rajadhyaksha.
Study supervision: Rajadhyaksha, Nehal, Rossi.

Conflict of Interest Disclosures: Dr Rajadhyaksha reports being a former employee of and owning equity in Caliber Imaging and Diagnostics (formerly Lucid Inc), the company that manufactures and sells the VivaScope confocal microscope. The VivaScope is the commercial version of an original laboratory prototype that he had developed at Massachusetts General Hospital, Harvard Medical School. No other disclosures were reported.

Funding/Support: This study was funded by grant R01EB020029 from the National Institute of Biomedical Imaging and Bioengineering, National Institutes of Health (NIH); in part by Cancer Center Support grant P30 CA008748 from the National Cancer Institute, NIH; and by the Beca Excelencia Fundación Piel Sana (Dr Yélamos).

Role of the Funder/Sponsor: The sponsors had no role in the design and conduct of the study; in the collection, analysis, and interpretation of data; in the preparation, review, or approval of the manuscript; or in the decision to submit the manuscript for publication.

Additional Information: The video is available online at http://www.archdermatol.com.

REFERENCES

1. Star P, Guitera P. Lentigo maligna, macules of the face, and lesions on sun-damaged skin: confocal makes the difference. *Dermatol Clin*. 2016;34(4):421-429.

2. Osborne JE, Hutchinson PE. A follow-up study to investigate the efficacy of initial treatment of lentigo maligna with surgical excision. *Br J Plast Surg*. 2002;55(8):611-615.

3. Pitman GH, Kopf AW, Bart RS, Casson PR. Treatment of lentigo maligna and lentigo maligna melanoma. *J Dermatol Surg Oncol*. 1979;5(9):727-737.

4. Hazan C, Dusza SW, Delgado R, Busam KJ, Halpern AC, Nehal KS. Staged excision for lentigo maligna and lentigo maligna melanoma: a retrospective analysis of 117 cases. *J Am Acad Dermatol*. 2008;58(1):142-148.

5. Gaudy-Marqueste C, Perchenet AS, Taséi AM, et al. The "spaghetti technique": an alternative to Mohs surgery or staged surgery for problematic lentiginous melanoma (lentigo maligna and acral lentiginous melanoma). *J Am Acad Dermatol*. 2011;64(1):113-118.

6. Etzkorn JR, Sobanko JF, Elenitsas R, et al. Low recurrence rates for in situ and invasive melanomas using Mohs micrographic surgery with melanoma antigen recognized by T cells 1 (MART-1) immunostaining: tissue processing methodology to optimize pathologic staging and margin assessment. *J Am Acad Dermatol*. 2015;72(5):840-850.

7. Robinson JK. Use of digital epiluminescence microscopy to help define the edge of lentigo maligna. *Arch Dermatol*. 2004;140(9):1095-1100.

8. Walsh SB, Varma R, Raimer D, et al. Utility of Wood's light in margin determination of melanoma in situ after excisional biopsy. *Dermatol Surg*. 2015;41(5):572-578.

9. Dengel L, Turza K, Noland MM, Patterson JW, Slingluff CL Jr. Skin mapping with punch biopsies for defining margins in melanoma: when you don't know how far to go. *Ann Surg Oncol*. 2008;15(11):3028-3035.

10. Jeneby TT, Chang B, Bucky LP. Ultraviolet-assisted punch biopsy mapping for lentigo maligna melanoma. *Ann Plast Surg*. 2001;46(5):495-499.

11. Rajadhyaksha M, Grossman M, Esterowitz D, Webb RH, Anderson RR. In vivo confocal scanning laser microscopy of human skin: melanin provides strong contrast. *J Invest Dermatol*. 1995;104(6):946-952.

12. Rajadhyaksha M, Marghoob A, Rossi A, Halpern AC, Nehal KS. Reflectance confocal microscopy of skin in vivo: from bench to bedside. *Lasers Surg Med*. 2017;49(1):7-19.

13. Guitera P, Pellacani G, Crotty KA, et al. The impact of in vivo reflectance confocal microscopy on the diagnostic accuracy of lentigo maligna and equivocal pigmented and nonpigmented macules of the face. *J Invest Dermatol*. 2010;130(8):2080-2091.

14. Guitera P, Moloney FJ, Menzies SW, et al. Improving management and patient care in lentigo maligna by mapping with in vivo confocal microscopy. *JAMA Dermatol*. 2013;149(6):692-698.

15. Champin J, Perrot JL, Cinotti E, et al. In vivo reflectance confocal microscopy to optimize the spaghetti technique for defining surgical margins of lentigo maligna. *Dermatol Surg*. 2014;40(3):247-256.

16. Menge TD, Hibler BP, Cordova MA, Nehal KS, Rossi AM. Concordance of handheld reflectance confocal microscopy (RCM) with histopathology in the diagnosis of lentigo maligna (LM): a prospective study. *J Am Acad Dermatol*. 2016;74(6):1114-1120.

17. Hibler BP, Yélamos O, Cordova M, et al. Handheld reflectance confocal microscopy to aid in the management of complex facial lentigo maligna. *Cutis*. 2017;99(5):346-352.

18. Kose K, Cordova M, Duffy M, Flores ES, Brooks DH, Rajadhyaksha M. Video-mosaicing of reflectance confocal images for examination of extended areas of skin in vivo. *Br J Dermatol*. 2014;171(5):1239-1241.

19. Yélamos O, Hibler BP, Cordova M, et al. Handheld reflectance confocal microscopy for the detection of recurrent extramammary Paget disease. *JAMA Dermatol*. 2017;153(7):689-693.

20. Marino ML, Rogers T, Sierra Gil H, Rajadhyaksha M, Cordova MA, Marghoob AA. Improving lesion localization when imaging with handheld reflectance confocal microscope. *Skin Res Technol*. 2016;22(4):519-520.

21. Joyce KM, Joyce CW, Jones DM, et al. An assessment of histological margins and recurrence of melanoma in situ. *Plast Reconstr Surg Glob Open*. 2015;3(2):e301.

22. McGuire LK, Disa JJ, Lee EH, Busam KJ, Nehal KS. Melanoma of the lentigo maligna subtype: diagnostic challenges and current treatment paradigms. *Plast Reconstr Surg*. 2012;129(2):288e-299e.

23. Lalla R, Brown TL, Griffiths RW. Where to draw the line: the error in marking surgical excision margins defined. *Br J Plast Surg*. 2003;56(6):603-606.

24. Felton S, Taylor RS, Srivastava D. Excision margins for melanoma in situ on the head and neck. *Dermatol Surg*. 2016;42(3):327-334.

25. Moyer JS, Rudy S, Boonstra PS, et al. Efficacy of staged excision with permanent section margin control for cutaneous head and neck melanoma. *JAMA Dermatol*. 2017;153(3):282-288.

26. Connolly KL, Busam KJ, Nehal KS. Optimizing outcomes for cutaneous head and neck melanoma. *JAMA Dermatol*. 2017;153(3):267-268.

27. Prieto VG, Argenyi ZB, Barnhill RL, et al. Are en face frozen sections accurate for diagnosing margin status in melanocytic lesions? *Am J Clin Pathol*. 2003;120(2):203-208.

28. Blasdale C, Charlton FG, Weatherhead SC, Ormond P, Lawrence CM. Effect of tissue shrinkage on histological tumour-free margin after excision of basal cell carcinoma. *Br J Dermatol*. 2010;162(3):607-610.

29. Ali FR, Craythorne EE. Gummed rings as the outer marker of microscopically examined tissue (GROMMETs) as mapping adjuncts to in vivo reflectance confocal microscopy (RCM). *J Am Acad Dermatol*. 2016;75(3):e103-e104.

30. Kose K, Gou M, Yélamos O, et al. Automated video-mosaicking approach for confocal microscopic imaging in vivo: an approach to address challenges in imaging living tissue and extend field of view. *Sci Rep*. 2017;7(1):10759.

Supplementary Online Content

Yélamos O, Cordova M, Blank N, et al. Correlation of handheld reflectance confocal microscopy with radial video mosaicing for margin mapping of lentigo maligna and lentigo maligna melanoma. *JAMA Dermatol*. Published online October 11, 2017. doi:10.1001/jamadermatol.2017.3114

eFigure. Example of Surgical Margin Calculation in Case 2, Quadrant 4

eTable. Characteristics of Participants and Measures for Surgical and Handheld Reflectance Confocal Microscopy Margins

This supplementary material has been provided by the authors to give readers additional information about their work.

eFigure. Example of Surgical Margin Calculation in Case 2, Quadrant 4

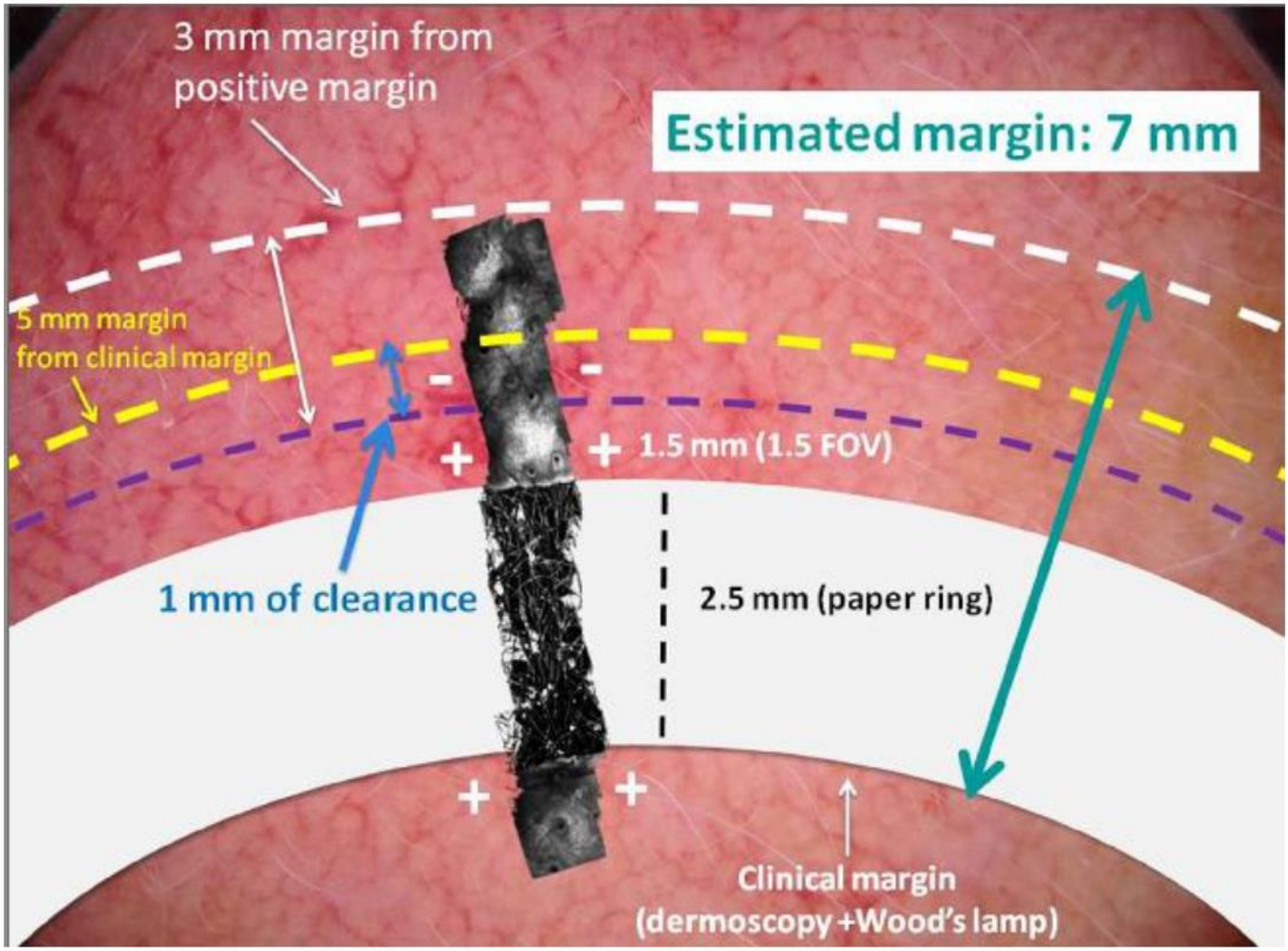

Reflectance confocal microscopy found positive (+) lentigo maligna up to a margin of 1.5 mm outside the paper ring (purple dashed line). Initial 5 mm surgical margin after staged excision (yellow dashed line) outside clinical margin would have yielded 1 mm of clearance (blue arrow) of reflectance confocal microscopy-derived positive margin. This was considered insufficient, as >3mm of negative margins were required to consider the margin clear. Predicted surgical margin (white dashed line) estimated 7 mm from clinical margin to allow 3mm of histologic clearance, which in this case accurately corresponded to the final surgical margin.

eTable. Characteristics of Participants and Measures for Surgical and Handheld Reflectance Confocal Microscopy Margins

Case	Sex	Ethnicity	Location	Breslow (mm)	Prior treatment	No.of surgical stages	Maximum clinical diameter (cm)	Clinical area (cm^2)	RCM LM area (cm^2)	RCM-predicted surgical area (cm^2)	Surgical area (cm^2)
1	Man	White	R Cheek	0	No	4	0.6	0.33	2.87	4.7	5.93
2	Woman	White	R Cheek	0.39	No	2	0.5	0.26	1.31	2.79	2.82
3	Woman	White	R Cheek	0	No	3	1	0.54	6.54	8.52	9.15
4	Woman	White	Nose	0	No	2	1.4	0.95	1.84	3.81	4.92
5	Man	White	L Forehead	0	No	1	1.4	0.87	1.75	3.42	3.39
6	Woman	White	L Cheek	0	Surgery	2	3.1	4.2	4.7	7.1	17.84
7	Man	White	R Cheek	0	Surgery	2	4.9	3.98	6.93	10.43	17.1
8	Man	White	Vertex Scalp	0	No	2	2.1	1.31	2.95	6.3	7.21
9	Man	White	L Cheek	0	Surgery	2	3.9	6.54	8.92	15.27	17.43
10	Man	White	R Scalp	0	No	1	1.4	1.06	1.09	3.5	3.5
11			L Scalp	0	No	2	1.8	1	1.18	4.16	4.34
12	Woman	White	R Cheek	0.35	No	1	1.6	1.17	2.2	4.25	5.22
13	Man	White	Nose	0.3	Surgery, Cryotherapy	3	2.6	2.86	5.13	7.19	7.46
14	Woman	White	L Cheek	0	Cryotherapy	3	1.4	1.14	4.79	6.44	11.5
15	Man	White	L Cheek	1.05	Cryotherapy, 5FU	2	2.2	1.78	4.51	7.38	9.47
16	Woman	White	R Cheek	0	No	1	2.8	3.07	4.03	7.09	7.25
17	Woman	White	L Cheek	0	No	2	0.8	1.03	2.4	3.74	3.38
18	Man	White	R Cheek	0	No	3	0.8	0.82	3.44	6.15	6.58
19	Woman	White	Nose	0	No	1	1.5	1.14	1.66	4.35	4.75
20	Man	White	Glabella	0	No	1	1.5	1.71	1.96	3.78	3.12
21	Woman	White	Nose	0	No	3	1.2	0.58	1.11	1.87	1.61
22	Man	White	Vertex Scalp	0	No	1	3.6	6.03	15.97	19.53	19.67
23	Man	White	R Cheek	0	No	2	0.8	0.5	2.6	4.19	4.54

Abbreviations: R, right; L, left; RCM, reflectance confocal microscopy; y, years; 5FU, 5-fluorouracil

Publication 3: Handheld Reflectance Confocal Microscopy for the Detection of Recurrent Extramammary Paget Disease

Oriol Yélamos, Brian P. Hibler, Miguel Cordova, Travis J. Hollmann, Kivanc Kose, Michael A. Marchetti, Patricia L. Myskowski, Melissa P. Pulitzer, Milind Rajadhyaksha, Anthony M. Rossi, Manu Jain

JAMA Dermatol. 2017 Jul 1;153(7):689-693. doi: 10.1001/jamadermatol.2017.0619.

SUMMARY

Background: Extramammary Paget disease (EMPD) is commonly refractory to surgical and nonsurgical therapies. Identifying recurrent or persistent EMPD is challenging because the disease is multifocal, and multiple blind scouting biopsies are usually performed in this setting. Handheld reflectance confocal microscopy (HRCM) has been used to diagnose and map primary EMPD and therefore may be used to identify EMPD recurrences.

Aims: To evaluate HRCM's diagnostic accuracy in the setting of recurrent or persistent EMPD as well as its potential diagnostic pitfalls.

Material and Methods: This prospective case series study included patients referred to the Dermatology Service at Memorial Sloan Kettering Cancer Center between January 1, 2014, and December 31, 2016, with biopsy-proven EMPD in whom HRCM was used to monitor treatment response. Five patients were included, and 22 sites clinically concerning for recurrent or persistent disease were evaluated using HRCM and histopathologic examination. In 2 patients, video mosaics were created to evaluate large areas. Sensitivity and specificity of HRCM in identifying recurrent or persistent EMPD; causes for false-negative results according to their location, histopathologic findings, and previous treatments.

Results: Of the 22 clinically suspicious sites evaluated in 5 patients (4 men, 1 woman; median [range] age, 70 [56-77] years), 9 (40.9%) were positive for recurrent disease on HRCM and histopathologically confirmed, and 13 (59.1%) sites were negative on HRCM, but 3 of the 13 were positive for EMPD on histopathological examination. In general, HRCM had a sensitivity of 75% and a specificity of 100% in identifying recurrent or persistent EMPD. False-negative results were found in 2 patients and occurred at the margins of EMPD, close to previous biopsy sites. Creating video mosaics (or video mosaicking) seemed to improve the detection of EMPD.

Conclusions: Handheld reflectance confocal microscopy is a useful auxiliary tool for diagnosing EMPD recurrences and can be used to guide scouting biopsies, thus reducing the number of biopsies needed to render a correct diagnosis.

JAMA Dermatology | Brief Report

Handheld Reflectance Confocal Microscopy for the Detection of Recurrent Extramammary Paget Disease

Oriol Yélamos, MD; Brian P. Hibler, MD; Miguel Cordova, MD; Travis J. Hollmann, MD; Kivanc Kose, PhD; Michael A. Marchetti, MD; Patricia L. Myskowski, MD; Melissa P. Pulitzer, MD; Milind Rajadhyaksha, PhD; Anthony M. Rossi, MD; Manu Jain, MD

IMPORTANCE Extramammary Paget disease (EMPD) is commonly refractory to surgical and nonsurgical therapies. Identifying recurrent or persistent EMPD is challenging because the disease is multifocal, and multiple blind scouting biopsies are usually performed in this setting. Handheld reflectance confocal microscopy (HRCM) has been used to diagnose and map primary EMPD and therefore may be used to identify EMPD recurrences.

OBJECTIVE To evaluate HRCM's diagnostic accuracy in the setting of recurrent or persistent EMPD as well as its potential diagnostic pitfalls.

DESIGN, SETTING, AND PARTICIPANTS This prospective case series study included patients referred to the Dermatology Service at Memorial Sloan Kettering Cancer Center between January 1, 2014, and December 31, 2016, with biopsy-proven EMPD in whom HRCM was used to monitor treatment response. Five patients were included, and 22 sites clinically concerning for recurrent or persistent disease were evaluated using HRCM and histopathologic examination. In 2 patients, video mosaics were created to evaluate large areas.

MAIN OUTCOMES AND MEASURES Sensitivity and specificity of HRCM in identifying recurrent or persistent EMPD; causes for false-negative results according to their location, histopathologic findings, and previous treatments.

RESULTS Of the 22 clinically suspicious sites evaluated in 5 patients (4 men, 1 woman; median [range] age, 70 [56-77] years), 9 (40.9%) were positive for recurrent disease on HRCM and histopathologically confirmed, and 13 (59.1%) sites were negative on HRCM, but 3 of the 13 were positive for EMPD on histopathological examination. In general, HRCM had a sensitivity of 75% and a specificity of 100% in identifying recurrent or persistent EMPD. False-negative results were found in 2 patients and occurred at the margins of EMPD, close to previous biopsy sites. Creating video mosaics (or video mosaicking) seemed to improve the detection of EMPD.

CONCLUSIONS AND RELEVANCE Handheld reflectance confocal microscopy is a useful auxiliary tool for diagnosing EMPD recurrences and can be used to guide scouting biopsies, thus reducing the number of biopsies needed to render a correct diagnosis.

Author Affiliations: Dermatology Service, Department of Medicine, Memorial Sloan Kettering Cancer Center, New York, New York (Yélamos, Hibler, Cordova, Kose, Marchetti, Myskowski, Rajadhyaksha, Rossi, Jain); Dermatology Department, Hospital Clínic, Universitat de Barcelona, Barcelona, Spain (Yélamos); Pathology Department, Memorial Sloan Kettering Cancer Center, New York, New York (Hollmann, Pulitzer).

Corresponding Author: Manu Jain, MD, Dermatology Service, Department of Medicine, Memorial Sloan Kettering Cancer Center, 16 E 60th St, New York, NY 10022 (jainm@mskcc.org).

JAMA Dermatol. doi:10.1001/jamadermatol.2017.0619
Published online May 10, 2017.

Extramammary Paget disease (EMPD) is a rare cutaneous adenocarcinoma that is difficult to visually assess because of its nonspecific clinical appearance (**Figure**, A) and multifocal growth.[1] Surgery is the mainstay of treatment for EMPD because nonsurgical therapy responses are variable and difficult to monitor. However, disease recurrence is common after both surgical and nonsurgical approaches.[1] As such, mapping skin biopsies are often performed to assess therapeutic response.[2]

Reflectance confocal microscopy (RCM) is a noninvasive imaging technique that allows visualization of the epidermis and papillary dermis with cellular-level resolution.[3] This technique has been used as a diagnostic adjunct for mammary Paget disease and EMPD.[2,4-10] Traditional wide-probe RCM (Vivascope 1500; Caliber I.D.) requires attaching a metal ring onto the skin, which is challenging on the genitalia. Conversely, the handheld RCM (HRCM [Vivascope 3000; Caliber I.D.]) allows free-form translation on the skin along any spontaneously user-chosen, unconstrained path, permitting its use on curved areas such as the genitalia. Recently, HRCM has been reported to guide surgical management of EMPD.[4] In addition, RCM has been used to monitor other types of skin cancer, such as lentigo maligna, after therapies such as imiquimod.[11] However, no studies have evaluated HRCM in monitoring EMPD after treatment. The aim of this study was to evaluate the diagnostic accuracy of HRCM in the setting of recurrent EMPD and HRCM's potential pitfalls.

Key Points

Question Is handheld reflectance confocal microscopy useful for identifying recurrent or persistent extramammary Paget disease?

Findings In this study of 5 patients with previously treated extramammary Paget disease, handheld reflectance confocal microscopy had a sensitivity of 75% and a specificity of 100% in identifying recurrent or persistent extramammary Paget disease.

Meaning Handheld reflectance confocal microscopy is an auxiliary tool for diagnosing recurrences of extramammary Paget disease and can guide scouting biopsies and thus reduce the number of biopsies needed to render a correct diagnosis in such a sensitive location.

Methods

We prospectively included patients with biopsy-proven EMPD referred to the Dermatology Service at Memorial Sloan Kettering Cancer Center between January 1, 2014, and December 31, 2016, in whom HRCM was used to monitor treatment response. Handheld RCM was used to evaluate areas clinically concerning for active disease. In patients 3, 4, and 5, adhesive paper rings (product No. 1529; 3M) were placed at the clinically defined areas to facilitate imaging localization.[12] Stacks of images were taken of clinically suspicious areas. In patients 4 and 5, videos were taken in the en face planes at different depths and converted into video mosaics. To create the video mosaics, we extracted the video frames and, using a novel algorithm based on previous studies,[13] stitched these frames together to compose an overall mosaic of the imaged area. This study was approved by the institutional review board of Memorial Sloan Kettering Cancer Center. Written patient informed consent was obtained before each imaging session.

As in previous studies,[5,6,8] we considered the site to be RCM-positive if we identified Paget cells (PCs)—which are seen as dark holes 1 to 2 times the size of keratinocytes or as target structures with a bright center and surrounding dark halo—in the epidermis or forming nests at the dermoepidermal junction. Epidermal disarray or increased dermal vessels were considered supportive features but were not specific for the diagnosis of EMPD.

Biopsies were taken either at areas that were positive after HRCM evaluation or at areas that were highly suspicious for recurrence, such as eroded areas or intensely erythematous areas. Histopathologic results were later correlated with the HRCM findings.

Results

We included 5 patients (4 men and 1 woman) with a median (range) age of 70 (56-77) years. One patient had an associated malignant neoplasm in an internal organ, and previous treatments for EMPD included surgery, radiotherapy, imiquimod, and *ERBB2* (formerly *HER2* or *HER2/neu*) tyrosine kinase inhibitor (ERBB2-TKI) (**Table**).

In total, 22 clinically suspicious sites (4 in the center and 18 at the margins) were interrogated with HRCM and subsequently biopsied. Of those, 9 sites (40.9%) were positive for EMPD on HRCM and histopathologically confirmed (Figure, B and C). Conversely, 13 sites (59.1%) were negative on HRCM; of these, 3 were positive for EMPD on histopathologic examination (Table). Overall, the sensitivity of HRCM in identifying recurrent or persistent disease was 75% and the specificity was 100%. The false-negatives (FNs) were found in 2 patients: patient 2 had received topical imiquimod (5% cream), and patient 3 had received radiotherapy followed by oral ERBB2-TKI, 240 mg daily, prior to assessment.

When assessing the location of the biopsies, we found that all the lesions biopsied in the center were correctly identified with HRCM, whereas the 3 FNs occurred in the margins. The FNs occurred in areas close to previous biopsy sites (Table). To identify any additional cause for misdiagnosis, we reviewed RCM images and histopathologic slides from the FNs. The patient treated with imiquimod (patient 2; Figure, D) had focal dark holes on RCM in the stratum spinosum (Figure, E) that corresponded to scattered individual PCs within the epidermis on histopathologic examination (Figure, F). Conversely, the patient treated with ERBB2-TKI had unequivocal EMPD on histopathologic examination that was not identified on RCM.

Discussion

Our results suggest that, because of its high specificity, HRCM is useful in identifying recurrent or persistent EMPD

Figure. Representative Cases of a Confocal False-Negative Extramammary Paget Disease and a Confocal True-Positive Extramammary Paget Disease

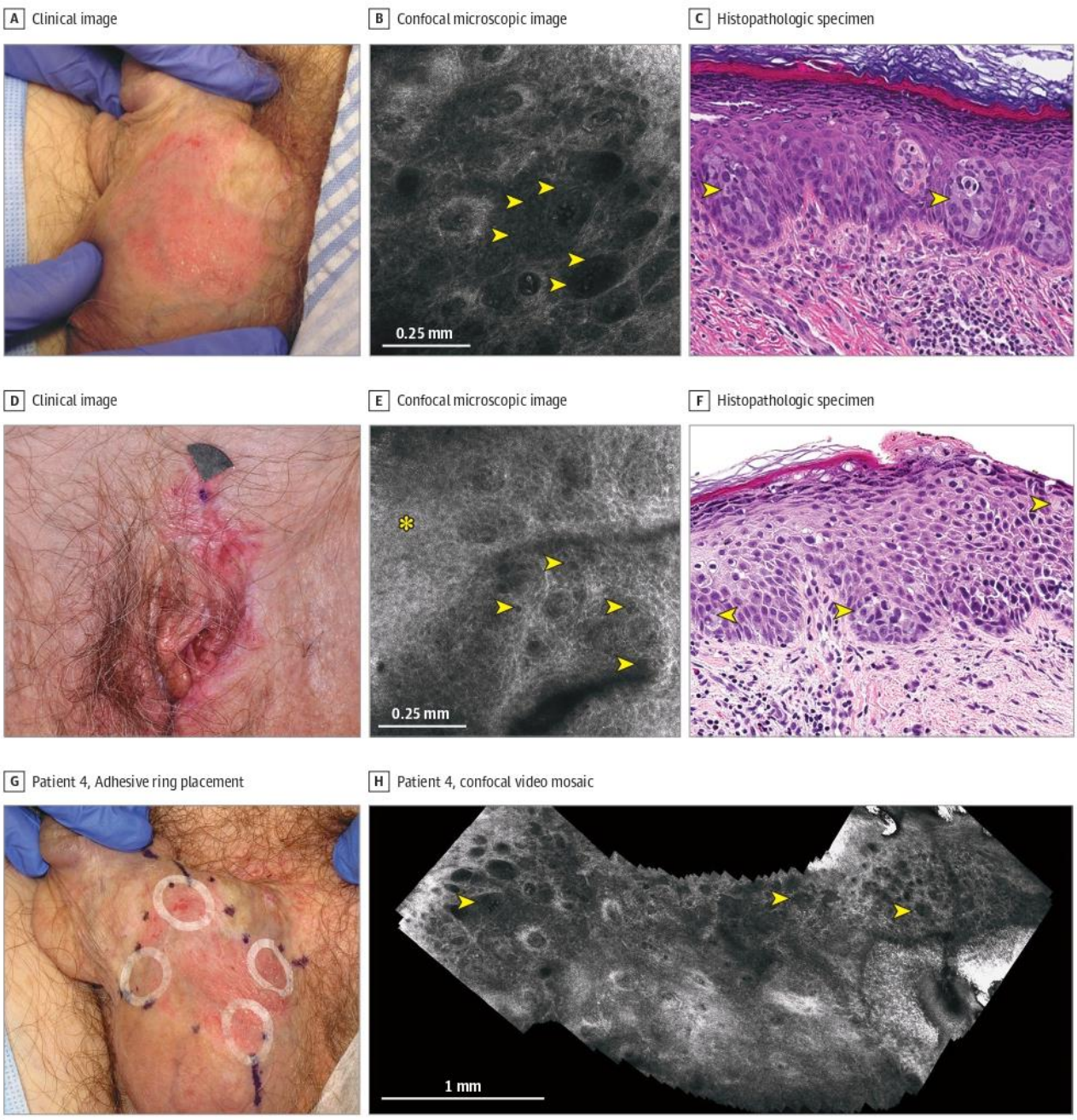

A, Clinical appearance of a scrotal extramammary Paget disease (patient 4). B, Confocal examination revealed multiple target cells (yellow arrowheads) with bright center and peripheral dark halo forming nests at the dermoepidermal junction. C, Histopathological examination showed large cells, with pale cytoplasm forming nests (yellow arrows) in the lower epidermis confirming the diagnosis of extramammary Paget disease (hematoxylin-eosin, original magnification ×20). D, Clinical appearance of a vulvar recurrent extramammary Paget disease (patient 2). E, Confocal examination of the mons pubis was interpreted as negative, although, after reevaluation, focal dark holes (yellow arrowheads) were identified in the stratum spinosum (asterisk). F, Histopathologically, patient 2 showed scattered Paget cells (yellow arrowheads) in the inflamed and spongiotic epidermis (hematoxylin-eosin, original magnification ×20). G, In select cases, adhesive paper rings were placed at 12, 3, 6, and 9 o'clock to improve confocal navigation and were later moved to adjacent areas to cover the entire margins and to reduce sampling bias (patient 4). H, Confocal video mosaic taken at the dermoepidermal junction captured inside 1 paper ring to facilitate identification of large nests of Paget cells (yellow arrows) over a larger field of view (patient 4).

and guiding scouting biopsies. This finding is particularly useful because HRCM may reduce the number of biopsies needed to render a correct diagnosis in such a sensitive location. However, negative HRCM findings should be interpreted with caution when monitoring treatment response because FNs may occur.

In patient 2, we identified lower PC density within the epidermis, making visualization of PCs difficult with HRCM.

Table. Summary of the Demographic and Clinical Findings and Its Confocal and Histopathologic Diagnoses

Patient No./Sex[a]	Concomitant Internal Malignant Neoplasm	Date of RCM Imaging	Treatments for EMPD Prior to RCM, y	Clinical Description and Location	Margin or Center of Lesion	Diagnosis	
						RCM	Histopathologic Examination
1/M	None	March 2014	Surgery	Erythematous macule, anterior perineum	Margin	Negative	Negative
				Erythematous macule, right perineum	Margin	Negative	Negative
				Erythematous macule, posterior perineum	Margin	EMPD	EMPD
2/F	None	June 2014	Surgery	Erythematous macule, mons pubis	Margin	EMPD	EMPD
		November 2014	Recurrent EMPD treated with imiquimod	Approximate area of previous biopsy, mons pubis	Margin	Negative	EMPD
				Erythematous patch, labia minora	Margin	EMPD	EMPD
3/M	None	June 2015	RT	Erythematous patch, left anterior scrotum	Margin	Negative	Negative
				Erythematous patch, left inferior scrotum	Center	EMPD	EMPD
				Erythematous patch, left mid inguinal crease	Margin	Negative	Negative
				Erythematous patch, anterior perineum	Margin	Negative	Negative
				Erythematous patch, posterior perineum	Margin	Negative	Negative
				Erythematous patch, right lateral scrotum	Margin	Negative	Negative
		January 2016	Recurrent EMPD treated with oral ERBB2-TKI	Erythematous patch, left inferior scrotum next to biopsy scar	Margin	Negative	EMPD
				Erythematous patch, left inferior scrotum below biopsy scar	Margin	Negative	EMPD
4/M	Papillary renal cell carcinoma	January 2016	Surgery; residual EMPD treated with RT	Erythematous patch, penile shaft	Margin	EMPD	EMPD
				Erythematous patch, left scrotum	Center	EMPD	EMPD
5/M	None	April 2016	WLE; Mohs surgery	Erythematous patch, right anterior scrotum	Margin	EMPD	EMPD
				Erythematous patch, left anterior scrotal margin	Margin	EMPD	EMPD
				Erythematous patch, center of scrotum	Center	EMPD	EMPD
				Eroded erythematous patch, right posterior scrotum	Center	Negative	Negative
				Erythematous macule, outside right border of the inguinal crease	Margin	Negative	Negative
				Erythematous macule, margin of previous graft in the right ventral penile shaft	Margin	Negative	Negative

Abbreviations: EMPD, extramammary Paget disease; ERBB2-TKI, *ERBB2* (formerly *HER2* or *HER2/neu*) tyrosine kinase inhibitor; RCM, reflectance confocal microscopy; RT, radiotherapy; WLE, wide local excision.

[a] All patients self-reported their race/ethnicity as white.

We hypothesized that this lower density was the effect of skin-directed therapies on the epidermis and the fact that the area evaluated was located at the lesion margin (instead of the center), where lower density of PCs is expected. However, this hypothesis was not true for the false-positives in patient 3 that were also located on the margins. In addition, the 3 FNs were close to recent biopsy sites, suggesting that scarring may obscure the identification of PCs on HRCM. However, after histopathologic review of the FNs, no significant fibrosis was present. Hence, the most plausible explanation for FNs seems to be sampling bias given that PCs are hyporeflective on RCM and can be easily missed when sparse.

To overcome sampling bias, we used an innovative approach in patients 4 and 5 that combined adhesive paper rings (Figure, G) and video mosaics (Figure, H). A common challenge with HRCM is locating on the skin the findings identified on the screen. This challenge is especially relevant in EMPD because PCs are distributed multifocally over a broad and curved area. Recently, Marino and colleagues[12] used adhesive paper rings to locate the boundaries of a given lesion during HRCM. After the publication of that study, we began using adhesive paper rings also to delineate the margins of large lesions and to facilitate HRCM navigation. In patients 4 and 5, we placed adhesive paper rings at areas of clinical interest, and we obtained image stacks and videos of the areas within the paper rings. The videos were later converted into video mosaics and then reviewed to identify PCs.

Video mosaicking allows the visualization of large areas (centimeters), making the identification of focal features easier than when evaluating the native HRCM small field of view (1 × 1 mm to 0.75 × 0.75 mm depending on the device generation). Therefore, video mosaicking combined with using adhesive paper rings may be valuable for identifying and locating scattered PCs. Interestingly, no FNs occurred

when this approach was used. In addition, newer video mosaicking algorithms, including mosaic composition in real time and integration of the method into the RCM software, are needed to achieve diagnostic assessment at the bedside.

Limitations

Although our results show good diagnostic accuracy to identify recurrent EMPD, we acknowledge that our sample is small, we had no control group, and we only tested the paper ring and video mosaicking approach in 2 patients. Thus, more studies are needed to assess the effect of HRCM and video mosaicking on detection of recurrent disease and therefore reduction of sampling bias.

Conclusions

Handheld RCM can be a useful auxiliary tool for diagnosing EMPD recurrences but may fail to identify foci of scattered PCs. Reassuringly, we have not had false-positive cases, suggesting that HRCM can be used as an alternative to biopsy in EMPD cases with positive confocal findings and thus potentially reduce the need for confirmatory skin biopsies.

ARTICLE INFORMATION

Accepted for Publication: February 18, 2017.

Published Online: May 10, 2017. doi:10.1001/jamadermatol.2017.0619

Author Contributions: Drs Yélamos and Jain had full access to all the data in the study and take responsibility for the integrity of the data and the accuracy of the data analysis.
Study concept and design: Yélamos, Cordova, Marchetti, Myskowski, Rajadhyaksha, Rossi, Jain.
Acquisition, analysis, or interpretation of data: Yélamos, Hibler, Cordova, Hollmann, Kose, Myskowski, Pulitzer, Rossi, Jain.
Drafting of the manuscript: Yélamos, Hibler, Marchetti, Rossi.
Critical revision of the manuscript for important intellectual content: Cordova, Hollmann, Kose, Marchetti, Myskowski, Pulitzer, Rajadhyaksha, Rossi, Jain.
Statistical analysis: Yélamos, Hibler.
Obtained funding: Rajadhyaksha.
Administrative, technical, or material support: Cordova, Kose, Myskowski, Pulitzer, Rajadhyaksha, Rossi.
Study supervision: Marchetti, Pulitzer, Rajadhyaksha, Rossi, Jain.

Conflict of Interest Disclosures: Dr Rajadhyaksha reported being a former employee of and equity owner in Caliber Imaging and Diagnostics (formerly Lucid Inc), the company that manufactures and sells the Vivascope confocal microscope. The Vivascope is the commercial version of an original laboratory prototype that Dr Rajadhyaksha had developed at Massachusetts General Hospital, Harvard Medical School. No other disclosures were reported.

Funding/Support: This research was funded in part by grant R01CA199673 from the National Institutes of Health/National Cancer Institute (NIH/NCI), support grant P30 CA008748 from the NIH/NCI Cancer Center, and the Beca Excelencia Fundación Piel Sana (Dr Yélamos).

Role of the Funder/Sponsor: The funding sources had no role in the design and conduct of the study; collection, management, analysis, and interpretation of the data; preparation, review, or approval of the manuscript; and decision to submit the manuscript for publication.

REFERENCES

1. Lopes Filho LL, Lopes IM, Lopes LR, Enokihara MM, Michalany AO, Matsunaga N. Mammary and extramammary Paget's disease. *An Bras Dermatol*. 2015;90(2):225-231.

2. Kim BJ, Park SK, Chang H. The effectiveness of mapping biopsy in patients with extramammary Paget's disease. *Arch Plast Surg*. 2014;41(6):753-758.

3. Rajadhyaksha M, González S, Zavislan JM, Anderson RR, Webb RH. In vivo confocal scanning laser microscopy of human skin, II: advances in instrumentation and comparison with histology. *J Invest Dermatol*. 1999;113(3):293-303.

4. Terrier JE, Tiffet O, Raynaud N, Cinotti E. In vivo reflectance confocal microscopy combined with the "spaghetti" technique: a new procedure for defining surgical margins of genital Paget disease. *Dermatol Surg*. 2015;41(7):862-864.

5. Longo C, Fantini F, Cesinaro AM, Bassoli S, Seidenari S, Pellacani G. Pigmented mammary Paget disease: dermoscopic, in vivo reflectance-mode confocal microscopic, and immunohistochemical study of a case. *Arch Dermatol*. 2007;143(6):752-754.

6. Guitera P, Scolyer RA, Gill M, et al. Reflectance confocal microscopy for diagnosis of mammary and extramammary Paget's disease. *J Eur Acad Dermatol Venereol*. 2013;27(1):e24-e29.

7. Debarbieux S, Dalle S, Depaepe L, Jeanniot PY, Poulalhon N, Thomas L. Extramammary Paget's disease of the scalp: examination by in vivo and ex vivo reflectance confocal microscopy. *Skin Res Technol*. 2014;20(1):124-126.

8. Pan ZY, Liang J, Zhang QA, Lin JR, Zheng ZZ. In vivo reflectance confocal microscopy of extramammary Paget disease: diagnostic evaluation and surgical management. *J Am Acad Dermatol*. 2012;66(2):e47-e53.

9. Cinotti E, Perrot JL, Labeille B, Cambazard F. The contribution of reflectance confocal microscopy in the diagnosis of Paget's disease of the breast [in French]. *Ann Dermatol Venereol*. 2013;140(12):829-832.

10. Suppa M, Marneffe A, Miyamoto M, Rorive S, Boone M, Del Marmol V; groupe imagerie cutanée non invasive de la Société française de dermatologie. Contribution of reflectance confocal microscopy in the diagnosis of extra-mammary Paget's disease [in French]. *Ann Dermatol Venereol*. 2015;142(1):70-73.

11. Alarcon I, Carrera C, Alos L, Palou J, Malvehy J, Puig S. In vivo reflectance confocal microscopy to monitor the response of lentigo maligna to imiquimod. *J Am Acad Dermatol*. 2014;71(1):49-55.

12. Marino ML, Rogers T, Sierra Gil H, Rajadhyaksha M, Cordova MA, Marghoob AA. Improving lesion localization when imaging with handheld reflectance confocal microscope. *Skin Res Technol*. 2016;22(4):519-520.

13. Kose K, Cordova M, Duffy M, Flores ES, Brooks DH, Rajadhyaksha M. Video-mosaicing of reflectance confocal images for examination of extended areas of skin in vivo. *Br J Dermatol*. 2014;171(5):1239-1241.

Publication 4: Reflectance confocal microscopy-guided laser ablation of basal cell carcinomas: initial clinical experience

Heidy Sierra, Oriol Yélamos, Miguel Cordova, Chih-Shan Jason Chen, and Milind Rajadhyaksha

J Biomed Opt. 2017 Aug;22(8):1-13. doi: 10.1117/1.JBO.22.8.085005.

SUMMARY:

Background: Laser ablation offers a procedure for precise, fast, and minimally invasive removal of superficial and early nodular (low risk) basal cell carcinomas (BCCs). However, the lack of histopathological confirmation has been a limitation toward widespread use in the clinic. A reflectance confocal microscopy (RCM) imaging-guided approach offers cellular-level histopathology-like feedback directly on the patient, which may then guide and help improve the efficacy of the ablation procedure. In addition, the use of videomosaics obtained from the videos acquired directly inside the laser wound may expand the field of view and help identify residual tumor.

Aim: To determine the feasibility, image quality and effectivity of RCM-guided laser ablation of low-risk BCC.

Material and Methods: Following an ex vivo benchtop, we performed an initial study on 44 BCCs on 21 patients in vivo, using a pulsed erbium:ytterbium aluminum garnet laser and a contrast agent (aluminum chloride). In 10 lesions on six patients, the RCM imaging guided detection of either presence of residual tumor or complete clearance was immediately confirmed with histopathology. Additionally, 34 BCCs on 15 patients were treated with RCM imaging-guided laser ablation, with immediate confirmation for clearance of tumor (no histopathology), followed by longer-term monitoring, currently in progress, with follow-up imaging (again, no histopathology) at 3, 6, and 18 months.

Results: We observed BCC clearance in 19 cases of 22 cases, with follow-ups ranging from 6 to 21 months. An additional 12 cases with 1 to 3 months of follow-ups has shown clearance of tumor but a longer follow-up time is required to establish conclusive results.

Conclusions: Thus far, the imaging resolution obtained with handheld RCM and videomosaicking appears to be sufficient and consistent for monitoring efficacy of ablation in the wound, both immediately post-ablation and subsequently during recovery. In addition, laser treatment seems to be a good alternative method to treat low-risk BCC.

Journal of Biomedical Optics

BiomedicalOptics.SPIEDigitalLibrary.org

Reflectance confocal microscopy-guided laser ablation of basal cell carcinomas: initial clinical experience

Heidy Sierra
Oriol Yélamos
Miguel Cordova
Chih-Shan Jason Chen
Milind Rajadhyaksha

SPIE.

Heidy Sierra, Oriol Yélamos, Miguel Cordova, Chih-Shan Jason Chen, Milind Rajadhyaksha, "Reflectance confocal microscopy-guided laser ablation of basal cell carcinomas: initial clinical experience," *J. Biomed. Opt.* **22**(8), 085005 (2017), doi: 10.1117/1.JBO.22.8.085005.

Journal of Biomedical Optics 22(8), 085005 (August 2017)

Reflectance confocal microscopy-guided laser ablation of basal cell carcinomas: initial clinical experience

Heidy Sierra,[a,*,†] **Oriol Yélamos,**[a,b] **Miguel Cordova,**[a] **Chih-Shan Jason Chen,**[a,‡] **and Milind Rajadhyaksha**[a,‡]
[a]Memorial Sloan Kettering Cancer Center, Dermatology Service, New York, New York, United States
[b]Universitat de Barcelona, Hospital Clínic, Dermatology Department, Barcelona, Spain

Abstract. Laser ablation offers a procedure for precise, fast, and minimally invasive removal of superficial and early nodular basal cell carcinomas (BCCs). However, the lack of histopathological confirmation has been a limitation toward widespread use in the clinic. A reflectance confocal microscopy (RCM) imaging-guided approach offers cellular-level histopathology-like feedback directly on the patient, which may then guide and help improve the efficacy of the ablation procedure. Following an *ex vivo* benchtop study (reported in our earlier papers), we performed an initial study on 44 BCCs on 21 patients *in vivo*, using a pulsed erbium:ytterbium aluminum garnet laser and a contrast agent (aluminum chloride). In 10 lesions on six patients, the RCM imaging-guided detection of either presence of residual tumor or complete clearance was immediately confirmed with histopathology. Additionally, 34 BCCs on 15 patients were treated with RCM imaging-guided laser ablation, with immediate confirmation for clearance of tumor (no histopathology), followed by longer-term monitoring, currently in progress, with follow-up imaging (again, no histopathology) at 3, 6, and 18 months. Thus far, the imaging resolution appears to be sufficient and consistent for monitoring efficacy of ablation in the wound, both immediately postablation and subsequently during recovery. The efficacy results appear to be promising, with observed clearance in 19 cases of 22 cases with follow-ups ranging from 6 to 21 months. An additional 12 cases with 1 to 3 months of follow-ups has shown clearance of tumor but a longer follow-up time is required to establish conclusive results. Further instrumentation development will be necessary to cover larger areas with a more automatically controlled instrument for more uniform, faster, and deeper imaging of margins. [DOI: 10.1117/1.JBO.22.8.085005]

Keywords: image-guided therapy; laser ablation; confocal microscopy; skin cancer; basal cell carcinoma.

Paper 170228PR received Apr. 11, 2017; accepted for publication Jul. 26, 2017; published online Aug. 23, 2017.

1 Introduction

Basal cell carcinoma (BCC) is one of the most common types of cancer prevalent around the world.[1,2] BCCs appear mostly on the face and head-and-neck areas. Mohs surgery is one of the standard procedures to precisely remove BCCs, while minimizing damage to the surrounding normal tissue.[3] Mohs surgery is guided by the preparation and examination of histopathology, performed in parallel during surgery, which makes the process highly effective with high cure rates, but labor intensive, time consuming, and high cost.

Nearly 600,000 superficial and early nodular types of BCCs are currently treated in the USA with Mohs surgery every year, accounting for an estimated 30% to 40% of cases. Because these are superficial (within ~200-μm depth), low-risk, nonaggressive, nonmetastatic, slow-growing, and nonfatal cancers, they are being increasingly treated with alternative less invasive, with some being potentially lower cost, treatments, such as curettage and electrodessication, topical drug therapy, photodynamic therapy, radiotherapy, and laser therapy.[2,4] Laser therapies, in the form of ablation, offer relatively quick, highly localized, and precise removal of superficial and early nodular BCCs. Laser therapy with carbon dioxide (CO_2), pulsed dye, erbium:yttrium aluminum garnet (Er:YAG), and neodymium: yttrium aluminum garnet (Nd:YAG) has been explored for treatment of BCCs.[5–18]

However, laser therapy is yet to become a widely used treatment because the skin is either vaporized or coagulated, and there is no tissue available for immediate histopathological confirmation of clearance of tumor. Consequently, the resulting efficacy and cure rate have been variable, and thus a major barrier against further advances and more widespread use.[10] However, with new advances in high-resolution optical and ultrasound imaging technology, image-guided laser therapy seems to be a possible logical solution to address these obstacles. Instead of histopathology, imaging may be performed directly on patients, to confirm clearance and monitor long-term efficacy. Initial clinical studies appear to be promising.[17,18]

In a previous benchtop study on skin tissue *ex vivo*, we demonstrated that high-resolution nuclear-level reflectance confocal microscopy (RCM) imaging can detect the presence of residual tumor or clearance in postablated skin tissue.[19,20] Ablation was performed using an Er:YAG laser (2900 nm) with a pulse duration of 250 μs. The depth of ablation was characterized as a function of fluence (range 6.3 to 25.0 J/cm^2) and number of passes (range 1 to 6, one pass was equal to four pulses). The results showed that a single treatment of 1 to 6 passes, each

*Address all correspondence to: Heidy Sierra, E-mail: heidy.sierra1@upr.edu

†Current address: University of Puerto Rico Mayaguez, Department of Computer Science and Engineering, Mayaguez, Puerto Rico, United States.

‡The authors contributed equally to this work.

with a fluence of 25 J/cm^2 (i.e., maximum total fluence of 150 J/cm^2) allows removal of BCCs, with very minimal thermal coagulation on the wound surface and the surrounding intact (untreated) tissue. Consequently, RCM imaging, with a topically applied contrast agent to enhance nuclear contrast, can be then used to detect the presence or absence of tumor postablation. Results also showed that, by introducing ~2 s of waiting time after six passes to allow for tissue cooling, further treatment with more passes could be performed, and thermal coagulation can be well controlled to allow for high-quality imaging postablation.

Following the benchtop study, we proceeded to initial testing in two patients,[18] as the first baby step in the surgical setting, toward a subsequent larger study. The testing showed the feasibility of RCM imaging to provide immediate histopathology-like feedback for detection of either residual BCCs or clearance directly on the patient after laser ablation. Aluminum chloride (routinely used for hemostasis after skin biopsies or excisions) was used as a contrast agent, topically applied on the surface of the postablated wound to enhance contrast of nuclear patterns and tumor morphology. (In an early imaging study, aluminum chloride was serendipitously discovered to brighten nuclei and behave as a contrast agent for BCCs.[21]) Confirmation of the imaging findings with histopathology showed RCM imaging quality and performance similar to that observed in the earlier *ex vivo* studies.

Building upon our *ex vivo* study and initial *in vivo* testing, we then developed an RCM imaging-guided laser ablation protocol for larger-scale implementation and testing. In this paper, we present a detailed description of the protocol and our initial experience in the implementation on patients. The protocol has been tested in 44 lesions on 21 patients, each diagnosed as nodular and/or superficial BCC. The protocol consists of preablation detection of lateral and deep margins of BCCs, which then guides the choice of ablation parameters (fluence, number of pulses), followed by laser ablation, and, finally, imaging of the peripheral epidermis and the deeper dermis in the wound bed to provide feedback on the presence of residual tumor or clearance. In the initial 10 lesions, for which diagnostic biopsy was available, the postablation RCM findings were immediately confirmed with a thin excision and histopathology. The subsequent 34 lesions, which were clinically diagnosed [i.e., with only clinical (visual) examination and dermoscopy but without diagnostic biopsy], were treated with imaging-guided laser ablation, followed by immediate confirmation of clearance of tumor (no histopathology), and further longer-term monitoring, currently in progress, with follow-up imaging (again, no histopathology). We present the imaging performance and results for both the initial 10 lesions and the subsequent 34 lesions, and discuss the current limitations of this approach and possible solutions for further advances.

2 Materials and Methods

2.1 *Laser Ablation Instrumentation*

A pulsed erbium-doped yttrium aluminum garnet (Er:YAG, 2.94 μm) laser (Sciton Profile, Palo Alto, California), equipped with a pulse duration of ~250 μs (fixed), spot diameter of 4 mm, and fluence up to 25.0 J/cm^2 was used. More details can be found in our earlier papers.[19,20] One "pass" of ~161 ms duration consists of a set of four individual pulses, each separated by 40 ms. [Note that shorter pulse durations, relative to the thermal relaxation time in skin, are usually preferable, such as femtosecond or picosecond lasers, which would result in highly selective "pure" ablation of thin cellular-level layers of tissue without any underlying thermal coagulation. Our particular choice of laser and pulse duration was mainly due to the routine use of Er:YAG lasers in dermatologic clinical settings, and thus the easy availability and access to the laser used by our collaborating Mohs surgeon (coauthor CSJC). For ablating superficial or nodular BCCs of ~150- to 200-μm depth, very high selectivity is not necessary, and longer pulse durations on the order of 10 to 100 microseconds are clinically sufficient.] In this study, the fluence was fixed at 25.0 J/cm^2 for a single pass and, when necessary, a higher fluence was obtained by performing several passes, to produce a depth of ablation that reached the tumor's deepest margins. The selection of the number of passes was based on an *ex vivo* study in human skin specimens, previously conducted, to characterize the depth of ablation versus number of passes. Increasing the number of passes to produce higher fluence values also increases the thermal residual damage to surrounding intact tissue postablation.[22] As reported in our previous benchtop studies, the thermal damage depth for these laser parameters is 5 to 20 μm, confirming the literature.[22] Our study provided a set of parameters (number of passes at fixed fluence) to ablate BCCs while controlling thermal coagulation in the underlying wound and surrounding intact skin, to subsequently allow the uptake of contrast agent and enhance the appearance of nuclear patterns and tumor morphology for the detection of presence (or absence) of tumor postablation with RCM imaging. Thus, the uptake of aluminum chloride (seen in this *in vivo* study as well as in the previous benchtop studies), along with the wound healing and recovery process, indicates that healthy tissue remains undamaged. Further details may be gleaned from our earlier papers.[19,20]

2.2 *Patients and Basal Cell Carcinomas Lesions*

Twenty-one patients, with forty-four lesions, each with a diagnosis of superficial and/or nodular BCC, participated in this study. Prior to enrollment, patients gave consent to a research protocol, approved by Memorial Sloan Kettering Cancer Center's (MSKCC's) Institutional Review Board, for imaging and ablation. An initial group of six patients, with 10 BCCs that were confirmed with diagnostic biopsy, consented for RCM imaging-guided laser ablation. On these patients, immediately postablation, a thin excision was performed and the resulting frozen histology used for confirmation. A second set of 15 patients, on whom 34 superficial and early nodular BCCs had been clinically diagnosed [i.e., with only clinical (visual) examination and dermoscopy but without diagnostic biopsy], was treated with RCM imaging-guided laser ablation only (i.e., with no subsequent excision or histopathology), and all of these lesions are currently being followed up and noninvasively monitored with imaging.

2.3 *Reflectance Confocal Microscopy Imaging*

Imaging on patients was performed with two reflectance confocal microscopes [Vivascope 1500 and Vivascope 3000, Caliber Imaging and Diagnostics (formerly, Lucid Inc.), Rochester, New York]. In both, the illumination is with the near-infrared wavelength of 830 nm, and imaging was done with a gel-immersion objective lens of magnification 30× and 0.9 numerical aperture, optical sectioning of ~3 μm and lateral resolution of

~1 μm. High-resolution RCM images were collected to a depth of ~150 to 200 μm.

2.3.1 *Preablation reflectance confocal microscopy imaging*

Preablation imaging of intact skin was performed with a larger version of the microscope (VivaScope 1500) through a tissue contact ring and polycarbonate window, which sits directly in contact with the skin to stabilize the area to be imaged. Oil is applied to the skin to match the refractive indices of both the window and the topmost stratum corneum layer of skin. The microscope allows the acquisition of single images and stacks of images with a field of view of 500 μm × 500 μm. By the use of an automated stepper that rasters the objective lens in two dimensions (2-D), a 2-D matrix of contiguous images can be captured and processed to create mosaics to increase the field of view to up to 8 mm × 8 mm. The mosaics of images can be captured and generated in ~2 min. Further details are below and more may be also gleaned from our earlier papers.[23]

2.3.2 *Postablation reflectance confocal microscopy imaging*

The surface of the wound was imaged using a smaller handheld version of the microscope (Vivascope 3000), with a small and integrated lens-to-skin tissue contact cap and polycarbonate window. While gently pressing the contact cap and window against the tissue and manually moving the microscope over the wound surface, images and/or videos are captured while covering a larger field of view. The videos are processed into video mosaics to show larger areas of tissue, in long strips of up to ~1 mm × ~30 mm, to show the peripheral epidermal margin and deeper dermal margins (base of the wound).

Further details on the video mosaicking approach are below and more may also be gleaned from an earlier paper.[24]

2.4 *Image-Guided Laser Ablation Protocol*

Figures 1–3 show the complete perioperative imaging-guided protocol, with histopathology-like feedback obtained

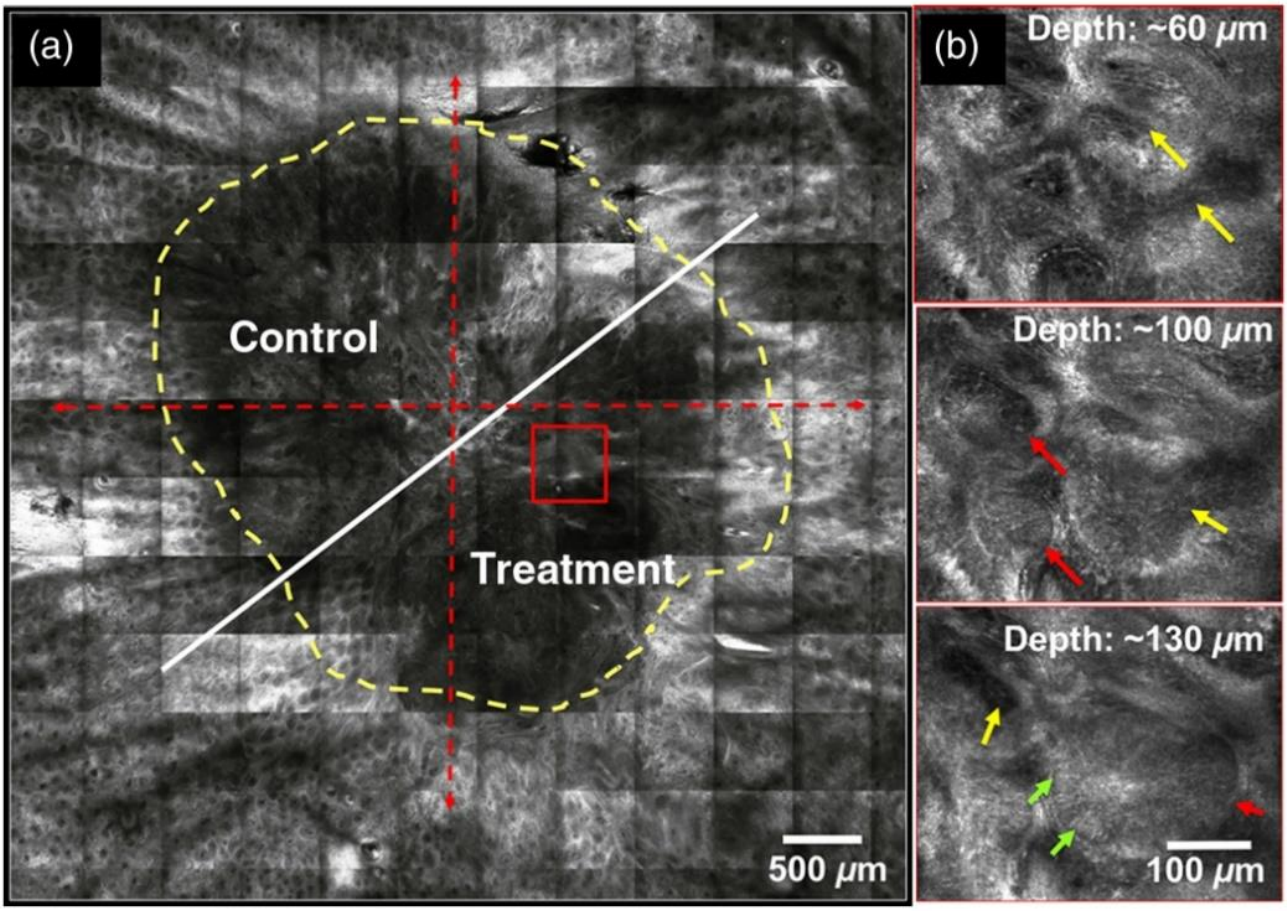

Fig. 1 Detection and demarcation of preablation margins with RCM imaging. (a) Example of an 8 mm × 8 mm mosaic captured at the dermal–epidermal junction. The red dashed lines from 12 to 6 and 3 to 9 o'clock indicate the quadrants utilized to keep localized record of the tumor location and estimated depth. The quadrants are defined in clockwise orientation. The tumor margins are delineated with the dashed yellow boundary, and the corresponding selected regions for control and ablation are shown (this is only for those 10 cases in which a thin excision was performed immediately postablation for histology correlation). (b) Images at different depths from a stack, captured at the location of the red square in (a), contain features of BCC used for estimation of tumor depth: at ~60 μm (epidermal layer) enlarged blood vessels (yellow arrows); at 100 μm enlarged blood vessels (yellow arrows) and tumor islands (red arrows); and at ~160 μm enlarged blood vessels (yellow arrow), tumor island (red arrow), and cell palisading (green arrow) surrounding the tumor island.

directly on the patient before, during, and after the ablation treatment.

2.4.1 *Lateral and deep tumor margins imaging preablation*

Figure 1 shows the protocol. The preablation imaging was guided by the surgeon's initial visual demarcation of the clinical margins of the lesion using surgical pen ink. Three RCM mosaics (8 mm × 8 mm) centered within the lesion were collected with a Vivascope 1500, one above the basal layer in the epidermis, one including the basal layer at the dermal–epidermal junction, and one below in the underlying papillary dermis, to estimate the general location, lateral margins, and depth of tumor. The more exact location of the tumor margins was subsequently recorded by further demarcating the lesion area (i.e., to-be-imaged area) in four quadrants, using 12, 6, 9, and 3 o'clock as reference points denoted by surgical marks. To facilitate RCM navigation, we placed adhesive paper rings outside the wound margins (paper fibers are visible with high contrast in RCM).[25] Stacks of images, with 5-μm axial separation, were collected in each quadrant where tumor was detected to more exactly estimate the corresponding depth. Half of the lesion was selected for ablation and the remaining intact half served as a control. The two halves were separated by a line ink-marked on the skin of the patient by the surgeon (Fig. 1). Each quadrant of the imaged area was ablated with a number of passes to achieve a depth of ablation (using our Table 1) corresponding to the estimated depth of tumor by RCM. When the lesion was larger than 8 mm × 8 mm, the surrounding tumor served as a control as well.

In Fig. 1(a), an example of a mosaic collected at the epidermal layer (at ~60-μm depth from the top layer), in which presence of BCC tumors (dark silhouette delineated by the dashed yellow line) was detected at the center of the mosaic. In Fig. 1(b), three images from a stack of 30 images collected at the location of the red square in Fig. 1(a) at ~60, 100, and ~160 μm show features of BCCs, such as enlarged blood vessels (yellow arrows), tumor islands (red arrows), and palisading (green arrow) around the tumor island. A detailed description of the characteristic features of BCCs under RCM imaging in intact tissue can be found in our previous work.[23]

2.4.2 *Selection of number of passes and depth of ablation*

The estimated depth of tumor provided by the RCM stacks was used to select the number of passes. This was based on our previous study results in human skin specimens[19,20] and the initial testing on patients.[17]

2.4.3 *Topical application of contrast agent postablation*

Figure 2(a) show the geometry of the wound. Postablation, the surface of the shallow wound was swabbed with 35% aluminum chloride solution for 30 s using sterile applicators, followed by filling the cavity with sterile gel. More details of the technique have been reported in our earlier papers.[17] Aluminum chloride was previously discovered to enhance nuclear contrast in RCM images[21] and its development for the intraoperative detection of residual BCCs in surgical wounds has been reported in previous studies.[21,26,27] Topical application for 30 s, with concentration of 35%, was found to be optimal.[26,27] Higher concentrations and/or longer application produces dehydration and necrosis in tissue, whereas lower concentrations and/or shorter times does not brighten nuclear morphology.

2.4.4 *Lateral and deep margins imaging postablation*

Figure 2 shows the protocol for imaging in the wound postablation. Imaging was at 8 frames/s while using a Vivascope 3000 to rapidly assess the area of ablation. Videos were acquired along the superficial epidermal and deep dermal margins starting at the 12 o'clock position. The 12 o'clock position was surgically marked on the patient's intact skin by the surgeon preablation. The wound was divided into quadrants, e.g., 12 to 3, 3 to 6, 6 to 9, and 9 to 12 to keep records of the exact location of the imaging findings. Stacks of images were captured at those suspicious areas where the potential presence of residual tumor was detected. The stack allows visualization of the suspicious features as a function of depth. After the stacks were captured, the microscope was switched back to video mode to continue imaging and capturing videos of the remaining margins.

2.4.5 *Video mosaics*

The captured videos were processed (i.e., sequence of video images stitched together) to generate video mosaics to display

Table 1 Depth of ablation versus number of passes for fluence of 25 J/cm^2. In this study, fluence was constant at 25 J/cm^2. The small differences between the *ex vivo* and *in vivo* measurements are explained in the text (Sec. 3.2).

	No. of passes 25 J/cm^2		
Depth of ablation	4 to 5 passes	6 to 7 passes	8 to 11 passes
Measured *in vivo* with histology	~80 to 122 μm complete epidermis	~130 to 160 μm papillary dermis	~170 to 200 μm partial reticular dermis
Number of lesions	2	3	5
Estimated *in vivo* with RCM	~90 to 136 μm complete epidermis	~130 to 160 μm papillary dermis and partial reticular dermis	~180 to 200 μm partial deeper reticular dermis
Number of lesions	9	15	10
Measured *ex vivo*	~85 to 120 μm papillary dermis to partial deeper reticular dermis	~150 to 170 μm partial reticular dermis	~170 to 220 μm partial deeper reticular dermis

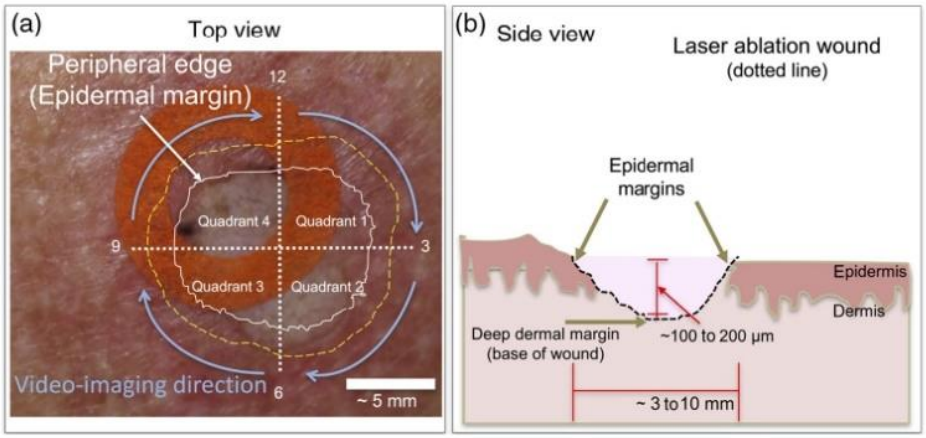

Fig. 2 Postlaser-ablated wound topography and RCM video-imaging approach. (a) The lines and arrows on the clinical photograph illustrate the approach of using a paper ring (orange ring) to isolate each quadrant of the wound for imaging and provide a more precise location of findings with respect to the clinical coordinates established by the surgeon. The wound edge (white boundary) is used as a reference for imaging along the epidermal margins, and imaging of the peripheral dermal margins below the edge (yellow dotted boundary) and at the center of the wound. The blue arrows illustrate that videos were acquired along the epidermal margin, starting from the 12 to 3, and proceeding from 3 to 6, 6 to 9, and 9 to 12 o'clock positions. (b) A cartoon of the side view of a postlaser-ablated wound showing the epidermal margins and deep dermal margins (base of wound).

a field of view 1-mm wide with the length defined by the length of the video that covered the entire epidermal margin. For small wounds (3 to 5 mm in diameter), videos were acquired in individual quadrants starting at the 12 o'clock position in a clockwise direction [Fig. 2(b)]. A single video was collected of the peripheral epidermal margin of each quadrant (from 12 to 3, 3 to 6, 6 to 9, and 9 to 12 o'clock), displaying intact surrounding skin and exposed epidermis. The corresponding video mosaics for each quadrant have dimensions of ~1 mm × 7.5 mm. For small wounds, the imaging of the periphery was followed by a video captured at the central portion of the wound (base of wound). For larger wounds (>5 mm in diameter), additional videos of the deep dermal margins were collected in the center of each quadrant. The videos were collected in clockwise circular paths. Some of the videos contained spatial overlap due to the manually controlled video capture approach that led to variable lengths of the video mosaics. More details of the software and implementation can be found in other papers.[24,26]

Confirmation of clearance of BCCs on the second set of 34 lesions was based on real-time examination of the videos as they were captured on patients. At present, processing videos and creating video mosaics requires ~3 to 5 min per quadrant (for a length of ~1 mm × ~7.5 mm). Since the length of the videos for deep dermal margins was variable due to the uncontrolled manual video capture approach, the processing time for video mosaics was 2 to 5 min. As such, video mosaics were not available in real time during imaging on patients and could not be used to determine clearance of margins during the laser ablation treatment. However, they were employed later on for further image analysis, to correlate imaging findings to histopathology results for the first 10 lesions, and to further confirm the original real-time (i.e., immediately postablation) findings on the remaining 34 lesions.

Figure 3 shows the comprehensive perioperative RCM imaging-guided laser ablation procedure, which mimics the procedure for frozen pathology-guided Mohs surgery. Preablation:

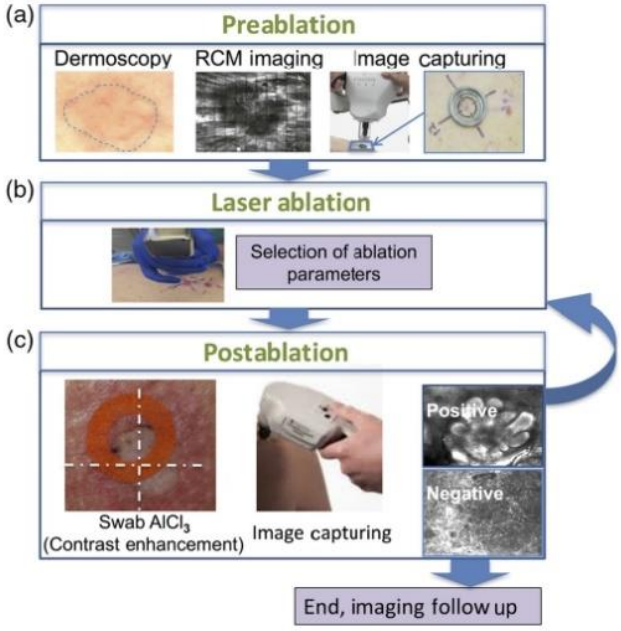

Fig. 3 Laser ablation guided with perioperative feedback from RCM imaging of BCC tumor morphology with cellular-level resolution. (a) Preablation: mosaics and stacks are acquired to estimate BCC margins and tumor depth preablation. The use of Vivascope 1500 with a tissue contact ring to acquire mosaics and stacks preablation (top row, two panels on the right). (b) Laser ablation: number of passes is selected based on the estimated depth of tumor to obtain the sufficient depth of ablation for complete removal of tumor. (c) Postablation: videos are acquired with a Vivascope 3000 to verify clearance of margins and stacks to review suspicious areas as a function of depth after ablation (bottom). Video mosaics are generated to visualize larger fields of view postablation. The ablation guided by RCM imaging protocol mimics the standard procedure of Mohs surgery guided by frozen pathology.

RCM mosaics and stacks are acquired to estimate BCC margins and tumor depth preablation; laser ablation: number of passes are selected based on the estimated depth of tumor to obtain the sufficient depth of ablation for complete removal of tumor; and postablation: videos are acquired with a 3000 Vivascope (handheld RCM) to verify clearance of margins and stacks to review suspicious areas as a function of depth after ablation (bottom). Video mosaics are generated to visualize larger fields of view postablation.

2.5 *Imaging-Guided Laser Ablation with Immediate Histology Confirmation*

Ten BCCs lesions were treated and the imaging results immediately confirmed with histology. An 8 mm × 8 mm area, centered within the lesion containing tumor, was selected for RCM imaging and ablation. The tumor in the surrounding area served as control when the lesion was greater in size. If the lesion was smaller than 8 mm × 8 mm, half of the lesion was selected for ablation with the remaining portion serving as control. RCM imaging-guided laser ablation protocol was executed and the postablation imaging detected the presence of residual tumor or complete clearance. Immediately afterward, our Mohs surgeon (coauthor CSJC) performed a thin excision and sent it to the laboratory for histology preparation to validate the imaging findings.

2.5.1 *Correlation to and validation against histopathology*

The excised tissue was embedded for preparation of hematoxylin and eosin (H&E)-stained sections. Vertical sections (oriented perpendicular to the tissue surface) were prepared to visualize the location of the residual tumor, if any (or, clearance, if none). The excised tissue was oriented so that the frozen sections would include both ablated and control regions. The presence and appearance of residual BCCs (or clearance) in H&E sections was analyzed under light microscopy and compared with postablation RCM findings.

2.5.2 *Depth of ablation*

Lesions treated with 4 to 5, 6 to 7, and 8 to 9 passes were chosen for performing depth of ablation measurements. A frozen section containing the center of the ablated area was selected. Two measurements were made from each section: one at the shallowest location (edge of postablated wound) and another at the deepest (center) of the ablated region relative to the adjacent nonablated skin, to provide a range for the depth of ablation values.

2.6 *Imaging-Guided Laser Ablation with Immediate Reflectance Confocal Microscopy Confirmation and Longer-Term Follow-Up (No Histopathology)*

Thirty four superficial and early nodular BCCs were treated with RCM imaging-guided laser ablation for complete tumor removal. All lesions were diagnosed clinically and dermoscopically, and also confirmed with BCC features under RCM before the ablation. The number of passes was guided by the imaging and imaging-based measurement of depth until clearance of tumor was confirmed with immediate imaging. No histology was performed. This method was limited to relatively small lesions of diameter <10 mm.

Follow-up imaging is being currently conducted to measure the accuracy of the imaging-guided approach to detect clearance of tumor postablation, and to monitor the longer-term efficacy of the ablation treatment and achieve follow-up periods of at least 12 months for all treated lesions. Video imaging and mosaicking of the peripheral epidermal and dermal margins and the deeper dermal margins at the center region (base of wound) of the treated lesions is being conducted at 1 to 3, 6, and 18 months after treatment.

2.7 *Assessment Depth of Ablation, Uptake of Contrast Agent, Reflectance Confocal Microscopy Images, Video-Mosaics*

Image stacks were collected (where presence of tumor was detected) to estimate tumor depth, which then allowed us to select the appropriate number of passes to provide the depth of ablation required for complete removal of the tumor.

The qualitative evaluation of postablation imaging was focused on the uptake of contrast agent and detectability of tumor and normal features as a function of depth of ablation and number of passes. Three clinicians (coauthors CSJC, MC, and OY) with experience in reading and analyzing confocal images of BCCs evaluated the quality of RCM images, stacks, videos, and video mosaics. The overall quality was qualitatively assessed as acceptable or not for resolution, contrast, and visualization of nuclear and morphological detail. The visualization of bright nuclear morphology in the exposed peripheral epidermal margin, dermal structures, such as collagen bundles, hair follicles, eccrine glands, and inflammatory cells in the deeper dermal margin (base of wound), as well as the presence or absence of tumor in each quadrant of the wound were analyzed.

3 Results

We determined that, overall, RCM imaging, with the topical use of aluminum chloride in Er:YAG laser-ablated wounds, is feasible. Nuclear labeling in epidermal margins was consistent and repeatable in all the imaged wounds, enhancing nuclear brightness that facilitated the detection of presence or absence of residual tumor after ablation.

The acquisition of videos with the handheld microscope (Vivascope 3000) is reasonably rapid, reasonably efficient, and allows imaging of the superficial epidermal and deep dermal margins of the shallow wound cavity. The acquisition of videos required ~5 min for wounds of 8 mm in diameter. Conversion of videos to video mosaics requires a bit more time; ~10 to 15 min a video that covers the complete peripheral margin. The video mosaics allow visualization of the surrounding tissue morphology and cellular structures, and detection of the presence or absence of tumor. What we observed in the video mosaics provided confirmation of the real-time observations in the videos when they were being captured in the clinic during treatment.

3.1 *Uptake of Contrast Agent in the Superficial Epidermal and Deep Dermal Margins of the Ablated Wounds*

In Fig. 4, a video mosaic generated from a video captured from the surface of a laser ablation wound is shown.

Figure 4(a) shows an example video-mosaic postablation, in this case with seven passes of 25 J/cm^2. In Fig. 4(b), details of the superficial margins are shown. From left to right, we see

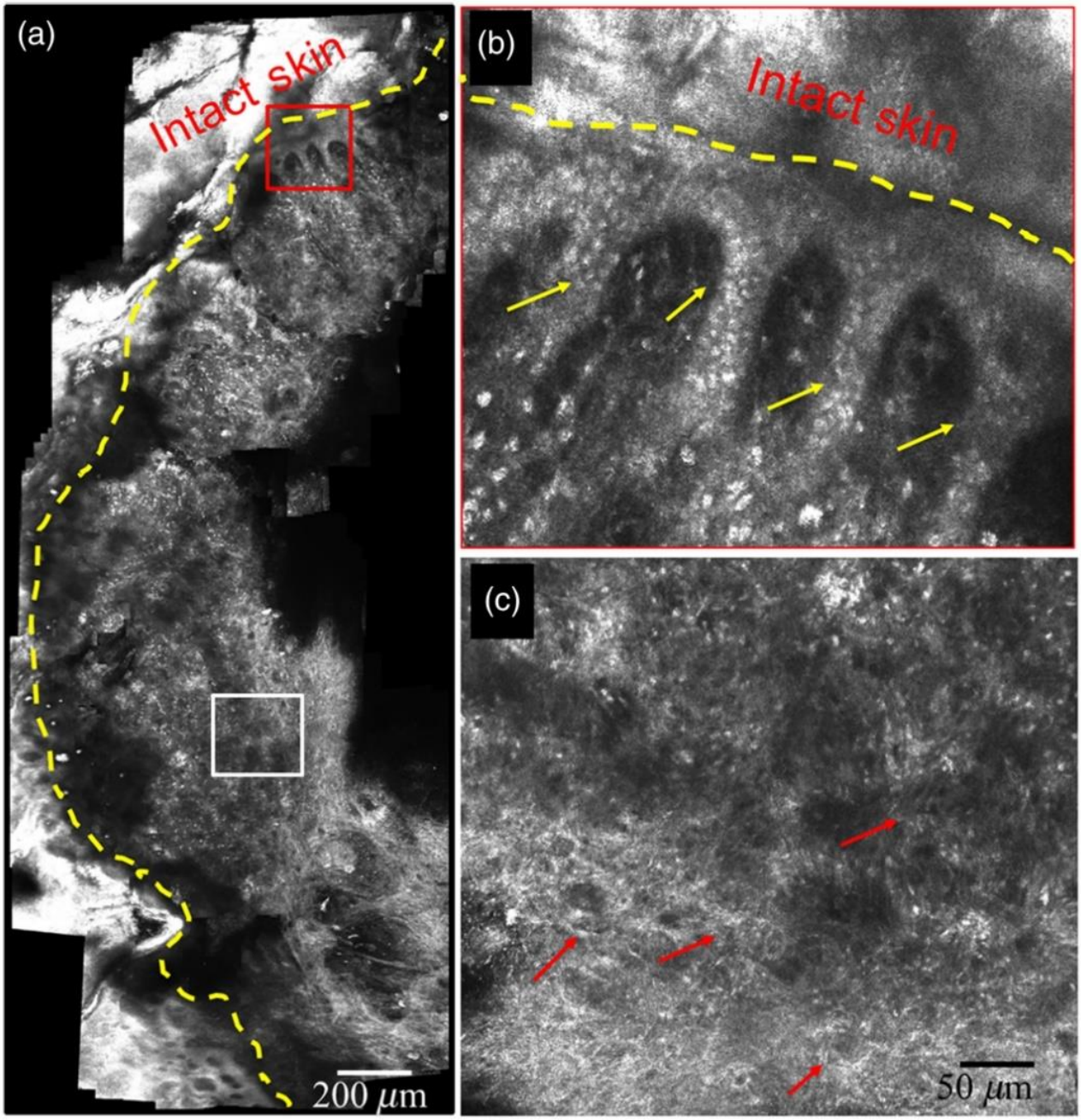

Fig. 4 Video mosaic of a postablation wound that was produced from an RCM imaging video. (a) Clearance of tumor is seen after the removal of ~130 μm of tissue with six passes of 25 J/cm^2; (b) enlarged view [of the red square in (a)] of the peripheral epidermal margin showing intact skin (left of yellow dotted line), bright nuclei of the basal cells, due to uptake of contrast agent (aluminum chloride), at the dermal–epidermal layer (shown with the yellow arrows); and (c) enlarge view of collagen fibers in the normal dermis at the deeper margin (inside of the white square, indicated by red arrows).

intact skin, bright nuclei of basal cells at the epidermal margin, suggesting the uptake of contrast agent (yellow arrows) and in Fig. 4(c), collagen fibers in normal dermis in the deeper dermal margin (red arrows).

Overall, aluminum chloride produced repeatable and consistent brightening of nuclear morphology and enhanced the contrast and detectability of residual BCC and normal structures after laser ablation with four to nine passes of 25 J/cm^2 fluence. However, improper (such as excess or no uniform) application or tissue heterogeneity was found to sometimes produce saturation artifacts. In three postablation imaging cases, we observed saturation due to the contrast agent, preventing the distinction of normal from abnormal cellular patterns. However, as seen in Fig. 5, the nuclei, cellular detail, and dermal morphology, such as inflammatory cells, hair follicles, collagen fibers, eccrine, and sebaceous glands, could be differentiated.

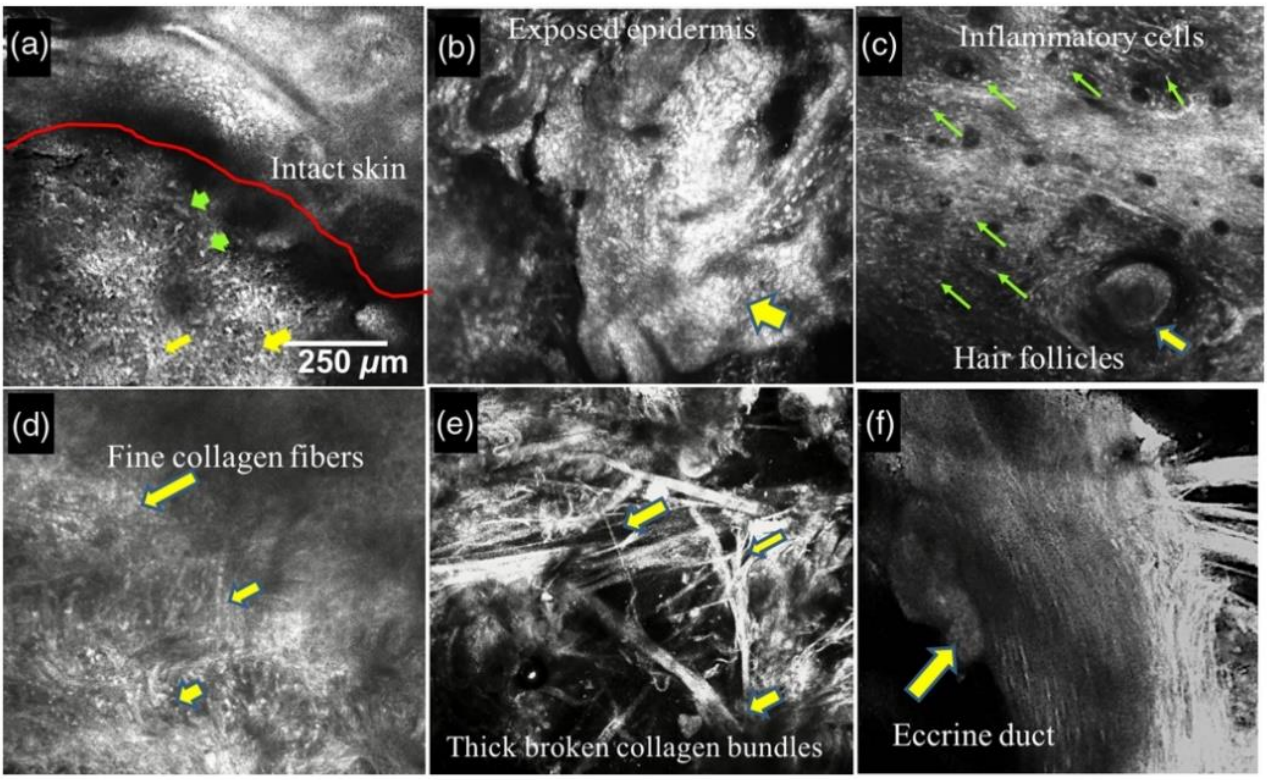

Fig. 5 RCM images showing morphologic structures that are typically seen in postablation wounds: (a) the wound edge (red line), with intact skin (top) showing the honeycomb pattern of dark nuclei and bright cytoplasm of the epidermal cells, at the wound edge bright nuclei (green arrows) of the exposed epidermis (enhanced by the aluminum chloride) and deeper in the dermis (lower side) collagen fibers at the dermis level (yellow arrows); (b) exposed of epidermis in the wound with cobblestone pattern of bright nuclei (yellow arrow); (c) inflammatory cells (green arrows), bright rounded small nuclei as seen in the deep dermal margin and hair follicles (lower yellow arrow); (d) bright fibrillar structures corresponding to fine collagen bundles; (e) thick collagen bundles seen in the deep dermis; and (f) eccrine glands (yellow arrow). Scale bar is 250 μm for all images.

Thirty one out of thirty four laser-ablated wounds could be visually graded as being of clinically acceptable imaging quality, in terms of resolution, contrast, and detectability of features. Those graded as being of unacceptable image and/or video quality were due to artifacts, such as bubbles (created by an excess amount of gel and/or smearing of the gel during imaging), which resulted in completely or partially blocking the field of view, and saturation of brightness and loss of contrast, which compromised the distinction of cellular structures. Other reasons for low-quality videos included loss of information (dark images) due to sudden changes in wound topography, variability in operator movement and speed causing motion blur, and variability of pressure against skin, all of which produced discontinuities in the videos during the imaging.

3.1.1 *Epidermal margin: at the peripheral edge (at the rim) of the ablated wound*

At the periphery of the wound, the direct exposure to topically applied aluminum chloride produced brightening of nuclei. In the intact skin surrounding the wound, nuclei appear dark, as is normally seen during imaging *in vivo*. (The intact stratum corneum prevents diffusion of aluminum chloride into the epidermis.) The difference between bright nuclear details in the exposed epidermis against the dark nuclear details in intact skin was easily distinguished and facilitated the detection of the edges of each wound during imaging. Figure 4(b) shows an example of the transition from intact to exposed epidermis (across the yellow dotted line from left to right).

3.1.2 *Peripheral dermal margin: the superficial papillary dermis (below the epidermal rim) of the ablated wound*

The dermal–epidermal junction appears as semicircle patterns of bright cells, contrasting with the darker background [yellow arrows in Fig. 4(b)]. At deeper levels in the wound, collagen bundles are also visualized [red arrows in Fig. 4(c)].

3.1.3 *Deep dermal margin: reticular dermis at the base of the ablated wound*

In the deeper layers, the base of the wound appeared more uniform with less cellular structures but containing bright fibrillary structures that corresponded to collagen fibers.

3.2 *Depth of Ablation*

The depth of ablation values range from 80 to 122 μm for 4 to 5 passes, 140 to 170 μm for 6 to 7 passes and 170 to 200 μm for 8 to 9 passes as a function of passes. In Table 1, these values are shown as a function of the number of passes. The depth of

Table 2 Imaging guided laser ablation with correlation to histology in 10 BCC lesions on six patients.

Lesion	BCC subtype	Estimate *d* depth	Number of passes	Residual BCC in assessed by RCM	Residual BCC on vertical histology postablation
1	Superficial and early nodular	175	9	Yes	Yes
2	Superficial and early nodular	180	8	Yes	Yes
3	Superficial intradermal component	210	9	Yes	Yes
4	Superficial and infiltrative nodular	180	9	Suspicious	Yes
5	Superficial and early nodular	150	8	No	No
6	Superficial	85	5	No	No
7	Superficial	88	5	No	No
8	Superficial	116	6	No	No
9	Superficial	125	7	No	No
10	Superficial and early nodular	135	7	No	No

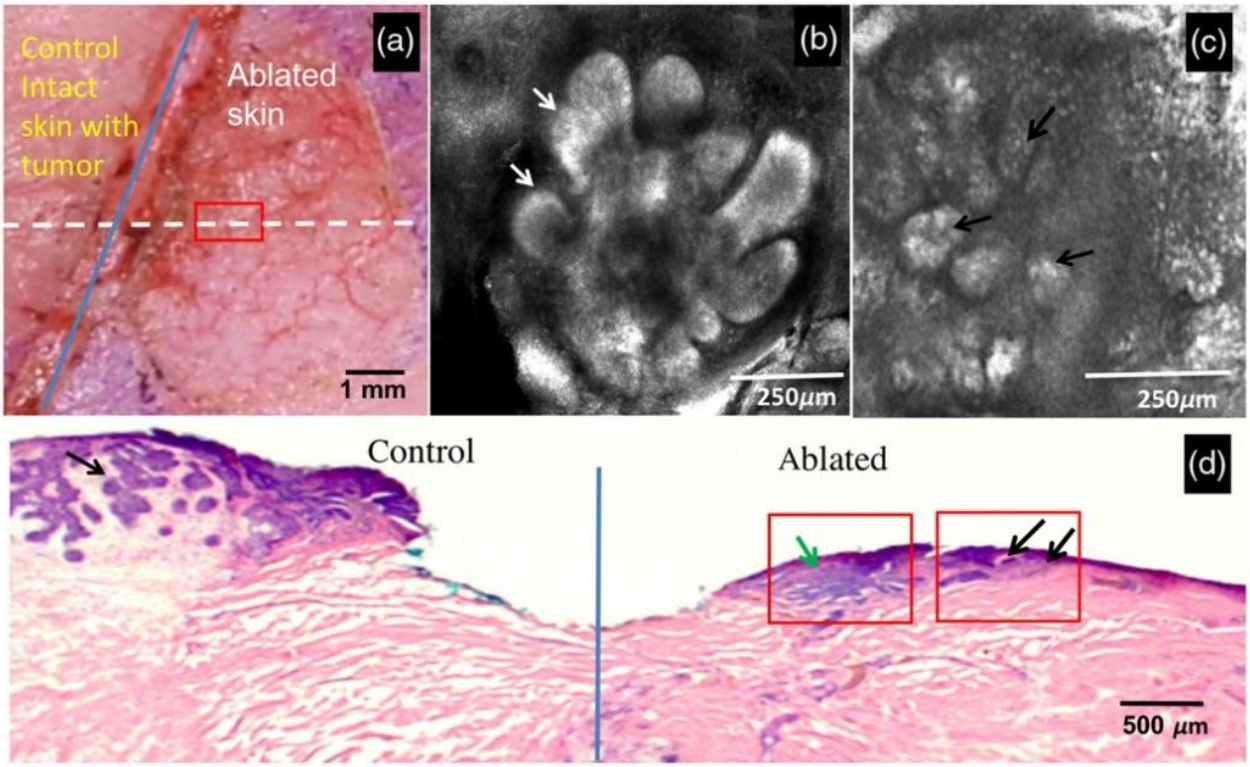

Fig. 6 *In vivo* detection of clearance of tumor or presence of residual tumor postablation, for ablation with four passes at fluence of 25 J/cm^2. (a) A clinical photograph image of the lesion postablation, with a solid blue demarcation line, showing the intact area of the lesion that contains tumor (left, nonablated control area) and the ablated area (right); (b)–(c) RCM image of residual nodular BCC (white and black arrows) at the peripheral epidermal margin, located inside the solid red square in (a); (d) H&E-stained histopathology that confirms RCM findings, showing intact tumor [black arrow at the left of the solid blue line, corresponding to the nonablated control area in (a)] and the surgical margin (made by Mohs surgeon JC and labeled with light blue ink before treatment); and residual tumor in the ablated area (right of the solid blue line inside the solid red squares) corresponds to that in (b) (white arrows) and (c) black arrows. The vertically sectioned histology allows visualization of the residual tumor (green and black arrows) at the edge of the crater-shaped wound validating the continuity of the tumor from the nonablated control area to the ablated region.

ablation measurements from our previous *ex vivo* study is also shown. In general, there is reasonable agreement between the measurements *in vivo* and those *ex vivo*. Variations between *in vivo* and *ex vivo* measurements are attributed to variations in skin sites and hydration conditions on patients, the presence of stratum corneum, and motion artifact due to the laser beam being slightly noncollimated and slightly diverging (the ablation was performed manually, such that slight variations in the distance between the laser scanner and the patient could result in slight variations in fluence). Nonetheless, the results indicate that the depth of ablation versus number of passes measurements *ex vivo* can be a reasonable initial "look up table" guide for choosing ablation parameters (fluence, number of passes) based on RCM-guided measurements of depth of tumor *in vivo*.

3.3 *Correlation to Histology in the First Six Patients (10 Basal Cell Carcinomas) for Presence or Absence of Tumor*

Table 2 shows the selected laser ablation parameters (number of passes for fluence of 25 J/cm^2) based on depth of tumor that was estimated by preablation RCM imaging. For all lesions, a thin excision was taken for histology postablation. In 3 out of 10 lesions, residual BCCs were detected by RCM postablation. For those cases, the residual tumors were not further removed with laser ablation, but were surgically excised, and then confirmed and correlated to histology. The correlation of imaging findings to histology resulted in three true positives, six true negatives, and one false positive. For the false positive case, the presence of saturation artifacts in the imaging

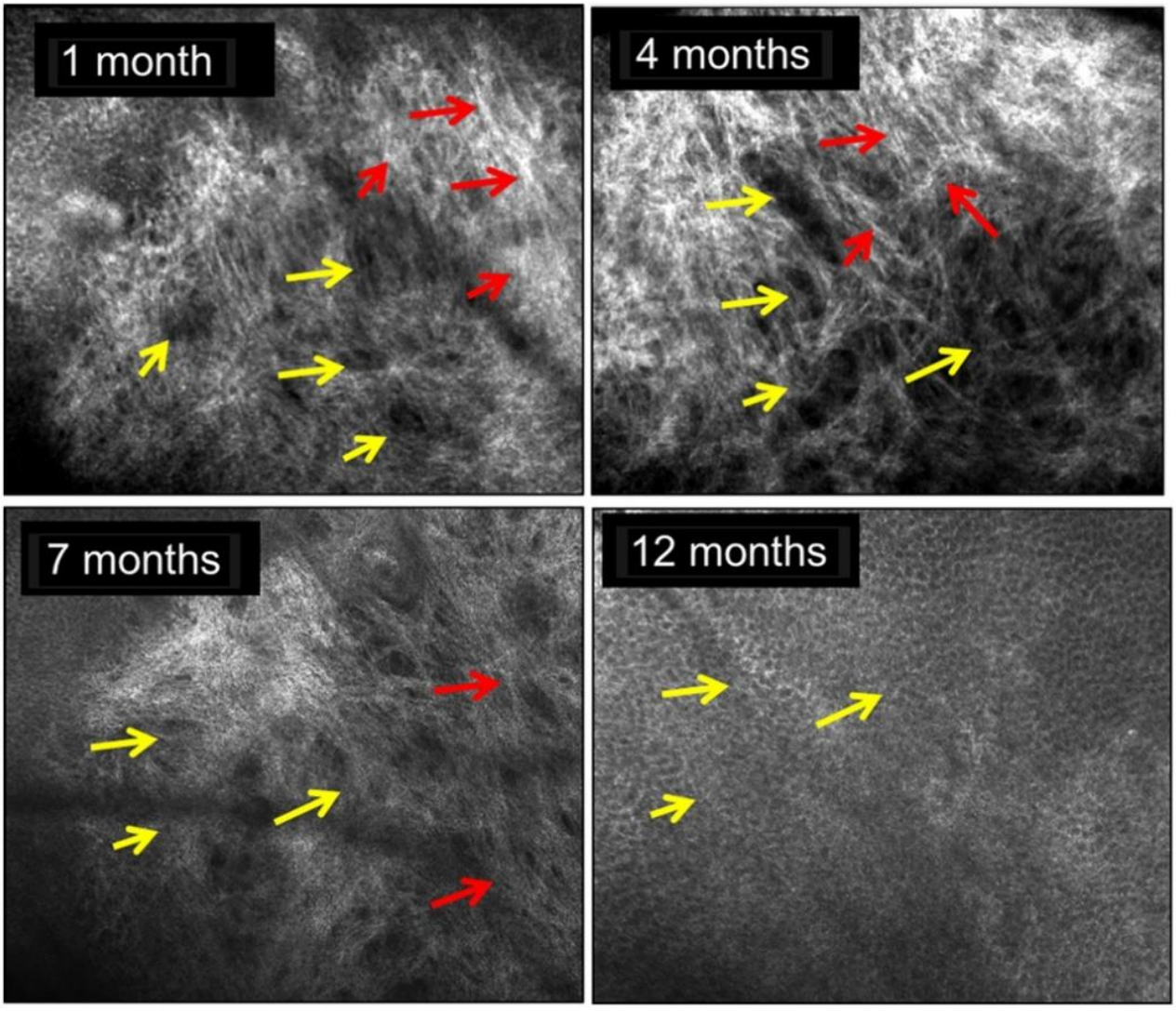

Fig. 7 Follow-up RCM imaging of lesion number 3 (superficial BCC) at 1, 4, 7, and 12 months after ablation. In this case, ablation was with six passes at fluence of 25 J/cm^2. Presence of enlarged blood vessels (yellow arrows) and amorphous collagen fibers (red arrows) at 1 and 4 months (top) were observed as part of the wound healing process. At 7 months, presence of enlarged blood vessel (yellow arrows) was still observed with thickened collagen fibers (red arrows). Normal skin patterns without features of BCC were seen at 12 months of postablation. Dark nuclei patterns (yellow arrows, lower right) similar to that observed in normal skin epidermis.

prevented our clinical imaging reading expert (coauthor MC) from reaching conclusive identification of the residual tumor.

An example of detection of residual tumor postablation with four passes of 25 J/cm^2 is shown in Fig. 6. In Fig. 6(a), a clinical photograph (routinely taken in the clinic) of the lesion is shown, along with a solid blue line on the surgical scoring (performed by the Mohs surgeon) demarcating the ablated region (right side) and intact region as control (left). Postablation imaging detected residual tumor at the peripheral margins. Figures 6(b)–6(c) show RCM images of typical features of BCCs indicating the presence of residual tumor, corresponding to the region enclosed in the solid red rectangle in Fig. 6(a). In (b), the high density nuclei enhanced in contrast by the aluminum chloride form a flower shaped structure that is typical of BCCs surrounded by a palisading pattern (white arrows). Figure 6(c) shows small island of tumor formed by bright nuclei (black arrows). In Fig. 6(d), an H&E section taken at the location of the white dashed line in Fig. 6(a) is shown. At the left side, the intact tumor (black arrow) intentionally left for control and the surgical margin (the crater with the edge labeled with light blue ink) serves as a reference to identify the ablated region. At the right side, the green and black arrows indicate details of the presence of residual BCCs at the epidermal margins confirming the findings shown in Figs. 6(b) and 6(c), respectively.

3.4 *Image-Guided Laser Ablation with Imaging Follow-Up on Remaining 15 Patients (34 Basal Cell Carcinomas)*

Initial follow-up results are available for 26 superficial, six superficial and early nodular, and two early nodular BCCs that were treated with only the RCM imaging-guided laser ablation approach (i.e., no histopathology). The number of passes varied from 5 to 11 as shown in Table 1 (row 2). After the first ablation treatment RCM imaging detected clearance of tumor in 27 lesions and residual tumor in seven lesions (two treated with eight passes and five treated with 5 to 6 passes) for which a second treatment (of 2 to 4 passes) was applied to attain clearance of tumor. The results for 31 lesions show that the uptake of $AlCl_3$ as contrast agent to label nuclei appears to be effective and consistent in wounds, with estimated depths of ablation from 80 to 200 μm. However, in three cases (ablated with 6 to 8 passes), saturation was observed in the images that challenged the detection of nuclear structures. All lesions are currently being followed up and the ablation treatment monitored with imaging at 1 to 3 (7 lesions), 6 to 7 (12 lesions), and 10 to 21 (15 lesions) months. The monthly time points tend to vary a bit due to patients' schedule for the follow-up appointments.

To date, 31 lesions have shown good cosmetic outcome and clearance of tumor under RCM images. Only two of the lesions (superficial and superficial/nodular types of BCCs at 7 and 17 months of follow-up, respectively) have shown recurrence after 6 months, respectively, where imaging showed features indicating presence of BCC. In one lesion (superficial type of BCC at 7 months follow-up), persisting large blood vessels and elongated nuclei patterns at the epidermis layer were observed as suspicious features of presence of BCC.

At early stages, most of the lesions were more raised and slightly erythematous. After 12 months, most of the followed lesions were the same color as surrounding skin or pink. Hypopigmented macules in five lesions (>16 months of follow-up), pink macules in two lesions (>16 months of follow-up), pink papules (raised) in three lesions (>6 months of follow-up), erythematous macules in three lesions (>6 months of follow-up), and hypertrophic scarring in one lesion (at 2 months of follow-up) were observed.

An example of follow-up imaging, collected at 1, 4, 7, and 12 months, is shown in Fig. 7, for one of the lesions (with 20 months of follow-up) representing the evolution of treated superficial type of BCC. The regrowth skin layers are seen at the first follow-up. However, significant presence of enlarged blood vessels (yellow arrows) and amorphous and thin collagen fibers (yellow arrows) are seen at 1 and 4 months. At 7 months, more normal dermis is visualized still presence of enlarged blood vessels with thickened collagen fibers (red arrows) were observed (Fig. 7-left bottom). The appearance and morphology of the epidermal layers were seen normal compared to untreated surrounding normal skin at 12 months (Fig. 7-right bottom).

4 Discussion

This paper reports another step in our ongoing development of RCM imaging methodologies to guide treatment of BCCs on patients. In this case, the treatment is ablation with an Er:YAG laser. Ablation vaporizes tissue such that none is available for traditional pathology, and the treatment is guided purely with imaging. This study represents our initial clinical experience using RCM imaging in superficial ablated wounds. The imaging addresses, to some extent, the current major limitation of lack of histological confirmation as reported in previous studies. As described herein, RCM imaging can eloquently map lateral and deep tumor margins directly on patients preablation, helping refine the laser ablation parameters (optimal fluence and/or number of passes) for precise destruction of BCCs without excessive loss of surrounding normal tissue, as well as detect residual tumor or confirm clearance postablation, again, directly on patients.

The initial pilot study on 10 lesions with histology confirmation allowed us to explore the efficacy of ablating superficial and early nodular BCCs when guided by RCM *in vivo*. The selection of a control region containing BCC within the lesion demarcated the intact (nonablated) tumor versus ablated BCCs helped for correlation and validation of the RCM imaging findings to histology. Out of 10 lesions, only one case was misread, as a false positive, due to saturation artifacts. Admittedly, 10 cases can be considered a small number, but, nonetheless, these first results on patients confirm the findings from our earlier *ex vivo* studies and build upon our initial experience on patients.

Three residual BCC cases (lesion numbers 1 to 3 in Table 2) detected with postablation RCM were confirmed with histology. Those cases had an early nodular component. In these cases, we observed the presence of bright tumor islands (enhanced due to the use of aluminum chloride), elongated nuclei, and clefting in RCM images. The other case (lesion number 4 in Table 2) that showed suspicious tumor on RCM was a BCC with an infiltrative component. Infiltrative BCCs are often deeper than RCM can image and this component was not detected before ablation. (Infiltrative, micronodular, and mixed types of BCCs were not included in this study.) After ablation, too, residual infiltrative BCCs are often difficult to detect due to their small size and the limited specificity of reflectance contrast in RCM images. Furthermore, it is important to note that, after several passes, ablated epidermal cells under RCM can sometimes appear elongated, similar to the polarized nuclear morphology in BCCs and

akin to that seen on histology. Therefore, it is ideal to balance the proper amount of ablation and thermal coagulation by controlling the number of passes and fluence to effectively treat tumor while preserving enough tissue architecture to be able to image and diagnose under RCM. This finding could also explain the challenge in identifying residual BCC in the fourth case, where the features of tumor were not strikingly evident in RCM images but were clearly identified in histology. However, since these were among the first-treated lesions with the RCM imaging approach, the initial lack of experience in reading images in ablated tissue may have also played a role in the missed detection of BCCs in postablated tissue.

The subsequent study on 34 lesions, with only RCM imaging but no histopathology, allowed us to further explore and test this approach on a larger number of patients. RCM imaging found residual BCC for seven of the 34 treated lesions after ablation. For these lesions, an additional second set of 2 to 4 passes was required to achieve clearance of BCC. The failure to complete removal of tumor after the first set of passes may have been due to the undercalculation of the depth of tumor by RCM. This may be a consequence of the limited depth of RCM imaging and the decrease in resolution in the deeper layers of the skin (~150 to 200 μm), which prevents accurate and repeatable estimation of the deeper margins and depth of tumors. Clearance in 31 lesions over a follow-up range of 1 to 21 months (mean follow-up 13 months) has been observed. However, for the seven lesions with 1 to 3 months follow-up, the results are still premature to clinically state cure of tumor at such short follow-up times. At such short times, features innate to the healing and scarring process (higher presence of blood vessels, inflammatory cells, etc.) appear under the imaging and may result in a biased evaluation. Nonetheless, this limitation notwithstanding, we have, to date, seen promising outcomes and clinicians continue the follow-up imaging to complete the follow-up to more than 12 months for all 34 lesions for complete clinical evaluation.

To overcome RCM's limited depth of imaging, a multimodal approach may be considered. Optical coherence tomography (OCT) and ultrasound imaging have been proven to detect BCCs at depths of ~1 mm.[27,28] Combining RCM imaging with OCT or ultrasound will likely address this limitation. The optical synergy of OCT and RCM, in particular, facilitates the integration of the two modalities into a single device. Indeed, preliminary benchtop instrumentation work and recent development of a handheld prototype has shown the possibility of OCT to provide an integrated complementary tool to RCM for the purpose of imaging deeper margins and to improve estimation of tumor depth preablation.[29,30]

Another limitation of this first study is the mostly uncontrolled manual operation of the RCM device and inability of the imaging operator to manually cover the entire deep dermal margins (surface of the wound base). These limitations may be solved with the development of a smaller RCM device, with a smaller objective lens, and a less manual and more automated approach to ensure complete imaging in the wound, especially the dermal margins, without missing any areas.

Along with a smaller device and an automated approach, video mosaicking (converting videos into mosaics) will be a useful related advance to display larger areas of tissue. Video capture with the handheld confocal microscope (Vivascope 3000) allowed the user to rapidly access large areas in wounds (and entire areas in smaller wounds), including the entire epidermal margin and deeper dermal margins. The video acquisition procedure provides the flexibility for the imaging to be adapted to the arbitrary topography of the wound. However, discontinuities or "jumps" in the videos due to sudden microscopic topographical changes on the wound surface occurred, along with blurring and artifacts (dark or saturated areas), all of which must be processed by partitioning the videos into subvideos to create submosaics. This partitioning is currently done manually and consumes considerable time, therefore, more work on the automation of the video-mosaicking approach is required. Development of an automated approach is in progress, with initial demonstrated capability for imaging margins of BCC lesions.[24]

For all the lesions, our clinicians (coauthors CSJC, MC, and OY) found that images, videos, and video mosaics exhibited overall clinically acceptable quality with regard to resolution, contrast, and appearance of features postablation. Identification of the epidermal, peripheral, and deep dermal margins was feasible due to the immediate recognition of relevant features specific to each region. Furthermore, the presence of artifacts (air bubbles, saturation) was accurately identified in the image and video assessments of each margin. Saturation in the images and videos appeared to be due to dryness of the postablated tissue that varied due to lesion location or patient characteristics. Thus, our approach, with optimal choice of laser ablation parameters to control thermal coagulation and enable postablation RCM imaging with a contrast agent, appears to be inherently working, and we believe that it should be advanced toward larger clinical studies and testing. Of course, further development in instrumentation and methodology will be necessary to support further advances in the clinic. While aluminum chloride appears to work well, reflectance contrast may sometimes fail to detect small tumors that may look similar to dermal structures such as hair follicles. Surely, a more specific contrast agent that further enhances tumor-to-dermis contrast could help for differentiating small residual tumors from normal dermal structures.

Disclosures

Milind Rajadhyaksha is a former employee of and owns equity in Caliber Imaging and Diagnostics (formerly, Lucid Inc.), the company that manufactures and sells the VivaScope confocal microscope. The VivaScope is the commercial version of an original laboratory prototype that was developed by Rajadhyaksha when he was at Massachusetts General Hospital, Harvard Medical School. None for the other coauthors.

Acknowledgments

We thank the NIH for funding support (grant R01EB020029 from NIBIB's Image-guided Interventions program, and partially, MSKCC's Center Core grant P30CA008748). Dr. Yélamos thanks the Beca Excelencia Fundación Piel Sana. We are grateful to Mr. Steven Wilson and Mr. Reza Afzalneia for preparing frozen histology and Ms. Christine Chang for her help with the patient consents. Finally, we thank Dr. Kivanc Kose for providing technical assistance with image stitching and producing videomosaics.

References

1. A. Lomas, J. Leonardi-Bee, and F. Bath-Hextall, "A systematic review of worldwide incidence of nonmelanoma skin cancer," *Br. J. Dermatol.* **166**(5), 1069–1080 (2012).
2. C. Berking et al., "Basal cell carcinoma-treatments for the commonest skin cancer," *Dtsch Arztebl Int.* **111**(22), 389–395 (2014).

3. H. T Greenway et al., "Mohs microscopic surgery and cutaneous oncology," in *Surgery of the Skin: Procedural Dermatology*, J. K. Robinson et al., Eds., 3rd ed., Elsevier Saunders (2015).
4. G. Goldenberg and O. Hamid, "Nonsurgical treatment options for basal cell carcinoma—focus on advanced disease," *J. Drugs Dermatol.* **12**(12), 1369–1378 (2013).
5. O. A. Ibrahimi et al., "755 nm alexandrite laser for the reduction of tumor burden in basal cell nevus syndrome," *Lasers Surg. Med.* **43**(2), 68–71 (2011).
6. H. Kavoussi and A. Ebrahimi, "Treatment and cosmetic outcome of superpulsed CO_2 laser for basal cell carcinoma," *Acta Dermatovenerol. Alp. Pannonica Adriat.* **22**(3), 57–61 (2013).
7. J. Del Pozo and L. Rosende, "Basal cell carcinoma. Treatment with carbon dioxide laser vaporization," *Adv. Cancer Res. Treat.* **2013**, 1–11 (2013).
8. H. Kavoussi, A. Ebrahimi, and M. Rezaei, "Treatment and cosmetic outcome of superpulsed CO_2 laser for basal cell carcinoma," *Acta Dermatovenerol. Alp. Pannonica Adriat.* **22**, 1–5 (2013).
9. Z. Tannous, "Combined 585 nm pulsed-dye and 1,064 nm Nd:YAG lasers for the treatment of basal cell carcinoma," *Lasers Surg. Med.* **46**(1), 1–7 (2014).
10. S. Iyer et al., "Treatment of basal cell carcinoma with the pulsed carbon dioxide laser: a retrospective analysis," *Dermatol. Surg.* **30**(9), 1214–1218 (2004).
11. H. R. Jalian et al., "Combined 585 nm pulsed-dye and 1,064 nm Nd:YAG lasers for the treatment of basal cell carcinoma," *Lasers Surg. Med.* **46**(1), 1–71 (2014).
12. B. T. Nguyen et al., "Treatment of superficial basal cell carcinoma and squamous cell carcinoma in situ on the trunk and extremities with ablative fractional laser-assisted delivery of topical fluorouracil," *J. Am. Acad. Dermatol.* **72**(3), 558–560 (2014).
13. A. E. Ortiz, R. R. Anderson, and M. M. Avram, "1064 nm long-pulsed Nd:YAG laser treatment of basal cell carcinoma," *Lasers Surg. Med.* **47**(2), 106–110 (2015).
14. M. U. Javed and M. Murison, "The combined CO_2 laser and photodynamic therapy of multiple BCC's in a facial port wine stain," *J. Plast Reconstr. Aesthetic Surg.* **69**(1), e10–e12 (2016).
15. R. Smucler et al., "Ultrasound guided ablative-laser assisted photodynamic therapy of basal cell carcinoma (US-aL-PDT)," *Photomed. Laser Surg.* **30**(4), 200–205 (2012).
16. S. A. Fox et al., "Raman spectroscopy differentiates squamous cell carcinoma (SCC) from normal skin following treatment with a high-powered CO_2 laser," *Lasers Surg. Med.* **46**(10), 757–772 (2014).
17. C. S. Chen et al., "Confocal microscopy-guided laser ablation for superficial and early nodular Basal cell carcinoma: a promising surgical alternative for superficial skin cancers," *JAMA Dermatol.* **150**(9), 994–998 (2014).
18. B. P. Hibler et al., "Carbon dioxide laser ablation of basal cell carcinoma with visual guidance by reflectance confocal microscopy: a proof-of-principle pilot study," *Br. J. Dermatol.* **174**, 1359–1364 (2016).
19. H. Sierra et al., "Confocal microscopy to guide erbium:yttrium aluminum garnet laser ablation of basal cell carcinoma: an ex vivo feasibility study," *J. Biomed. Opt.* **18**(9), 095001 (2013).
20. H. Sierra et al., "Confocal imaging-guided laser ablation of basal cell carcinomas: an ex vivo study," *J. Invest. Dermatol.* **135**, 612–615 (2014).
21. Z. Tannous, A. Torres, and S. Gonzalez, "In vivo real-time confocal reflectance microscopy: a noninvasive guide for Mohs micrographic surgery facilitated by aluminum chloride, an excellent contrast enhancer," *Dermatol. Surg.* **29**, 839–846 (2003).
22. M. Lukac, B. Majaron, and T. Rupnik, "Ablative and thermal effects of Er:YAG laser on human tissue," in *Laser in der Medizin Laser in Medicine*, W. Waidelich, R. Waidelich, and J. Waldschmidt, Eds., Springer, Berlin, Heidelberg (1998).
23. B. Larson et al., "Fundamentals and technology advances: fundamentals of reflectance confocal microscopy," Chapter 1 in *Reflectance Confocal Microscopy of Cutaneous Tumors*, 2nd Ed., S. G. Gonzalez et al., Eds., NovaTechset Publishers, Madrid (2017).
24. K. Kose et al., "Video-mosaicing of reflectance confocal images for examination of extended areas of skin in vivo," *Br. J. Dermatol.* **171**(5), 1239–1241 (2014).
25. M. L. Marino et al., "Improving lesion localization when imaging with handheld reflectance confocal microscope," *Skin Res. Technol.* **22**(4), 519–520 (2016).
26. E. S. Flores et al., "Intraoperative imaging during Mohs surgery with reflectance confocal microscopy: initial clinical experience," *J. Biomed. Opt.* **20**(6), 061103 (2014).
27. A. Scope et al., "In vivo reflectance confocal microscopy of shave biopsy wounds: feasibility of intraoperative mapping of cancer margins," *Br. J. Dermatol.* **163**(6), 1218–1228 (2010).
28. D. J. Rohrbach et al., "Preoperative mapping of nonmelanoma skin cancer using spatial frequency domain and ultrasound imaging," *Acad. Radiol.* **21**(2), 263–270 (2014).
29. N. Iftimia et al., "Combined reflectance confocal microscopy-optical coherence tomography for delineation of basal cell carcinoma margins: an ex vivo study," *J. Biomed. Opt.* **21**(1), 016006 (2016).
30. N. Iftimia et al., "Handheld optical coherence tomography-reflectance confocal microscopy probe for detection of basal cell carcinoma and delineation of margins," *J. Biomed. Opt.* **22**(7), 076006 (2017).

Heidy Sierra is an assistant professor at the University of Puerto Rico Mayaguez, Mayaguez Puerto Rico. Her work at Memorial Sloan Kettering Cancer Center included image-guided therapy approaches for the treatment of skin cancer. Her current research interests include computational imaging, machine learning, confocal microscopy, phase microscopy, and multimodal imaging, all to be applied for guidance of diagnosis and therapy of diseases. She is a member of SPIE and a member of OSA. She is the author/coauthor of several peer-reviewed publications and a book chapter.

Biographies for the other authors are not available.

Publication 5: Peri-operative delineation of non-melanoma skin cancer margins in vivo with handheld reflectance confocal microscopy and video-mosaicking

Eileen Flores, Oriol Yélamos, Miguel Cordova, Kivanc Kose, William Phillips, Erica H. Lee, Anthony M. Rossi, Kishwer Nehal, Milind Rajadhyaksha

SUMMARY

Background: The surgical removal of non-melanoma skin cancers (NMSCs) is guided by the pathologic examination of margins. However, the preparation of histopathology is time consuming, labor-intensive, and requires separate laboratory infrastructure. Furthermore, when histopathology indicates positive margins, patients must return for re-excisions. Reflectance confocal microscopy (RCM) with a new video-mosaicking approach can noninvasively delineate margins directly on patients and potentially guide surgery in real-time, augmenting the traditional approaches of histopathology.

Aims: To assess a new peri-operative RCM video-mosaicking approach for comprehensive delineation of NMSC margins on patients in vivo.

Material and Methods: Thirty-five patients undergoing Mohs micrographic surgery (MMS) in the Mohs surgery unit at Memorial Sloan Kettering Cancer Center, New York, NY were included in the study. RCM imaging was performed before and after the first staged excision by acquiring videos along the surgical margins (epidermal, peripheral and deep dermal) of each wound, which were subsequently processed into video-mosaics. Two RCM evaluators read and assessed video-mosaics, and subsequently compared to the corresponding Mohs frozen histopathology.

Results: RCM videos and video-mosaics displayed acceptable imaging quality (resolution and contrast), pre-operatively in 32/35 (91%) NMSC lesions, and intra-operatively in 29/35 lesions (83%). Pre-operative delineation of margins correlated with the histopathology in 32/35(91%) lesions. Intra-operative delineation correlated in 10/14 (71%) lesions for the presence of residual tumor and in 18/21 (86%) lesions for absence. Sensitivity/specificity were 71%/86% and 86%/81% for two RCM video-mosaic evaluators, and overall agreement was 80% and 83% with histopathology, with moderate inter-evaluator agreement ($k=0.59$, $p<0.0002$).

Conclusions: Peri-operative RCM video-mosaicking of NMSC margins directly on patients may potentially guide surgery in real-time, serve as an adjunct to histopathology, reduce time spent in clinic and reduce the need for re-excisions. Further testing in larger studies is needed.

ORIGINAL ARTICLE

Peri-operative delineation of non-melanoma skin cancer margins *in vivo* with handheld reflectance confocal microscopy and video-mosaicking

E. Flores,[1,2,*] O. Yélamos,[1,3] M. Cordova,[1] K. Kose,[1] W. Phillips,[1] E.H. Lee,[1] A. Rossi,[1] K. Nehal,[1] M. Rajadhyaksha[1]

[1]Dermatology Service, Memorial Sloan Kettering Cancer Center, New York, NY, USA
[2]Public Health Science Department, Penn State College of Medicine, Hershey, PA, USA
[3]Dermatology Department, Hospital Clínic, Universitat de Barcelona, Barcelona, Spain
*Correspondence: E. Flores. E-mail: esf51@psu.edu

Abstract

Background The surgical removal of non-melanoma skin cancers (NMSCs) is guided by the pathologic examination of margins. However, the preparation of histopathology is time consuming, labour-intensive and requires separate laboratory infrastructure. Furthermore, when histopathology indicates positive margins, patients must return for re-excisions. Reflectance confocal microscopy (RCM) with a new video-mosaicking approach can noninvasively delineate margins directly on patients and potentially guide surgery in real-time, augmenting the traditional approaches of histopathology.

Objective To assess a new peri-operative RCM video-mosaicking approach for comprehensive delineation of NMSC margins on patients *in vivo*.

Methods Thirty-five patients undergoing Mohs micrographic surgery (MMS) in the Mohs surgery unit at Memorial Sloan Kettering Cancer Center, New York, NY were included in the study. RCM imaging was performed before and after the first staged excision by acquiring videos along the surgical margins (epidermal, peripheral and deep dermal) of each wound, which were subsequently processed into video-mosaics. Two RCM evaluators read and assessed video-mosaics, and subsequently compared to the corresponding Mohs frozen histopathology.

Results Reflectance confocal microscopy videos and video-mosaics displayed acceptable imaging quality (resolution and contrast), pre-operatively in 32/35 (91%) NMSC lesions and intra-operatively in 29/35 lesions (83%). Pre-operative delineation of margins correlated with the histopathology in 32/35 (91%) lesions. Intra-operative delineation correlated in 10/14 (71%) lesions for the presence of residual tumour and in 18/21 (86%) lesions for absence. Sensitivity/specificity were 71%/86% and 86%/81% for two RCM video-mosaic evaluators, and overall agreement was 80% and 83% with histopathology, with moderate inter-evaluator agreement ($k = 0.59$, $P \leq 0.0002$).

Conclusions Peri-operative RCM video-mosaicking of NMSC margins directly on patients may potentially guide surgery in real-time, serve as an adjunct to histopathology, reduce time spent in clinic and reduce the need for re-excisions. Further testing in larger studies is needed.

Received: 19 November 2018; Accepted: 18 January 2019

Conflict of Interest

Milind Rajadhyaksha is a former employee of and owns equity in Caliber Imaging and Diagnostics (formerly Lucid Inc.), the company that manufactures and sells the Vivascope confocal microscope. The Vivascope is the commercial version of an original laboratory prototype that he had developed at Massachusetts General Hospital, Harvard Medical School. The other authors have no disclosures or conflicts of interest to report. Rajadhyaksha (Former employee and holds equity, Caliber Imaging and Diagnostics).

Funding source

This research was funded in part by the NIH (grants R01EB012466 and R01EB020029 from NIBIB's Image-Guided Interventions program), the NIH/NCI Cancer Center Support Grant P30 CA008748, and the Fundación Piel Sana (Beca Excelencia Fundación Piel Sana).

Introduction

The surgical removal of non-melanoma skin cancers (NMSCs) is guided by the pathologic examination of margins.[1,2] The clearance of margins is confirmed either with postoperative permanent pathology for standard surgical excision or with intra-operative frozen pathology of each staged excision during Mohs micrographic surgery (MMS). However, the preparation of histopathology is time consuming, labour-intensive and requires separate laboratory infrastructure.[3,4] Furthermore, when histopathology indicates positive margins, the patient must return for re-excision. In the case of MMS, the patient must undergo additional staged excisions. A non-invasive real-time high-resolution optical imaging modality such as reflectance confocal microscopy (RCM) offers a complementary approach: peri-operative detection of margins directly on patients *in vivo*. RCM imaging diagnoses NMSCs *in vivo* with high sensitivity and specificity.[5–7] Beyond diagnosis, we can detect margins, to potentially guide treatment and to augment the standard approaches of pathology.

Several pilot studies have reported the feasibility of RCM imaging for detecting basal cell carcinomas (BCCs) in wounds during and after surgeries,[8–11] as well as for assessing risk of recurrence.[12–14] In a recent study, RCM evaluation correctly delineated clinically and dermoscopically ill-defined margins of BCCs, and pre-operatively guided surgical re-excision, resulting in clear margins.[14]

In all previous studies, however, the demonstrated feasibility and the imaging of margins were limited to a small number of discrete locations in the NMSC lesions. Furthermore, the sampling of the margins at each location was limited to either single images or small square-shaped areas, displayed in mosaics of images. (Mosaicking of a two-dimensional sequence of RCM images is currently a widely used approach to increase the sampling area.).[15] However, comprehensive delineation of margins requires imaging over larger freeform-shaped and contiguous areas. This is now possible with our newly developed RCM video-mosaicking algorithm.[16] Instead of acquiring (and mosaicking) still images, we acquire videos with a handheld confocal microscope. The videos are subsequently processed into video-mosaics to display larger and contiguous freeform-shaped areas. Our approach for RCM video-mosaicking is similar, in concept, to capturing of a widefield panorama picture with a mobile phone camera.

In a clinical study, we tested a peri-operative RCM video-mosaicking approach for the delineation of NMSC margins directly on patients undergoing Mohs surgery. We report the results of this study and discuss current limitations and future potential utility of RCM video-mosaicking for real-time delineation of NMSC margins *in vivo*.

Materials and methods

Study population

Patients undergoing Mohs surgery for NMSCs were recruited and consented under a research protocol approved by the Memorial Sloan Kettering Cancer Center (MSKCC) Institutional Review Board.

Instrumentation and imaging procedure

Imaging was performed with a handheld reflectance confocal microscope (Vivascope 3000; Caliber Imaging and Diagnostics, Rochester, NY). The lens includes a window that provides a contact interface to skin. The window was gas sterilized between use on patients, with no loss of imaging quality. Imaging was performed on all patients before the start of Mohs surgery and immediately after Mohs stage I excision.

We utilized an imaging protocol that was previously developed for RCM imaging in Mohs surgical wounds (Figure S1, Supporting Information).[17] As per standard procedure, the Mohs surgeon ink-marked the entire surgical margin of each lesion, followed by infiltration of local anaesthesia. A score was performed with a scalpel along the entire ink-marked margin, as well as at the 12, 3, 6 and 9 o'clock positions. A drop of Crodamol STS oil (Croda Inc., Edison, NJ, U.S.A.) was applied to the surface of the skin. We acquired videos along the scored surgical margin of the lesion in a clockwise fashion. Videos were acquired at a single depth (approximately 120–150 μm) at the dermal-epidermal junction. After pre-operative imaging, Mohs stage I excision was performed. After excision, we topically applied 35% aluminium chloride ($AlCl_3$) inside the wound, using sterile applicators, for 30 s. $AlCl_3$ has been shown to brighten nuclear morphology and enhance contrast of NMSC tumours in RCM images.[8,10,17] Afterwards, the wound cavity was filled with sterile gel (Surgilube, Fougera, Melville, NY). Again, RCM imaging was performed, this time, inside the wound, along the surgical margin in a clockwise fashion.

Acquisition of videos and video-mosaics

Pre- and intra-operative imaging was performed in quadrants.[17] Either one or two videos, depending on the lesion size, were acquired pre-operatively in each quadrant, starting at the 12 o'clock position and traversing in a 360° clockwise direction, along the scored surgical margin of each lesion. Similarly, videos were acquired intra-operatively in the surgical wound bed starting at the 12 o'clock position and traversing in a 360° clockwise direction, along the peripheral edge (epidermal and peripheral dermal margin) and including the base (deep dermal margins) of the wound.

In most cases, videos were taken from the 12 to 3, 3 to 6, 6 to 9 and 9 to 12 o'clock positions. For select small lesions of diameter less than 1 cm, only one video was acquired, starting and

ending at the 12 o'clock position. Videos were acquired by two trained clinicians, a dermatologist (O.Y.) and a clinical imaging researcher (M.C.). Video acquisition was controlled for quality by gently pressing the lens and sterile window against the skin. Videos were acquired slowly and carefully to minimize blur and motion artifacts, by moving the microscope smoothly over the area of interest, while maintaining constant depth throughout the imaging process. The total video acquisition time ranged from 1–2 min for small (diameter < 1 cm) wounds and 3–5 min for larger wounds. Each RCM video was processed into a video-mosaic, using our newly developed video-mosaicking algorithm.[16] Additional details on the imaging procedure are available elsewhere.[17]

Pre- and intra-operative assessment of RCM videos and video-mosaics and histopathological correlation

Reflectance confocal microscopy videos and video-mosaics were evaluated by our dermatologist and our imaging researcher (O.Y. and M.C., respectively). The overall quality of each video and video-mosaic was assessed as clinically acceptable or not. If the quality was acceptable, the video and video-mosaic were further evaluated for resolution, contrast and visualization of nuclear and morphologic detail. The nuclear and morphologic features that have been defined in our previous studies[10,17] were compared to those seen in histopathology.

Histopathology was available for comparison to the RCM videos and video-mosaics. Mohs stage I excisions were processed into frozen sections with haematoxylin & eosin staining, as per standard protocol. These sections were in the *en face* orientation, similar to that of the RCM images. Diagnoses for initial diagnostic biopsies and all Mohs frozen sections were obtained from pathology reports.

Statistical analysis

All descriptive and comparative data analyses were performed using STATA software (version 12.0; StataCorp LP). Parameters for imaging quality and presence or absence of residual tumour were stratified by NMSC subtype (either BCC or SCC). Sensitivity and specificity and the overall agreement between RCM videos and video-mosaics and histopathology for presence or absence of residual tumour were determined for our two evaluators (M.C. and O.Y). Inter-evaluator agreement between the two of them was calculated using the Cohen's kappa statistic. A two-sided p-value of < 0.05 was considered significant.

Results

We imaged a total of 45 patients (41 with biopsy-proven BCC, 4 with biopsy-proven SCC). The lesion diameter ranged from 0.2 cm to 2 cm (mean = 0.7 cm). The lesions were located on various body sites including the arm ($n = 3$), hand ($n = 1$), face ($n = 17$), neck ($n = 4$), scalp ($n = 2$), chest ($n = 4$), shoulder/back ($n = 7$) and leg ($n = 7$).

Training set ($n = 10$) for acquisition of videos and video-mosaicking

Imaging on the first 10 patients served as a training set for our dermatologist and imaging researcher (O.Y. and M.C.) to test the use of $AlCl_3$ (swabbing times up to 1 min) and test the acquisition of videos and processing into video-mosaics. The objective was to test a previously developed RCM imaging and video-acquisition protocol (details available elsewhere)[17] and to establish a standardized approach for this study.

We acquired RCM videos, both pre- and intra-operatively, on 10 patients (9 with biopsy-proven BCC and 1 with biopsy-proven SCC). We determined that in four patients with nodular and infiltrative subtypes of BCC lesions, imaging at the dermo-epidermal junction was too superficial and had to be performed at a deeper level for similar lesions in the test set. For the remaining six superficial subtypes of lesions (superficial BCCs, SCCs), pre-operative imaging at the dermo-epidermal junction was determined to be adequate. We determined that the use of $AlCl_3$ (concentration 35% for topical application of 30 s) produced consistent and uniform contrast with minimal saturation and allowed consistent visualization of nuclear morphology in the videos and video-mosaics.

Test set ($n = 35$) for delineation of margins

In the remaining 35 patients (32 with biopsy-proven BCC and 3 with biopsy-proven SCC), the standardized imaging protocol and topical use of $AlCl_3$ were implemented. Pre- and intra-operative imaging was performed on all 35 patients. For the 16 superficial lesion subtypes, pre-operative imaging was performed at the dermo-epidermal junction (approximately 100–125 μm). For the remaining 19 nodular and infiltrative subtypes of lesions, pre-operative imaging was performed at a relatively deeper depth (approximately 125–150 μm).

Pre-operative evaluation of lateral margins with RCM ($n = 35$)

Thirty-two (91%) of 35 biopsy-proven NMSCs (29 BCCs, 3 SCCs) were observed with acceptable imaging quality, resolution and contrast (Table 1). All 32 videos allowed for visualization of nuclear and morphologic features. The remaining three videos were not acceptable, mainly due to motion blur artifacts. However, visualization of normal nuclear detail such as sebaceous glands, inflammatory cells and eccrine ducts was still possible. All acceptable 32 lesions exhibited the following normal features: honeycomb pattern (dark nuclei within bright cytoplasm), dermal rings, eccrine ducts, sebaceous glands and hair follicles. For BCC lesions, the following features were observed: erosion, streaming, atypical honeycomb pattern, dark silhouettes, thickened and bundled collagen, tumour nests containing palisading cells, clefting, cord-like structures with palisading, melanophages and small inflammatory cells in dermis (Figure S2, Supporting Information). For SCC lesions, the following features were observed: erosion, parakeratosis, atypical honeycomb pattern,

Table 1 Evaluation of pre- and intra-operative RCM imaging

	Pre-operative			Postoperative			
	BCC (n = 32)	SCC (n = 3)	Total (n = 35)	Residual BCC (n = 13)	Residual SCC (n = 1)	Absence (n = 21)	Total (n = 35)
Acceptable quality (video & video-mosaic)	29	3	32 (91%)	9	1	19	29 (83%)
Unacceptable quality (video & video-mosaic)	3	0	3 (9%)	4	0	2	6 (17%)
Total	32	3	35 (100%)	12	1	22	35 (100%)

epidermal disarray, keratinocyte pleomorphism and inflammatory cells (Fig. 1, example).

Intra-operative evaluation of surgical wounds with RCM (n = 35)

Twenty-nine (83%) of 35 surgical wounds were observed with acceptable imaging quality, resolution and contrast, with respect to the videos and video-mosaics (Table 1). All 29 videos could be converted into video-mosaics. The remaining six videos were considered unacceptable due to the presence of motion blur artifacts and thus could not be converted to video-mosaics.

In the videos and video-mosaics (Fig. 2, example) that exhibited acceptable quality, nuclear and cellular structures at the epidermal, peripheral and deep dermal margins were identified:

1 Epidermal Margin – at the peripheral edge of the surgical wound.
At the periphery of the wound, bright nuclei within small polygonal cells (corresponding to epidermal keratinocytes) were seen in a cobblestone pattern. Each cell was separated by a light reflective border. The direct exposure to aluminium chloride, and thus nuclei brightening, was due to the lack of a stratum corneum in the surgical wound. In contrast, the epidermal keratinocytes in the surrounding intact skin were seen as polygonal cells with dark nuclei and bright thin cytoplasm displayed in a honeycomb pattern. The difference between the cobblestone and honeycomb patterns was easily distinguished and defined the peripheral edges of each surgical wound.
2 Peripheral Dermal Margin – at the peripheral (papillary) dermis of the surgical wound.
Deeper level images showed the dermo-epidermal junction (DEJ) and dermal papillae surrounded by a rim of bright cells, contrasting with the dark background. Hyper-reflective structures forming web-like structures corresponding to papillary collagen bundles within dermal papillae were seen at deeper levels of the wound cavity.

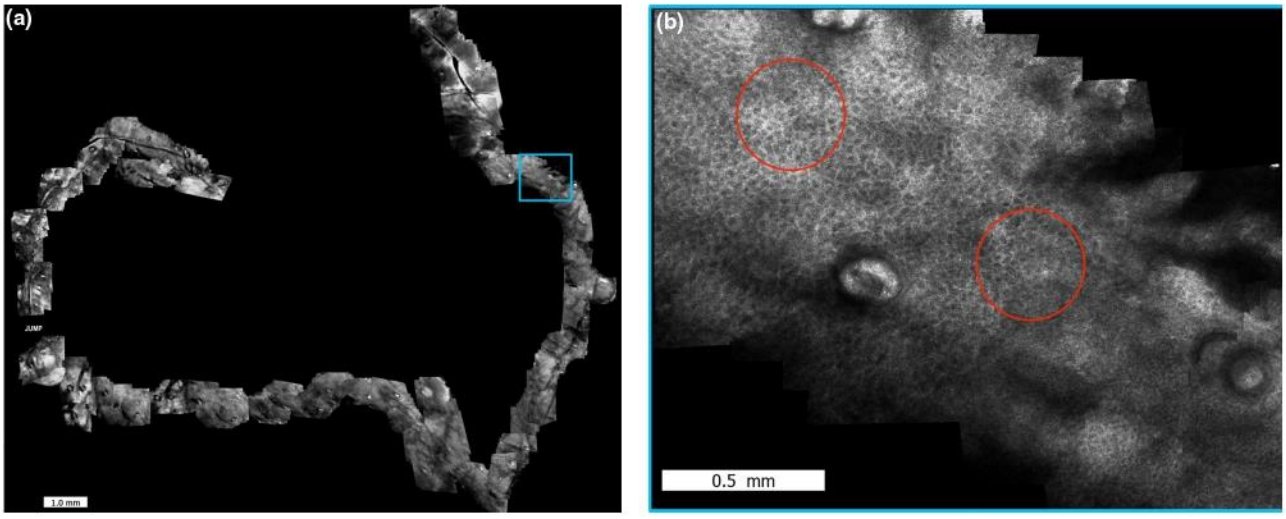

Figure 1 Pre-operative RCM video-mosaic of biopsy-proven SCC. Features observed along the scored surgical lateral margins of this lesion: (a) epidermal disarray and atypical honeycomb pattern from 12 to 2 o'clock position in the first quadrant (inset area in blue rectangle), and (b) shown in a magnified view of the inset (area in red circles). Seen, at approximately the 9 o'clock position is a break or discontinuity (labelled "JUMP") in the video-mosaic.

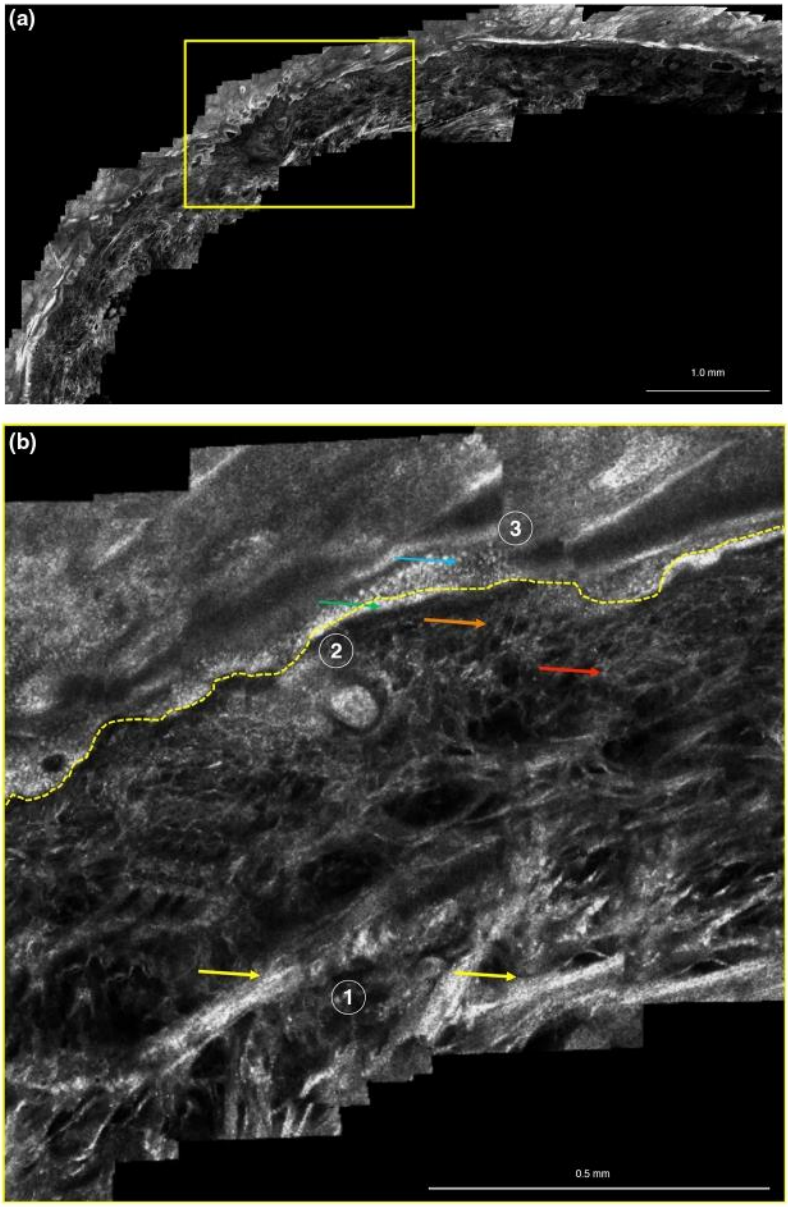

Figure 2 Intra-operative RCM video-mosaic showing absence (clearance) of NMSC tumour. The entire video-mosaic in the third quadrant, from 9 to 12 o'clock, is seen (a), along with a magnified view of the inset area in the yellow rectangle (b). The video-mosaic shows three depths of wound margins: 1. Deep dermal margin – showing near the base of a dark shaved wound cavity containing hyper-reflective fibrillar structures corresponding to reticular collagen bundles (yellow arrows). 2. Peripheral dermal margin – showing polygonal-shaped cells (keratinocytes) with bright nuclei arranged in a cobblestone pattern surrounding the shaved wound cavity (green arrows). Deeper level images showed the dermo-epidermal junction (DEJ) and dermal papillae surrounded by a rim of bright cells, contrasting with the dark background (orange arrow). Hyper-reflective structures forming web-like structures, corresponding to papillary collagen bundles within dermal papillae, were seen at deeper levels of the wound cavity (red arrow). 3. Epidermal margin and the wound edge (yellow dotted line) – At the periphery of the wound, bright nuclei within small polygonal cells, corresponding to epidermal keratinocytes, were seen in a cobblestone pattern (blue arrow). Each cell was separated by a light reflective border. The direct exposure to $AlCl_3$, and thus nuclei brightening, was due to the lack of a stratum corneum in the surgical wound. In contrast, the epidermal keratinocytes in the surrounding intact skin appeared as polygonal cells with dark nuclei and bright thin cytoplasm displayed in a honeycomb pattern. The difference between the cobblestone and honeycomb patterns was easily distinguished and defined the peripheral edges of each surgical wound.

3 Deep Dermal Margin – at the base of the surgical wound. The base of the shaved wound cavity appeared dark, containing hyper-reflective fibrillar structures, which corresponded to reticular collagen bundles.

RCM videos and video-mosaics and histopathological correlation

Pre-operative imaging Image quality (resolution, contrast) and visualization of nuclear detail were acceptable in 32 of 35 NMSC lesions (Table 1). In these lesions, we also observed correlation between the RCM videos and video-mosaics and pre-operative diagnoses for presence of tumour. BCC and SCC features were visualized in the RCM videos and video-mosaics of 29 biopsy-proven BCCs and 3 biopsy-proven SCCs. In 24 of the 32 acceptable videos and video-mosaics, visualization of tumour-specific features was observed to be unequivocally BCC or SCC. For the remaining eight lesions, the videos and video-mosaics needed to be reviewed twice to confirm the features.

Intra-operative imaging Among the 14 NMSCs with histopathologically confirmed residual tumour, we observed correlation between the RCM videos/video-mosaics and the corresponding Stage I histopathology for presence of tumour in 10 lesions (nine residual BCC, one residual SCC; Table 2; Fig. 3, example). The observed features in the RCM videos/video-mosaics were consistent with those seen on histopathology. In the 21 lesions with absence of residual tumour, we observed correlation for absence of tumour in 18 lesions (Table 1). Overall image quality (resolution, contrast and visualization of nuclear detail) was acceptable in 29 of 35 NMSC lesions (Table 1).

RCM evaluator and histopathology correlation and inter-evaluator agreement (n = 35)

Sensitivity/specificity for our two RCM evaluators (O.Y. and M.C.) was 71%/86% and 81%/86%, respectively (Table 2). Overall agreement between each evaluator and histopathology was 80% and 83%, respectively. Inter-evaluator agreement was found to have moderate correlation (k = 0.59, $P \leq 0.0002$).

Table 2 Summary of intra-operative RCM and histopathological correlation

Histopathology	Reader 1		Reader 2	
	Presence	Absence	Presence	Absence
Presence of BCC residual tumour (n = 13)	9	4	11	2
Presence of SCC residual tumour (n = 1)	1	0	1	0
Absence of residual tumour (n = 21)	3	18	4	17
Sensitivity	71%		86%	
Specificity	86%		81%	
Overall agreement	80%		83%	

Discussion

Our paper reports a novel advancement in RCM imaging for potentially guiding surgery of NMSCs, with a new video-mosaicking approach that can peri-operatively delineate margins on patients *in vivo*. Video-mosaics can display NMSC margins in freeform-shaped and contiguous areas that can be determined by the user in real-time "on the fly" during imaging (Figs 1-3; Figures S2–S4, Supporting information).

We found that examination of the surgical margin utilizing both videos and video-mosaics in a synergistic manner was critical for an accurate and consistent assessment for the presence of residual tumour. This was our experience in the 29 cases with acceptable videos and video-mosaics (Table 1). Among the intra-operative videos and video-mosaics, features that appeared bright round, cord-like, palisading, elongated and nodular were often marked as suspicious for residual BCC. In three such videos, BCC structures were later determined to be normal structures (hair follicles, sebaceous glands and eccrine ducts) in histopathology, thus leading to false positives. Similarly, in one video, features that included an area with clefting with palisading cells were read as positive for residual tumour, but later determined to be negative. Video-mosaics were useful for orientation along the surgical margin and initial assessment for the presence or absence of residual tumour, while in ambiguous cases, videos were useful for additional confirmation. Only a small percentage (9% pre-operative; 17% intra-operative) of lesions presented unacceptable video quality and could not be processed into video-mosaics (Table 1). In these videos, there was too much motion blur and/or tissue distortion and warping, and/or incomplete coverage with "jumps" (due to sudden changes in depth or topography) and/or significant variations in image brightness (saturation due to too much $AlCl_3$ and/or too much illumination; Figures S3 and S4, Supporting Information). Further development of the video-mosaicking approach may minimize such errors.

Prior knowledge of the diagnosis allowed the user to adjust the imaging depth during pre-operative imaging. Typically, our imaging researchers (M.C., O. Y.) set the level of imaging at the dermo-epidermal junction, which does not always capture deeper infiltrative features that are seen in some NMSCs. In our study, RCM identified tumour-specific structures in 11 of 14 lesions with residual NMSC tumour (13 BCC, 1 SCC). However, for the three lesions that exhibited both superficial and infiltrative features, several videos at multiple depths would have been necessary, to capture both superficial and infiltrative BCC. Although the user can change depth while imaging with the handheld microscope, too much change in depth does not allow for creating seamless and contiguous video-mosaics. For

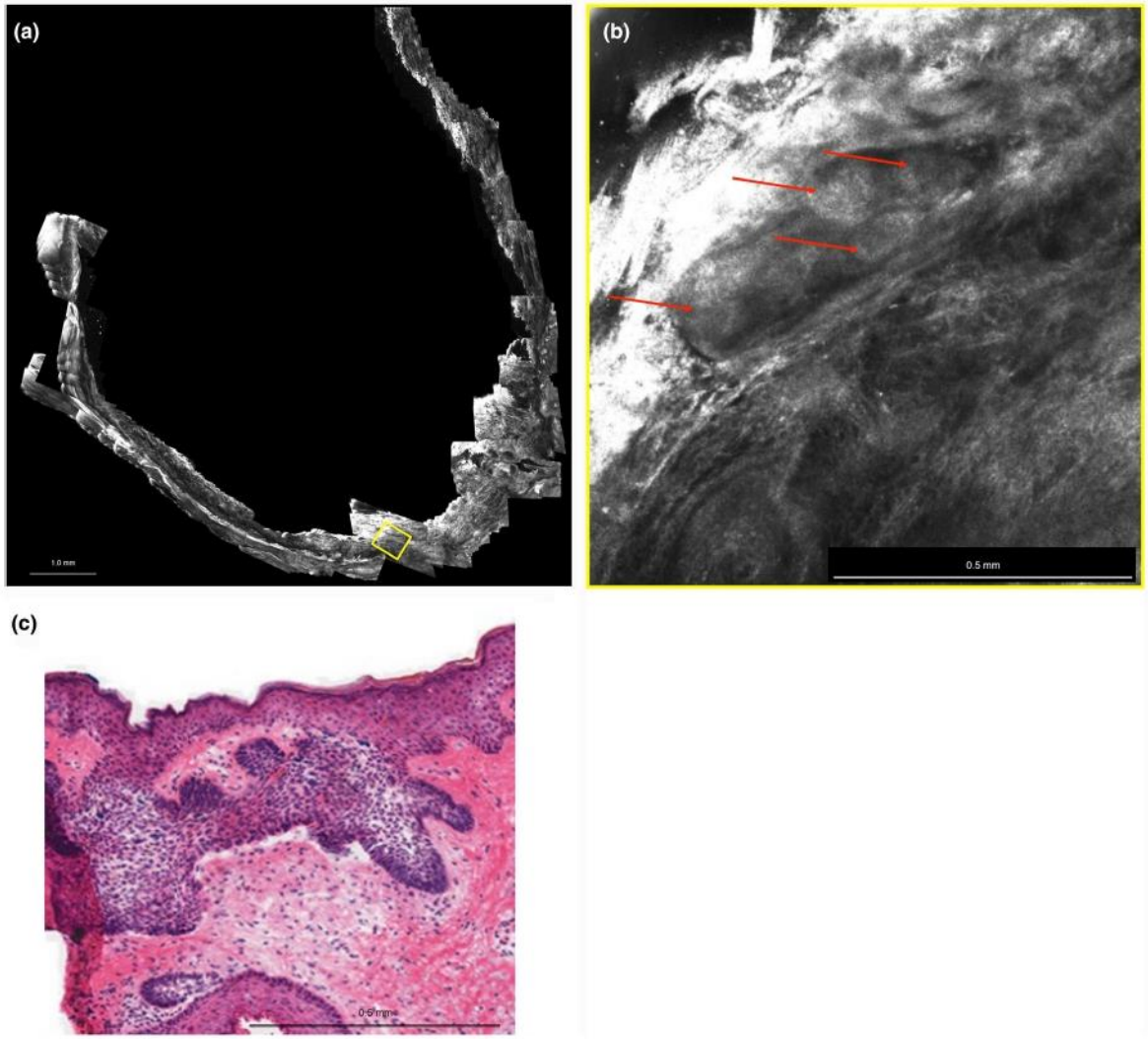

Figure 3 Intra-operative RCM video-mosaic showing presence of residual BCC tumour along the surgical wound, along with histopathology correlation. Observed features are (a) a tumour island (inset area in yellow rectangle), (b) showing presence of a nodular BCC in a magnified view (red arrows), and (c) confirmed by the corresponding histopathology.

superficial BCCs and SCCs, the depth was more superficial as opposed to micronodular or infiltrative BCCs, which required deeper imaging. In the future, the combination of RCM with optical coherence tomography (OCT), which images deeper[18] and can detect deeper margins,[19] may be useful for assessing depth of infiltrative features.

At present, the main limitation of the RCM video-mosaicking approach is inherent in the algorithm itself. Depending on the size of the lesion, video acquisition can be quick (1–2 min per quadrant, up to 8 min per lesion), but the subsequent processing is relatively slow (25–45 min per lesion, depending on number of videos). We are developing a faster approach, based on machine learning with deep neural networks, to process and produce video-mosaics in real-time. Other approaches towards quicker detection of margins may be to synergistically combine RCM video-mosaicking with either a faster but lower-resolution approach such as OCT,[19–21] or faster but widefield approaches such as multimodal polarization-enhanced reflectance and fluorescence imaging (PERFI) and optical polarization imaging (OPI).[22,23] The ability of OCT imaging to quickly delineate normal skin, and then guide RCM imaging towards detection of BCCs in the remaining suspicious areas was recently reported.[18,19] Similarly, PERFI or OPI may delineate unequivocally normal or positive areas and then guide RCM imaging towards detection in the remaining suspicious areas.

Interpretation of RCM videos and video-mosaics, itself, appears to be relatively straightforward. When assessing the videos and video-mosaics, we found that our evaluators' sensitivity and specificity were both reasonably high (Table 2), when visualizing nuclear detail for the presence or absence of residual tumour, despite artifacts due to scoring and surgery and distortions of the anatomy due to the procedure. Overall agreement between the evaluator's and histopathology was good, and agreement between them was moderate (Table 2). These levels of sensitivity, specificity and agreement are reasonably promising and suggests that improvements in the video-mosaicking algorithm, imaging procedure and reading of video-mosaics may provide a clinically useful tool at the bedside.

In conclusion, delineation of NMSC margins directly on patients with RCM video-mosaicking may potentially serve as an adjunct to traditional histopathology, by providing increased and comprehensive sampling (overcoming the limitations in previous approaches), and helping improve accuracy for clearing margins at the bedside. With further development and prospective validation in larger studies, handheld RCM video-mosaicking may become useful to guide surgery in real-time. In the Mohs surgery setting, this may allow for better patient counselling, fewer staged excisions and reduction of time spent in clinic.

References

1 Correia de Sa TR, Silva R, Lopes JM. Basal cell carcinoma of the skin (part 2): diagnosis, prognosis and management. *Future Oncol* 2015; **11**: 3023–3038.

2 Lane JE, Kent DE. Surgical margins in the treatment of nonmelanoma skin cancer and Mohs micrographic surgery. *Curr Surg* 2005; **62**: 518–526.

3 Jain M, Rajadhyaksha M, Nehal K. Implementation of fluorescence confocal mosaicking microscopy by "early adopter" Mohs surgeons and dermatologists: recent progress. *J Biomed Opt* 2017; **22**: 24002.

4 Longo C, Ragazzi M, Rajadhyaksha M *et al. In vivo* and *ex vivo* confocal microscopy for dermatologic and Mohs surgeons. *Dermatol Clin* 2016; **34**: 497–504.

5 Kadouch DJ, Schram ME, Leeflang MM, Limpens J, Spuls PI, de Rie MA. *In vivo* confocal microscopy of basal cell carcinoma: a systematic review of diagnostic accuracy. *J Eur Acad Dermatol Venereol* 2015; **29**: 1890–1897.

6 Nguyen KP, Peppelman M, Hoogedoorn L, Van Erp PE, Gerritsen MP. The current role of *in vivo* reflectance confocal microscopy within the continuum of actinic keratosis and squamous cell carcinoma: a systematic review. *Eur J Dermatol* 2016; **26**: 549–565.

7 Xiong YD, Ma S, Li X, Zhong X, Duan C, Chen Q. A meta-analysis of reflectance confocal microscopy for the diagnosis of malignant skin tumours. *J Eur Acad Dermatol Venereol* 2016; **30**: 1295–1302.

8 Tannous Z, Torres A, Gonzalez S. *In vivo* real-time confocal reflectance microscopy: a noninvasive guide for Mohs micrographic surgery facilitated by aluminium chloride, an excellent contrast enhancer. *Dermatol Surg* 2003; **29**: 839–846.

9 Marra DE, Torres A, Schanbacher CF, Gonzalez S. Detection of residual basal cell carcinoma by *in vivo* confocal microscopy. *Dermatol Surg* 2005; **31**: 538–541.

10 Scope A, Mahmood U, Gareau DS *et al. In vivo* reflectance confocal microscopy of shave biopsy wounds: feasibility of intraoperative mapping of cancer margins. *Br J Dermatol* 2010; **163**: 1218–1228.

11 Webber SA, Wurm EM, Douglas NC *et al.* Effectiveness and limitations of reflectance confocal microscopy in detecting persistence of basal cell carcinomas: a preliminary study. *Australas J Dermatol* 2011; **52**: 179–185.

12 Pan ZY, Lin JR, Cheng TT, Wu JQ, Wu WY. *In vivo* reflectance confocal microscopy of Basal cell carcinoma: feasibility of preoperative mapping of cancer margins. *Dermatol Surg* 2012; **38**: 1945–1950.

13 Gualdi G, Venturini M, Zanca A, Calzavara-Pinton PG, Pellacani G. Presurgical basal cell carcinoma margin definition: the SMART approach. *J Eur Acad Dermatol Venereol* 2016; **30**: 474–476.

14 Venturini M, Gualdi G, Zanca A, Lorenzi L, Pellacani G, Calzavara-Pinton PG. A new approach for presurgical margin assessment by reflectance confocal microscopy of basal cell carcinoma. *Br J Dermatol* 2016; **174**: 380–385.

15 Larson B, Rajadhyaksha M, Abeytunge S. Fundamentals of Reflectance Confocal Microscopy. In Gonzalez S, eds. *Reflectance Confocal Microscopy of Cutaneous Tumors*. 2nd ed. CRC Press, Boca Raton, FL, 2017: 2–10, chap 1.

16 Kose K, Gou M, Yelamos O *et al.* Automated video-mosaicking approach for confocal microscopic imaging *in vivo*: an approach to address challenges in imaging living tissue and extend field of view. *Sci Rep* 2017; **7**: 10759.

17 Flores ES, Cordova M, Kose K *et al.* Intraoperative imaging during Mohs surgery with reflectance confocal microscopy: initial clinical experience. *J Biomed Opt* 2015; **20**: 61103.

18 Iftimia N, Yelamos O, Chen CJ *et al.* Handheld optical coherence tomography-reflectance confocal microscopy probe for detection of basal cell carcinoma and delineation of margins. *J Biomed Opt* 2017; **22**: 76006.

19 Sahu A, Yelamos O, Iftimia N *et al.* Combined handheld reflectance confocal microscopy – optical coherence tomography probe for detection and depth assessment of basal cell carcinoma: a prospective pilot study. *JAMA Dermatol* 2018; **154**: 1175–1183.

20 De Carvalho N, Schuh S, Kindermann N, Kästle R, Holmes J, Welzel J. Optical coherence tomography for margin definition of basal cell carcinoma before micrographic surgery-recommendations regarding the marking and scanning technique. *Skin Res Technol* 2018; **24**: 145–151.

21 Alawi SA, Kuck M, Wahrlich C *et al.* Optical coherence tomography for presurgical margin assessment of non-melanoma skin cancer – a practical approach. *Exp Dermatol* 2013; **22**: 547–551.

22 Yaroslavsky AN, Feng X, Neel VA. Optical mapping of nonmelanoma skin Cancers-A pilot clinical study. *Lasers Surg Med* 2017; **49**: 803–809.

23 Rohani P, Yaroslavsky AN, Feng X, Jermain P, Shaath T, Neel VA. Collagen disruption as a marker for basal cell carcinoma in presurgical margin detection. *Lasers Surg Med* 2018; **50**: 902–907.

Supplementary data

Peri-operative delineation of non-melanoma skin cancer margins *in vivo* with handheld reflectance confocal microscopy and video-mosaicking

E Flores,[11]* O Yélamos,[1,2] M Cordova,[1] K Kose, [1] W Phillips, [1] E H. Lee, [1] A Rossi, [1] K Nehal, [1] M Rajadhyaksha[1]

[1]Dermatology Service, Memorial Sloan Kettering Cancer Center, New York, NY; USA

[2]Dermatology Department, Hospital Clínic, Universitat de Barcelona, Barcelona, Spain

[*]**Corresponding author:**

Eileen Flores,

360 Shea Drive,

New Milford, NJ 07646

Phone number: 201-315-0777

Email: esf51@psu.edu

[1]Public health science department, Penn state college of medicine, PA.

eFigure 1. Schematic of RCM imaging and video-acquisition procedure.

(Figure reproduced from Flores et al, 2015 (17).

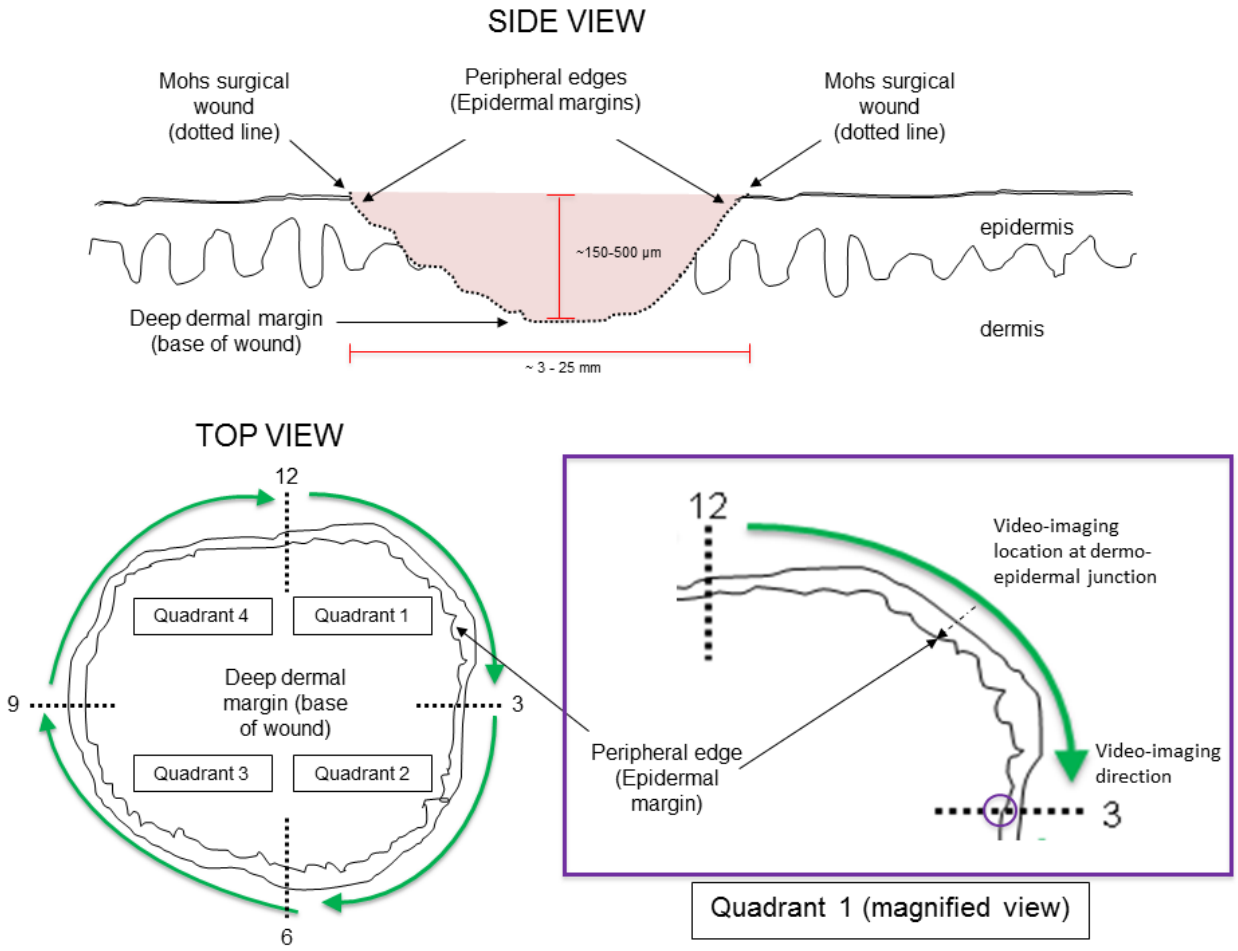

eFigure 2. Pre-operative RCM video-mosaic of biopsy-proven BCC.

Pre-operative RCM video-mosaic of biopsy-proven BCC. Features observed along the scored surgical lateral margins of this lesion: (a) small inflammatory cells, reticular collagen fibers, epidermal disarray and irregular honeycomb pattern from 11 to 12 o'clock in the first quadrant (inset area in yellow rectangle), and (b) shown in a magnified view of the inset. The features are seen in more detail: small inflammatory cells (red arrows), reticular collagen fibers (yellow arrows), epidermal disarray and irregular honeycomb pattern (blue arrows).

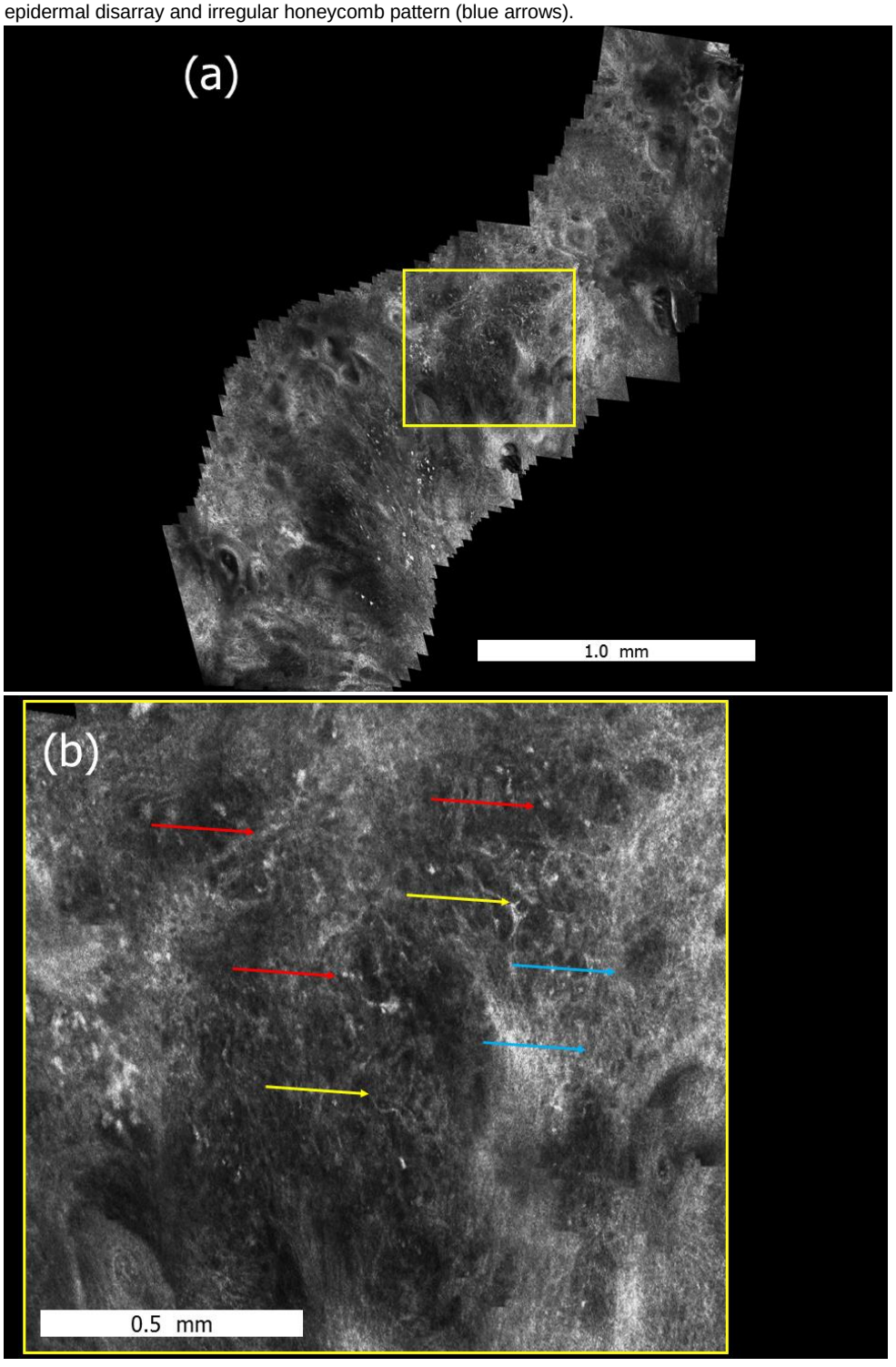

eFigure 3. Pre-operative video-mosaic of a biopsy-proven basal cell carcinoma.

Features observed along the scored surgical lateral margins of this lesion: (a) tumor with clefting and palisading cells (inset area in purple rectangle), and (b) shown in magnified view of the inset (red asterisk).

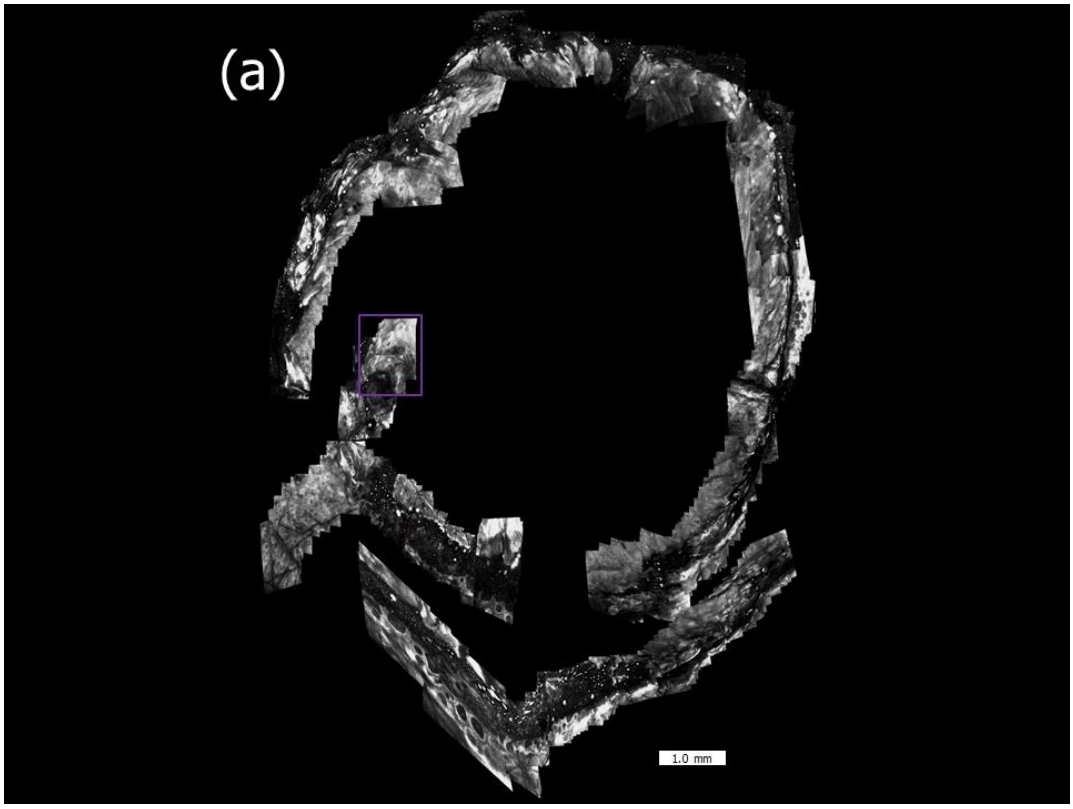

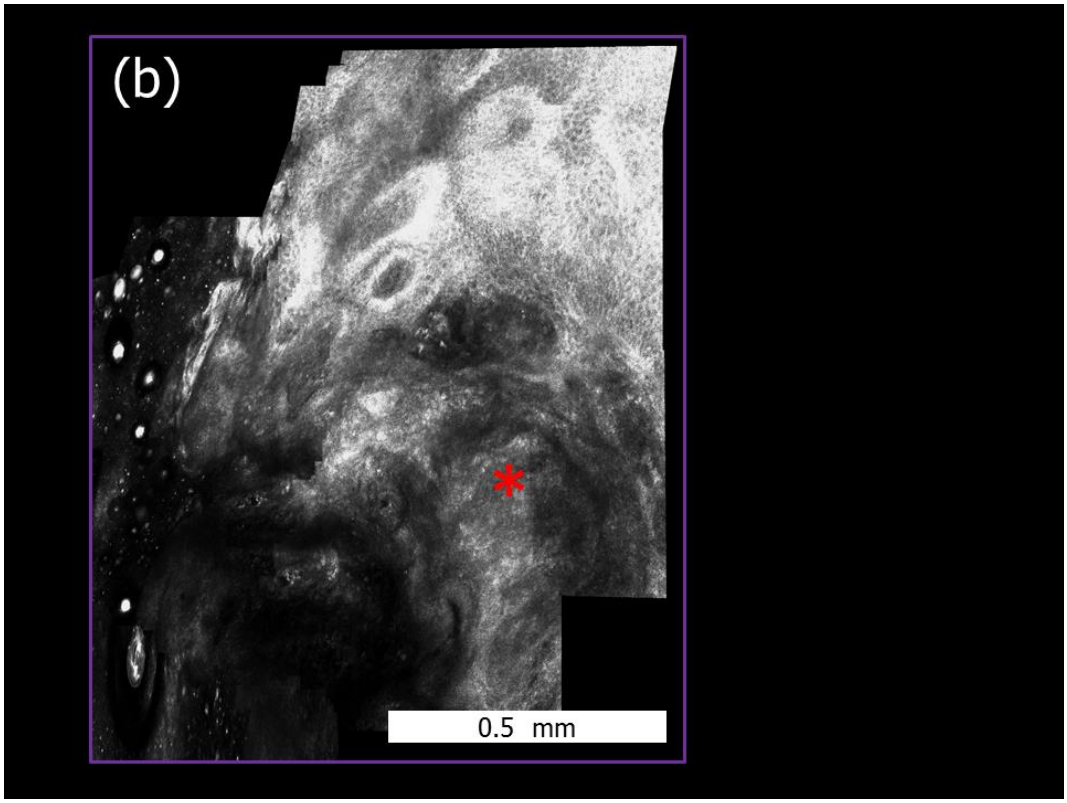

eFigure 4. Pre-operative video-mosaic of a biopsy-proven basal cell carcinoma.

Features observed along the scored surgical lateral margins of this lesion: (a) polarization and epidermal disarray (inset in green rectangle), and (b) shown in magnified view of the inset (area in red circles). Seen, at approximately the 9 o'clock position is a break or discontinuity (labeled "JUMP") in the video-mosaic.

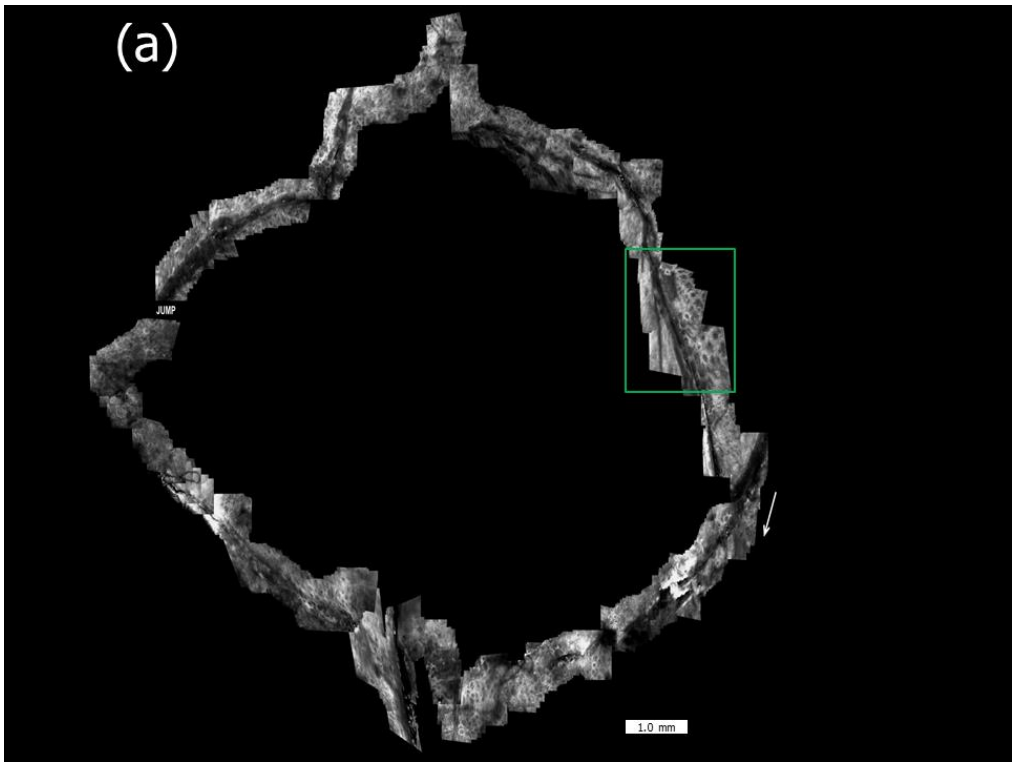

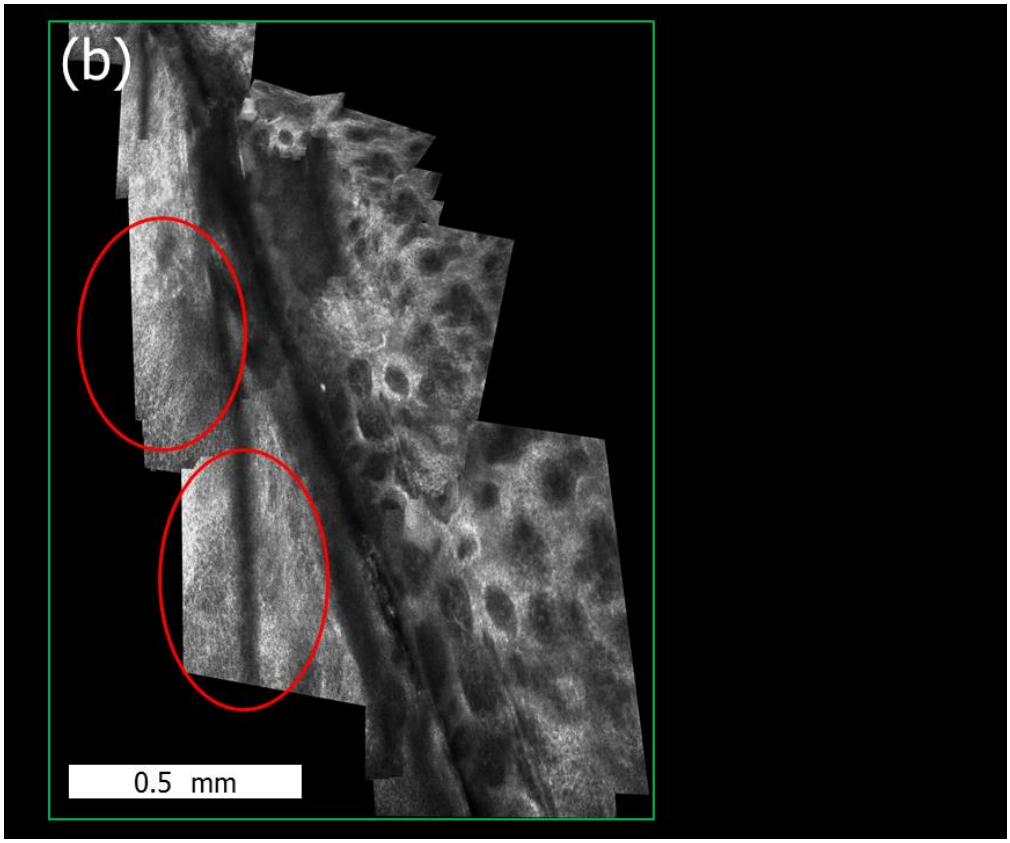

DISCUSSION

1. Expanding the field of view of handheld reflectance confocal microscopy by developing an automated videomosaicking algorithm

RCM is a skin imaging technique with a lateral resolution of 1 µm, but with a small field of view between 0.5 to 1 mm. Since its resolution is quasi-histological, it allows to evaluate details at the cellular level. However, at times it is also necessary to obtain architectural information to better evaluate skin tumors, similarly to conventional histopathological analysis. To achieve this, traditional wide-probe RCM acquires individual high resolution images which are later automatically stitched in mosaics of images up to 8 x 8 mm. However, sometimes skin lesions are larger than 8 mm or sometimes they cannot be assessed with traditional wide-probe RCM devices since it requires attaching a 2 cm metal ring to the patient's skin. In this sense, handheld RCM devices were developed to allow a free and dynamic evaluation in any anatomical area, including concave or convex areas. These devices, more versatile, have the disadvantage that they do not have the capacity to automatically generate mosaics; therefore, the evaluation of the images is reduced to individual small FOVs.[115] In addition, the free movement on the skin of the HRCM makes orientation challenging.[115] As an example of possible consequences of these issues, Castro et al. [116] showed that the diagnostic accuracy is inferior when using the HRCM as opposed to the wide-probe RCM, due to a limited FOV and the lack of mosaicking capabilities. To solve these issues, we developed a computer algorithm that allows generating automated mosaics from videos obtained with the HRCM, called videomosaics. With these videomosaics large areas of tissue can be evaluated and carefully reviewed after image acquisition.

Our videomosaic algorithm is unique because it addresses the 3 big issues encountered when imaging live tissue: (i) deformations due to physical changes (angle, pressure) at the microscope-to-skin contact, (ii) abrupt motion artifacts (“jumps”) caused by sudden changes in depth or in motion (iii) detail and resolution differences between consecutive images due to scattering and aberrations induced by changes in depth and morphology. A scheme of these challenges and the solutions suggested are depicted in Figure 36. Briefly, the algorithm identifies around 1000 keypoints and matches them in tandem in the consecutive frame using SIFT and RANSAC algorithms. Then the two images are aligned by designing affine transformations to allow warping among consecutive frames. This allows addressing the deformations by modeling them. In addition, the properties of the resulting affine transformations are also used to detect abrupt motion artifacts between frames. In other words, when alignment is not possible the algorithm automatically detects the jump and stops stitching more frames to the current videomosaic. This prevents incorrect stitching of frames which would lead to incorrect

architectural and cellular details. With the current version of the algorithm when a "jump" is identified, the videomosaic generation stops at that point but automatically resumes afterwards with a following set of frames. This generates multiple sub-mosaics that can be placed together manually or semi-automatically in an image editor. We acknowledge this is suboptimal and ideally the algorithm should be able to place the different sub-mosaics together. Another way to circumvent this issue would be having the generation of videomosaics "on the fly" or live, so the operator acquiring the images could know whether he/she is located at the right plane of imaging.

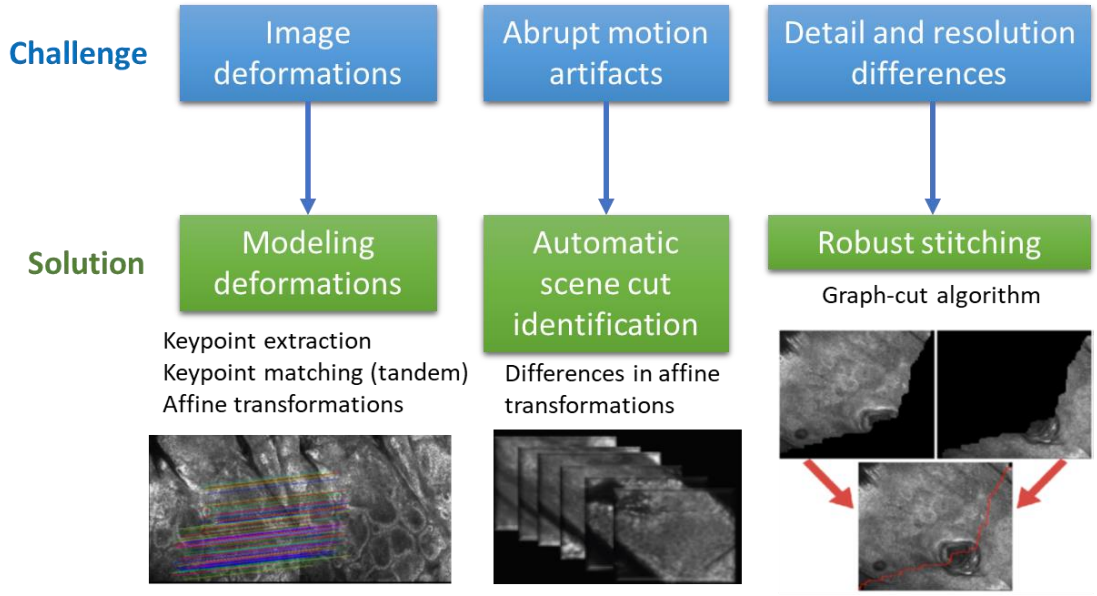

***Figure 36**: General framework of our videomosaicking algorithm showing the challenges and the solutions implemented.*

Finally, the last novelty of our algorithm is the use of a graph-cut approach for image stitching. While this is widely used in computational photography, to our knowledge this is the first application of a graph-cut approach in a microscopy setting. This is important because typical stitching methods average the findings present in two adjacent images. However, averaging the frames may not be correct when evaluating skin cancers with RCM, since slight differences in the plane may allow to visualize a given cell or not, and averaging could make a given cell "disappear" or be less sharp. In addition, since RCM images are highly texturized, averaging them would lead to blurry images. However, our graph-cut approach identifies the area of minimal difference between two adjacent frames, and stitches the two frames based on this imaginary line (Figure 37). This allows a clear and sharp visualization of all the elements present in the two frames, which is crucial when evaluating for example focal dendritic cells at the edge of a LM/LMM. Hence, this approach maximizes the features present in the microscopic videos and allows to have a full representation of all the elements present in the images.

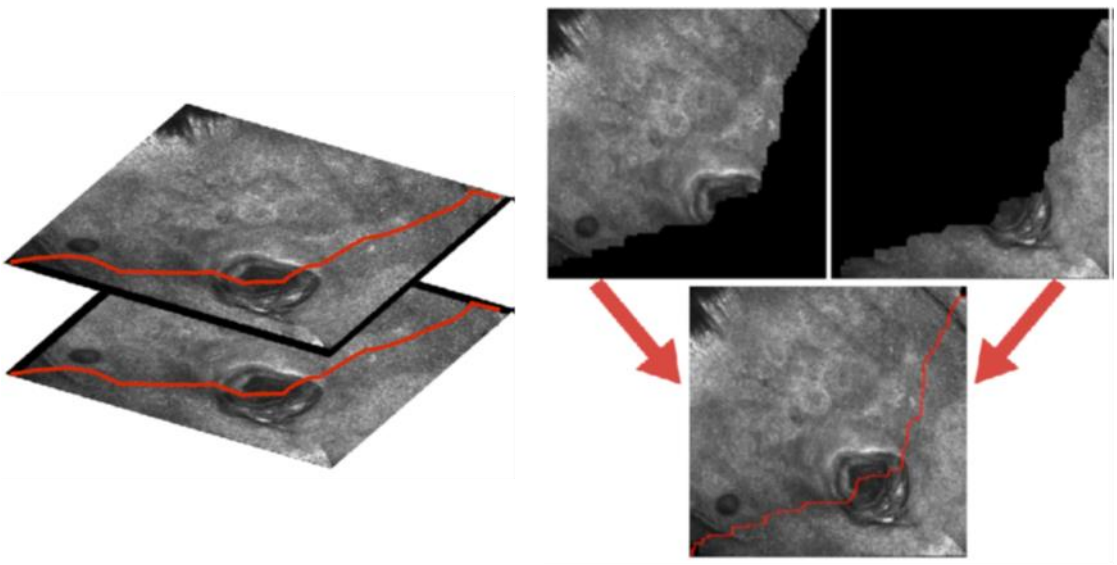

***Figure 37**: The graph-cut algorithm identifies a path that has the minimal differences between two adjacent frames. Later the two frames are then stitched using this line.*

Using this algorithm we have shown that it is possible to obtain large videomosaics over curved areas and therefore **expand the HRCM FOV to more than 1 x 1 mm**, even inside surgical wounds where the wide-probe RCM could not be fitted.

In addition, in this thesis we have implemented automated videomosaics in different clinical scenarios when managing skin cancers. The first scenario illustrated how videomosaicking can help **improve HRCM orientation** by the adjunct use of reference elements such as surgical scores or adhesive paper rings. The second scenario showed how videomosaicking can determine the preoperative margins of LM/LMM and KCs, where the need for **accurate planning of surgical margins** at non-flat corrugated and irregular anatomical sites is met by videomosaicking over arbitrarily large predefined areas of tissue. Our videomosaicking method can offer a streamlined diagnostic and therapeutic procedure. A third scenario showed how videomosaicking can help **detecting focal sites of cancer** within large areas for diagnosing and monitoring persistent/recurrent EMPD, as well as detecting residual KC in surgical wounds both after MMS and after laser ablation.

2. Improving the navigation of handheld reflectance confocal microscopy using videomosaics and scoring methods

Navigating over the skin when using HRCM can be challenging since there is no visual guidance when moving along the skin. To date, orientation depends on the operator, who will decide the motion and the direction of the exploration based on his/her experience, the dim light slightly visible from the laser source of the microscope, as well as the indentation left on the skin by the pressure the microscope cap. The latter was described by Champin et al.[117] to help in the mapping of LM/LMM prior to surgical removal using the spaghetti-technique. Since the tip of the cap of the 3rd generation HRCM microscope has a diameter of 5 mm, one could see the 5 mm indentation of the skin after pressing the cap against the skin. However, with the newer generation of HRCM microscopes with a cap diameter of 1.5 cm this method is not possible.

Another strategy to improve navigation is marking the outer borders of a given lesion by performing a score with a scalpel. This method, reported in several publications,[89,118] is useful in the intraoperative setting since it allows to know whether the operator is located inside or outside the region of interest. We have used this method in the Mohs study (publication number 5, Figure 38)[119] in which we could obtain acceptable imaging in ~92% of cases. However, in the remaining 8% of cases, we could not obtain acceptable images due to motion artifacts. Since tissue can move due to the presence of a physical score, the microscope can get stuck inside the score leading to abrupt movements which result in blurry images. Therefore, now we prefer another method to guide HRCM imaging which combines the use of paper rings and videomosaics.

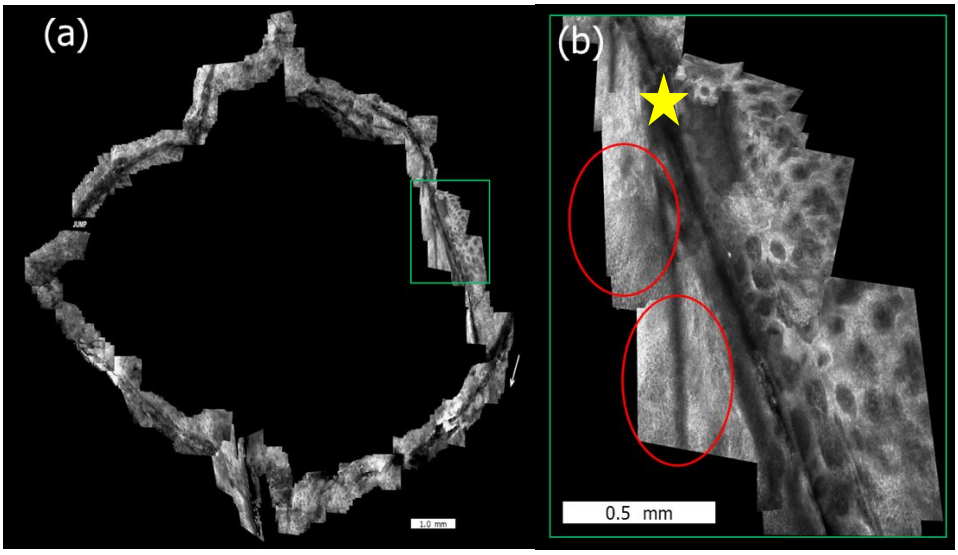

***Figure 38**: Example of a videomosaic obtained on the borders of a basal cell carcinoma prior to Mohs surgery (a). Note the surgical score along the lesion (b, star) to delineate the imaging margins.*

Our group[90] described an easy method to improve the navigation of HRCM by using adhesive paper rings. Since the paper fibers are visible on RCM, one can place paper rings outside the region of interest and demarcate which area needs to be imaged. This method has many advantages as opposed to surgically scoring the skin: it is non-invasive, it is cheap, and it can be used in any surface since paper rings are flexible. Many paper rings are commercially-available, but one can also customize the adhesive rings by simply cutting a piece of adhesive paper tape, or cutting or punching holes in adhesive plastic.[91] In this thesis paper rings have been used together with videomosaics to improve the navigation and the localization of skin cancers such as EMPD (publication 3) or residual BCC after laser ablation (publication 4). However, paper rings and videomosaics can also be used to accurately make distance and area calculations.

As stated in the introduction, the FOV of the HRCM microscope ranges from 0.75 x 0.75 mm to 1 x 1 mm depending on the device generation. In addition, typically this measurement equals 1000 x 1000 pixels regardless of the device generation (Figure 39, B). Since the videomosaic algorithm stitches the individual frames to create a larger image, one can calibrate the videomosaic image using for example Mirror software or ImageJ by assigning that 1000 pixels correspond to 1 mm (if using the 2nd HRCM device), and later one can measure the number of pixels within a videomosaic and determine the distance in mm. However, with the development of new devices, it is possible that the user does not know which are the specifications of the device and whether the FOV corresponds to 1mm or to 0.75mm. Hence, placing an element with a known length within the videomosaic may allow to overcome this issue.

In publication number 2 we have used paper rings and automated videomosaics to calculate the subclinical extent of a series of 23 LM/LMM, and therefore correlate it with the actual surgical defects after staged excision. The paper rings used were commercially-available (product number 1529; 3M), had varying diameters but a fixed rim width of 2.5 mm. Hence, since the paper fibers are visible under RCM, we used the presence of paper rim as a "ruler" to calibrate our videomosaics and make accurate calculations (Figure 39). In other words, since we knew that the paper ring rim was 2.5 mm, we could calibrate the image and make accurate calculations without needing to know which was the device used.

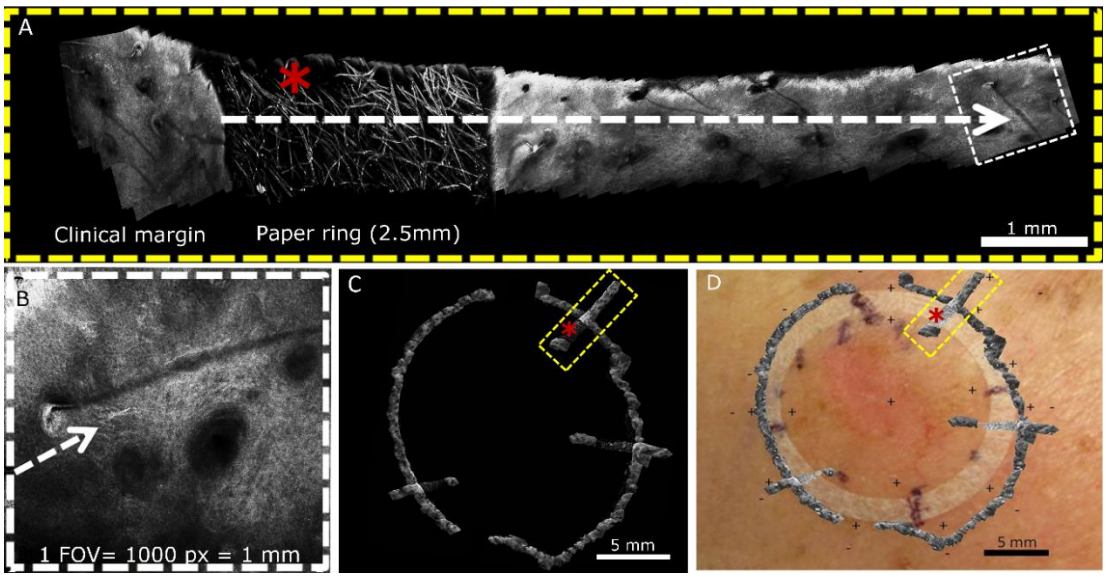

Figure 39: *Example of the combined use of paper rings and videomosaics to perform distance calculations. Since the paper ring has a known width of 2.5 mm, one can calculate the subclinical extent of skin cancers (in this case lentigo maligna) and potentially use this calculations to guide surgery.*

This approach combining paper rings and videomosaics has multiple advantages: it helps navigate within a region of interest, it allows to perform distance calculations, and it overcomes the need of knowing which is the FOV of the microscope used. However, it also has some disadvantages: it does not allow to see what is under the paper fibers, and the paper may detach while sliding on top of it (although it rarely happens). Hence, in the future distance calculation should be integrated in automated videomosaics happening "on the fly" based on the intrinsic specifications of the device (FOV) although it may be useful to have a ruler on the screen in order to more easily contextualize the size of the elements present in a videomosaic. Additional efforts on improving the navigation of HRCM have been described by using a wide-field miniature camera directly on the FOV of the HRCM, thus allowing a near-dermoscopic guidance of the imaging process.[120,121]

3. Planning of surgical margins of skin cancers using handheld reflectance confocal microscopy and automated videomosaics

a) Planning the pre-surgical margins of lentigo maligna/ lentigo maligna melanoma

In cutaneous oncology, some tumors are especially challenging to remove due to its ill-defined borders. An example of such are LM/LMM which occur on heavily sun-damaged skin and present with slightly pigmented flat lesions with ill-defined borders. Typically, several methods have been used to improve the pre-surgical delineation of its margins and include dermoscopy, Wood lamp and scouting biopsies.[66] However, false positives and false negatives occur, even with biopsies, since melanocytic hyperplasia is difficult to contextualize if one cannot evaluate the entire trailing edge of a LM/LMM. Since RCM allows the detection of small amounts of melanin, RCM is a fantastic tool to map amelanotic and hypomelanotic skin lesions such as LM/LMM.[122,123]

Typically, in order to obtain a more comprehensive picture, the wide-probe RCM device has been used to map LM/LMM prior to surgery.[85] However, since LM/LMM can have a considerable size and present in uneven areas, mapping LM/LMM with the wide-probe RCM can be labor-intensive and typically requires 1 hour per lesion.[85] Therefore, it is intuitive that the HRCM device is the ideal tool to map such large lesions located in uneven areas. Previously, other groups have used HRCM to map LM/LMM prior to the spaghetti technique.[117] However, their mapping strategy followed a clockwise approach, thus emulating the surgical approach of the spaghetti technique. However, this has the limitation that is relatively easy to lose orientation, as well as it does not allow to contextualize whether some atypical cells come from the trailing edge of a LM/LMM or are simply activated melanocytes present in photodamaged skin. Therefore, it seems logical that imaging in such cases should be performed from the center to the periphery, in order to see if the atypical cells present at the periphery of a LM/LMM actually correspond to the tumor or not.

In this thesis we have performed a prospective study imaging a series of 23 consecutive LM/LMMs in which the margins were determined by using radial videomosaics from the center to the periphery. Since we have shown that videomosaics together with paper rings improve the HRCM navigation and allow distance calculations (section 2 in the discussion), we have studied whether a good correlation exists between our HRCM mapping method and the actual surgical defect after staged excision of LM/LMM. Our results showed that the mean surgical defect predicted with HRCM and radial videomosaicking were slightly smaller than the actual surgical defect (6.34 vs 7.74 cm^2, $P = 0.01$). In fact, after controlling by age and previous surgery, the margins predicted with HRCM were a mean of 0.76 mm (95%CI, 0.67-0.84 mm; $P < 0.001$) smaller than the actual surgical margins, which is a surprisingly small difference (Figure 41).

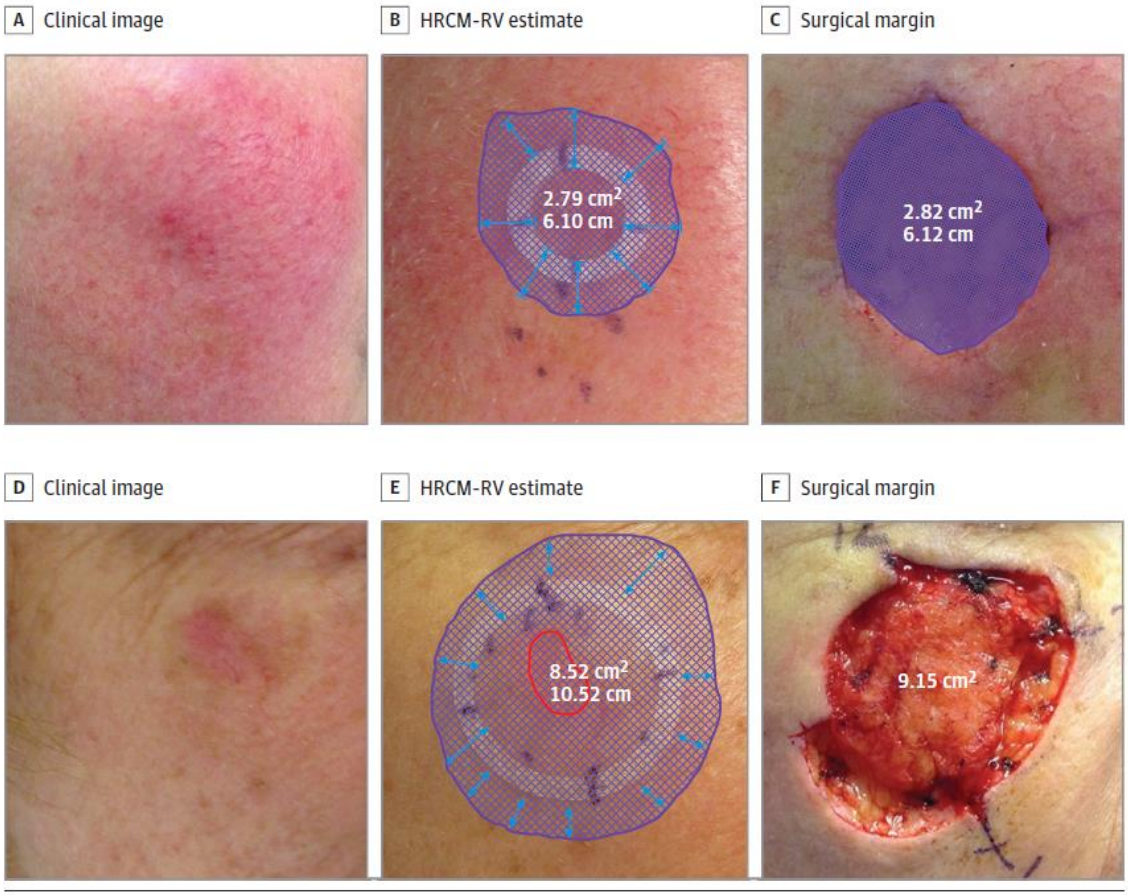

***Figure 40**: Examples of lentigo maligna melanoma imaged with handheld reflectance confocal microscopy with radial video mosaicking and corresponding surgical defects after staged excision. Note that overall the predicted defect was slightly smaller than the actual defect.*

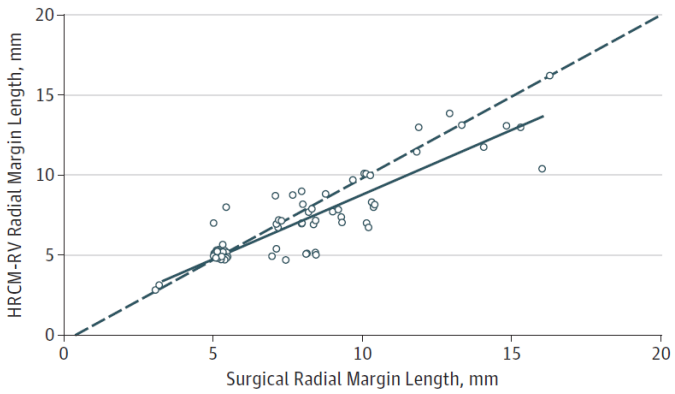

***Figure 41**: Graphical representation of the measurements obtained with handheld confocal microscopy and radial videomosaicking (HRCM-RV) and its concordance with the surgical margins. The dashed line represents the surgical measures and solid line represents the regression line for HRCM-RV. Overall, from our random-effects regression model and controlling for patient age and previous surgery, surgical margins were a mean of 0.76 mm (95%CI, 0.67-0.84 mm; P < .001) larger than the HRCM-RV estimates.*

Our calculations were accurate in most of the quadrants (63%), smaller in 27.2% and only in 9.8% of the quadrants we overestimated the surgical margins. The latter is relevant because in such cases if the surgeon would have followed our indications the defect would have been clear but larger than necessary. Interestingly, these cases, as well as the ones with bigger differences, corresponded to patients who had undergone previous treatments (Table 4, red rectangle), thus suggesting our approach performs better in primary (untreated) LM/LMM. This may be due to the fibrosis present in the

scar tissue surrounding treated LM/LMM. However, our results are encouraging and we are planning on performing a study on untreated LM/LMM using this approach to evaluate the clinical impact of this imaging approach to guide surgery, since our imaging approach could potentially reduce the number of stages of surgery thus reducing costs and streamlining the surgical procedure. In fact, although it was not a primary aim in this study, one can see that the number of stages could have been reduced if HRCM margins were used to guide surgery since good correlation existed between HRCM and the final surgical defect (Table 4, green rectangle). However, these results need to be validated in further larger prospective studies.

Case	Sex	Ethnicity	Location	Breslow (mm)	Prior treatment	No.of surgical stages	Maximum clinical diameter (cm)	Clinical area (cm^2)	RCM LM area (cm^2)	RCM-predicted surgical area (cm^2)	Surgical area (cm^2)
1	Man	White	R Cheek	0	No	4	0.6	0.33	2.87	4.7	5.93
2	Woman	White	R Cheek	0.39	No	2	0.5	0.26	1.31	2.79	2.82
3	Woman	White	R Cheek	0	No	3	1	0.54	6.54	8.52	9.15
4	Woman	White	Nose	0	No	2	1.4	0.95	1.84	3.81	4.92
5	Man	White	L Forehead	0	No	1	1.4	0.87	1.75	3.42	3.39
6	Woman	White	L Cheek	0	Surgery	2	3.1	4.2	4.7	7.1	17.84
7	Man	White	R Cheek	0	Surgery	2	4.9	3.98	6.93	10.43	17.1
8	Man	White	Vertex Scalp	0	No	2	2.1	1.31	2.95	6.3	7.21
9	Man	White	L Cheek	0	Surgery	2	3.9	6.54	8.92	15.27	17.43
10	Man	White	R Scalp	0	No	1	1.4	1.06	1.09	3.5	3.5
11			L Scalp	0	No	2	1.8	1	1.18	4.16	4.34
12	Woman	White	R Cheek	0.35	No	1	1.6	1.17	2.2	4.25	5.22
13	Man	White	Nose	0.3	Surgery, Cryotherapy	3	2.6	2.86	5.13	7.19	7.46
14	Woman	White	L Cheek	0	Cryotherapy	3	1.4	1.14	4.79	6.44	11.5
15	Man	White	L Cheek	1.05	Cryotherapy, 5FU	2	2.2	1.78	4.51	7.38	9.47
16	Woman	White	R Cheek	0	No	1	2.8	3.07	4.03	7.09	7.25
17	Woman	White	L Cheek	0	No	2	0.8	1.03	2.4	3.74	3.38
18	Man	White	R Cheek	0	No	3	0.8	0.82	3.44	6.15	6.58
19	Woman	White	Nose	0	No	1	1.5	1.14	1.66	4.35	4.75
20	Man	White	Glabella	0	No	1	1.5	1.71	1.96	3.78	3.12
21	Woman	White	Nose	0	No	3	1.2	0.58	1.11	1.87	1.61
22	Man	White	Vertex Scalp	0	No	1	3.6	6.03	15.97	19.53	19.67
23	Man	White	R Cheek	0	No	2	0.8	0.5	2.6	4.19	4.54

***Table 4**: Characteristics of the patients and measures of their LM/LMM. The red rectangle highlights the differences in the surgical areas predicted with our approach vs the actual surgical defects. The green rectangle highlights the number of surgical stages that were needed to achieve clear margins, thus suggesting the potential of our approach in reducing surgical stages.*

b) Planning the pre-surgical margins of keratinocyte carcinomas

Another important challenge in cutaneous oncologic surgery is that Mohs surgery, widely used in the USA, is not always available elsewhere due to cost constraints, as well as the need of a separate laboratory with trained technicians and surgeons who are capable of handling the specimens. In this sense, RCM can be of great help since it can delineate the margins of KC thus emulating MMS. Previous studies have used mostly the wide-probe RCM in delineating the preoperative margins[89] which sometimes is not possible due to the presence of KC in uneven surfaces or a lesion size larger than 8 x 8 mm. Since HRCM and videomosaics allow the evaluation of large uneven areas (as shown in section 1 of the discussion), we have performed a study using the HRCM and videomosaicking along the margins of previously-biopsied KC (publication number 5).[119] We obtained videos along the margins of 32 BCC and 3 SCC before being removed with MMS. The lesion size ranged from 0.2 to 2 cm (mean 0.7 cm) and the majority of the lesions were located in the head and neck area (n=21). Among the 35 cases, image quality was good in 32 cases and tumor was identified in all the cases, thus suggesting that tumor margins can be identified with HRCM and videomosaicking. In the remaining 3 cases, image quality was poor and tumor could not be identified. The reasons for poor quality were mostly motion artifacts which led to blurry images. Therefore, although our results are promising and show that it is possible to use our approach to plan surgery of KC, a more refined acquisition method, such as using a robotic arm attached to the RCM and controlled using a joystick, may reduce motion artifacts and allow accurate pre-surgical delineation of skin cancers.

4. Detection of small foci of tumor cells using handheld reflectance confocal microscopy and automated videomosaics

The research presented in this thesis has shown that by using HRCM and videomosaics it is possible to identify small foci of tumor in different clinical scenarios. This is crucial in cutaneous oncology where small foci of cells left after treatment may be responsible for disease recurrences impacting negatively on the patient. We have used HRCM and videomosaics in two situations to identify small foci of skin cancer: 1) detecting recurrent/persistent EMPD; 2) identifying small foci of KC after Mohs surgery and after laser ablation.

a) Using HRCM and videomosaics to identify small foci of Paget cells

As stated earlier in this thesis, EMPD is a very challenging disease due to its location (mostly the genital and perianal area) which limits its surgical margins thus leading to a high rate of recurrences/persistence. These recurrences are mainly caused by the suboptimal elimination of tumor cells after treatment, due not only to the location but also due to the patchy distribution of the cancer cells which makes even Mohs surgery challenging. HRCM has been used in previous studies to map preoperatively the surgical margins of EMPD, with good but variable results.[86,124] However, no studies had assessed its usefulness in identifying recurrent/persistent EMPD.

EMPD is characterized by the presence of patchy foci of a subset of tumor cells called Paget cells. Hence, identifying these cells can be very challenging especially after treatment has been performed, leading to numerous scouting biopsies which are not always possible or desirable, and which can also show false negatives. RCM is a non-invasive alternative that may help guide biopsies. However, identifying Paget cells on RCM is very challenging due to 1) Paget cells have low brightness due to a large cytoplasm devoid of melanin (Figure 42) 2) Paget cells may be located in a patchy distribution of clustered or single cells.[125] Therefore, in the setting of EMPD, HRCM evaluation needs methods to expand its FOV to identify isolated cells.

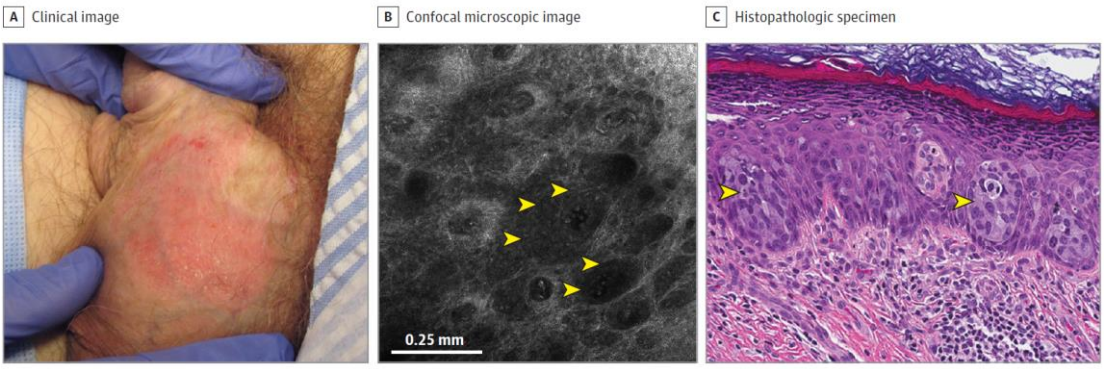

Figure 42: *correlation between clinical, confocal and histological findings in an EMPD case. Note that in the confocal images (B), the Paget cells are large and hyporefractive, sometimes making their identification challenging (Adapted from Yélamos et al. JAMA Dermatol. 2017 Jul 1;153(7):689-693).*

In this sense we performed a study to assess the performance of HRCM in identifying Paget cells in a series of 22 locations present in 5 previously-treated EMPD patients. The study showed an overall sensitivity and specificity of 75% and 100%, respectively, to identify recurrent/persistent EMPD. We have identified 3 false positives locations out of 22 areas interrogated with HRCM. Initially, we believed that these false positive were due to the presence of old fibrosis which may have obscured the HRCM evaluation. However, when reviewing the histopathological findings, no significant fibrosis was found, thus suggesting that the areas were missed simply due to sampling bias. These 3 samples came from 3 patients in whom videomosaics were not used, and were imaged prior to the development of the videomosaicking algorithm. However, in the last 2 patients we used our navigation approach with paper rings and videomosaics to explore 8 EMPD sites since the videomosaicking algorithm had been developed. Using this approach we could better select the areas in which Paget cells were identified (Figure 43).

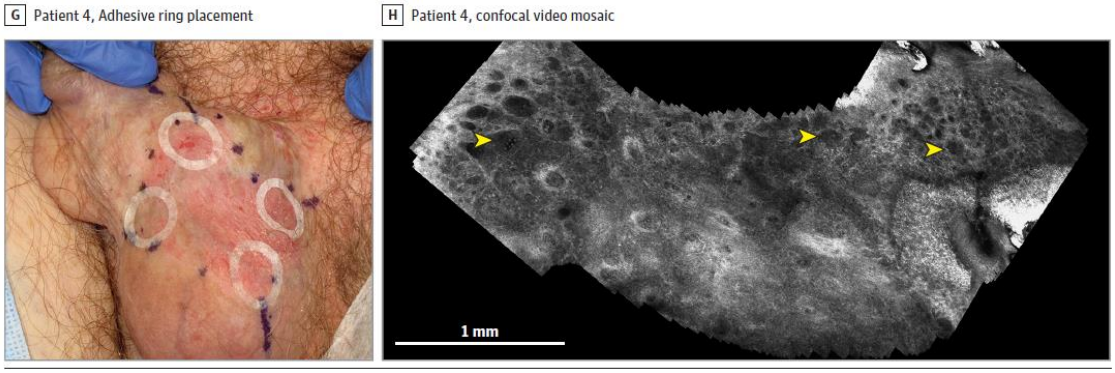

Figure 43*: A large area in a patient with suspected recurrent EMPD was explored with HRCM. First we placed paper rings at the regions of interest and videomosaics were obtained in quadrants to assess the skin surface (Adapted from Yélamos et al. JAMA Dermatol. 2017 Jul 1;153(7):689-693).*

Although not present in the manuscript published in JAMA Dermatology due to editorial decisions, our results showed that videomosaics improve the diagnostic accuracy of HRCM in identifying recurrent/persistent EMPD, with an increase in the sensitivity from 57.1% to 100% (no false negatives) while retaining a 100% specificity (P = 0.0339) (Figure 44).

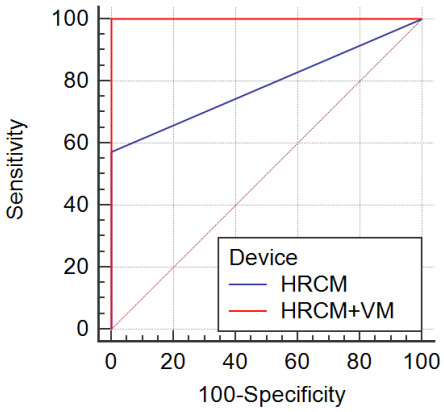

***Figure 44**: Comparison of independent ROC curves between handheld reflectance confocal microscopy (HRCM) alone vs HRCM with videomosaicking (HRCM+VM) for the detection of recurrent/persistent EMPD. Using the DeLong test there was a statistically significant difference in the diagnostic accuracy (P = 0.0339) showing that the addition of videomosaics increases the diagnostic accuracy of HRCM.*

However, we also acknowledge that our results, although promising, need to be taken with caution since the cases evaluated with HRCM and HRCM with videomosaics were not the same. Furthermore, improved learning curved over time may have impacted positively in the identification of EMPD in the last 2 patients. Nevertheless, we believe the addition of videomosaics to conventional HRCM could greatly improve the diagnostic accuracy of EMPD not only to identify recurrences but to also plan surgery of such challenging skin cancers. Future lines of research should focus in developing imaging techniques which may allow the identification of Paget cells located deeper than 250 µm (for example using the recently described combined RCM-optical coherence tomography [OCT][126,127] or line-field confocal OCT [LC-OCT][128] devices), as well as developing in vivo staining methods such as photodynamic diagnosis together with RCM[129] that may enhance the visualization of isolated Paget cells.

b) Using HRCM and videomosaics to identify small residual keratinocyte carcinomas immediately after treatment

Keratinocyte carcinomas (KC) are the most common skin cancers and its incidence is rising. Mohs micrographic surgery (MMS) is used as a standard method to precisely remove KC while preserving healthy skin. However, MMS is time-consuming, expensive and requires a separate laboratory to perform the analysis. Hence, alternative methods to treat KC are being developed as an alternative to conventional margin-controlled surgical methods. In this sense, RCM is a promising tool since can be used to delineate the preoperative margins when surgery is chosen (as shown in section 3 of the discussion) but can also help guide laser ablation as well as identify small residual tumor immediately after treatment directly in the wound bed.

In order to show if it was feasible to identify focal residual KC after surgery, we have used HRCM and videomosaics to assess the surgical wound of a series of 35 KC (32 BCC, 3 SCC) treated with MMS (publication number 5).[119] Briefly, using a sterile cap attached to the HRCM device, we have obtained videos directly inside the surgical wounds in the 4 quadrants of the lesion in a clockwise fashion (Figure 45), as well as videos inside the central part of the wound. These videos were later converted into videomosaics to assess the presence of absence of tumor after the first stage of MMS.

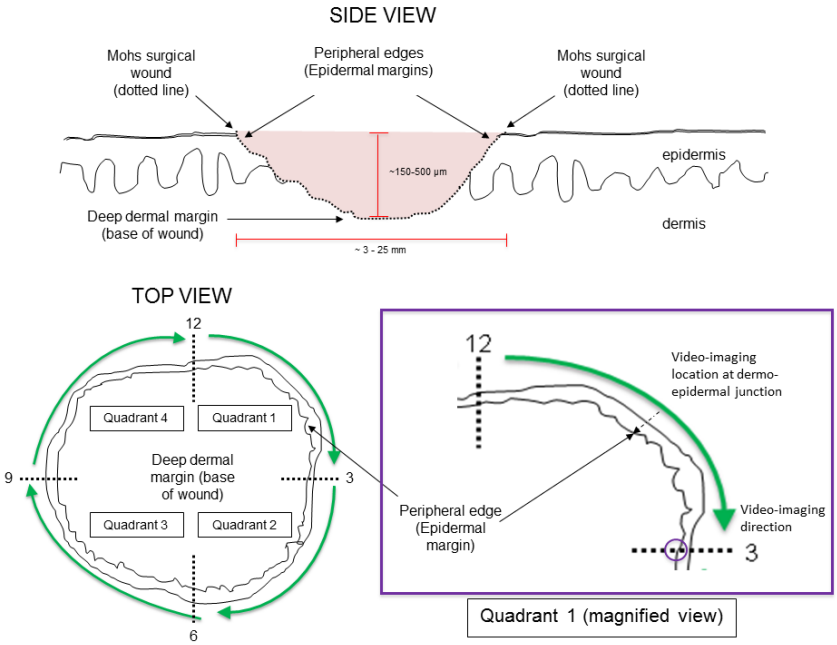

***Figure 45**: Imaging method performed inside the surgical wound just after the first stage of Mohs surgery (Adapted with permission from Flores et al. J Biomed Opt. 2015 Jun;20(6):61103)*

Our results showed that it is feasible to obtain videos and videomosaics inside the surgical wound thus allowing the identification of residual tumor after MMS. Among the 32 cases with good imaging quality, 14 cases had residual tumor on histopathology which in 10 cases were correctly identified with HRCM and videomosaicking. The 4 false negatives were indeed cases with an infiltrative tumor component or tumor present deeper than 250 µm. When assessing the histologically-negative cases, 18 cases were correctly classified with HRCM and videomosaicking but in 3 cases HRCM and videomosaicking suggested the presence of tumor (Table 5). Interestingly, these 3 false positives were due to the presence of tumor mimickers such as sebaceous glands, eccrine ducts and hair follicles. Taken all the results together, our imaging approach had a 71.4% sensitivity and 85.7% specificity for identifying residual KC intraoperatively directly in the surgical wound. We acknowledge that these results are good (they prove it is possible to identify residual tumor in the surgical wound) but not excellent, and further improvement of the technique is needed.

		Histology	
		Positive	Negative
HRCM + VM	Positive	10	3
	Negative	4	18

Table 5: Concordance between the evaluation with handheld reflectance confocal microscopy and videomosaics and histology for the intraoperative evaluation just after the first stage of Mohs surgery. Abbreviations: HRCM: HRCM, Handheld Reflectance Confocal Microscopy; VM, videomosaics)

In addition to using RCM as an adjunct to conventional or Mohs surgery, RCM has also been used to guide laser ablation of small low-risk BCC as well as identify small residual BCC after ablation. Since a significant number of BCC are superficial or early nodular, they could be treated with methods alternative to Mohs surgery. Laser ablation has been suggested as a fast and safe treatment modality for BCC with potential benefit in cosmetic outcome. This modality could be particularly useful in patients with numerous KCs such as patients who underwent radiotherapy or patients with the Gorlin syndrome. However, the major limitation of laser ablation is the lack of histological margin control, and, therefore, the inability to confirm tumor clearance. RCM offers non-invasive cellular visualization of the epidermis and superficial dermis and has been successfully used to detect BCC in vivo with a sensitivity and specificity of 92-100% and 88-97%, respectively.[130-132] Hence, RCM can be used to identify residual BCC after ablative techniques such as laser ablation and thus overcoming the limitation of not obtaining histological confirmation of complete tumor removal. In this sense, we designed a study in which RCM helped guide the number of passes of Erbium:YAG laser ablation as well as confirmed complete BCC removal (publication number 4).[55]

Briefly, (Figure 46) RCM mosaics of the lesions were obtained using the wide-probe RCM prior to laser ablation to determine lateral and deep margins of the tumor. After local anesthesia and following the RCM findings, BCC were treated using an Erbium:YAG laser. Total laser energy delivered was based on the depth of tumor and previous benchtop studies.[133] Aluminum chloride 35% was then applied for hemostasis and to enhance nuclear contrast.[134] To screen for residual BCC after the ablation, HRCM was performed directly onto the wound and edges moving in a clockwise fashion (Figure 47). The borders were delimited with paper rings to improve orientation. If BCC nests were identified, additional laser ablation was performed focally until total clearance was determined by HRCM.

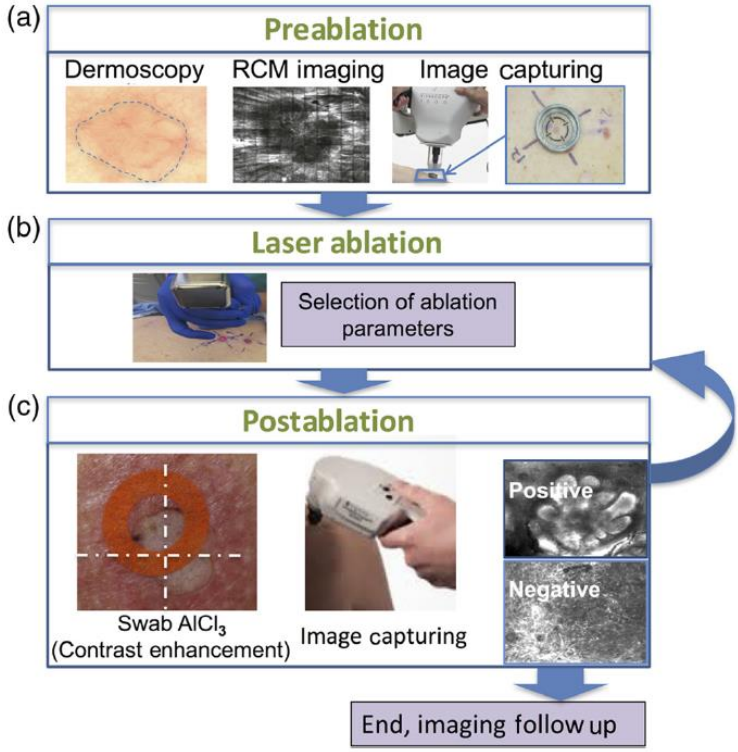

Figure 46: Scheme of the basal cell carcinoma laser ablation protocol.

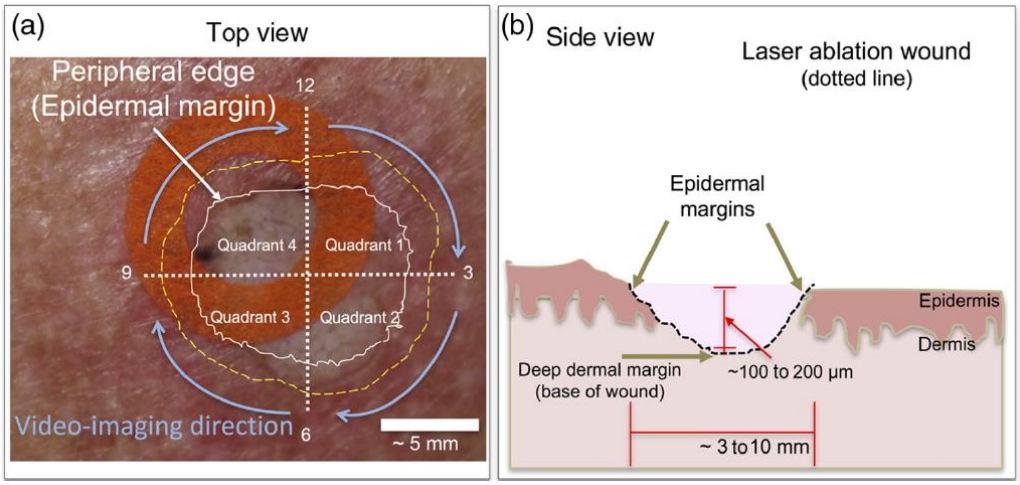

Figure 47: Method used to evaluate the presence of residual BCC after laser ablation. The white line represents the wound margin, and the yellow line represents the outer area imaged. Therefore, the videomosaic is obtained within the tissue delimited by these two lines. Note that the paper ring is moved along the quadrants in order to navigate through the laser-ablated wound.

Our study had two phases; in the first phase, 10 BCCs were laser-ablated and later excised to confirm the presence or absence of residual tumor. In this phase, we acquired videos in the different lesion quadrants which were later processed into videomosaics to assess the presence or absence of residual tumor. In these 10 lesions, HRCM with videomosaicking correctly classified all the lesions, although in one case (number 4) the diagnosis of persistence was rendered with low confidence (Table 6).

Lesion	BCC subtype	Estimate *d* depth	Number of passes	Residual BCC in assessed by RCM	Residual BCC on vertical histology postablation
1	Superficial and early nodular	175	9	Yes	Yes
2	Superficial and early nodular	180	8	Yes	Yes
3	Superficial intradermal component	210	9	Yes	Yes
4	Superficial and infiltrative nodular	180	9	Suspicious	Yes
5	Superficial and early nodular	150	8	No	No
6	Superficial	85	5	No	No
7	Superficial	88	5	No	No
8	Superficial	116	6	No	No
9	Superficial	125	7	No	No
10	Superficial and early nodular	135	7	No	No

Table 6: *Results of the first phase of the BCC laser ablation study. Note that HRCM + videomosaics correctly identified the 4 cases where residual BCC was still present after Er:YAG laser ablation (in case 4 with low confidence)*

In the second phase of this study, we used HRCM to assess the presence or absence of residual tumor after laser ablation in a series of 34 BCC cases which later would be followed over time. However, videomosaics were not readily available in the clinical setting just after ablation since currently videomosaics cannot be obtained “on the fly” and require post-processing. Hence, decisions were made based on the live visualization of the epidermal margin and wound bed using only HRCM. Using this approach, we identified 3 recurrences in the 22 cases with long follow-up (>6 months). This suggests that we have missed very small tumor areas after laser ablation which were not identified with HRCM alone. Since the concordance between HRCM + videomosaics and histology was excellent in the first phase, whereas recurrences occurred in the second phase where no videomosaics were available, one could suggest that videomosaics improve the detection of small foci of tumor.

We believe that having “on the fly” videomosaics could have improved our outcomes by reducing sampling bias since it expands the FOV and helps orientation. This is supported by the fact that we did not see residual BCC in the first phase of our laser ablation study where videomosaics were generated for evaluation and later confirmed with histology. However, we also acknowledge that possibly the recurrences seen in these patients may have occurred due to the presence of a deeper tumor component beyond 250 µm. A similar problem was encountered in the Mohs study, in which HRCM and videomosaics missed 4 positive cases with a deep component. However, this is something that can be overcome with the development of technologies that can image deeper such as OCT.

5. Future directions in skin imaging in vivo

In this thesis, we have described a novel computer algorithm to generate automated mosaics from videos obtained with HRCM. We have shown that HRCM videomosaics expand the FOV of HRCM to evaluate large skin areas even in uneven surfaces, allow distance calculations which can be used to better plan surgical procedures, improve the detection of small foci of tumor cell, and enable a better orientation while using HRCM together with the use of scoring methods such as paper rings. In the near future we expect videomosaics to be integrated into the HRCM native software for routine use, ideally by providing live "on the fly" videomosaics which automatically will allow the calculation of distances. In addition, although our algorithm was used in skin RCM, it can be applicable to virtually any live microscope. In fact, we have also tested this algorithm in videos obtained from mucosal RCM using a telescopic probe in a case of buccal amalgam tattoo (*Figure 48*), and efforts are performed to study intraoral SCC with this device.

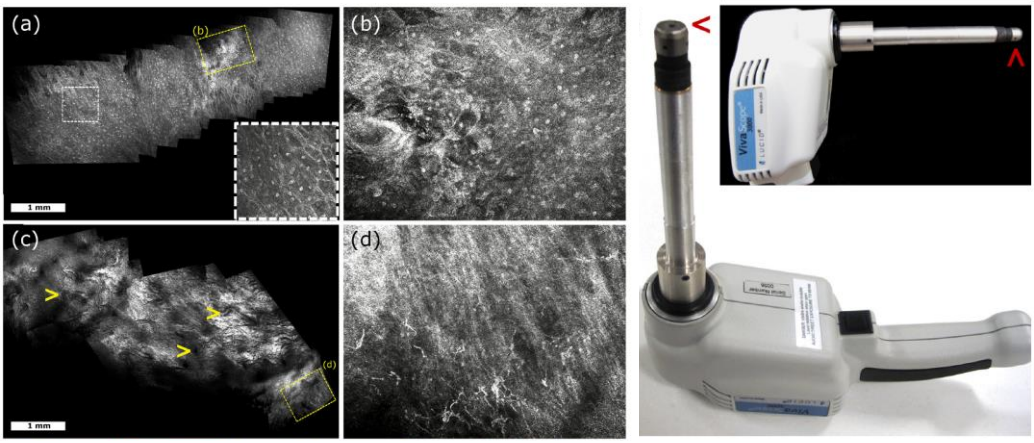

Figure 48: Examples of videomosaics obtained in the oral mucosa to assess an amalgam tattoo using a telescopic probe attached to the HRCM (Adapted with permission from Yélamos et al. Dermatol Pract Concept. 2017 Oct 31;7(4):13-16)[135] Present in addendum 2.

However, our current approach has limitations and needs to be improved. Future lines of research should focus on making this algorithm faster using artificial intelligence and machine learning methods (currently it takes around 10 minutes to generate a videomosaic obtained from a 1 minute video). Another potential field of improvement is the simultaneous acquisition of videos and videomosaics at different depths (e.g. epidermis, dermal-epidermal junction and dermis) by using multiple laser sources. This would allow a more comprehensive imaging which could be very useful for example when mapping pre-surgically or intraoperatively. Currently, one of the main limitations of RCM in general is the fact that its resolution is limited to 250 µm in depth. To overcome this limitation, our group has worked in developing a novel multimodal imaging device that combines RCM and OCT in the same FOV, thus expanding the FOV

laterally to 2 mm and in depth to 1 mm, thus helping identify tumor cells deeper than 250 µm (Figure 49, addendum 3 and 4). [126,127,136] High frequency ultrasonography also seems a promising tool, since it is cheaper than other techniques, includes the possibility to assess blood vessels using the Doppler mode, and has been used to determine tumor margins both in vivo[137] and ex vivo.[100,138] Alternatively, the recent development of line-field confocal optical coherence tomography (LC-OCT),[128] a technology with a FOV similar to OCT (1 cm) but a resolution similar to RCM (~1 µm), may represent an absolute revolution in the future of skin imaging.

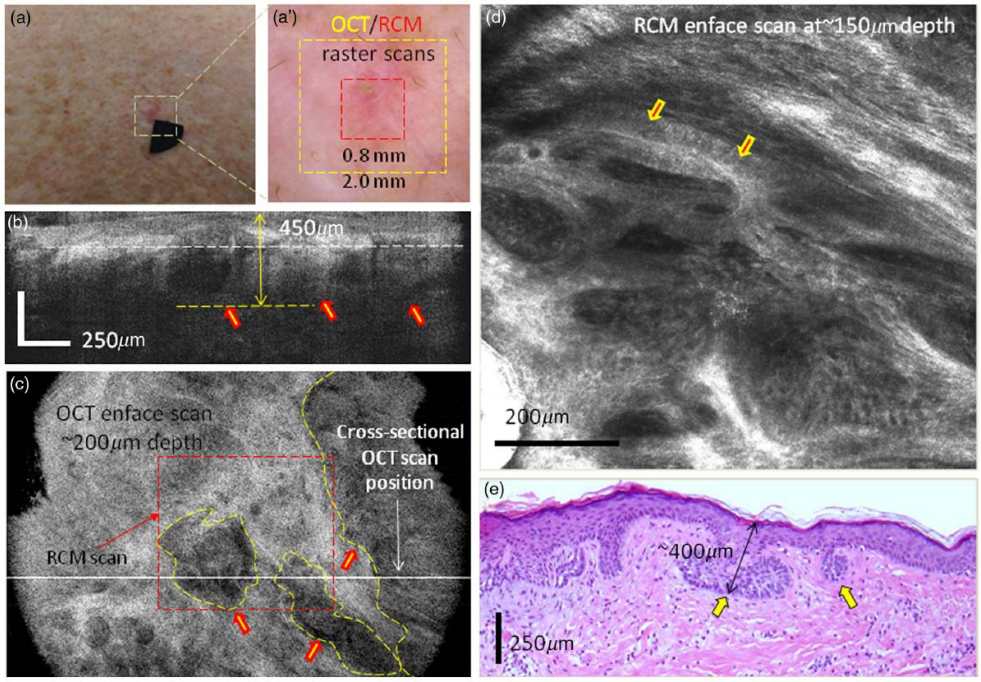

***Figure 49**: Example of a basal cell carcinoma evaluated with the combine RCM-OCT device. Tumor cords are visible with OCT (c) and with RCM (d) in the same field of view. (Adapted from Iftimia et al. J Biomed Opt. 2017 Jul 1;22(7):76006.)*

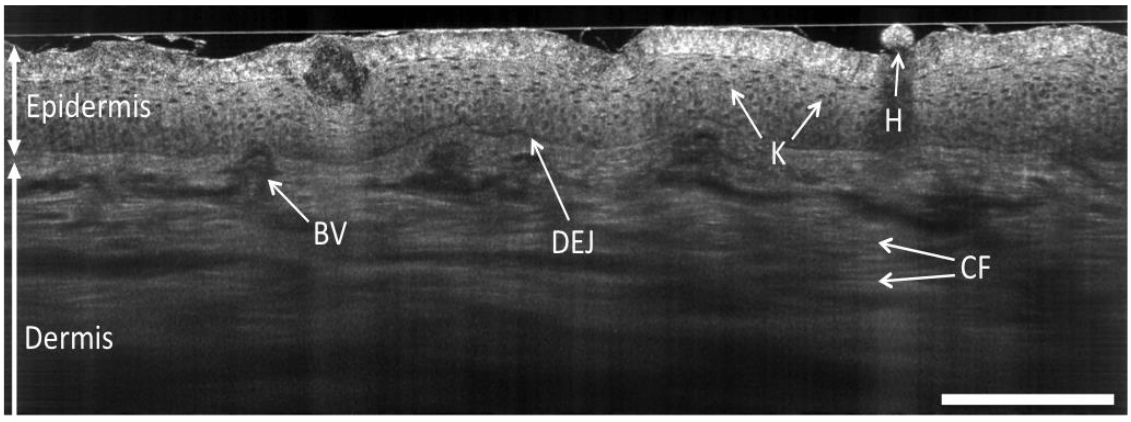

***Figure 50:** Cross-section of normal skin using line-field confocal optical coherence tomography. Note the high resolution and increased imaging depth. (Source http://damaemedical.fr)*

In the future one may envision RCM as a multimodal combination of different imaging technologies attached to a robotic arm. In this setting, the probe could move in a standardized manner but if needed one could detach the probe and use it freely over the skin by obtaining automated videomosaics, either using manual navigation or a more controlled navigation using a joystick. Since machine learning algorithms are showing promising results in diagnosing skin cancers using clinical and dermoscopic images,[139,140] it is also a matter of time to have these algorithms integrated in the RCM or other imaging devices. In fact, currently several algorithms have been described that identify automatically the DEJ,[141,142] but in the future additional algorithms may not only identify structures or provide a diagnosis but may identify whether there is residual tumor on the margins of a scar.

Later, real time images of the tumor could be generated and projected onto the skin or visualized using augmented or mixed reality lenses, thus guiding surgeons on where to cut with safety margins. Although this may sound science fiction, currently mixed reality devices such as Microsoft HoloLens® (**Figure 51**) have already been described in multiple medicine fields such as neurosurgery or orthopedics[143,144] (**Figure 52**).

Figure 51: *An orthopedic surgeon in the Avicenne de Bobigny Hospital in France using HoloLens to assist a surgical procedure*

(source:https://immersive-technology-healthcare.hcs-pharma.com/2017/12/13/france-performs-worlds-first-virtual-reality-surgery/)

Figure 52: *Example of a pre-operative spinal procedure guided by Microsoft HoloLens®, a mixed reality device which has already been already approved by the FDA to be used pre-operatively in some procedures (source: https://www.realitytechnologies.com/first-augmented-reality-system-for-microsoft-hololens-cleared-by-fda-for-surgical-use/)*

Finally, one may argue that using RCM to guide treatment and serve as an alternative is not possible option due to its current high cost. However, a newer low-cost reflectance confocal microscope attached to a smartphone has been developed,[145] thus expanding its potential availability. Since the efficiency of technology increases over time as well as its costs decrease as determined by the Moore's law, it is just a matter of time that RCM will become another of the tools that physicians and researchers may use routinely, and who knows if it will become the evolution of the 21st century dermatoscope (**Figure 53**).

Figure 53*: Simulation of a small portable reflectance confocal microscope. In the future one can envision a portable microscope which could be coupled to a smartphone (Source: Dr Ashfaq Marghoob®).*

CONCLUSIONS

1. Our algorithm addresses the main problems encountered in skin imaging by (i) directly modeling deformations, (ii) automatically detecting abrupt motion artifacts (discontinuities) in the image sequence, and (iii) robustly stitching the registered frames with an approach that combines overlapped images flexibly, in a data-driven fashion, without blurring or loss of resolution.

2. HRCM with automated videomosaicking allows detailed imaging of non-flat, corrugated and irregular anatomical sites over arbitrarily large predefined areas.

3. Paper rings with predefined sizes are helpful to get spatial information while using HRCM, and help calibrate the videomosaics thus allowing accurate distance calculations.

4. HRCM with automated videomosaicking is accurate in delineating the pre-surgical margins of LM/LMM (mean difference of 0.76mm [95%CI, 0.67-0.84 mm; $P < 0.001$] smaller than the actual surgical defect).

5. HRCM with automated videomosaicking is promising in delineating the pre-surgical margins of BCC/SCC, but may fail to identify a deeper component.

6. HRCM videos can be obtained inside a cutaneous wound after surgery or laser ablation and can be converted into videomosaics with good quality.

7. HRCM and videomosaicking can detect small and focal sites of tumor within widely spread areas for diagnosing and monitoring of skin cancers such as EMPD or residual BCC/SCC after treatment.

8. HRCM has good diagnostic accuracy (sensitivity 75% and specificity 100%) for identifying recurrent/persistent EMPD, and seems to be enhanced by the addition of automated videomosaics.

9. HRCM and videomosaics obtained from surgical wounds can rapidly identify residual KC in most cases, but may fail to identify tumor if deeper than 250 µm

10. Peri-operative HRCM videomosaicking of skin cancer margins directly on patients can guide surgery, serve as an adjunct to histopathology, reduce time spent in clinic and reduce the need for re-excisions.

REFERENCES

1. Rogers HW, Weinstock MA, Feldman SR, Coldiron BM. Incidence Estimate of Nonmelanoma Skin Cancer (Keratinocyte Carcinomas) in the U.S. Population, 2012. *JAMA Dermatol.* 2015;151(10):1081-1086.
2. Que SKT, Zwald FO, Schmults CD. Cutaneous squamous cell carcinoma: Incidence, risk factors, diagnosis, and staging. *J Am Acad Dermatol.* 2018;78(2):237-247.
3. Karagas MR, Stukel TA, Greenberg ER, Baron JA, Mott LA, Stern RS. Risk of subsequent basal cell carcinoma and squamous cell carcinoma of the skin among patients with prior skin cancer. Skin Cancer Prevention Study Group. *JAMA.* 1992;267(24):3305-3310.
4. Siegel RL, Miller KD, Jemal A. Cancer statistics, 2018. *CA Cancer J Clin.* 2018;68(1):7-30.
5. Lopes Filho LL, Lopes IM, Lopes LR, Enokihara MM, Michalany AO, Matsunaga N. Mammary and extramammary Paget's disease. *An Bras Dermatol.* 2015;90(2):225-231.
6. Kim BJ, Park SK, Chang H. The Effectiveness of Mapping Biopsy in Patients with Extramammary Paget's Disease. *Arch Plast Surg.* 2014;41(6):753-758.
7. Wu X, Elkin EE, Marghoob AA. Burden of basal cell carcinoma in USA. *Future Oncol.* 2015;11(22):2967-2974.
8. Kauvar AN, Cronin T, Jr., Roenigk R, Hruza G, Bennett R. Consensus for nonmelanoma skin cancer treatment: basal cell carcinoma, including a cost analysis of treatment methods. *Dermatol Surg.* 2015;41(5):550-571.
9. Tromme I, Legrand C, Devleesschauwer B, et al. Cost-effectiveness analysis in melanoma detection: A transition model applied to dermoscopy. *Eur J Cancer.* 2016;67:38-45.
10. Koelink CJ, Vermeulen KM, Kollen BJ, et al. Diagnostic accuracy and cost-effectiveness of dermoscopy in primary care: a cluster randomized clinical trial. *J Eur Acad Dermatol Venereol.* 2014;28(11):1442-1449.
11. Thomas L, Puig S. Dermoscopy, Digital Dermoscopy and Other Diagnostic Tools in the Early Detection of Melanoma and Follow-up of High-risk Skin Cancer Patients. *Acta Derm Venereol.* 2017.
12. Yélamos O, Braun R, Liopyris K, et al. Usefulness of dermoscopy/dermatoscopy to improve the clinical and histopathologic diagnosis of skin cancers. *J Am Acad Dermatol.* 2019;80(2):365-377.
13. Karimkhani C, Boyers LN, Dellavalle RP, Weinstock MA. It's time for "keratinocyte carcinoma" to replace the term "nonmelanoma skin cancer". *J Am Acad Dermatol.* 2015;72(1):186-187.
14. Amin B, Nehal K, Jungbluth A, et al. Histologic distinction between subungual lentigo and melanoma. *Am J Surg Pathol.* 2008;32(6):835-843.
15. Wollina U, Goldman A, Bieneck A, Abdel-Naser MB, Petersen S. Surgical Treatment for Extramammary Paget's Disease. *Curr Treat Options Oncol.* 2018;19(6):27.
16. Wade TR, Ackerman AB. The many faces of basal-cell carcinoma. *J Dermatol Surg Oncol.* 1978;4(1):23-28.
17. Marzuka AG, Book SE. Basal cell carcinoma: pathogenesis, epidemiology, clinical features, diagnosis, histopathology, and management. *Yale J Biol Med.* 2015;88(2):167-179.
18. Lewin JM, Carucci JA. Advances in the management of basal cell carcinoma. *F1000Prime Rep.* 2015;7:53.
19. Wu X, Marghoob AA. Contemporary approaches to basal cell carcinoma diagnosis and treatment. *Future Oncol.* 2015;11(22):2965-2966.
20. Goldman G. The current status of curettage and electrodesiccation. *Dermatol Clin.* 2002;20(3):569-578, ix.

21. Miller SJ, Alam M, Andersen J, et al. Basal cell and squamous cell skin cancers. *J Natl Compr Canc Netw.* 2010;8(8):836-864.
22. Bolognia J, Schaffer JV, Duncan KO, Ko CJ. *Dermatology essentials.* Oxford: Saunders/Elsevier; 2014.
23. Brantsch KD, Meisner C, Schonfisch B, et al. Analysis of risk factors determining prognosis of cutaneous squamous-cell carcinoma: a prospective study. *Lancet Oncol.* 2008;9(8):713-720.
24. Minagawa A, Omodaka T, Okuyama R. Melanomas and Mechanical Stress Points on the Plantar Surface of the Foot. *N Engl J Med.* 2016;374(24):2404-2406.
25. Matas-Nadal C, Malvehy J, Ferreres JR, et al. Increasing incidence of lentigo maligna and lentigo maligna melanoma in Catalonia. *Int J Dermatol.* 2019;58(5):577-581.
26. Nehal K, Busam K. *Lentigo Maligna Melanoma.* Cham, Switzerland: Springer; 2017.
27. Swetter SM, Tsao H, Bichakjian CK, et al. Guidelines of care for the management of primary cutaneous melanoma. *J Am Acad Dermatol.* 2018.
28. Hazan C, Dusza SW, Delgado R, Busam KJ, Halpern AC, Nehal KS. Staged excision for lentigo maligna and lentigo maligna melanoma: A retrospective analysis of 117 cases. *J Am Acad Dermatol.* 2008;58(1):142-148.
29. Kunishige JH, Brodland DG, Zitelli JA. Surgical margins for melanoma in situ: when 5-mm margins are really 9 mm. *J Am Acad Dermatol.* 2015;72(4):745.
30. Alarcon I, Carrera C, Alos L, Palou J, Malvehy J, Puig S. In vivo reflectance confocal microscopy to monitor the response of lentigo maligna to imiquimod. *J Am Acad Dermatol.* 2014;71(1):49-55.
31. Fogarty GB, Hong A, Scolyer RA, et al. Radiotherapy for lentigo maligna: a literature review and recommendations for treatment. *Br J Dermatol.* 2014;170(1):52-58.
32. Badgwell C, Rosen T. Treatment of limited extent extramammary Paget's disease with 5 percent imiquimod cream. *Dermatol Online J.* 2006;12(1):22.
33. Cohen PR, Schulze KE, Tschen JA, Hetherington GW, Nelson BR. Treatment of extramammary Paget disease with topical imiquimod cream: case report and literature review. *South Med J.* 2006;99(4):396-402.
34. Guerra R, Misra S. Management of Extramammary Paget's Disease: A Case Report and Review of the Literature. *Case Rep Dermatol Med.* 2013;2013:436390.
35. Pflugfelder A, Kochs C, Blum A, et al. Malignant melanoma S3-guideline "diagnosis, therapy and follow-up of melanoma". *J Dtsch Dermatol Ges.* 2013;11 Suppl 6:1-116, 111-126.
36. Stratigos A, Garbe C, Lebbe C, et al. Diagnosis and treatment of invasive squamous cell carcinoma of the skin: European consensus-based interdisciplinary guideline. *Eur J Cancer.* 2015;51(14):1989-2007.
37. Network NCC. Basal Cell Skin Cancer (Version 1.2018). 2018.
38. Gaudy-Marqueste C, Perchenet AS, Tasei AM, et al. The "spaghetti technique": an alternative to Mohs surgery or staged surgery for problematic lentiginous melanoma (lentigo maligna and acral lentiginous melanoma). *J Am Acad Dermatol.* 2011;64(1):113-118.
39. Moyer JS, Rudy S, Boonstra PS, et al. Efficacy of Staged Excision With Permanent Section Margin Control for Cutaneous Head and Neck Melanoma. *JAMA Dermatol.* 2017;153(3):282-288.
40. Mohs FE. Chemosurgery. *Am J Proctol.* 1959;10:357-367.
41. Mohs FE. Chemosurgical treatment of cancer of the ear; a microscopically controlled method of excision. *Surgery.* 1947;21(5):605-622.
42. Brodland DG, Amonette R, Hanke CW, Robins P. The history and evolution of Mohs micrographic surgery. *Dermatol Surg.* 2000;26(4):303-307.
43. Hendi A, Brodland DG, Zitelli JA. Extramammary Paget's disease: surgical treatment with Mohs micrographic surgery. *J Am Acad Dermatol.* 2004;51(5):767-773.

44. Lee KY, Roh MR, Chung WG, Chung KY. Comparison of Mohs micrographic surgery and wide excision for extramammary Paget's Disease: Korean experience. *Dermatol Surg.* 2009;35(1):34-40.
45. Serra-Guillen C, Sanmartin O, Llombart B, et al. Correlation between preoperative magnetic resonance imaging and surgical margins with modified Mohs for dermatofibrosarcoma protuberans. *Dermatol Surg.* 2011;37(11):1638-1645.
46. Guy GP, Jr., Machlin SR, Ekwueme DU, Yabroff KR. Prevalence and costs of skin cancer treatment in the U.S., 2002-2006 and 2007-2011. *Am J Prev Med.* 2015;48(2):183-187.
47. Linos E, Parvataneni R, Stuart SE, Boscardin WJ, Landefeld CS, Chren MM. Treatment of nonfatal conditions at the end of life: nonmelanoma skin cancer. *JAMA Intern Med.* 2013;173(11):1006-1012.
48. Arits AHMM, Mosterd K, Essers BAB, et al. Photodynamic therapy versus topical imiquimod versus topical fluorouracil for treatment of superficial basal-cell carcinoma: a single blind, non-inferiority, randomised controlled trial. *The Lancet Oncology.* 2013;14(7):647-654.
49. Read T, Noonan C, David M, et al. A systematic review of non-surgical treatments for lentigo maligna. *J Eur Acad Dermatol Venereol.* 2016;30(5):748-753.
50. Machida H, Moeini A, Roman LD, Matsuo K. Effects of imiquimod on vulvar Paget's disease: a systematic review of literature. *Gynecol Oncol.* 2015;139(1):165-171.
51. Sheridan AT, Dawber RP. Curettage, electrosurgery and skin cancer. *Australas J Dermatol.* 2000;41(1):19-30.
52. Mirza FN, Khatri KA. The use of lasers in the treatment of skin cancer: A review. *J Cosmet Laser Ther.* 2017;19(8):451-458.
53. Zane C, Facchinetti E, Arisi M, Ortel B, Calzavara-Pinton P. Pulsed CO2 Laser Ablation of Superficial Basal Cell of Limbs and Trunk: A Comparative Randomized Clinical Trial With Cryotherapy and Surgical Ablation. *Dermatol Surg.* 2017;43(7):920-927.
54. Chen CS, Sierra H, Cordova M, Rajadhyaksha M. Confocal microscopy-guided laser ablation for superficial and early nodular Basal cell carcinoma: a promising surgical alternative for superficial skin cancers. *JAMA Dermatol.* 2014;150(9):994-998.
55. Sierra H, Yelamos O, Cordova M, Chen CJ, Rajadhyaksha M. Reflectance confocal microscopy-guided laser ablation of basal cell carcinomas: initial clinical experience. *J Biomed Opt.* 2017;22(8):1-13.
56. Kittler H, Pehamberger H, Wolff K, Binder M. Diagnostic accuracy of dermoscopy. *Lancet Oncol.* 2002;3(3):159-165.
57. Braun RP, Saurat JH, French LE. Dermoscopy of pigmented lesions: a valuable tool in the diagnosis of melanoma. *Swiss Med Wkly.* 2004;134(7-8):83-90.
58. Wolner ZJ, Yelamos O, Liopyris K, Rogers T, Marchetti MA, Marghoob AA. Enhancing Skin Cancer Diagnosis with Dermoscopy. *Dermatol Clin.* 2017;35(4):417-437.
59. Yélamos O, Braun R, Liopyris K, et al. Dermoscopy/dermatoscopy and dermatopathology correlates of cutaneous neoplasms. *J Am Acad Dermatol.* 2019;80(2):341-363.
60. Soyer HP, Argenziano G, Chimenti S, Ruocco V. Dermoscopy of pigmented skin lesions. *Eur J Dermatol.* 2001;11(3):270-276; quiz 277.
61. Wood RW. Secret communications concerning light rays. *J Physiol.* 1919;5 serie:IX.
62. Walsh SB, Varma R, Raimer D, et al. Utility of Wood's light in margin determination of melanoma in situ after excisional biopsy. *Dermatol Surg.* 2015;41(5):572-578.
63. Klatte JL, van der Beek N, Kemperman PM. 100 years of Wood's lamp revised. *J Eur Acad Dermatol Venereol.* 2015;29(5):842-847.
64. Reyes BA, Robins P. Wood's lamp and surgical margins in malignant melanoma in situ. *J Dermatol Surg Oncol.* 1988;14(1):22.
65. Paraskevas LR, Halpern AC, Marghoob AA. Utility of the Wood's light: five cases from a pigmented lesion clinic. *Br J Dermatol.* 2005;152(5):1039-1044.

66. Robinson JK. Use of digital epiluminescence microscopy to help define the edge of lentigo maligna. *Arch Dermatol.* 2004;140(9):1095-1100.
67. Peng X, Qian W, Hou J. 5-aminolevulinic acid (5-ALA) fluorescence-guided Mohs surgery resection of penile-scrotal extramammary Paget's disease. *Biosci Trends.* 2017;11(5):595-599.
68. Wan M, Ma H, Zhao Y, Xie L, Chen Z. Clinical Benefits of Preoperative Conventional Fluorescence Diagnosis in Surgical Treatment of Extramammary Paget Disease. *Dermatol Surg.* 2018;44(3):375-382.
69. Neus S, Gambichler T, Bechara FG, Wohl S, Lehmann P. Preoperative assessment of basal cell carcinoma using conventional fluorescence diagnosis. *Arch Dermatol Res.* 2009;301(4):289-294.
70. Rajadhyaksha M, Gonzalez S, Zavislan JM, Anderson RR, Webb RH. In vivo confocal scanning laser microscopy of human skin II: advances in instrumentation and comparison with histology. *J Invest Dermatol.* 1999;113(3):293-303.
71. Waddell A, Star P, Guitera P. Advances in the use of reflectance confocal microscopy in melanoma. *Melanoma Manag.* 2018:Epub ahead of print.
72. Rajadhyaksha M, Grossman M, Esterowitz D, Webb RH, Anderson RR. In vivo confocal scanning laser microscopy of human skin: melanin provides strong contrast. *J Invest Dermatol.* 1995;104(6):946-952.
73. Hofmann-Wellenhof R, Pellacani G, Malvehy J, Soyer HP, SpringerLink. Reflectance Confocal Microscopy for Skin Diseases. *Springer eBooks*. Berlin, Heidelberg: Springer Berlin Heidelberg Imprint Springer; 2012.
74. Pellacani G, Guitera P, Longo C, Avramidis M, Seidenari S, Menzies S. The Impact of In Vivo Reflectance Confocal Microscopy for the Diagnostic Accuracy of Melanoma and Equivocal Melanocytic Lesions. *J Invest Dermatol.* 2007;127(12):2759-2765.
75. Segura S, Puig S, Carrera C, Palou J, Malvehy J. Development of a two-step method for the diagnosis of melanoma by reflectance confocal microscopy. *J Am Acad Dermatol.* 2009;61(2):216-229.
76. Guitera P, Pellacani G, Crotty KA, et al. The impact of in vivo reflectance confocal microscopy on the diagnostic accuracy of lentigo maligna and equivocal pigmented and nonpigmented macules of the face. *J Invest Dermatol.* 2010;130(8):2080-2091.
77. Que SK, Grant-Kels JM, Longo C, Pellacani G. Basics of Confocal Microscopy and the Complexity of Diagnosing Skin Tumors: New Imaging Tools in Clinical Practice, Diagnostic Workflows, Cost-Estimate, and New Trends. *Dermatol Clin.* 2016;34(4):367-375.
78. Alarcon I, Carrera C, Palou J, Alos L, Malvehy J, Puig S. Impact of in vivo reflectance confocal microscopy on the number needed to treat melanoma in doubtful lesions. *Br J Dermatol.* 2014;170(4):802-808.
79. Yélamos O, Manubens E, Jain M, et al. Impact of reflectance confocal microscopy on the physician's diagnostic confidence and decision making of equivocal skin tumors: outcomes after 1 year follow-up. *Poster 6903 presented at the 2018 American Academy Meeting.* 2018.
80. Borsari S, Pampena R, Lallas A, et al. Clinical Indications for Use of Reflectance Confocal Microscopy for Skin Cancer Diagnosis. *JAMA Dermatol.* 2016.
81. Stanganelli I, Longo C, Mazzoni L, et al. Integration of reflectance confocal microscopy in sequential dermoscopy follow-up improves melanoma detection accuracy. *Br J Dermatol.* 2015;172(2):365-371.
82. Manubens E, Barreiro A, Bennassar A, et al. Fast evaluation and monitoring of ingenol mebutate treatment of multiple basal cell carcinomas by in vivo hand-held reflectance confocal microscopy. *J Eur Acad Dermatol Venereol.* 2017;31(6):e284-e286.
83. Segura S, Puig S, Carrera C, Lecha M, Borges V, Malvehy J. Non-invasive management of non-melanoma skin cancer in patients with cancer predisposition genodermatosis: a

role for confocal microscopy and photodynamic therapy. *J Eur Acad Dermatol Venereol.* 2011;25(7):819-827.
84. Venturini M, Sala R, Gonzalez S, Calzavara-Pinton PG. Reflectance confocal microscopy allows in vivo real-time noninvasive assessment of the outcome of methyl aminolaevulinate photodynamic therapy of basal cell carcinoma. *Br J Dermatol.* 2013;168(1):99-105.
85. Guitera P, Moloney FJ, Menzies SW, et al. Improving management and patient care in lentigo maligna by mapping with in vivo confocal microscopy. *JAMA Dermatol.* 2013;149(6):692-698.
86. Pan ZY, Liang J, Zhang QA, Lin JR, Zheng ZZ. In vivo reflectance confocal microscopy of extramammary Paget disease: diagnostic evaluation and surgical management. *J Am Acad Dermatol.* 2012;66(2):e47-53.
87. Scope A, Mahmood U, Gareau DS, et al. In vivo reflectance confocal microscopy of shave biopsy wounds: feasibility of intraoperative mapping of cancer margins. *Br J Dermatol.* 2010;163(6):1218-1228.
88. Flores ES, Cordova M, Kose K, et al. Intraoperative imaging during Mohs surgery with reflectance confocal microscopy: initial clinical experience. *J Biomed Opt.* 2015;20(6):61103.
89. Venturini M, Gualdi G, Zanca A, Lorenzi L, Pellacani G, Calzavara-Pinton PG. A new approach for pre-surgical margin assessment of basal cell carcinoma by reflectance confocal microscopy. *Br J Dermatol.* 2015.
90. Marino ML, Rogers T, Sierra Gil H, Rajadhyaksha M, Cordova MA, Marghoob AA. Improving lesion localization when imaging with handheld reflectance confocal microscope. *Skin Res Technol.* 2016.
91. Ali FR, Craythorne EE. Gummed rings as the outer marker of microscopically examined tissue (GROMMETs) as mapping adjuncts to in vivo reflectance confocal microscopy (RCM). *J Am Acad Dermatol.* 2016;75(3):e103-104.
92. Kose K, Cordova M, Duffy M, Flores ES, Brooks DH, Rajadhyaksha M. Video-mosaicing of reflectance confocal images for examination of extended areas of skin in vivo. *Br J Dermatol.* 2014;171(5):1239-1241.
93. Ulrich M, Themstrup L, de Carvalho N, et al. Dynamic Optical Coherence Tomography in Dermatology. *Dermatology.* 2016;232(3):298-311.
94. De Carvalho N, Schuh S, Kindermann N, Kastle R, Holmes J, Welzel J. Optical coherence tomography for margin definition of basal cell carcinoma before micrographic surgery-recommendations regarding the marking and scanning technique. *Skin Res Technol.* 2018;24(1):145-151.
95. Cheng HM, Lo S, Scolyer R, Meekings A, Carlos G, Guitera P. Accuracy of optical coherence tomography for the diagnosis of superficial basal cell carcinoma: a prospective, consecutive, cohort study of 168 cases. *Br J Dermatol.* 2016.
96. Ferrante di Ruffano L, Dinnes J, Deeks JJ, et al. Optical coherence tomography for diagnosing skin cancer in adults. *Cochrane Database Syst Rev.* 2018;12:CD013189.
97. Desai TD, Desai AD, Horowitz DC, Kartono F, Wahl T. The use of high-frequency ultrasound in the evaluation of superficial and nodular basal cell carcinomas. *Dermatol Surg.* 2007;33(10):1220-1227; discussion 1226-1227.
98. Alfageme F, Salguero I, Najera L, Suarez ML, Roustan G. Increased Marginal Stiffness Differentiates Infiltrative From Noninfiltrative Cutaneous Basal Cell Carcinomas in the Facial Area: A Prospective Study. *J Ultrasound Med.* 2018.
99. Hernandez-Ibanez C, Blazquez-Sanchez N, Aguilar-Bernier M, Funez-Liebana R, Rivas-Ruiz F, de Troya-Martin M. Usefulness of High-Frequency Ultrasound in the Classification of Histologic Subtypes of Primary Basal Cell Carcinoma. *Actas Dermosifiliogr.* 2016.

100. Pasquali P, Freites-Martinez A, Fortuno-Mar A. Ex vivo high-frequency ultrasound: A novel proposal for management of surgical margins in patients with non-melanoma skin cancer. *J Am Acad Dermatol.* 2016;74(6):1278-1280.
101. Feng X, Fox MC, Reichenberg JS, et al. Biophysical basis of skin cancer margin assessment using Raman spectroscopy. *Biomed Opt Express.* 2019;10(1):104-118.
102. Cameron MC, Lee E, Hibler BP, et al. Basal cell carcinoma: Contemporary approaches to diagnosis, treatment, and prevention. *J Am Acad Dermatol.* 2019;80(2):321-339.
103. Szeliski R. Image Alignment and Stitching: A Tutorial. *Foundations and Trends® in Computer Graphics and Vision.* 2006;2(1):1-104.
104. Szeliski R. Video Mosaics for Virtual Environments. *IEEE Computer Graphics and Applications.* 1996;16(2):22-30.
105. Bergen T, Wittenberg T. Stitching and Surface Reconstruction From Endoscopic Image Sequences: A Review of Applications and Methods. *IEEE J Biomed Health Inform.* 2016;20(1):304-321.
106. Girod B. Keypoint Detection. *Stanford University.* 2013;Available at https://web.stanford.edu/class/ee368/Handouts/Lectures/2014_Spring/Combined_Slides/12-Keypoint-Detection-Combined.pdf: Last Accessed 4.11.2018.
107. Samsudin S, Adwan S, Arof H, Mokhtar N, Ibrahim F. Development of automated image stitching system for radiographic images. *J Digit Imaging.* 2013;26(2):361-370.
108. Lowe DG. Object recognition from local scale-invariant features. *Proceedings of the International Conference on Computer Vision.* 1999;2:1150-1157.
109. Urtrasun R. Computer Vision: Image Aligment. 2013;Available at: https://www.cs.toronto.edu/~urtasun/courses/CV/lecture06.pdf. Last Accessed 25 November, 2018.
110. Pulli K. Stitching and Blending.Available at: https://web.stanford.edu/class/cs231m/lectures/lecture-5-stitching-blending.pdf. Last Accessed 25 November, 2018.
111. Nyman P. Image Stitching using Watersheds and Graph Cuts.Available at: http://www2.maths.lth.se/matematiklth/personal/petter/rapporter/panorama2.pdf. Last Accessed 25 November, 2018.
112. Giacomelli MG, Sheikine Y, Vardeh H, Connolly JL, Fujimoto JG. Rapid imaging of surgical breast excisions using direct temporal sampling two photon fluorescent lifetime imaging. *Biomed Opt Express.* 2015;6(11):4317-4325.
113. Saldua MA, Olsovsky CA, Callaway ES, Chapkin RS, Maitland KC. Imaging inflammation in mouse colon using a rapid stage-scanning confocal fluorescence microscope. *J Biomed Opt.* 2012;17(1):016006.
114. Bedard N, Quang T, Schmeler K, Richards-Kortum R, Tkaczyk TS. Real-time video mosaicing with a high-resolution microendoscope. *Biomed Opt Express.* 2012;3(10):2428-2435.
115. Que SK, Grant-Kels JM, Rabinovitz HS, Oliviero M, Scope A. Application of Handheld Confocal Microscopy for Skin Cancer Diagnosis: Advantages and Limitations Compared with the Wide-Probe Confocal. *Dermatol Clin.* 2016;34(4):469-475.
116. Castro RP, Stephens A, Fraga-Braghiroli NA, et al. Accuracy of in vivo confocal microscopy for diagnosis of basal cell carcinoma: a comparative study between handheld and wide-probe confocal imaging. *J Eur Acad Dermatol Venereol.* 2015;29(6):1164-1169.
117. Champin J, Perrot JL, Cinotti E, et al. In vivo reflectance confocal microscopy to optimize the spaghetti technique for defining surgical margins of lentigo maligna. *Dermatol Surg.* 2014;40(3):247-256.
118. Gualdi G, Venturini M, Zanca A, Calzavara-Pinton PG, Pellacani G. Pre-surgical basal cell carcinoma margin definition: the SMART approach. *J Eur Acad Dermatol Venereol.* 2016;30(3):474-476.

119. Flores E, Yelamos O, Cordova M, et al. Peri-operative delineation of non-melanoma skin cancer margins in vivo with handheld reflectance confocal microscopy and video-mosaicking. *J Eur Acad Dermatol Venereol.* 2019.
120. Dickensheets DL, Kreitinger S, Peterson G, Heger M, Rajadhyaksha M. Wide-field imaging combined with confocal microscopy using a miniature f/5 camera integrated within a high NA objective lens. *Opt Lett.* 2017;42(7):1241-1244.
121. Dickensheets DL, Kreitinger S, Peterson G, Heger M, Rajadhyaksha M. Dermoscopy-guided reflectance confocal microscopy of skin using high-NA objective lens with integrated wide-field color camera. *Proc SPIE Int Soc Opt Eng.* 2016;9689.
122. Guitera P, Menzies SW, Argenziano G, et al. Dermoscopy and in vivo confocal microscopy are complimentary techniques for the diagnosis of difficult amelanotic and light colored skin lesions. *Br J Dermatol.* 2016.
123. Yelamos O, Nehal KS. Integrating clinical information, dermoscopy and reflectance confocal microscopy to improve the diagnostic accuracy and confidence of amelanotic and lightly pigmented melanomas. *Br J Dermatol.* 2016;175(6):1147-1148.
124. Terrier JE, Tiffet O, Raynaud N, Cinotti E. In Vivo Reflectance Confocal Microscopy Combined With the "Spaghetti" Technique: A New Procedure for Defining Surgical Margins of Genital Paget Disease. *Dermatol Surg.* 2015;41(7):862-864.
125. Guitera P, Scolyer RA, Gill M, et al. Reflectance confocal microscopy for diagnosis of mammary and extramammary Paget's disease. *J Eur Acad Dermatol Venereol.* 2013;27(1):e24-29.
126. Sahu A, Yélamos O, Iftimia N, et al. Evaluation of a combined reflectance confocal microscopy–optical coherence tomography device for detection and depth assessment of basal cell carcinoma. *JAMA Dermatol.* 2018.
127. Iftimia N, Yélamos O, Chen C-SJ, et al. Handheld optical coherence tomography–reflectance confocal microscopy probe for detection of basal cell carcinoma and delineation of margins. *J Biomed Opt.* 2017;22(7):076006.
128. Dubois A, Levecq O, Azimani H, et al. Line-field confocal optical coherence tomography for high-resolution noninvasive imaging of skin tumors. *J Biomed Opt.* 2018;23(10):1-9.
129. Huang L, Wang Y, Wu M, et al. Diagnosis of subclinical extramammary Paget's disease with a combination of noninvasive photodynamic diagnosis and reflectance confocal microscopy. *Indian J Dermatol Venereol Leprol.* 2019.
130. Gonzalez S, Sanchez V, Gonzalez-Rodriguez A, Parrado C, Ullrich M. Confocal microscopy patterns in nonmelanoma skin cancer and clinical applications. *Actas Dermosifiliogr.* 2014;105(5):446-458.
131. Nori S, Rius-Diaz F, Cuevas J, et al. Sensitivity and specificity of reflectance-mode confocal microscopy for in vivo diagnosis of basal cell carcinoma: a multicenter study. *J Am Acad Dermatol.* 2004;51(6):923-930.
132. Guitera P, Menzies SW, Longo C, Cesinaro AM, Scolyer RA, Pellacani G. In vivo confocal microscopy for diagnosis of melanoma and basal cell carcinoma using a two-step method: analysis of 710 consecutive clinically equivocal cases. *J Invest Dermatol.* 2012;132(10):2386-2394.
133. Sierra H, Cordova M, Chen CS, Rajadhyaksha M. Confocal imaging-guided laser ablation of basal cell carcinomas: an ex vivo study. *J Invest Dermatol.* 2015;135(2):612-615.
134. Tannous Z, Torres A, Gonzalez S. In vivo real-time confocal reflectance microscopy: a noninvasive guide for Mohs micrographic surgery facilitated by aluminum chloride, an excellent contrast enhancer. *Dermatol Surg.* 2003;29(8):839-846.
135. Yélamos O, Cordova M, Peterson G, et al. In vivo intraoral reflectance confocal microscopy of an amalgam tattoo. *Dermatol Pract Concept.* 2017;7(4):13-16.
136. Iftimia N, Peterson G, Chang EW, Maguluri G, Fox W, Rajadhyaksha M. Combined reflectance confocal microscopy-optical coherence tomography for delineation of basal cell carcinoma margins: an ex vivo study. *J Biomed Opt.* 2016;21(1):16006.

137. Barcaui Ede O, Carvalho AC, Valiante PM, Barcaui CB. High-frequency ultrasound associated with dermoscopy in pre-operative evaluation of basal cell carcinoma. *An Bras Dermatol.* 2014;89(5):828-831.
138. Vilas-Sueiro A, Alfageme F, Salguero I, De Las Heras C, Roustan G. Ex Vivo High-Frequency Ultrasound for Assessment of Basal Cell Carcinoma. *J Ultrasound Med.* 2019;38(2):529-531.
139. Esteva A, Kuprel B, Novoa RA, et al. Dermatologist-level classification of skin cancer with deep neural networks. *Nature.* 2017;542(7639):115-118.
140. Marchetti MA, Codella NCF, Dusza SW, et al. Results of the 2016 International Skin Imaging Collaboration International Symposium on Biomedical Imaging challenge: Comparison of the accuracy of computer algorithms to dermatologists for the diagnosis of melanoma from dermoscopic images. *J Am Acad Dermatol.* 2018;78(2):270-277 e271.
141. Kurugol S, Kose K, Park B, Dy JG, Brooks DH, Rajadhyaksha M. Automated delineation of dermal-epidermal junction in reflectance confocal microscopy image stacks of human skin. *J Invest Dermatol.* 2015;135(3):710-717.
142. Bozkurt A, Kose K, Alessi-Fox C, Dy JG, Brooks DH, Rajadhyaksha M. Unsupervised delineation of stratum corneum using reflectance confocal microscopy and spectral clustering. *Skin Res Technol.* 2017;23(2):176-185.
143. Condino S, Turini G, Parchi PD, et al. How to Build a Patient-Specific Hybrid Simulator for Orthopaedic Open Surgery: Benefits and Limits of Mixed-Reality Using the Microsoft HoloLens. *J Healthc Eng.* 2018;2018:5435097.
144. Lee C, Wong GKC. Virtual reality and augmented reality in the management of intracranial tumors: A review. *J Clin Neurosci.* 2019;62:14-20.
145. Freeman EE, Semeere A, Osman H, et al. Smartphone confocal microscopy for imaging cellular structures in human skin in vivo. *Biomed Opt Express.* 2018;9(4):1906-1915.

ADDENDUM

Additional publications related to reflectance confocal microscopy and published during the PhD research period:

1. Hibler BP, Yélamos O, Cordova M, Sierra H, Rajadhyaksha M, Nehal KS, Rossi AM. Handheld reflectance confocal microscopy to aid in the management of complex facial lentigo maligna. Cutis. 2017 May;99(5):346-352.

2. Yélamos O, Cordova M, Peterson G, Pulitzer MP, Singh B, Rajadhyaksha M, DeFazio JL. In vivo intraoral reflectance confocal microscopy of an amalgam tattoo. Dermatol Pract Concept. 2017 Oct 31;7(4):13-16. doi: 10.5826/dpc.0704a04.

3. Iftimia N, Yélamos O, Chen CJ, Maguluri G, Cordova MA, Sahu A, Park J, Fox W, Alessi-Fox C, Rajadhyaksha M. Handheld optical coherence tomography-reflectance confocal microscopy probe for detection of basal cell carcinoma and delineation of margins. J Biomed Opt. 2017 Jul 1;22(7):76006. doi: 10.1117/1.JBO.22.7.076006.

4. Sahu A, Yélamos O, Iftimia N, Cordova M, Alessi-Fox C, Gill M, Maguluri G, Dusza SW, Navarrete-Dechent C, González S, Rossi AM, Marghoob AA, Rajadhyaksha M, Chen CJ. Evaluation of a Combined Reflectance Confocal Microscopy-Optical Coherence Tomography Device for Detection and Depth Assessment of Basal Cell Carcinoma. JAMA Dermatol. 2018 Oct 1;154(10):1175-1183. doi: 10.1001/jamadermatol.2018.2446.

5. O Yélamos, E Manubens, M Jain, SV Pulijal, SW. Dusza, MA. Marchetti, A Barreiro, ML. Marino, J Malvehy, MA. Cordova, AM. Rossi, M Rajadhyaksha, AC. Halpern, S Puig, AA. Marghoob, C Carrera. Improvement of diagnostic confidence and management of equivocal skin lesions by integration of reflectance confocal microscopy in daily practice: prospective study in two referral skin cancer centers. Accepted J Am Acad Dermatol. May 2019.

RESUM COMPLET DE LA TESI DOCTORAL

INTRODUCCIÓ

a) Epidemiologia i tipus de càncers de pell

El càncer de pell representa un important problema de salut pública ja que la seva incidència no ha parat d'augmentar en les darreres dècades. Els càncers de pell són el més freqüents en l'espècie humana, essent els carcinomes queratinocítics (CQ), anteriorment coneguts con càncers cutanis no melanoma, i en concret els carcinomes basocel·lulars (CBC) els més freqüents de tots. Els CQ, que inclouen els CBC però també els carcinomes escatosos o espinocel·lulars (CEC), estan íntimament relacionats amb l'exposició solar crònica i per això apareixen típicament en zones fotoexposades. Per altra banda, els melanomes són càncers de pell molt menys freqüents però molt més agressius i que es relacionen amb la genètica i l'exposició solar intermitent en la majoria dels casos. Tanmateix, en alguns subtipus de melanomes, com el lentigen maligne (LM) o la seva variant invasiva el LM melanoma (LMM), l'exposició solar crònica també hi té rellevància, duent doncs a la seva aparició en zones cop el cap i el coll. Existeixen altres càncers cutanis menys freqüents depenent de la cèl·lula de la qual s'originin; un subtipus interessant és la malaltia de Paget, que s'origina a partir de cèl·lules presents als ductes i glàndules apocrines. La malaltia Pagets, doncs, s'origina en zones riques amb glàndules apocrines com ara la mama (malaltia de Paget mamària) i els genitals (malaltia de Paget extramamària). Una de les particularitats d'aquest càncer cutani és la seva proliferació multifocal, que fa que el seu tractament i seguiment siguin molt difícils de realitzar requerint sovint múltiples biòpsies cutànies que desafortunadament poden ser negatives en casos de persistència o recurrència tumoral

b) Tractament dels càncers de pell

El tractament de la majoria dels càncers cutanis requereix l'ús de **cirurgia**, tot i que no sempre és possible o desitjable de realitzar amb els marges de seguretat tradicionals degut a la seva localització en zones sensibles com la cara o genitals. A més a més, diversos tipus de càncers de pell tenen els marges mal definits, com ara els CBC infiltants, els LM/LMM o la malaltia de Paget extramamària (MPEM), fet que dificulta enormement la cirurgia i poder obtenir marges quirúrigics lliures de malaltia en una sola etapa. En aquest sentit es va desenvolupar la cirurgia de Mohs per a poder eliminar completament el tumor respectant al màxim la preservació de teixit sa. Aquesta tècnica en la seva variant actual s'inicia amb l'exèresi del tumor visible (debulking) seguida d'una exèresi controlada de cada quadrant que posteriorment es marca, congela, tenyeix i analitza durant el mateix acte quirúrgic. Els quadrants tenen la particularitat que s'extirpen a 45º pertement així que l'anàlisi histològica sigui mitjançant talls horitzontals, avaluant així el 100% dels marges. Si s'identifica un quadrant positiu per a tumor, la cirurgia segueix només allà on ha estat positiu i es van fent etapes successives fins que els marges són

nets. Un cop s'assoleixen els marges lliures de tumor, es procedeix a la reconstrucció del defecte quirúrgic, que sol realitzar-se normalment el mateix dia de la cirurgia.

S'han descrit diverses variants de la cirurgia de Mohs, com el Mohs diferit o la cirurgia per estadis (*staged excision*), en les quals s'envia la mostra al laboratori d'anatomia patològica per a fer tincions especials (per exemple tincions immunohistoquímiques) o tincions estàndard però realitzades de forma habitual amb parafina i no en tall congelat. Aquestes tècniques serien millors per exemple en tumors melanocítics com els melanomes, ja que es permetria l'ús de tècniques especials i s'evitaria l'artefacte de la congelació. Ara bé, tenen l'inconvenient de ser més lentes i diferir el tancament del defecte quirúrgic. Cal mencionar que en algunes d'aquestes tècniques, com la cirurgia per estadis, no es tallen els quadrants de forma horitzontal com a la cirurgia de Mohs sinó en vertical per poder avaluar l'evolució del tumor des del centre fins a la perifèria. Això és especialment útil en tumors amb marges mal definits com el LM/LMM ja que que perden càrrega tumoral a mesura que avancen cap a la perifèria, i només el context global permet avaluar la rellevància de cèl·lules atípiques aïllades a la perifèria.

Tot i que la cirurgia segueix sent el tractament de primera línia segons la majoria de les guies actuals, és possible emprar **tractaments no quirúrgics** per a tractar càncers cutanis superficials com ara els CBC superficials o nodulars incipients, els CEC in situ, o fins i tot els LM (ja que són localitzats a l'epidermis). Alguns d'aquests tractaments inclouen tractaments tòpics immunomoduladors (5-fluorouracil, imiquimod, ingenol mebutat, entre d'altres), o teràpies físiques com el curetatge amb electrocoagulació, la teràpia fotodinàmica, la crioteràpia, la radioteràpia, o l'ablació làser (usant làsers tipus CO2 o erbi:YAG). Aquests tractaments tenen diversos avantatges com ser generalment barats, accessibles i no requerir l'insfraestructura i l'entrenament que cal per a la cirurgia de Mohs. Per altra banda, el problema principal d'aquestes tècniques és que no permeten comprovar l'eliminació total de tumor mitjançant els mètodes clàssics d'anàlisi histològica, fet que en dificulta el seu seguiment. En aquest sentit, semblaria ideal poder emprar mètodes d'imatge no invasiva per a la detecció de tumor residual just després del tractament així com per a fer el seguiment de càncers cutanis després de llur tractament.

c) Mètodes d'imatge no invasiva en oncologia cutània

Existeixen diversos mètodes d'imatge no invasiva que s'han emprat amb èxit sobretot per al diagnòstic del càncer cutani com ara la dermatoscòpia, la llum de Wood o la microscòpia confocal de reflectància (MCR). La **dermatoscòpia** consisteix en l'ús d'una lupa de mà normalment de 10x acoblada a una font de llum que pot ser polaritzada o no polaritzada. L'ús d'aquest sistema permet visualitzar estructures no visibles amb l'ull nu i ha demostrat una alta sensibilitat i especificiat per a diagnosticar múltiples tipus de càncers cutanis. També s'ha emprat per a delimitar els marges cutanis en tumors mal

definits, així com per a identificar recurrència tumoral. L'avantge principal de la dermatoscòpia és el seu baix cost i accessibilitat, però té l'inconvenient que no permet identificar detalls cel·lulars, per tant podria no visualitzar certs focus microscòpics de tumor sobretot en lesions hipopigmentades. La **llum de Wood** consisteix en una font de llum ultravioleta acoblada a un vidre de silicat de bari que filtra la llum permetent visualitzar només la llum compresa entre 320-400 nm. Això permet visualitzar àrees amb pigment com ara la melanina, i avaluar els marges de tumors pigmentats com els LM/LMM. Tanmateix, aquesta tècnica pot tenir numerosos falsos positius i negatius sobretot en pells amb intens fotodany.

Finalment, una de les tècniques d'imatge més útils per avaluar de forma no invasiva els càncers cutanis és la **MCR**. Aquesta tècnica té una alta precisió diagnòstica per a diversos càncers cutanis i s'ha emprat també per avaluar-ne la resposta al tractament. La MCR es fonamenta en l'ús d'una font de llum làser de 830 nm que emet un feix de llum sobre un punt d'interès a la pell que és després retrodispersada. Aquesta llum es filtra posteriorment a través d'un forat (*pinhole*) que només recull llum des del punt d'interès, permetent així l'alineació del punt d'interès i el *pinhole* en el mateix pla focal (con-focal). Això permet fer una avaluació molt precisa de la pell, obtenint seccions òptiques de 4 µmamb una resolució lateral d'1 µm. Per tant, el principal avantatge d'aquesta tècnica és que poseeix resolució cel·lular pel que es pot considerar com una biòpsia virtual. Per altra banda, degut a aquesta gran resolució, la MCR només permet avaluar fins a profunditats d'unes 250 µm que corresponen a la dermis reticular superficial. Un altre gran avantatge de la MCR és la seva capacitat de detectar petites concentracions de pigment com ara la melanina, ja que són estructures que retrodispersen molt la llum (a diferència d'estructures "buides" com l'aigua), fent aquesta tècnia molt útil en lesions amelanòtiques o hipopigmentades com alguns carcinomes o LM.

Actualment existeixen 2 microscopis confocals de reflectància per a poder ser usats in vivo, un que requereix adherir una anella metàl·lica de 2 cm(o de plàstic en les darreres versions) directament a la pell, i un microscpi confocal de mà. El primer permet obtenir múltiples imatges de 0.5 x 0.5 mm de forma estandarditzada que després s'uneixen gràcies al programari de l'aparell en imatges anomenades mosaics. Aquests mosaics són imatges al llarg d'una superfície horitzontal de màxim 8 x 8 mm, que després es poden ampliar per a estudiar primer l'arquitectura i després la citologia (en paral·lel al procés diagnòstic habitual en anatomia patològica). En canvi, el microscopi de mà permet una navegació lliure al llarg de pell, permetent visualitzar una àrea de 0,75 x 0,75 mm o 1 x 1 mm (depenent de la versió del microscopi) ja sigui obtenint imatges o videos. L'avantatge de la MCR de mà (MCRM) és que l'usuari pot navegar lliurement per la pell sense haver d'enganxar cap anella, així com explorar grans àrees de teixit superiors a 8 x 8 mm. Tanmateix, té l'inconvenient que no diposa de sistemes de mosaics en el software natiu pel que la navegació, orientació i informació arquitectònica són molt difícils d'obtenir. Per a millorar la navegació, hom pot usar mètodes de marcatge com

ara talls amb bisturí o bé l'ús d'anelles de paper o plàstic que són visibles amb MCR. Altres mètodes podrien ser la fusió de múltiples imatges obtingudes a partir de videos de MCRM per a crear videomosaics. Aquests mètodes, descrits en alguns treballs de microendoscòpia digestiva o neurocirurgia, poden ser de gran utilitat a l'hora d'avaluar càncers de pell usant MCRM.

En aquest sentit, en aquesta tesi hem desenvolupat un algoritme informàtic que permet convertir videos obtinguts amb MCRM en mosaics (**videomosaics**), per tal de poder: 1) expandir el camp de visió; 2) obtenir informació arquitectònica de l'àrea avaluada; 3) identificar petits focus tumorals després del tractaments dels càncers cutanis així com durant el seu seguiment; 4) realitzar mesures per tal de definir els marges prequirúrgics en diferents càncers cutanis. Aquest algoritme es basa en les fases clàssiques de la fusió d'imatges en fotografia computacional (extracció de punts clau, concordança de punts clau, calibratge i barreja d'imatges), tant emprats avui en dia començant per les fotografies panoràmiques obtingudes per els nostres telèfons intel·ligents. Tanmateix, s'han hagut de superar alguns reptes que són presents en la microscòpia in vivo com ara interpretar i corregir les deformacions (la pell és laxa i es deforma), els canvis bruscos de moviment i profunditat, així com la pèrdua de qualitat (imatge borrosa) que es pot produir en fusionar imatges adjacents. Alhora, hem usat aquest algoritme en diferents situacions clíniques per a millorar el tractament i seguiment de diferents càncers cutanis. A continuació es detallen les hipòtesis i objectius de treball.

HIPOTÈSIS I OBJECTIUS

1 Hipotèsis

- És possible generar videomosaics automatitzats obtinguts a partir de vídeos adquirits amb MCRM que reflecteixin correctament els detalls arquitectònics de la pell.
- Els videomosaics permeten ampliar el camp de visió de la MCRCM i així ajudar a obtenir una visió arquitectònica de la pell.
- Els videomosaics juntament amb sistemes de marcatge permeten millorar l'orientació espacial mentre s'utilitza la MRCM.
- Els videomosaics automatitzats es poden obtenir a partir de vídeos adquirits amb MRCM directament dins de ferides quirúrgiques.
- La MCRM i els videomosaics complementen l'avaluació dermatoscòpica i de llum de Wood dels tumors cutanis hipopigmentats i permeten una delineació precisa dels marges tumorals preoperatoris.
- La MCRCM amb videomosaics ajuden a identificar tumors que es distribueixen de manera irregular (CBC, MPEM), just després del tractament o durant el seu seguiment.

2 Objectius

- Desenvolupar un algoritme per a generar videomosaics automàtics en MCRM.
- Utilitzar mètodes de marcatge que millorin l'orientació durant l'avaluació amb MCRM.
- Estimar els marges preoperatoris en casos de LM/LMM utilitzant MCRM i videomosaics, i correlacionar aquests marges amb els marges quirúrgics reals.
- Utilitzar MCRM amb videomosaics automatitzats per identificar els marges dels carcinomes queratinocítics abans i després de la cirurgia de Mohs.
- Utilitzar MCRM amb videomosaics per identificar carcinomes queratinocítics residuals després d'ablació làser.
- Avaluar la resposta al tractament després de l'ablació làser de carcinomes basocel·lulars mitjançant MCRM amb videomosaics automatitzats.
- Avaluar la precisió diagnòstica per identificar la malaltia de Paget extramamària persistent/recurrent mitjançant MRCM i videomosaics automatitzats.

MATERIAL I MÈTODES. RESULTATS. PUBLICACIONS

Publicació 1: Automated video-mosaicking approach for confocal microscopic imaging in vivo: an approach to address challenges in imaging living tissue and extend field of view

Kivanc Kose, Mengran Gou, Oriol Yélamos, Miguel Cordova, Anthony M. Rossi, Kishwer S. Nehal, Eileen S. Flores, Octavia Camp, Jennifer G. Dy, Dana H. Brooks & Milind Rajadhyaksha

Scientific Reports 2017 Sep 7;7(1):10759. doi: 10.1038/s41598-017-11072-9.

RESUM

Introducció: La microscòpia confocal de reflectància (MCR) és una tècnica d'imatge microscòpica, que permet examinar ràpidament el teixit in vivo. Proporcionant una resolució morfològica a nivell cel·lular, les imatges de MCR combinades amb el mosaics han demostrat ser molt sensibles i específiques per al diagnòstic i seguiment de càncer de pell de forma invasiva. No obstant, les tècniques actuals de mosaicització de MCR amb els microscopis existents s'han limitat a seqüències bidimensionals d'imatges fixes individuals, adquirides d'una manera molt controlada i al llarg d'un trajecte predefinit, que cobreix una àrea limitada. El desenvolupament recent de microscopis de mà petits permet l'adquisició de vídeos de manera relativament lliure i seguint un trajecte arbitrari. Per tant, cal disposar de mosaics d'imatges obtingudes a partir de vídeos (videomosaics) per a avaluar grans àrees de teixit.

Objectiu: Descriure un mètode computaritzat automatitzat de generació de mosaics obtinguts a partir de vídeos de microscòpia confocal de reflectànic a de mà (MCRM).

Material i mètodes: L'algoritme tracta els reptes únics que s'han trobat durant la captura de vídeo, com ara els artefactes de desenfocament a causa del moviment ràpid del microscopi a l'àrea de les imatges, la deformació a causa dels canvis en l'angle de contacte, i la resolució variable amb profunditat. Abordem tots aquests reptes mitjançant (i) la modelització directa de les deformacions, (ii) la detecció automàtica d'artefactes de moviment bruscos (discontinuitats) en la seqüència de la imatge i (iii) la fusió robusta de les imatges superposades de manera flexible, sense presentar imatges borroses ni pèrdua de resolució.

Resultats: Presentem l'algoritme i exemples clínics usant els videomosaics per al tractament i seguiment de càncer de pell, per demostrar-ne l'utilitat clínica potencial.

Conclusions: Els nostres mètodes de vídeomosaic aborden els reptes de la video-mosaicització automàtica en MCRM i es podrien incloure al programari natiu de la MRCM.

Publicació 2: Correlation of Handheld Reflectance Confocal Microscopy With Radial Video Mosaicing for Margin Mapping of Lentigo Maligna and Lentigo Maligna Melanoma

Oriol Yélamos, Miguel Cordova, Nina Blank, Kivanc Kose, Stephen W. Dusza, Erica Lee, Milind Rajadhyaksha, Kishwer S. Nehal, Anthony M. Rossi

JAMA Dermatology 2017 Dec 1;153(12):1278-1284. doi: 10.1001/jamadermatol.2017.3114.

RESUM

Introducció: El tractament del lentigen maligne (LM) i del LM melanoma (LMM) és difícil a causa de l'extensió subclínica i la seva aparició en àrees cosmèticament sensibles. La microscòpia confocal de reflectància (MCR) millora la precisió diagnòstica del LM i LMM i es pot utilitzar per a delimitar els seus marges.

Objectiu: Avaluar si la MCR de mà amb videomosaics radials (MCRM-VR) ofereix una avaluació prequirúrgica precisa dels marges de LM i LMM.

Material i mètodes: Aquest estudi prospectiu incloïa pacients consecutius amb LM i LMM provats per biòpsia situats a la zona del cap i del coll que van consultar des de l'1 de març de 2016 fins al 31 de març del 2017 al Servei de Dermatologia del Memorial Sloan Kettering Cancer Center. Es van estudiar 32 pacients amb MCRM-VR i finalment 22 pacients amb 23 LM o LMM van ser sotmesos a una cirurgia per estadis (staged excision) i es van incloure en l'anàlisi. Es va mesurar la dimensió i àrea de les lesions clíniques, l'àrea dels LM i LMM basada en els resultats de MCRM-VR, l'àrea del defecte quirúrgic estimada per MCRM-VR, i l'àrea del defecte quirúrgic observat final. A més, es van calcular els marges mesurats en mil·límetres estimats per a assolir marges lliures de tumor en cada quadrant basat en els resultats de MCRM-VR i es van comparar amb els marges quirúrgics reals.

Resultats: Es van incloure 22 pacients (12 homes i 10 dones; mitjana d'edat [DE], 69,0 [8,6] anys [rang, 46-83 anys]) amb 23 lesions. L'àrea mitjana (DE) de defecte quirúrgic estimada per MCRM-VR era de 6,34 (4,02) cm^2. L'àrea mitjana (DE) de l'excisió quirúrgica amb marges lliures era de 7,74 (5,28) cm^2. Controlant per l'edat del pacient i la presència o no de cirurgia prèvia, els marges quirúrgics eren una mitjana de 0,76 mm (95% IC, 0,67-0,84 mm; P <0,001) més grans que l'estimació feta per MCRM-VR.

Conclusions: El mapatge de LM i LMM amb MCRM-VR estima defectes similars, però lleugerament més petits, comparats amb la cirurgia per estadis. Per tant, el mapatge de LM utilitzant MCRM-VR pot ajudar a preservar teixit sà, reduint el nombre de biòpsies necessàries en àrees clínicament incertes i es pot utilitzar per a planificar el tractament de LM i LMM i assessorar adequadament els pacients.

Publicació 3: Handheld Reflectance Confocal Microscopy for the Detection of Recurrent Extramammary Paget Disease

Oriol Yélamos, Brian P. Hibler, Miguel Cordova, Travis J. Hollmann, Kivanc Kose, Michael A. Marchetti, Patricia L. Myskowski, Melissa P. Pulitzer, Milind Rajadhyaksha, Anthony M. Rossi, Manu Jain

JAMA Dermatol. 2017 Jul 1;153(7):689-693. doi: 10.1001/jamadermatol.2017.0619.

RESUM

Introducció: La malaltia de Paget extramamària (MPEM) és habitualment refractària a les teràpies quirúrgiques i no quirúrgiques. La identificació de MPEM recurrent o persistent és un repte perquè la malaltia és multifocal i normalment es realitzen múltiples biòpsies a cegues. S'ha utilitzat la microscòpia confocal de reflectància de mà (MCRM) per diagnosticar i mapejar la MPEM primària i, per tant, es podria utilitzar per identificar les recidives de MPEM.

Objectius: Avaluar la precisió diagnòstica de la MCRM en el marc de MPEM recurrent o persistent, així com les seves possibles dificultats de diagnòstic.

Material i mètodes: Aquest estudi prospectiu de sèrie de casos va incloure pacients referits al Servei de Dermatologia del Memorial Sloan Kettering Cancer Center entre l'1 de gener de 2014 i el 31 de desembre de 2016, amb MPEM comprovada per biòpsia en què es va utilitzar la MCRM per controlar la resposta al tractament. Es van incloure 5 pacients i es van avaluar 22 llocs clínicament relacionats amb la malaltia recurrent o persistent utilitzant MCRM i examen histopatològic. En 2 pacients, es van crear videomosaics per avaluar grans àrees. Es va avaaluar la sensibilitat i especificitat de la MCRM en la identificació de MPEM recurrent o persistent, i les causes de resultats falsos negatius segons la seva ubicació, troballes histopatològiques i tractaments previs.

Resultats: Dels 22 llocs clínicament sospitosos avaluats en 5 pacients (4 homes, 1 dona; mitjana [rang] d'edat, 70 [56-77] anys), 9 (el 40,9%) van ser positius per a malaltia recurrent emprant MCRM i confirmats histopatològicament, i 13 (59,1%) llocs van ser negatius per MCRM, però 3 dels 13 van ser positius per a MPEM en l'examen histopatològic. En general, la MCRM tenia una sensibilitat del 75% i una especificitat del 100% en la identificació de MPEM recurrent o persistent. Es van trobar resultats falsos negatius en 2 pacients i es van produir als marges de la MPEM, propers a llocs de biòpsia anteriors. La creació de mosaics de vídeo (o videomosaics) sembla millorar la detecció de MPEM.

Conclusions: La MCRM és una eina auxiliar útil per al diagnòstic de les recidives de la MPEM i es pot utilitzar per guiar les biòpsies d'exploració, reduint així el nombre de biòpsies necessàries per fer un diagnòstic correcte.

Publicació 4: Reflectance confocal microscopy-guided laser ablation of basal cell carcinomas: initial clinical experience

Heidy Sierra, Oriol Yélamos, Miguel Cordova, Chih-Shan Jason Chen, and Milind Rajadhyaksha

J Biomed Opt. 2017 Aug;22(8):1-13. doi: 10.1117/1.JBO.22.8.085005.

RESUM:

Introducció: L'ablació làser permet l'eliminació precisa, ràpida i mínimament invasiva de carcinomes basocel·lulars (CBC) superficials i nodulars incipients (de baix risc). No obstant, la manca de confirmació histopatològica ha estat una limitació per al seu ús generalitzat en la pràctica clínica diària. La microscòpia confocal de reflectància (MCR) és una tècnica d'imatge no invasiva que posseeix resolució cel·lular, pel que pot guiar i ajudar a millorar l'efectivitat de l'ablació làser. A més, l'ús de videomosaics obtinguts a partir de vídeos adquirits directament dins de la ferida làser pot ampliar el camp de visió i ajudar a identificar tumor residual.

Objectiu: Determinar la viabilitat, la qualitat de la imatge i l'efectivitat de l'ablació làser guiada per MCR en CBC de baix risc.

Material i mètodes: Després d'estudis ex vivo, s'ha realitzat un primer estudi sobre l'ús in vivo de l'ablació làser guiada per MCR en 44 CBCs presents en 21 pacients, utilitzant un làser pulsat d'erbi:ytterbium aluminum garnet (Er:YAG) i un agent de contrast (clorur d'alumini). En el primer grup de casos, 10 lesions provinents de 6 pacients van ser tractades amb làser guiat per MCR i després extirpardes per avaluar-ne la histopatologia. Addicionalment, 34 CBCs en 15 pacients van ser tractats amb ablació làser guiada per MCR, amb confirmació immediata de la destrucció del tumor mitjançant només MCR (sense histopatologia). Aquestes lesions van ser seguides amb MCR (de nou, sense histopatologia) als 3, 6 i 18 mesos.

Resultats: La qualitat d'imatge va ser bona en la majoria dels mosaics i videos de l'estudi. Es va observar eliminació de CBC en 19 de 22 casos, amb seguiments que van de 6 a 21 mesos. En un total de 12 casos amb un seguiment d'1 a 3 mesos tampoc s'ha identificat recidiva tumor, tot cal un temps de seguiment més llarg per establir resultats concloents.

Conclusions: Fins al moment, la resolució de les imatges obtinguda amb MCR i videomosaics sembla que és suficient i consistent per controlar l'efectivitat de l'ablació làser de CBCs de baix risc, tant immediatament després de l'ablació com posteriorment durant el seguiment.

Publicació 5: Peri-operative delineation of non-melanoma skin cancer margins in vivo with handheld reflectance confocal microscopy and video-mosaicking

Eileen Flores, Oriol Yélamos, Miguel Cordova, Kivanc Kose, William Phillips, Erica H. Lee, Anthony M. Rossi, Kishwer Nehal, Milind Rajadhyaksha

RESUM

Introducció: L'extirpació quirúrgica dels càncers cutanis no melanoma (CCNM) es guia per l'examen histopatològic dels marges. No obstant, la preparació de la histopatologia consumeix temps, requereix molta mà d'obra i requereix una infraestructura de laboratori addicional. A més, quan la histopatologia indica marges positius, els pacients han de tornar per reexcisions. La microscòpia confocal de reflectància (MCR) amb videomosaics pot definir de manera no invasiva els marges tumorals directament en els pacients i pot guiar la cirurgia en temps real, complementant la histopatologia tradicional.

Objectius: Avaluar un nou mètode d'imatge peri-operatori no invasiu mitjançant l'ús de MCR de mà i videomosaics directament en el llit quirúrgic de CCNM i de forma in vivo.

Material i mètodes: Es van incloure 35 pacients sotmesos a cirurgia de Mohs provinents de la unitat de cirurgia de Mohs del Memorial Sloan Kettering Cancer Center de Nova York. Les imatges de MCR es van realitzar abans i després de la primera etapa de cirurgia, adquirint vídeos al llarg dels marges quirúrgics (epidèrmics, perifèrics i profunds). Posteriorment els videos es es van transformar en videomosaics. Dos avaluadors independents van llegir i avaluar els videomosaics i els vídeos i, posteriorment, es van comparar amb el corresponent resultat histopatològic provinent de la cirurgia de Mohs.

Resultats: Els vídeos i els videomosaics obtinguts amb MCR de mà mostren una qualitat d'imatge acceptable (resolució i contrast) a nivell preoperatori en 32/35 (91%) casos, i a nivell intraoperatori en 29/35 (83%) casos. La delineació preoperatòria de marges tumorals obtinguda a través de MCR es correlaciona correctament amb la histopatologia en 32/35 (91%) casos. La delineació intraoperatòria es correlaciona correctament en 10/14 (71%) casos per la presència de tumor residual i en 18/21 (86%) casos per la seva absència. La sensibilitat/especificitat va ser del 71%/86% i del 86%/81%, respectivament, per a dos avaluadors de vídeomosaics de MCR, i l'acord general entre els avaluadors va ser del 80% i del 83% amb la histopatologia, amb un acord entre avaluadors moderat ($k = 0,59$, $p < 0,0002$). .

Conclusions: Els vídeomosaics de MCR a nivell perioperatori poden orientar la cirurgia de CCNM en temps real, servir de complement a la histopatologia, reduir el temps dedicat a la clínica i reduir la necessitat de reexcisions.

DISCUSSIÓ

La MCR és una tècnica d'imatge amb una resolució lateral d'1 µm, però amb un camp de visió petit entre 0,5 i 1 mm. Com que la seva resolució és quasi histològica, permet avaluar detalls a nivell cel·lular. No obstant, sovint també cal obtenir informació arquitectònica per avaluar millor els tumors de la pell, de manera similar a l'anàlisi histopatològica convencional. Per aconseguir-ho, el MCR tradicional adquireix imatges d'alta resolució que posteriorment s'uneixen automàticament en mosaics d'imatges de fins a 8 x 8 mm. Tanmateix, a vegades les lesions de la pell són més grans de 8 mm o no es poden avaluar amb dispositius tradicionals de sonda ampla, ja que requereixen l'adhesió d'un anell de metall de 2 cm a la pell del pacient. En aquest sentit, es van desenvolupar dispositius de mà per permetre una avaluació dinàmica i lliure en qualsevol àrea anatòmica. Aquests dispositius, més versàtils, tenen l'inconvenient que no tenen la capacitat de generar automàticament mosaics; per tant, l'avaluació de les imatges es redueix a les petites imatges de 0,75 o 1 mm. Per resoldre aquests problemes, hem desenvolupat un algoritme informàtic que permet generar mosaics automatitzats a partir de vídeos obtinguts amb MCRM, anomenats videomosaics. Amb aquests videomosaics es poden avaluar grans àrees de teixit i revisar-les acuradament després de l'adquisició d'imatges.

El nostre algoritme de videomosaica és únic, ja que aborda els 3 grans problemes presents en obtenir imatges in vivo sobre la pell: (i) deformacions a causa de canvis físics (angle, pressió) al contacte entre el microscopi i la pell, (ii) artefactes de moviment bruscos ("salts") causats per canvis bruscos de profunditat o de moviment (iii) diferències de detall i resolució entre imatges consecutives a causa de la dispersió i les aberracions induïdes pels canvis de profunditat i morfologia. Per a solucionar-ho l'algoritme identifica al voltant de 1000 punts clau i els fa coincidir amb la imatge adjacent del video utilitzant algoritmes predifinits com SIFT i RANSAC. A continuació, les dues imatges s'alineen mitjançant transformacions afins que permeten evitar la deformació modelant-la. A més, les propietats de les transformacions afins resultants també s'utilitzen per detectar artefactes de moviment brusc. En altres paraules, quan l'alineació no és possible, l'algoritme detecta automàticament el salt i deixa de fusionar imatges en el videomosaic actual. Això impedeix una fusió incorrecta dels fotogrames que donaria lloc a detalls arquitectònics i cel·lulars incorrectes. Amb la versió actual de l'algoritme quan s'identifica un "salt", la generació de videomosaic s'atura en aquest punt, però es reprèn automàticament al fotograma següent. Això genera múltiples sub-mosaics que es poden col·locar junts manualment o semi-automàticament en un editor d'imatges. Reconeixem que això és subòptim i, idealment, l'algoritme hauria de ser capaç de col·locar els diferents sub-mosaics junts. Una altra manera de solucionar aquesta qüestió seria que la generació de videomosaics esdevingués en viu, de manera que l'operador de MCRM pogués saber si està situat al pla focal adequat o si hi ha algun problema durant l'adquisició d'imatge.

Finalment, l'última novetat del nostre algoritme és l'ús del mètode *graph-cut* per a la fusió d'imatges. Tot i que s'utilitza àmpliament en la fotografia computacional, segons el nostre coneixement, aquesta és la primera aplicació d'aquest mètdode en microscòpia in vivo. El mètode *graph-cut* identifica les àrees de mínimes diferències entre dos fotogrames i els enganxa en aquell punt. Això és important perquè els mètodes típics de fusió d'imatge generalment fan una mitjana de les dues imatges, duent a imatges borroses que poden dur a una pèrdua de detalls cel·lulars. Això permet una visualització nítida de tots els elements presents en els dos fotogrames, que són crucials per a l'avaluació, per exemple, de cèl·lules dendrítiques focals a la perifèria d'un LM/LMM. Per tant, aquest mètode maximitza les característiques presents en els vídeos microscòpics i permet tenir una representació completa de tots els elements presents a les imatges.

En aquesta tesi hem implementat videomosaics automatitzats en diferents escenaris clínics en la gestió de càncers de pell. El primer escenari il·lustra com els videomosaics poden ajudar a millorar l'orientació de la MCRM mitjançant l'ús complementari d'elements de referència com ara talls quirúrgics o anells de paper adhesiu. En aquest sentit, emplaçant elements visibles durant el procés d'adquisició d'imatge, com anells de paper de mides conegudes, hom pot no només millorar la navegació de la MCRM però també realitzar càlculs que permeten estimar amb precisió els marges prequirúrgics de diversos càncers cutanis. Aquesta afirmació s'ha demostrat en el el segon escenari clínic descrit en aquesta tesi, que mostra com el videomosaicisme junt amb elements de referència ajuden a delimitar els marges preoperatoris de LM / LMM i de carcinomes queratinocítics, on es necessita una planificació precisa dels marges quirúrgics en llocs anatòmics irregulars. El nostre mètode de videomosaics pot oferir un procediment diagnòstic i terapèutic simplificat, menys invasiu que les biòpsies tradicionals, i més ràpid que els procediments quirúrgics tipus cirurgia de Mohs o cirurgia per etapes.

Un tercer escenari clínic estudiat en aquesta tesi demostra com el videomosaicisme ajuda a detectar zones focals de càncer dins de grans àrees de teixit, tal com s'ha demostrat per a diagnosticar i seguir casos de MPEM persistent / recurrent, així com detectar CQ residual en ferides quirúrgiques tant després de cirurgia de Mohs com després de l'ablació làser. Això pot tenir un gran impacte sobretot en tumors multifocals i localitzats en zones sensibles com els genitals, en les quals les biòpsies no són sempre possibles o desitjables. En aquest sentit, hem demostrat que els videomosaics incrementen la capacitat de detecció de tumor residual en el cas de la MPEM, amb un augment de la sensibilitat del 57,1% al 100% (sense falsos negatius) mantenint una especificitat del 100% (P = 0,0339). Pel que fa als carcinomes queratinocítics, hem pogut veure que els videomosaics de MCRM permeten identificar tumor residual després

d'ablació làser o després de cirurgia de Mohs, però només a nivell superficial, ja que la resolució de la MCR disminueix molt en profunditats superior a 250 µm. Per tant, creiem que noves tecnologies com l'ús combinat de la MCR juntament amb la tomografia de coherència òptica, amb més penetració en profunditat, podrien permetre una detecció completa del tumor residual, amb menys taxes de falsos negatius.

En resum, en aquesta tesi hem descrit un nou algoritme informàtic per a generar videomosaics automatitzats a partir de vídeos obtinguts amb MCRM. Hem demostrat que els videomosaics amplien el camp de visió de la MCRM, permeten avaluar grans àrees de pell fins i tot en superfícies irregulars, permeten càlculs precisos de distància i àrea que es poden utilitzar per a planificar millor els procediments quirúrgics, milloren la detecció de petits focus de cèl·lules tumorals i permeten una millor orientació durant l'ús de la MCRM juntament amb mètodes de marcatge com ara anells de paper. En un futur pròxim esperem que els videomosaics s'integrin en el programari natiu del MCRM per al seu ús en la pràctica clínica diària, idealment proporcionant videomosaics en directe que permetran automàticament el càlcul de les distàncies.

No obstant, el nostre mètode actual té limitacions i ha de millorar. Les futures línies d'investigació haurien de centrar-se en fer que aquest algoritme sigui més ràpid mitjançant la intel·ligència artificial i els mètodes d'aprenentatge automàtic (actualment es triga uns 10 minuts a generar un videomosaic obtingut a partir d'un vídeo d'1 minut). Un altre camp potencial de millora és l'adquisició simultània de vídeos i videomosaics a diferents profunditats (per exemple, epidermis, unió dermoepidèrmica i dermis) mitjançant l'ús de múltiples fonts làser. Un altre millora potencial seria l'ús simultatni de MCR i tomografia òptica de coherència que permetria arribar a uns 1-2 mm de profunditat. Un altre millora potencial podria ser la visualització directament sobre la pell del pacient o utilitzant sistemes de realitat augmentada o mixta per tal de poder realitzar cirurgia de precisió directament sobre el pacient. Finalment, l'avenç més important per a l'ús d'aquesta tecnologia és que el preu de l'aparell baixi, i en aquest sentit ja existeixen prototips "low cost" de MCRM que permetran que no d'aquí a molt temps tots els dermatòlegs duguem un MCRM de butxaca a la nostra bata, fent del MCRM el dermatoscopi del segle XXI.

CONCLUSIONS

1. El nostre algoritme soluciona els principals problemes trobats en la microscopia cutània in vivo (i) modela les deformacions, (ii) detecta automàticament artefactes produïts per moviment bruscos (discontinuitats) en la seqüència de la imatge i (iii) permet unir de forma robusta diferents imatges superposades de manera flexible, usant un algoritme tipus "graph-cut", sense pèrdua de resolució ni imatges borroses.
2. La MCRM amb videomosaics automatitzats permet obtenir imatges detallades de zones anatòmiques concavoconvexes, corrugades i irregulars sobre àrees grans.
3. Els anells de paper amb mides predefinides són útils per millorar la informació espacial mentre s'utilitza MCRM ja que ajuda a calibrar els videomosaics, permetent així càlculs de distància precisos.
4. La MCRM amb videomosaics automatitzats permet delimitar els marges pre-quirúrgics de LM/LMM de forma precisa (diferència mitjana de 0,76 mm més petita que el defecte quirúrgic real [95% CI, 0,67-0,84 mm; P <0,001]).
5. La MCRM amb videomosaics automatitzats permet delimitar els marges pre-quirúrgics de CBC/CEC, però pot no identificar un component tumoral profund.
6. És possible obtenir vídeos de MCRM dins mateix del llit quirúrgic després de cirurgia de Mohs o després d'ablació làser i convertir-los en videomosaics de bona qualitat.
7. La MCRM amb videomosaics pot detectar petits focus de tumor en el si d'àrees cutànies grans, millorant així el diagnòstic i seguiment de càncers de pell com la MPEM o CBC/CEC després del tractament.
8. La MCRM té una bona precisió diagnòstica (sensibilitat 75% i especificitat 100%) per identificar malaltia recurrent/persistent, que millora mitjançant la incorporació de videomosaics automatitzats.
9. La MCRM i els videomosaics obtinguts dins de ferides quirúrgiques permeten identificar ràpidament carcinomes queratinocítics residuals en la majoria dels casos, però poden no identificar el tumor si és més profund de 250 µm
10. La MCRM amb videomosaics realitzat de forma perioperatòria als marges del càncer de pell pot ajudar el procés quirúrgic, complementa la histopatologia, pot potencial reduir el temps del procediment quirúrigic i i reduir la necessitat de reexcisions.